FIRST ROW TRANSITION METAL COMPLEXES AS TRANSMISSIVE FILTERS FOR ASTRONOMICAL X-RAY POLARIMETRY

Thesis submitted for the degree of

Doctor of Philosophy

at the University of Leicester

By

Andrew Paul Armitage MChem Hons. (University of Leicester)

Department of Chemistry

University of Leicester

July 2011

STATEMENT OF ORIGINALITY

The accompanying thesis submitted for the degree of Ph.D. entitled, *First Row Transition Metal Complexes as Transmissive Filters for Astronomical X-ray Polarimetry*, is based on work conducted by the author in the Department of Chemistry at the University of Leicester, mainly during the period between July 2007 and July 2011. All the work recorded in this thesis is original unless otherwise acknowledged in the text or by reference. None of the work has been submitted for another degree in this or any other university.

Signed…………………………………… Date………………

ANDREW PAUL ARMITAGE

FIRST ROW TRANSITION METAL COMPLEXES AS TRANSMISSIVE FILTERS FOR ASTRONOMICAL X-RAY POLARIMETRY

ABSTRACT

This thesis aims to develop single crystals that can act as transmissive X-ray polarising filters at K-edge energies corresponding to the first row transition metal series (M = Cu–Ti; K-edge range = 8.9–4.9 keV). Discrete square-based pyramidal co-ordination complexes have been targeted in which the apical M–X or M=O bonds display a high degree of intermolecular alignment.

Chapter 1 provides an overview of X-ray polarisation dependence, existing X-ray polarimeters and current materials offering X-ray polarisation capabilities. Finally, a molecular design strategy for the thesis is outlined.

In **Chapter 2**, $[(4,4'-Me_2bipy)_2Cu_2Br_2(\mu-C_2O_4)]$ (**1a**) has been subjected to a successful dichroic evaluation at the Cu (8.9 keV) and Br K-edges (13.5 keV). The origins of the X-ray dichroism in **1a** have been modelled using two complementary theoretical methodologies; i) TD-DFT and ii) multiple scattering theory, which have identified the importance of the apical Cu–Br bond in SBP **1a**.

In **Chapter 3** the motif [(α-diimine)MBr(β-diketonate)] has been targeted as an all purpose platform for the Cu (**3–5**, 8.9 keV), Ni (**6**, 8.4 keV), Co (**7**, 7.7 keV), Fe (**10**, 7.1 keV) and Mn (**11**, 6.4 keV)] K-edges. Highly aligned SBP **3a** has been shown to display X-ray dichroism at the Cu K-edge. For **6**, **7**, **10** and **11**, five co-ordinate metal centres can indeed be accessed using suitably tailored pyridylarylimine chelates; however, the geometries of the metal centres can be anywhere between distorted trigonal bipyramidal and distorted square-based pyramidal while the intermolecular alignment is variable.

In **Chapter 4** macrocyclic tetraphenylporphyrinato (TPP^{2-}) has been employed as a rigid support to fill the basal co-ordination sites in SBP [(TPP)MX] (M = Co, X = Cl (**15a**); M = Co, X = Br (**15b**); M = Fe, X = Br (**16**); M = Mn, X = Br (**17**)] and [(TPP)MO] [M = V (**18**), Ti (**19**)]. Notable X-ray dichroism has been observed at the Co (7.7 keV), Fe (7.1 keV), V (5.5 keV) and Ti (4.9 keV) K-edges in highly aligned **15**, **16**, **18** and **19**, respectively. The observed dichroic features in **15a** and **18** have also been modelled using multiple scattering theory. In addition, compact *hybrid filters* were developed using TPP-modified [(Y$_2$-TPP)FeX] [(Y = Cl, X = Br (**20a**); Y = Br, X = Cl (**20b**); Y = X = Br (**20c**)], which offer multiple K-edges in one molecule.

Chapter 5 explores exclusively halides and oxides of the earlier transition metal elements [Cr (5.9 keV), V (5.5 keV), Ti (4.9 keV)], in which the pre-edge has been observed to reveal the most dominant X-ray polarisation dependence. Hence, M(III) complexes [(nacnac)MCl(β-diketonate] [M = Cr, β-diketonate = dbm (**21**), acac (**22**); M = V, β-diketonate = acac (**23a**), dbm (**23b**); M = Ti, β-diketonate = dbm (**24**)] have been targeted and selected examples have been deliberately oxidised to generate M(IV) oxides [(nacnac)MO(dbm)] [M = V (**25**), Ti (**26**)]. The FEFF code has been used to predict the polarised XAS spectra in an attempt to evaluate the feasibility of materials of this structural type.

Chapter 6 gives overarching conclusions of the key themes of the thesis with a summary that highlight the contributions to the area and science in general.

Glossary of Complexes

Chapter 2

[(4,4'-Me$_2$bipy)$_2$Cu$_2$Br$_2$(μ-ox)]	**(1a)**
[(5,5'-Me$_2$bipy)$_2$Cu$_2$Br$_2$)(μ-ox)]	**(1b)**
[(2,2'-bipy)Cu(μ-ox)]$_n$	**(2a)**
[(4,4'-Me$_2$bipy)Cu(μ-ox)]$_n$	**(2b)**
[(5,5'-Me$_2$bipy)Cu(μ-ox)]$_n$	**(2c)**

Chapter 3

[(2,2'-bipy)CuBr(acac)]	**(3a)**
[(2,2'-bipy)CuBr(bzac)]	**(3b)**
[(2,2'-bipy)CuBr(dbm)]	**(3c)**
[(1,10-phen)CuBr(acac)]	**(4a)**
[(1,10-phen)CuBr(bzac)]	**(4b)**
[(**L$_1$**)CuBr(dbm)]	**(5a)**
[{(**L$_1$**)CuBr(acac)}$_2$Cu$_2$Br$_2$]	**(5b)**
[(**L$_1$**)Ni(μ-Br)(acac)]$_2$	**(6a)**
[(**L$_2$**)NiBr(acac)]	**(6b)**
[(**L$_3$**)NiBr(acac)]	**(6c)**
[(**L$_4$**)NiBr(acac)]	**(6d)**
[(**L$_5$**)NiBr(acac)]	**(6e)**
[(**L$_1$**)CoBr(acac)]	**(7a)**
[(**L$_2$**)CoBr(acac)]	**(7b)**
[(**L$_3$**)CoBr(acac)]	**(7c)**
[(**L$_4$**)CoBr(acac)]	**(7d)**
[(**L$_5$**)CoBr(acac)]	**(7e)**
[(**L$_2$**)Ni(dbm)$_2$]	**(8a)**
[(**L$_3$**)Ni(dbm)$_2$]	**(8b)**
[(**L$_5$**)Ni(dbm)$_2$]	**(8c)**
[(**L$_2$**)Co(dbm)$_2$]	**(9a)**
[(**L$_3$**)Co(dbm)$_2$]	**(9b)**
[(**L$_5$**)Co(dbm)$_2$]	**(9c)**
[(**L$_2$**)FeBr(acac)]	**(10)**
[(**L$_2$**)MnBr(acac)]	**(11)**
[(**L$_2$**)Ni(chp)$_2$]	**(12a)**
[(**L$_3$**)Ni(chp)$_2$]	**(12b)**
[(**L$_2$**)$_2$Ni$_3$(O$_2$CPh)$_6$]	**(13a)**
[(**L$_3$**)$_2$Ni$_3$(O$_2$CPh)$_6$]	**(13b)**
[(**L$_3$**)Ni(O$_2$CPh)$_2$(MeOH)]	**(14)**

Chapter 4

[(TPP)CoBr]	**(15a$_{DCM}$)**
[(TPP)CoCl]	**(15b$_{DCM}$)**
[(TPP)FeBr]	**(16$_{DCM}$)**
[(TPP)MnBr] (toluene solvate)	**(17$_{toluene}$)**
[(TPP)MnBr] (DCM solvate)	**(17$_{DCM}$)**
[(TPP)MnBr] (benzene solvate)	**(17$_{benzene}$)**
[(TPP)VO]	**(18$_{DCM}$)**
[(TPP)TiO]	**(19$_{DCM}$)**
p-ClTPPH$_2$·2HCl	
[(Cl$_2$-TPP)FeBr]	**(20a$_{chloroform}$)**
[(Br$_2$-TPP)FeCl]	**(20b$_{chloroform}$)**
[(Br$_2$-TPP)FeBr]	**(20c$_{chloroform}$)**

Chapter 5

[(nacnac)CrCl(dbm)]	**(21)**
[(nacnac)CrCl(acac)(THF)]	**(22)**
[(nacnac)VCl(dbm)]	**(23a)**
[(nacnac)VCl(acac)]	**(23b)**
[(nacnac)TiCl(dbm)]	**(24)**
[(nacnac)VO(dbm)]	**(25)**
[(nacnac)TiO(dbm)]	**(26)**

Contents

Abbreviations

$\gamma(E)$	absorption co-efficient
Å	angstrom
°	angular degree
δ	chemical shift
σ^2	Debye-Waller factor
°C	degrees Celsius
μ_{eff}	effective magnetic moment
μ	figure of merit
R_γ	figure of merit
ν	infra-red stretching frequency
‖	parallel
⊥	perpendicular
^1H	proton

1,10-phen	1,10-phenanthroline
2,2'-bipy	2,2'-bipyridyl
4,4'-Me$_2$bipy	4,4'-dimethylbipyridyl
5,5'-Me$_2$bipy	5,5'-dimethylbipyridyl

ab initio	from the beginning
acac	acetylacetonate
ATR	attenuated total reflectance
A.U.	arbitary unit
Bis	two
BM	Bohr magneton
bzac	benzoylacetonate
ca.	*circa*
CSD	Cambridge structural database
cf.	*confer*
chp	6-chloro-2-hydroxypryidonate
CI	core ionisation
cm^{-1}	wavenumber
COSMO	conductor-like screening model
CP(PPP)	core-potential basis set
dbm	dibenzoylmethanato
DCM	dichloromethane
DDQ	2,3-dichloro-5,6-cyano-1,4-benzoquinone
DFT	density functional theory
DME	dimethoxyethane
DPA	dipyridylalcohol
e.g.	*exempla gratia*
ESA	European Space Agency
EtOH	ethanol
et al.	and all
EUV	extreme ultra-violet
eV	electron volt
EXAFS	extended X-ray absorption fine structure
FAB	fast atom bombardment
FEFF	effective multiple scattering [code]
g	gram
h	hour
HBr	hydrobromic acid
HCl	hydrochloric acid
HF	Hartree-Fock
H$_2$O	water

hp	2-hydroxypryidonate
idem	previously cited
IR	infra-red
IXO	International X-ray Observatory
K-edge	1s electron ionisation energy
keV	kilo-electron volt
LDOS	local density of states
m	metre
M	molarity
MDP	minimum detectable polarisation
MeOH	methanol
min	minute
ml	millilitre
mmol	millimole
mono	one
mp	melting point
MS	multiple scattering
m/z	mass/charge ratio
nacnac	4-(2,6-diisopropylamino)pent-3-en-2ylidine)-2,6-diisopropylanilide
NBA	nitrobenzyl alcohol
NHC	*N*-hetrocyclic carbene
NIR	near infra-red
NMR	nuclear magnetic resonance
NOE	nuclear Overhauser effect
OEP	octa-ethylporphyrin
OTf	triflate
ox	oxalate
O_2CPh	benzoate
RKS	restricted Kohn-Shah
SBP	square-based pyramidal
SCF	self consistent field
SOMO	single occupied molecular orbital
SRS	synchrotron radiation source
STO	Slater-type orbital
TBP	trigonal bipyramidal
TBPDSBP	trigonal bipyramidal distorted square-based pyramidal
TD-DFT	time dependent-density functional theory
THF	tetrahydrofuran
TMEN	tetramethylethylenediammonium
Torr.	unit of pressure 1 Torr = 1.3158×10^{-3} atmospheres
Tors	torsion
TPP	tetraphenylporphyrinato
tris	three
TZVP	triple zeta (ζ) valence potential
vide infra	see below
vide supra	see above
viz.	*vidalicet*
XANES	X-ray absorption near edge fine structure
XAS	X-ray absorption fine structure
XEUS	X-ray Evolving UniverSe
X-ray	electromagnetic radiation with wavelength in the range, $1 \times 10^{-11} - 1 \times 10^{-8}$ m
ZORA	zeroth order regular approximation

CHAPTER 1

Introduction

1.0 Introduction

This thesis will be concerned with the development of materials in the form of single crystals that can act as transmissive X-ray polarising filters at K-edge energies corresponding to the first row transition metal series [M = Cu (8979 eV), Ni (8333 eV), Co (7709 eV), Fe (7112 eV), Mn (6539 eV), Cr (5989 eV), V (5465 eV) and Ti (4966 eV)]. In particular, discrete Square-Based Pyramidal (SBP) co-ordination complexes will be targeted, in which an apical M–X or M=O bond displays a high degree of intermolecular alignment. Techniques such as polarised X-ray Absorption Spectroscopy (XAS) will be used to determine their X-ray polarisation dependence and their transmission and absorption properties towards X-rays. Where possible, these experimental studies will be supported by theoretical approaches to ascertain the electronic origin of the dichroic behaviour. Ultimately, these materials are being developed with a view to an application as simple transmissive filters for astronomical X-ray polarimetry, whereby they would provide a means of determining the magnitude of polarisation of celestial X-ray emitting astronomical sources at several discrete energies.[1]

1.1 Astronomical X-ray polarimetry: Design brief

Several pieces of information can be obtained by X-ray observations of celestial objects: images, energy spectra, time variation and polarisation.[2] Advances in X-ray astronomy have significantly progressed in the area of imaging and spectroscopic observations, however, the study of polarisation in celestial objects has not progressed since the observation of 19% polarisation in the X-ray emitting Crab nebula, the most unambiguous polarimetric measurement to date.[3–9] X-ray polarimetry can aid in gaining an improved understanding of celestial X-ray-emitting objects and shed light on the emission processes in order to discriminate between competing astrophysical models. The X-ray emission processes in celestial objects have been discussed in depth elsewhere[10] and there are two common emission classes which are noteworthy; thermal and non-thermal. X-ray photons that are emitted *via* thermal process are usually unpolarised unless acted upon by external forces (*e.g.*, large magnetic fields).

Conversely, photons which are not emitted thermally are inherently polarised. Therefore, the magnitude and angle of polarisation as a function of energy can provide data to elucidate competing astrophysical models and identify the underlying emission processes. Astrophysical X-ray polarisation is a challenging measurement to make because a significant number of photons are required to achieve a polarisation sensitivity of 1%, the level expected for many celestial sources.[12] Furthermore, as the sources of interest are typically distant; relatively few photons are received per unit time. As a consequence of these factors and the limitations of current methods for detecting polarisation, there is a lack of sensitive instrumentation to effectively study astronomical X-ray polarisation.[2,11] Based on this underlying problem the need arises to: *design and synthesise a dichroic material which is able to produce differing X-ray transmission spectra for two or more orientations (e.g., 0–360° and angles in between) when polarised X-ray radiation is incident upon itself.*

1.2 Polarisation phenomenon, linear dichroism and Malus' law

It is important to discuss briefly the optical properties of light, how polarisation arises and crucially, how this degree of polarisation can be quantified. Firstly, the application of Malus' law will be introduced.

Electromagnetic waves are transverse and contain electric and magnetic vector components at right angles to each other perpendicular to the direction of propagation. Unpolarised electromagnetic radiation has electric polarisation vectors that oscillate through a continuum of 360° perpendicular to the direction of propagation. Polarisation is the process of confining this continuum of arrays to some percentage of a bias polarisation vector, *e.g.*, plane polarised light contains vectors that are 100% biased to one direction.[13]

A material which can polarise light in such a fashion is termed *dichroic*. To be considered linearly dichroic, unpolarised electromagnetic radiation when incident upon the material experiences varying degrees of transmission as a function of angle.[13] This dichroic effect is dependent on the

directionality of the molecules within the material. Materials with high molecular anisotropy (directionality) tend to exhibit dichroism (Figure 1.1).
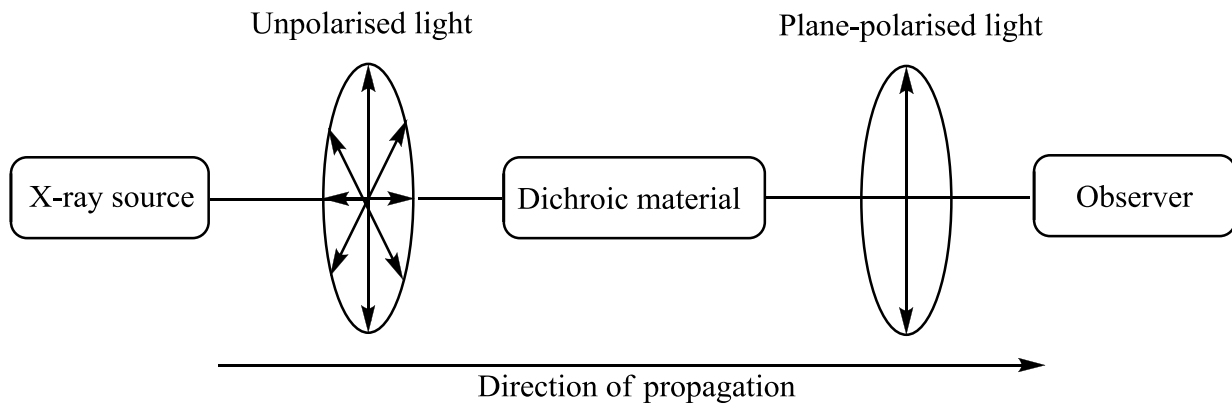
Figure 1.1 A schematic representation of the polarisation process involving a dichroic material. Plane polarised light is allowed to transmit in the plane of the dichroic axis, while other polarisation vectors at angles off the dichroic axis are not transmitted.

Malus' law (Equation 1.1) can be used to calculate the intensity, I, of radiation at a detector using a dichroic filter material with a polarised source of some intensity, I_0, for example, a polarised astronomical X-ray source (Figure 1.2).

$$I = I_0\cos^2\theta$$

Equation 1.1 I = measured intensity, I_0 = initial intensity, θ = polariser angle relative to axis of polarisation.
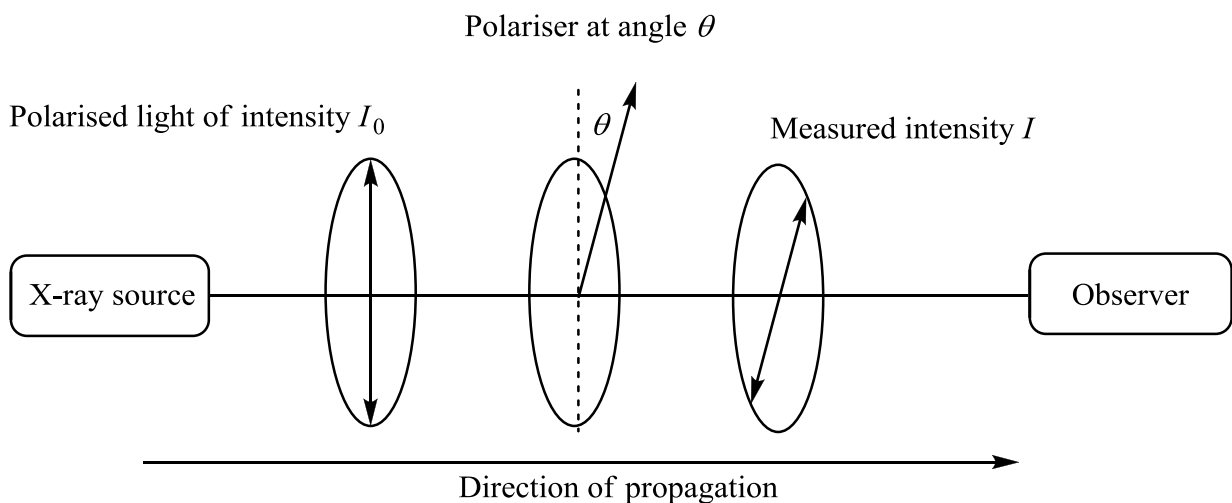
Figure 1.2 A schematic representation of Malus' law.

1.3 Quantifying the performance of a dichroic filter using figures of merit

There are several 'figures of merit' used in the field of polarimetry to quantify the effectiveness or efficiency of a device. A general measure of X-ray dichroism is the value R_γ (Equation 1.2) which takes into account the ratio of the absorption co-efficients of the material in the parallel ($\gamma\|$) and perpendicular ($\gamma\perp$) orientations relative to the incident polarisation axis at the energy of maximum dichroism.[14,15] It is noteworthy that the value of R_γ is useful to evaluate systems of the same structural type. Furthermore, R_γ is independent of thickness.

$$R_\gamma = min\left(\left(\frac{\gamma_\|}{\gamma_\perp}\right), \left(\frac{\gamma_\perp}{\gamma_\|}\right)\right)$$

Equation 1.2 γ = Absorption co-efficient, $\|$ and $\perp$ represent the parallel and perpendicular orientations, respectively.

However, sample thickness and transmittance can be related by the Beers law (Equation 1.3)[16] hence, a more appropriate numerical quantification which takes into account sample thicknesses can be established using the ideal figure of merit (μ)[17] (Equation 1.4). Crudely, μ can be related to R_γ by the transmittance. The ideal thicknesses of dichroic materials can be calculated using X-ray attenuations at various energies, obtained from an online program.[18]

$$T = e^{-\gamma t}$$

Equation 1.3 T = transmittance, γ = absorption co-efficient, t = sample thickness.

$$\mu = M\sqrt{T_\Sigma}$$

Equation 1.4 μ = Ideal figure of merit, M = modulation factor (Equation 1.5), T_Σ = sum of transmittances for $T\|$ and $T\perp$ at the energy of maximum dichroism (R_γ), respectively.

$$M = \left|\frac{(T_\| - T_\perp)}{(T_\| + T_\perp)}\right|$$

Equation 1.5 M = modulation factor, $T\|$ and $T\perp$ are parallel and perpendicular transmittances, respectively.

In the context of X-ray astronomy, a detector uses counting statistics and is dependent on the modulation factor[19] which represents the response of a detector to a 100% polarised source (Equation 1.5). The detector's ability to measure polarisation in an astronomical source is given by the Minimum Detectable Polarisation (MDP) (Equation 1.6) and defines the sensitivity of the polarimeter.[1,10,20] For an astronomical polarimeter, a material must have an MDP of *ca.* 1%.[21,22]

$$\text{MDP} = \frac{3}{MS}\left(2\left(\frac{S+B}{\tau}\right)\right)^{1/2}$$

Equation 1.6 MDP = minimum detectable polarisation, M = modulation factor, S = source counting rate, B = background counting rate, τ = observation time.

It is worth mentioning that the MDP cannot be calculated for a dichroic filter without information on the source flux and the observation time.[17] Therefore, μ is used in latter discussions (since it is independent of S and τ in Equation 1.6) (*vide infra*). However, μ can be inversely related to the MDP using Equation 1.7, thus providing a means of evaluating a material as a potential astronomical X-ray dichroic filter.

$$\text{MDP} = \frac{6}{\mu\sqrt{S\tau}}$$

Equation 1.7 MDP = minimum detectable polarisation, μ = ideal figure of merit, S = source counting rate, τ = observation time.

1.4 Current detector technology and limitations

Conventional X-ray polarimeters rely on reflection[24–26] or Thomson devices.[9,21,27–30] Thomson scattering devices can be constructed using blocks of low atomic number elements such as lithium, which scatter incident radiation onto surrounding detectors (Figure 1.3a). They are appropriate for energies above 10 keV but are insensitive for the low energies required in astronomical polarimetry (*vide infra*).[1] In addition, kinetic energy is lost during the scattering process which diminishes the intensity; this scattering process is inherently inefficient for the low atomic number elements employed. Bragg detectors consist of graphite which can be arranged in a mosaic fashion to enable parabolic dispersive *curved crystal detectors* (Figure 1.3b).

(a)

Telescope optical axis

Scattered
photons

Lithium crystal

Detector

(b)

Incident X-rays

Reflected X-ray polarised perpendicular to
plane of incidence

Large detector

Flat crystal
surface

A) Non-focusing polarimeter

Incident X-rays

Reflected X-ray polarised perpendicular to
plane of incidence

Small detector

Curved crystal
surface

B) Focusing polarimeter
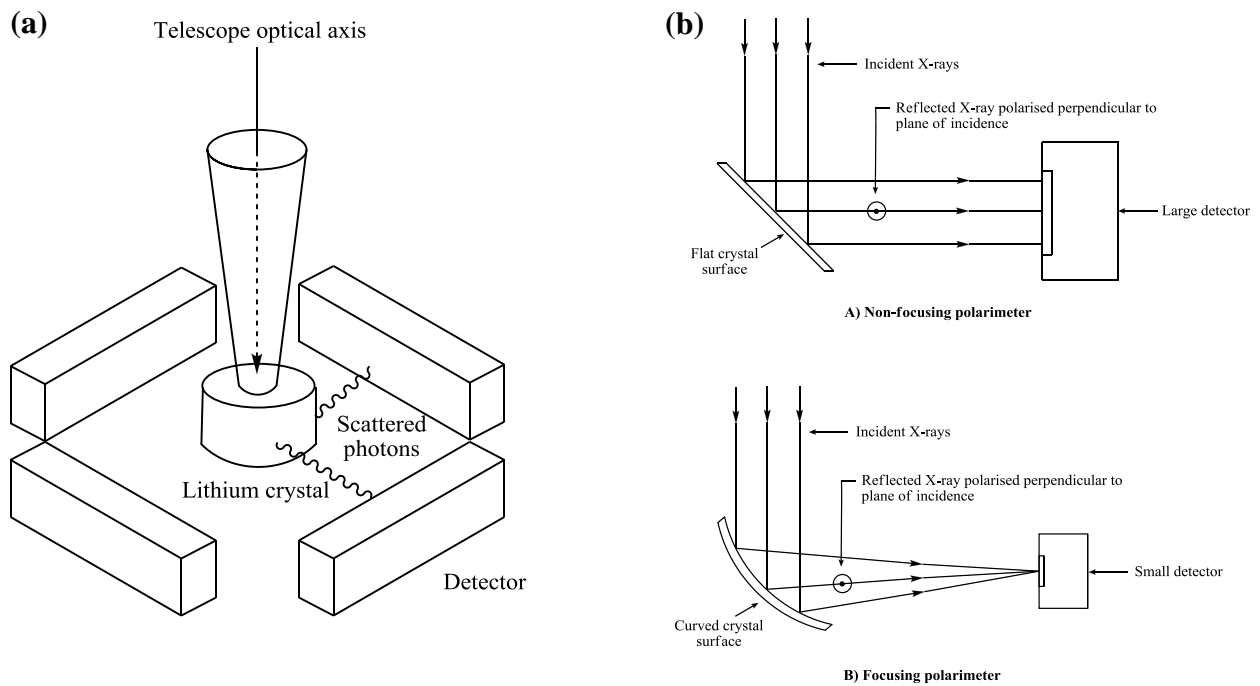
Figure 1.3 Illustrations comparing (a) Thomson scattering detectors[22] and (b) dispersive Bragg reflecting dectectors.[29]

The energy response of a Bragg crystal detector is limited to narrow bands centred on discrete photon energies which make Bragg crystals insensitive to low luminosity sources.[1,31] Nevertheless, they are compatible with the low energies required in astronomical polarimetry. Other types of detectors are known,[11,32] but will not be discussed in detail here. In contrast, an advantage of using dichroic filters as a means of determining polarisation over the conventional detector types is that they can be used with existing focal plane detectors (providing the detector has sufficient energy resolution) and no other optical interface need be applied.

1.5 Astronomical X-ray polarimetry: Target mission

In addition to understanding the fundamental science behind X-ray dichroism and the design of dichroic materials which can support this phenomena, there needs to be an awareness of the potential for any materials created in this thesis to be employed on board orbital observatories. In particular, one such observatory is the X-ray Evolving UniverSe (XEUS) observatory (European and Japanese space agency) which has recently combined with the Constellation-X (American space agency) to become the International X-ray Observatory (IXO) (Figure 1.4) under the cosmic vision programme (2008).[33] In the US Decadal Survey (Astro2010) held in August 2009, IXO was

highly rated and became one of three specifically named missions which Astro2010 deemed high priority. IXO is significant for X-ray polarimetry in that it offers mirrors which are large enough to capture sufficient photons to enable polarimetric measurements of the brighter X-ray-emitting objects in a manageable exposure time. The science case for IXO is beyond the scope of this thesis; however, the details can be found elsewhere.[34]
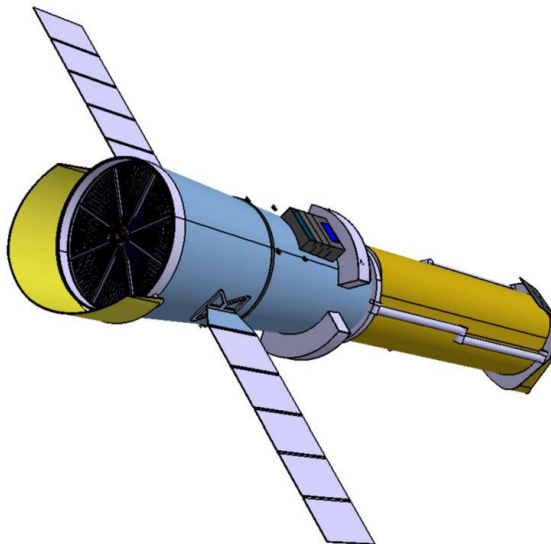
Figure 1.4 An artist impression of the IXO, ESA.

1.6 X-ray absorption in matter

An appropriate technique for studying X-ray dichroism in materials is polarised X-ray Absorption Spectroscopy (XAS) and in particular, synchrotron radiation can be employed which is inherently polarised. The general technique of XAS encompasses two specific regions, namely, X-ray Absorption Near Edge Structure (XANES) and Extended X-ray Absorption Fine Structure (EXAFS). XANES describes the region before and up to *ca.* 50 eV above the 'edge' (*vide infra*). The EXAFS on the other hand, probes the oscillatory structure above the absorption edge as a result of scattering of the photoelectron by neighbouring atoms.[35] Dichroic features are likely to be found in both parts of the polarised XAS. The X-ray absorption co-efficient is specifically determined by measuring the X-ray beam intensity as a function of distance through a material. This could be applied to the decay as it becomes absorbed by the material (Figure 1.5).[35]
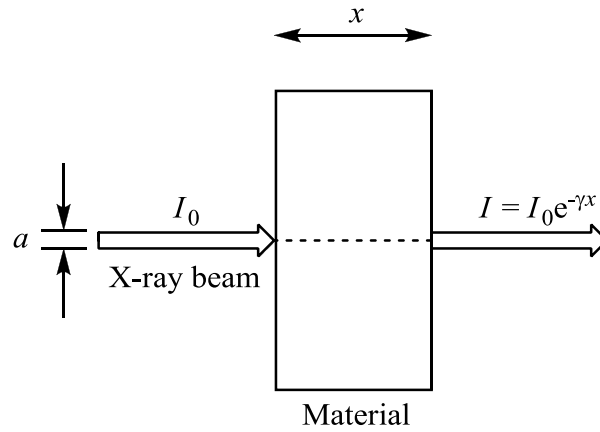
Figure 1.5 A schematic of X-ray absorption. I_0 = initial intensity, I = final intensity, x = material thickness, a = X-ray beam diameter and γ = absorption co-efficient.[35]

With reference to Figure 1.5, when an X-ray beam of diameter a and intensity I_0 is incident on a material of thickness x, the intensity of the incident beam decreases dI as it travels the distance x, therefore, the final intensity can be written, $I = I_0 e^{-\gamma x}$. The absorption co-efficient $\gamma(E)$ can be regarded as the change in intensity over distance ($-\mathrm{d}\ln I/\mathrm{d}x$) and can reveal the total absorption of the material.[37]

A plot of the absorption co-efficient as a function of photon energy reveals three key features (Figure 1.6). Firstly, a general decrease in absorbance with an increase in energy. Secondly, large increases in absorbance occur at specific energies unique to each atom, and thirdly, oscillations occur immediately after each edge. With regard to the second point, these absorbances correspond to the promotion of a core electron and are termed *edges*. These edges are representative of the binding energies of the respective core electrons, for example the K-edge is the excitation energy of the $1s$ electron which occurs at the binding energy of the $1s$ electron, whilst the L-edges are the binding energies of $2s$ and $2p$ electrons. In this work, K-edges are targeted as these are useful when determining the polarisation dependence of the X-ray dichroism phenomena (see *Fermi golden rule*, section 1.6.1) and tend to be strong.
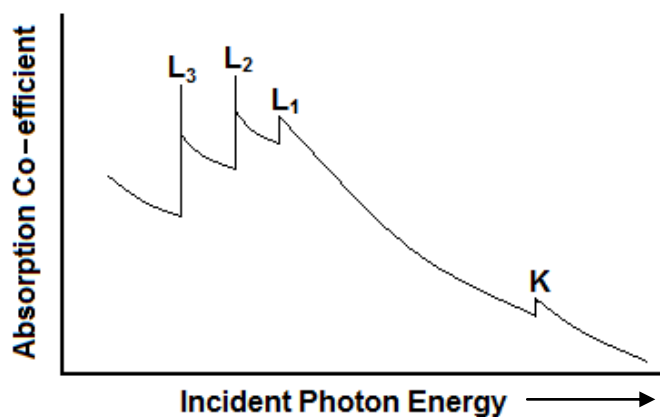
Figure 1.6 A plot depicting the absorption co-efficient as a function of photon energy with the K- and L-edges shown.[35]

1.6.1 Angular dependence of synchrotron X-ray absorption

The absorption co-efficient [$\mu(E)$] of a material arising from the transition of an electron between two states of energy $h\nu$ (h = Plank constant), denoted initial (i) and final (f), upon interaction of these states with a polarisation vector of incident X-ray radiation (ε) can best be described by the *Fermi golden rule* (Equation 1.8).[36,37]

$$\mu(E) = \Sigma |\langle \Psi_i | \boldsymbol{\varepsilon}.\boldsymbol{r_i} | \Psi_f \rangle|^2 \delta(E_i - E_f - h\nu)$$

Equation 1.8 μ = Absorption co-efficient, Ψ_i = initial wavefunction state, $\boldsymbol{\varepsilon}$ = incident X-ray beam polarisation vector, $\boldsymbol{r_i}$ = X-ray beam vector potential, Ψ_f = final wavefunction state, E_i = energy of initial state, E_f = energy of final state, $h\nu$ = energy of the incident radiation.

In a situation involving the promotion of a core $1s$ electron at the K-edge, the initial state is spherically symmetric, therefore only the symmetry of the final state is considered. Hence, a transition into the final state can only occur when the symmetry of this latter state is similar to the incident X-ray polarisation vector, leading to polarisation/angular dependence of the transition.

1.7 Dichroic filter materials

In order to design dichroic materials, it is important to examine existing technologies and take inspiration from their design. In this section, several dichroic materials will be highlighted and their limitations discussed. Firstly, *wire grid* materials such as Polarioid[TM] and its metallic derivatives will be discussed, followed by a more contemporary approach using host–guest chemistry which mimics the conventional wire grid-like material design.

1.7.1 Polaroid^{TM}

Polaroid[TM] was invented in 1929 and developed by Land.[38] Early Polaroid[TM] material, *e.g.*, J-sheet, consisted of a transparent nitrocellulose film doped with iodoquinoline sulphate (herapathite). Needles of this crystalline material were aligned during the manufacturing process by stretching or by the application of a magnetic field. J-sheet is able to absorb light with a polarisation vector parallel to the crystal alignment. Further developments led to H-sheet, which consists of stretched polyvinyl alcohol chains doped with iodine and is the most widely used Polaroid[TM] material. All Polaroid[TM] materials of this type have a comparable feature of using stretched polymer films which leads to a high degree of molecular anisotropy. In particular, Polaroid[TM] materials are often termed wire grid polarisers due to the wire-like behaviour of the stretched polymer chains. Polarisation vectors of visible light that are parallel to the alignment of the molecular chains are absorbed causing the electronic oscillations in the conducting iodine which is doped along the molecular chains. In the perpendicular orientation the light does not interact as strongly (due to destructive interference processes) leading to significant transmittance.

The polarisation dependence (linear X-ray dichroism) of Polaroid[TM] H-sheet was demonstrated by Collins at the iodine K-edge (33175 eV).[39,40] Polarised X-ray photons generated by a Synchrotron Radiation Source (SRS) were incident on Polaroid[TM] H-sheet with the polarisation vector (ε) aligned with ($\alpha = 0°$, see Figure 1.7) and perpendicular to ($\alpha = 90°$, see Figure 1.7) the polymer chains. A schematic of this experiment, which is of a type known as a *crossed Polaroid*[TM] *experiment* is depicted in Figure 1.7. Inspection of experimental XANES spectra at the iodine K-edge obtained by Collins suggests that when ε is parallel to the polymer chains, absorption occurs with low transmittance (Figure 1.8). On rotation of the H-sheet through 90°, the opposite trend can be established. It has been revealed elsewhere[41] that linear dichroism is envisaged to be the result of I[$1s$] $\rightarrow$ I[$4p$] electronic promotions occurring when the polarisation vector is parallel to the iodine-doped polymer chains.
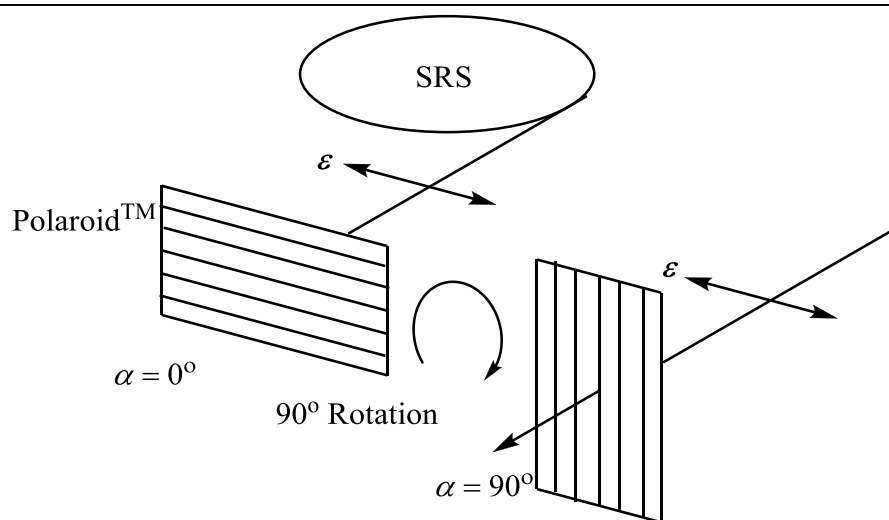
Figure 1.7 A crossed Polaroid^{TM} experiment. Figure recreated courtesy of Collins.[39]
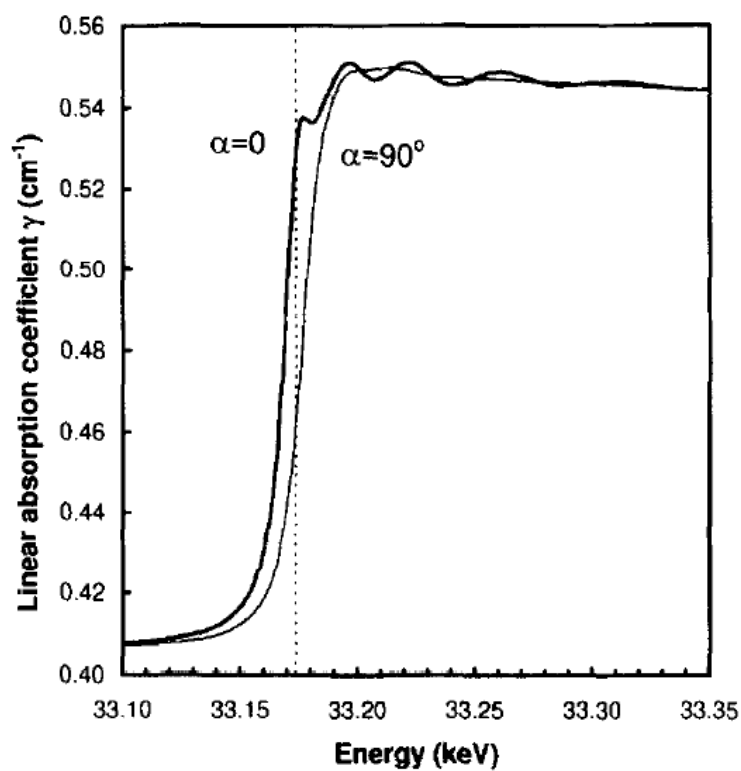
Figure 1.8 Experimental results obtained by Collins showing the transmission ratio in two orientations along with the XANES spectra at the iodine K-edge. [39]

1.7.2   Metallic Polaroid[TM] - type material

A wire grid polariser is able to polarise efficiently if the spacing between the wires (d) is equal or less than half the incident wavelength ($\leq \lambda/2$).[42] Polaroid[TM] H-sheet is effective for the visible light range, but theoretically its efficiency should be diminished at X-ray wavelengths. It is therefore likely, based on the results of Collins, that an alternative mechanism of polarisation is apparent for X-ray wavelengths which differ to that in the visible range. On the other hand, Bird and Parrish demonstrated a wire grid polariser at the Near Infra-Red (NIR) wavelength range[43] and calculated the theoretical wire spacing in the Extreme Ultra-Violet (EUV) range. This has been demonstrated experimentally by Gruntman[44] using gold grating with wire spacings of 2×10^{-6} m revealing 2% polarised transmission through the grating. These observations suggest the possibility that wire grid materials can potentially be used with high energy electromagnetic radiation.

1.7.3   Polaroid[TM] mimics: Inclusion compounds

In an attempt to mimic the highly aligned nature of Polaroid[TM], Harris *et al.* have investigated the use of host–guest chemistry to control the intermolecular alignment. Indeed, single crystal X-ray diffraction studies of these inclusion compounds have shown the guest molecules to be highly aligned in the solid state and moreover, these materials have proved successful dichroic materials towards X-ray polarimetry (*vide infra*).[31,45] In this section, a brief background to (thio)urea/halohydrocarbon inclusion compounds will be discussed with the view of putting into context the work of Harris *et al.*, followed by a discussion of their associated polarimetry.

An inclusion compound is defined as a system in which one species (guest) is spatially confined in another (host). The host matrix is often not acting as a cage nor a clathrate, where a strong host–guest interaction is required, but rather a mutual synergic existence is apparent between the host and guest. Specifically, urea/hydrocarbon synergic co-crystallisations were first reported by Bengen[46] and to date, urea-based inclusion compounds incorporating a range of hydrocarbon guest molecules are known (Figure 1.9).[47]
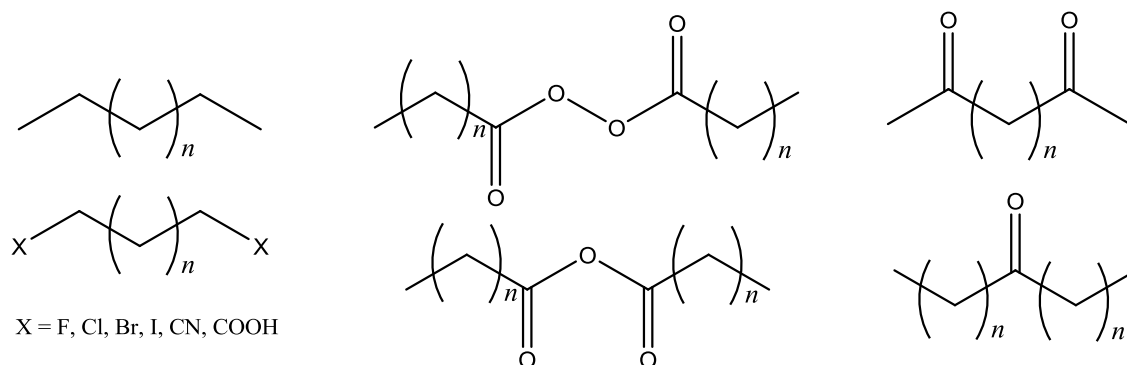
Figure 1.9 Examples of organic guest molecules able to form inclusion compounds with urea.

Harris *et al*. have shown that the halohydrocarbon 1,10-dibromodecane, forms a parallel alignment within a thiourea host tunnel matrix leading to the aligned 1,10-dibromodecane/thiourea inclusion compound (**A**) (Figure 1.10).[15] Indeed, X-ray dichroism at the Br K-edge (13474 eV) in **A** has been observed at ambient temperature when the tunnel axis is aligned with the polarisation vector of synchrotron radiation. However, at ambient temperature, thermal motion caused significant molecular motion of the guest molecules, namely the rotation of the already misaligned (θ) terminal C–Br bonds. As a consequence of this thermal motion, the dichroic efficiency decreased by a factor of 1.5.[47,48]
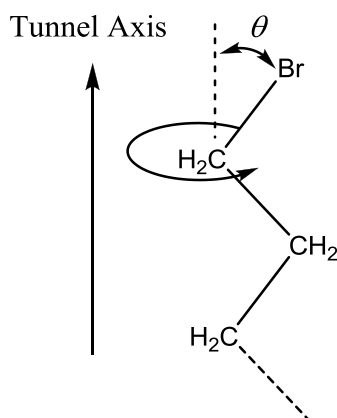
Figure 1.10 Terminal end of the guest in **A** showing the misalignment (θ) and rotation caused by thermal motion relative to the tunnel axis.

To minimise this apparent molecular motion, the more rigid 1-bromoadamantane guest molecule was incorporated within thiourea to give the 1-bromoadamantane/thiourea inclusion compound (**B**)[14] (Figure 1.11). In **B**, the aligned C–Br bonds are significantly constrained so that they do not undergo thermal motion. Hence, an improvement over **A** was evident and furthermore evaluation of **B** as a potential dichroic filter material has revealed an R_γ value of 0.34 (see section 1.3). Note: In this family of compounds the ideal R_γ value is calculated to be 0.31. The experimental XANES spectra of **B** in two orientations denoted Chi (χ) along with its sinusoidal modulation curve are depicted in Figure 1.12.[14,31,45] In this instance, χ_0 refers to the polarisation axis parallel to the tunnel axis and χ_{90} being perpendicular to the tunnel axis. While this dichroism measurement is outside the preferred astronomical range (1−10 keV), it does demonstrate the viability of using the approach which utilises highly ordered materials.

(a)

(b)
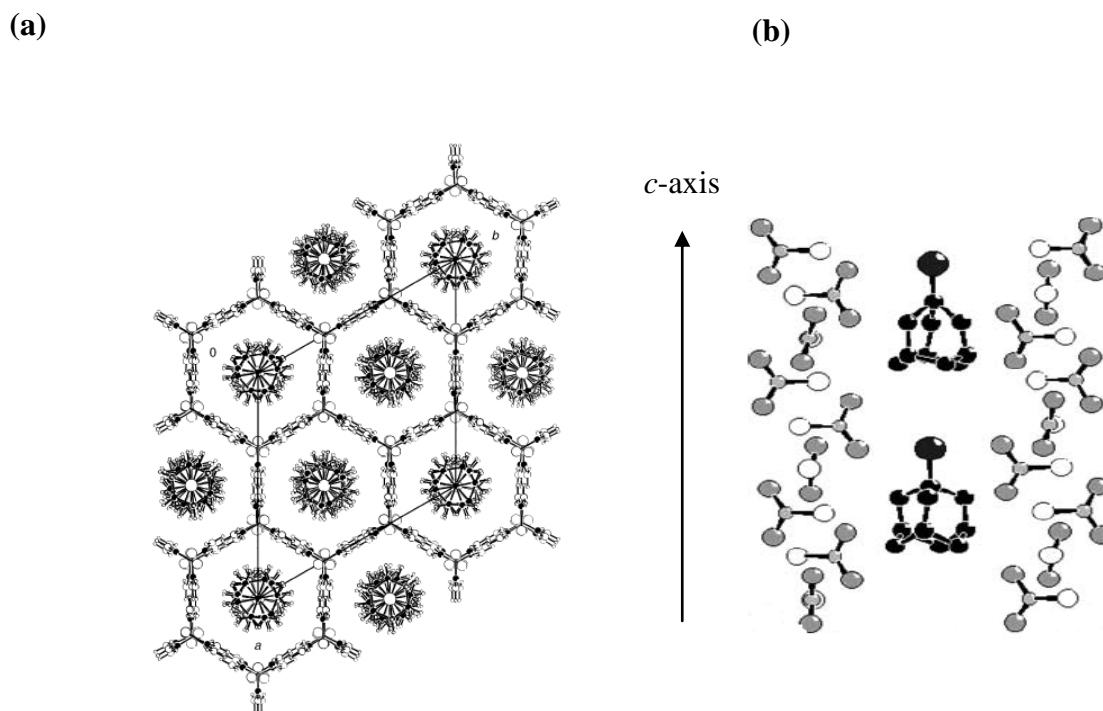
c-axis

Figure 1.11 (a) A view down the crystallographic *c*-axis of **B**. (b) 1-Bromoadamantane guest molecules aligned parallel to the *c*-axis within the thiourea host matrix.
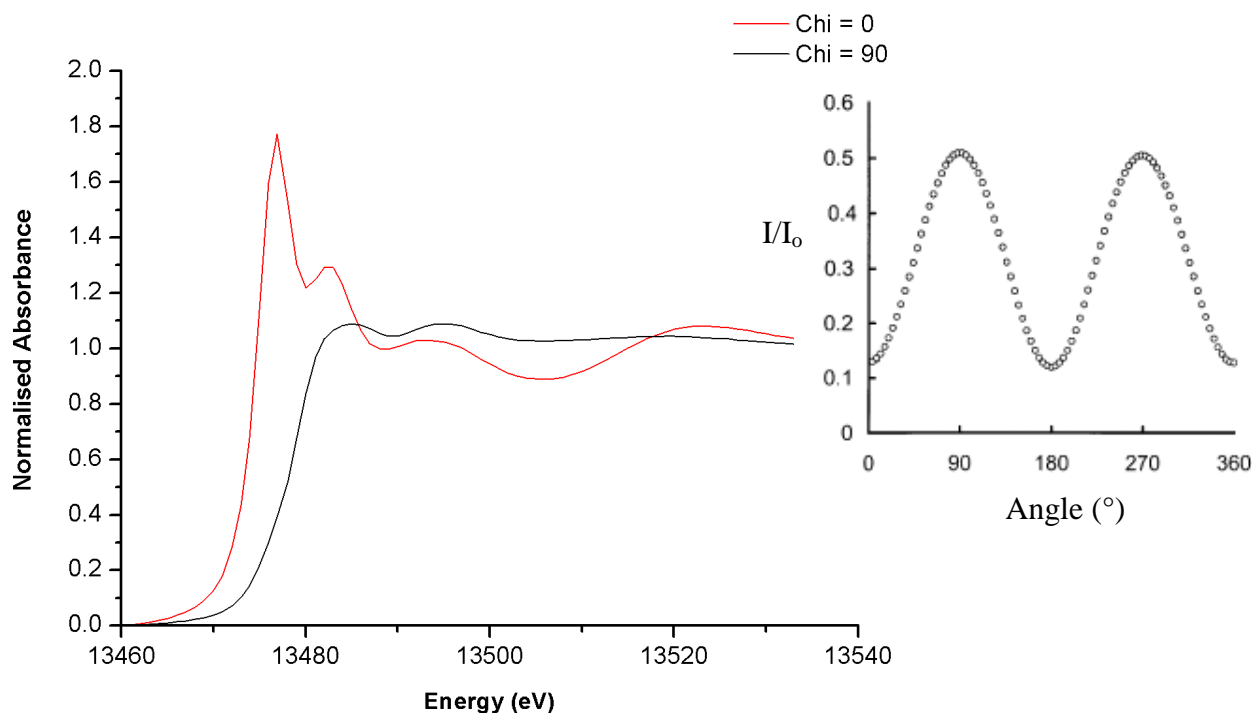
Figure 1.12 Normalised polarised XAS spectra at the Br K-edge for **B** for orientations of χ_0 and χ_{90} along with modulation curve (insert). The figure was recreated by the author using experimental data of Martindale[31,45] and Harris *et al.*[14] Note: The modulation curve does not use normalised data.

1.8 Target K-edges

It is clear on reviewing the properties of dichroic materials previously discussed in this chapter, *viz.*, Polaroid[TM] and inclusion compounds, that a need arises for highly aligned chemical bonds; a feature which needs to be taken into account when designing potential dichroic materials. In this thesis, one of the main aims is to explore materials that display highly aligned chemical bonds in the solid state and hence, mimic the wire grid design. It is also important to consider elements in which their K-edges fall within a specific range, dictated by the science goals of astronomical X-ray polarimetery.[1,49,50]

Astronomical dichroic polarimeters operate over a narrow energy range[51] particularly within the 100–10000 eV range. For the IXO polarimeter for example, the optimum energy range is 500–7000 eV with a resolution of 2–5 eV.[51] At these energies the effective area of a polarimeter instrument onto which X-rays are focused is the greatest (a quantity which is determined by the mirror reflectivity and detector sensitivity, Figure 1.13). Beyond 10000 eV the effective area of the detector decreases rapidly. Although there is some benefit in producing materials with K-edges

around 1000 eV (*e.g.*, Na, Mg), this thesis will only focus on K-edges that correspond to the first row transition metal elements (Ti–Cu; *ca.* 5000–9000 eV); K-edges for a range of elements are listed in Table 1.1. In addition, it is also useful to generate materials around the Fe K-edge (7112 eV), where polarisation from astronomical iron lines may yield useful information.[52,53]
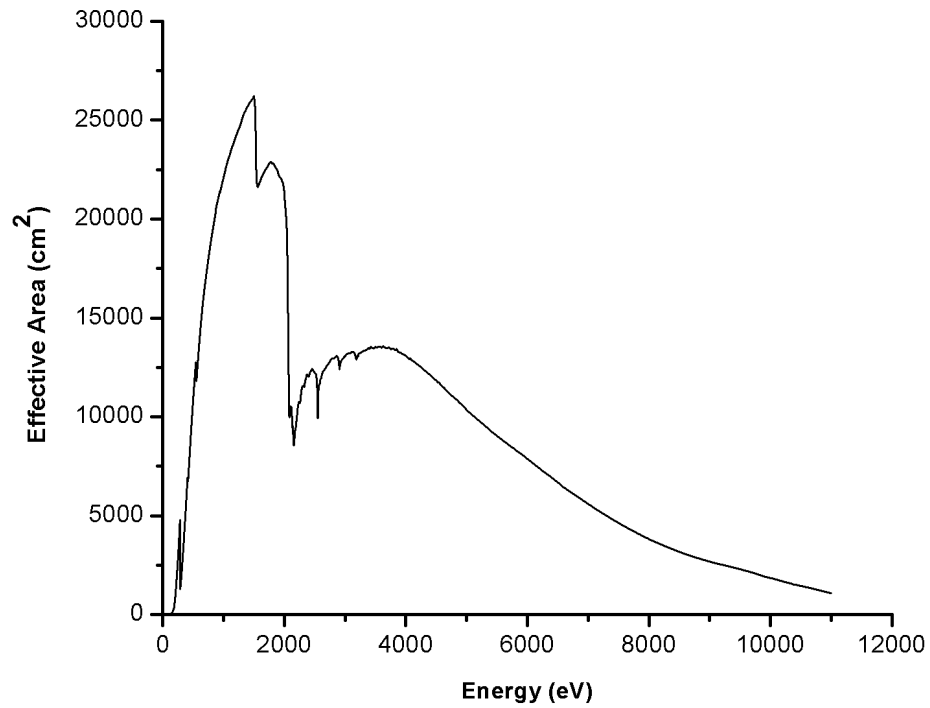
Figure 1.13 Effective focusing area of the mirror and detector as a function of energy for the polarimeter on-board the IXO.

Table 1.1 Selected elements and K-edge energies.[53]

Element	K-edge (eV)
Na	1071
Mg	1303
Cl	2822
K	3608
Ca	4038
Sc	4492
Ti	4966
V	5465
Cr	5989
Mn	6539
Fe	7112
Co	7709
Ni	8333
Cu	8979
Br	13474

1.9 Polarised K-edge X-ray Absorption Spectroscopy (XAS) of transition metal complexes

In the polarised XAS spectra of single crystals of transition metal complexes, several spectral regions are evident, namely, the pre-edge, main-edge and EXAFS regions; all of these regions could, in principle, be exploited for their dichroic phenomena. Early in the history of X-ray absorption spectroscopy, Kronig had suggested that there should be a difference between the XAS spectra of single crystals obtained from polarised and unpolarised X-ray radiation, due to the anisotropy of some crystal systems.[54] Specifically, the appearance of the polarised spectra depends on the direction of the polarisation vector relative to the crystal axis.[55,56]

1.9.1 The pre-edge spectral feature

The distinctive pre-edge feature[57] is a useful spectroscopic handle and can display strong polarisation dependence in polarised XAS (see section 1.11 and Table 1.3 for specific examples). This feature was first discovered by Coster in 1924[58] in the K-edge spectra of $KMnO_4$,[59] and there has been speculation and contention regarding its cause. A brief introduction to the feature is given here while the spectral origins of this peak are discussed in depth in Chapter 2. Interestingly, it is sensitive to a range of variables including, metal centre variation, oxidation state and geometric structure.[60]

a) Origins

It is generally accepted that the cause of the pre-edge peak in first row transition metals is the M [$1s$]→[$3d$] (M = transition metal) quadrupole transition, but this has been misinterpreted. Due to the quadrupole nature of the transition, its intensity would be one thousand times less than the corresponding dipole transition.[61] However, hybridisation of $3d$ orbitals with other orbitals of significant dipole character would enhance its intensity and hence, a more well established interpretation is that orbitals of significant dipole *p*-character mix.[62] Thus, the peak is actually the result of transitions to the dipole component of the [$1s$]→[$3d$–p] hybrid orbital. A full review of the angular dependence of the pre-edge peak is given by Brouder.[63]

b) Geometric effects

The pre-edge intensity decreases with an increase in co-ordination number[64] and co-ordination symmetry.[57,65] For example, some tetrahedral (T_d) co-ordination complexes may display intense pre-edge features as shown in selected absorption spectra at their respective K-edges of several metal oxides (due to appreciable π-bonding) spanning the first row transition metal series, [Ti: $K_6Ti_2O_7$,[67] V: $VO(^iPr)_3$,[67] Cr: $K_2Cr_2O_4$,[68] Mn: $KMnO_4$,[59] Fe: $KFe(OC_{10}H_{13})_4$,[69] Co: $CoAl_2O_4$,[70] Ni: $NiCr_2O_4$[71] and Cu: $CuAl_2O_4$[72,73]]. Regular octahedral (O_h) geometries on the other hand, display no pre-edge feature due to the forbidden nature of the transition; however, distortions in the octahedral co-ordination sphere allow weak transitions.[64]

By examining the irreducible representations of the T_d and O_h point groups (Table 1.2),[74] it is clear that there are five irreducible representations for the T_d point group and ten for the O_h point group. In the T_d point group the T_2 component contains both dipole (p) and quadrupole (d) overlapping functions, whereas in the O_h point groups no functions overlap. Therefore, there is significant dipole-quadrupole mixing in tetrahedral co-ordination complexes to allow an intense pre-edge feature.[60]

Table 1.2 Irreducible representations and functions for the T_d and O_h point groups.

	T_d	
	p (Linear)	d (Quadratic)
A_1		$x^2-y^2+z^2$
A_2		
E		$(2z^2-x^2-y^2, x^2-y^2)$
T_1	(R_x, R_y, R_z)	
T_2	(x, y, z)	(xz, yz, xy)

	O_h	
	p (Linear)	d (Quadratic)
A_{1g}		$x^2-y^2+z^2$
A_{2g}		
E_g		$(2z^2-x^2-y^2, x^2-y^2)$
T_{1g}	(R_x, R_y, R_z)	
T_{2g}		(xz, yz, xy)
A_{1u}		
A_{2u}		
E_u		
T_{1u}	(x, y, z)	
T_{2u}		

In complexes displaying the square-planar geometry (D_{4h}), the E_g function is common to both linear and quadratic functions, based on inspection of character tables. Thus, on this premise, these are able to display pre-edge features. However, it is likely that these are due to geometrical distortions. For example $CuCl_2 \cdot 2H_2O$, [creatinium]$_2$[CuCl$_4$] (see Chapter 2 for detailed discussion) and K_2[Ni(CN)$_4$]. Although these possess inherently high symmetry, their pre-edges are weaker, despite the p–d hybridisation. However, it is worthy of note that despite these weaker pre-edge features for the D_{4h} point groups, appreciable sharp features can be observed on the absorption edge corresponding to [1s]→[4p] transitions.[75]

With regard to the two geometric isomers of the five co-ordinate system, namely trigonal bipyramidal (TBP) (D_{3h}) and SBP (C_{4v}), both geometries contain hybridised p–d orbitals (overlaps occur in the E' irreducible representation for D_{3h} and E and a_1 irreducible representations for C_{4v}). In addition, the latter, along with the associated low symmetry of the point group, gives rise to a significantly enhanced pre-edge feature. Wong *et al.* showed with a series of vanadium oxides, the variation of co-ordination geometry on the pre-edge feature[76] (Figure 1.14) highlighting the significance of a SBP geometry. The vanadium(V) species V_2O_5 displays a SBP geometry and a sharp pre-edge peak is prominent in the XANES spectra at the V K-edge. Interestingly, the apical oxygen atom is significantly longer than the basal oxygen atoms.[77] In contrast, the vanadium(II) species VO adopts a sodium chloride-like solid state structure[78] and as expected, no significant pre-edge peak is evident for this regular centrosymmetric octahedral VO_6 unit. Between these two limits lie the vanadium(III) V_2O_3,[79] vanadium(IV) V_2O_4,[80,81] and vanadium(III/IV) V_4O_7[82] species which all adopt varying degrees of octahedral distortion and hence, weaker pre-edge features are prominent. The more intense pre-edge feature observed in V_2O_4 is the result of the vanadium metal centre being displaced significantly from the centre of the octahedron, leading to a heavily distorted six co-ordinate geometry.
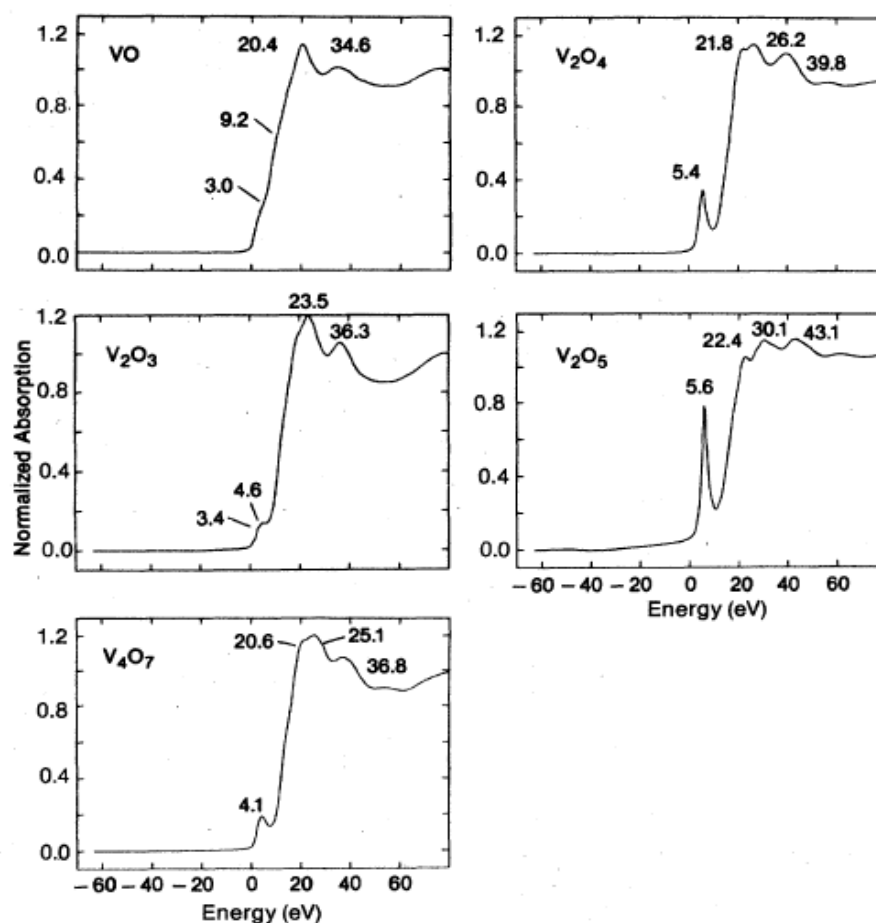
Figure 1.14 XANES spectra of a series of vanadium oxides.[76]

c) Metal centre variation

It has been shown elsewhere[83] that the pre-edge intensity is related linearly to the number of $3d$-electrons, with d^0 complexes generally displaying the largest peak height.[84] The cause of this observation is not fully understood but it has been theorised to be the result of transitions to unoccupied $3d$ orbitals. However, since the former discussion (section 1.9.1a) surmises that the origin of the pre-edge is not quadrupole ($1s \rightarrow 3d$), this conclusion is likely to be incorrect. A more plausible explanation is that the extent of the empty p-state overlap would increase with the decrease in the number of d-electrons, thus the greater p-contribution results in a stronger dipole allowed transition.[60]

1.9.2 Main-edge and EXAFS dichroism

In addition to the pre-edge and its potential polarisation dependence (see section 1.9.1), it is notable that only few detailed discussions exist regarding polarisation dependence in the main-edge and EXAFS region.[61,85] Herein, investigations will be made to attempt to observe X-ray dichroism not only at the pre-edge, but also at the main-edge and EXAFS regions. Moreover, with reference to previous discussion in this chapter (section 1.9.1), attempts will be made to appropriately enhance the pre-edge feature.

1.10 Five co-ordinate geometries: SBP *vs.* TBP

In order to distinguish between the ambiguous five co-ordinate geometric forms, SBP and TBP, Addison *et al*. have described the τ-value (Equation 1.9 and Figure 1.15)[86] which will be referred to frequently in this thesis. The τ-value utilises the largest bond angles obtained from crystallographic data to generate a linear arbitrary scale between zero and one. If the value of τ is zero the geometry can be described as regular SBP; conversely if the value of τ is one, the geometry can be assigned to a regular TBP. In between these two extremes, a τ-value of 0.5 can be best described as Trigonal Bipyramidal-Distorted Square-Based Pyramidal (TBPDSBP).

$$\tau = \frac{\alpha - \beta}{60}$$

Equation 1.9 τ = Tau value, α = largest angle, β = second largest angle.

$$\tau = \alpha - \beta/60 \ (180-180)/60 = 0 \qquad \tau = \alpha - \beta/60 \ (180-120)/60 = 1$$
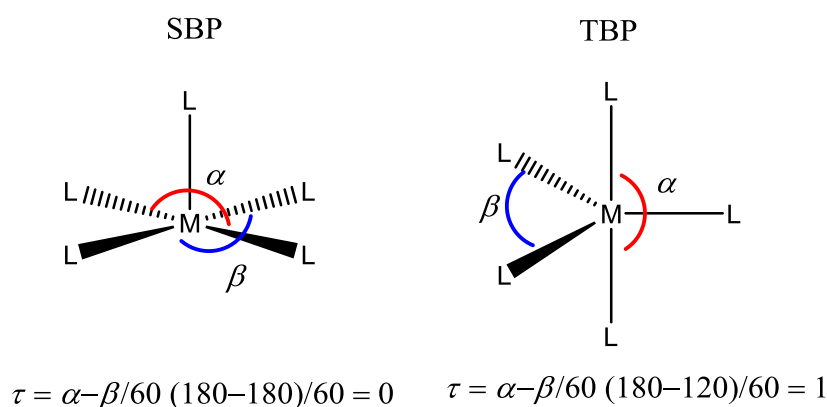
Figure 1.15 A graphical representation of the τ-value.

1.11 Examples of co-ordination complexes showing polarisation

In this section, the focus will be on literature reports where single crystals of various transition metal-containing complexes have shown polarisation dependence and, in particular, at the pre-edge peak. Table 1.3 gives a comprehensive list of all discrete transition metal complexes in the form of single crystals that have been the subject of polarised XAS. What are not shown however, are the numerous examples of network metal oxides (*e.g.*, TiO_4,[87-88] TiO_2,[89] V_2O_5,[76,87,90–92] and CrO_4[93]), metal depositions (*e.g.*, Langmuir–Blodgett films) and polymeric materials which have shown polarisation dependence; these are described in detail by Brouder.[63]

Table 1.3 Single crystals of discrete 3*d* transition metal complexes displaying polarised XAS spectra.[a]

Complex	Geometry	Reference
$[Co(NH_3)_6][ClO_4]_2[Cl]·KCl$	Distorted octahedral	94
$K_3[Cr(CN)_6]$	Distorted octahedral	75
$[CuCl_4][creatinium]_2$	Distorted square planar	See Chapter 2 (section 2.7.1).
$CuCl_2·2H_2O$	Distorted square-planar	See Chapter 2 (section 2.7.1).
$[Cu(1-methylimidazole)_2Cl_2]$	Distorted square-planar	95
$[Cu(1,2-dimethylimidazole)_2Cl_2]$	Distorted square-planar	95
$[Cu(2-methylpyridine)_2Cl_2]$	Distorted square-planar	95,96
$[Cu(imidazole)_2Cl_2]$	Distorted square-planar	95,96
$[Cu(imidazole)_4][ClO_4]_2$	Distorted square-planar	95,96
$[Cu(imidazole)_4][NO_2]_2$	Distorted square-planar	95,96
$[Cu(1,3,5-trimethylpyrazole)_4][BF_4]_2$	Distorted square-planar	95
$[Cu(1,3,5-trimethylimidazole)_4][ClO_4]_2$	Distorted square-planar	95,96
$[Cu(II)cyclam][S(C_6F_5)_2]$	Square-planar	96
$[Cu(II)cyclam][ClO_4]_2$	Square-planar	97
$[(porph)Fe]$	Square-planar	98
$K_3[Fe(CN)_6]$	Distorted octahedral	75
$Na_2[Fe(CN)_5(NO)]·2H_2O$	Distorted octahedral	75
$K_2[Ni(CN)_4]·H_2O$	Distorted square-planar	75
$[Ni(1,2-dicyanodithiolatoethane)_2]$	Square planar	99
$[Ni(diacetyloxime)_2][NBu_4]$	Distorted square-planar	100
$K_2[Mn(CN)_5]$	Distorted square-based pyramidal	75
$K_3[Mn(CN)_6]$	Distorted octahedral	75
$[Rh(en)_3][Mn(CN)_5N]_2$	Distorted octahedral	101
$[VO(malonato)_2][H_2tmen]·2H_2O$ (**E**)	Square-based pyramidal	102
$[VO(acetylacetonate)_2]$ (**F**)	Square-based pyramidal	103
$[VO(oxyoxime)_2]$	Square-based pyramidal	104

a) XAS spectra recorded at the corresponding metal K-edge.

On inspection of Table 1.3, it can be noted that, out of the 26 examples listed, 12 are copper-containing (50%), followed by three examples each from vanadium, manganese and iron. In addition, only one example each is found for chromium and cobalt. Interestingly, on further scrutiny of their co-ordination geometries, it is apparent that for the copper- and nickel-containing systems, the predominant geometry is square-planar. However, the pre-edge intensities reported for these

square-planar species are weak. On the other hand, for the vanadium(IV) oxide species **E** and **F**, where the geometries can best be described as SBP, the pre-edge is notably intense. For the manganese and chromium systems octahedral geometries pre-dominate along with only weak pre-edge features in their XAS spectra, while for the five co-ordinate manganese complex $K_2[Mn(CN)_5]$ an intense pre-edge feature is again observed. Given the desirable intense pre-edge features displayed by vanadium-containing **E** and **F** (Figure 1.16), a more thorough description of their structural and morphological features is warranted as are the results of the XANES studies. Both **E** and **F** display five co-ordinate SBP geometries (**E**, $\tau = 0.03$; **F**, $\tau = 0.02$) based on a VO core bound by two chelating O-donor ligands. Unlike neutral **F**, **E** exists as a cation-anion pair with the cation (tetramethylenediamonium, H_2TMEN) acting as a host matrix. In addition, a molecule of water is weakly bound in the sixth co-ordination site.
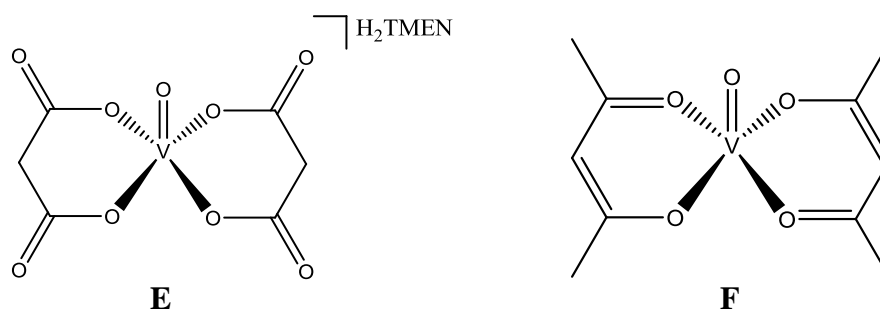
Figure 1.16 Complexes **E** and **F**.

The molecular packing of neutral **F** reveals two molecules in the unit cell which are highly aligned in the solid state with respect to neighbouring V=O bonds (tors: OV···VO = 180°). Likewise, the inclusion compound **E** is highly aligned within the tetramethylethylenediamonium tunnel matrix, where the V=O bonds are uniformly aligned in one direction in a fashion similar to the previously described 1-bromoadamantane/thiourea inclusion complex **B** (see section 1.7.3). In both cases the V=O bonds are aligned with the longest morphological crystal axis. Single crystals of **E** and **F** were aligned with the longest crystal axis parallel to the polarisation axis of synchrotron radiation and rotated such that the XANES spectra were recorded between two principal orientations corresponding to the single crystal being aligned parallel (0°) and perpendicular (90°) to the polarisation axis. This also corresponds to the V=O bond being aligned parallel and perpendicular

to the polarisation axis of the incident synchrotron radiation. In **F** only two spectra were recorded (0° and 90°), whilst in **E**, spectra were recorded through 360°. The XANES spectra of **E** and **F** both reveal similar spectral features, although only the XANES of **E** is shown herein (Figure 1.17). Firstly, a pre-edge peak is prominent at *ca*. 5450 eV, which notably changes in intensity as a function of angle of rotation. In addition, an intense main-edge peak is evident at *ca*. 5465 eV, which also appears to change in intensity as a function of angle, although the change is less dramatic than at the pre-edge and indeed is not highlighted by the authors.
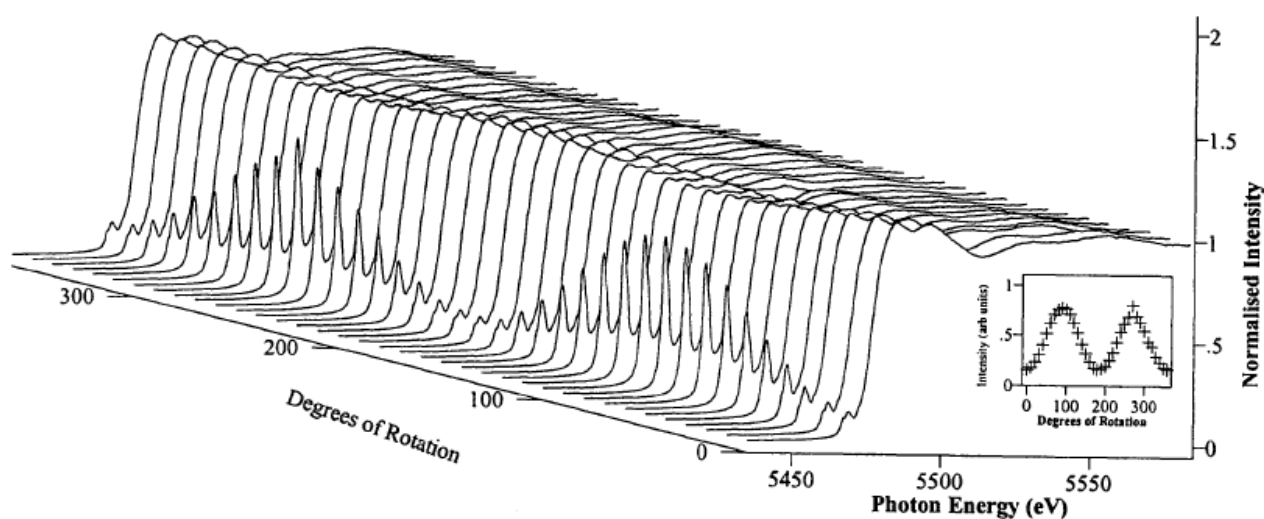
Figure 1.17 XANES plots as a function of angle of a single crystal of **E** with the modulation curve obtained from the pre-edge feature.[102]

The pre-edge peaks in the XAS spectra of **E** and **F** have been assigned to the V [$1s$] → V [$3d_{z^2}$] quadrupole transitions in which the intensity has been increased significantly with *p–d* mixing from the O [$2p_z$]; the orbital mixing is the result of the non-centrosymmetric, low symmetry C_{4v} geometry. The polarisation dependence of this transition is due to the orbitals being projected along the V=O bond, such that when the polarisation is aligned with the V=O bond, the Fermi condition is satisfied (see Equation 1.8) resulting in a *z*-polarised core electron transition.

1.12 Synchrotron beamstation considerations

Several beamlines will be used during the course of this study, namely, Daresbury station 16.3 along with Diamond Light Source stations I16, B16 and I18. It is notworthy that station I18 is a microfocus beamline and is only 70% polarised. In general, the X-ray electric vector was polarised horizontally.

Single crystals of target compounds can be mounted on a multi-directional goniometer capable of 360 degrees of geometric rotation confined to χ (Chi, goniometer axis rotation) and φ (Phi, spindle axis rotation) directions (Figure 1.18a). This thesis will be primarily concerned with χ rotations, with some mention in passing of φ rotations in Chapter 2. Figure 1.18b describes these particular χ and φ rotations with reference to a polarised synchrotron beam. In a typical experiment, a polarised synchrotron beam would be incident on the face of a single crystal mounted on the goniometer spindle (the single crystal parallel to the goniometer spindle is known for the purpose of this discussion as the crystal axis). The mounted single crystal would then be rotated about the polarisation axis of the incident X-ray beam and XAS measurements could be taken between two extreme orientations; χ_0 (X-ray beam polarisation vector parallel to the crystal axis) and χ_{90} (X-ray beam polariation vector perpendicular to the crystal axis).

(a)   **(b)**
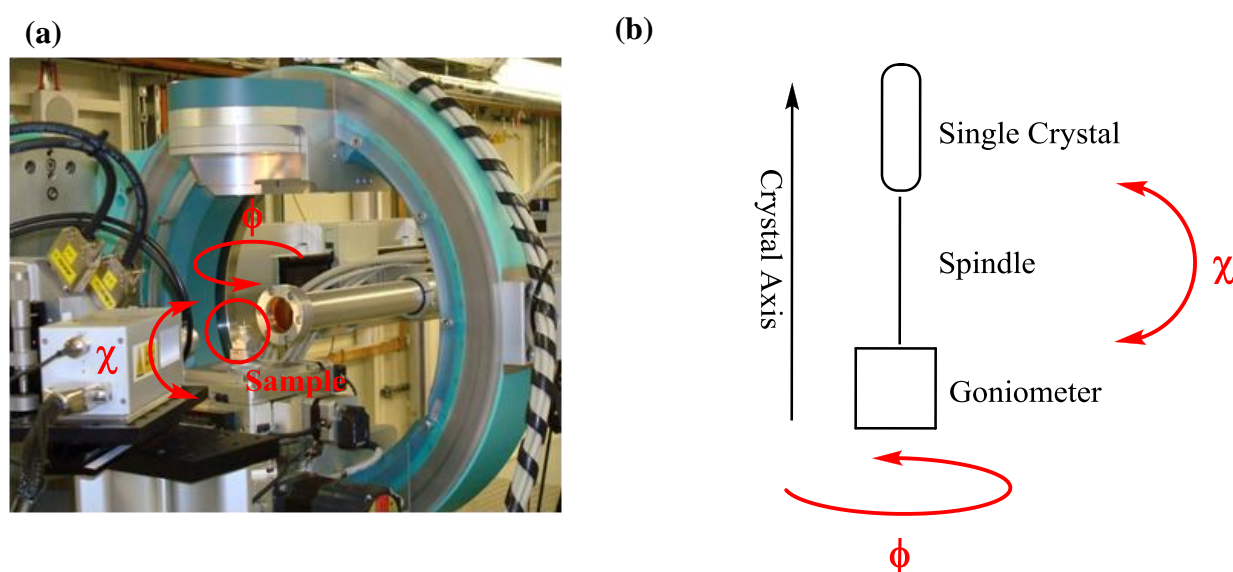
Figure 1.18 (a) The goniometer from Diamond station B16 along with (b) A schematic showing the χ and φ crystal rotations about a polarised synchrotron beam.

1.13 Molecular design criteria

From the above discussion it is apparent that a single crystal containing a five co-ordinate metal complex adopting a SBP geometry and displaying appreciable intermolecular alignment of an apical M-X bond should, in principle, lead to material capable of showing significant X-ray dichroism at the corresponding metal K-edge in one or more parts of the XAS spectrum (*viz.*, pre-edge, main-edge and EXAFS). Therefore, this thesis will aim to develop this design strategy for a range of first row metal centres using a metal oxide or metal halide as the aligned bond. Chelating ligands will be employed to fill the four other basal coordination sites.

As many first row transition metals prefer to adopt six co-ordinate octahedral co-ordination species, significant effort will be placed on modifying the chelating ligand to protect the sixth co-ordination site (see Chapter 3) and to drive the SBP geometry over the TBP form. Electronic features of particular metal centres which enforce SBP geometries will also be investigated (see Chapter 2).

1.14 Aims and objectives

- The principal aim of this thesis is to develop suitable metal-ligand platforms that can accommodate metal K-edge energies that fall in the specific range 100–10000 eV [M = Cu (8978 eV), Ni (8333 eV), Co (7709 eV), Fe (7112 eV), Mn (6539 eV), Cr (5989 eV), V (5465 eV) and Ti (4966 eV)], with a view to examining their potential to behave as transmissive X-ray polarising filters. More specifically, single crystals of discrete SBP complexes will be targeted in which an apical M–X (X = halide) or M=O bond exhibits a high degree of intermolecular alignment; the general types of metal-ligand frameworks to be developed are depicted in Figure 1.19.
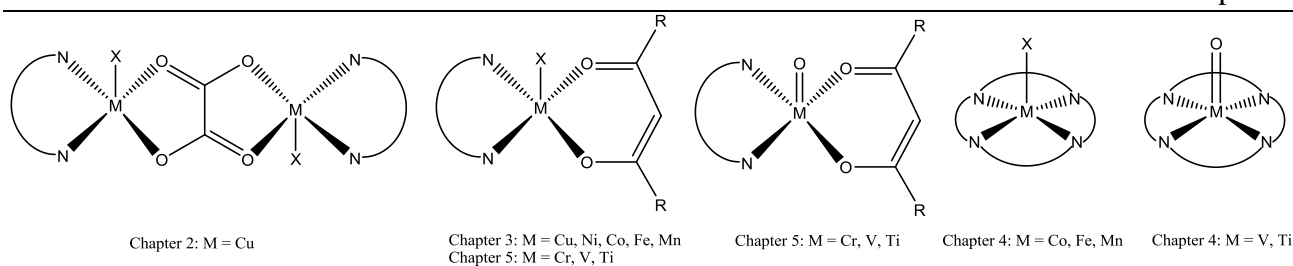
Figure 1.19 Target metal–ligand frameworks to be used in this thesis (X = halide, R = hydrocarbyl).

- Polarised XAS will be employed to evaluate the performance of selected materials as X-ray dichroic filters. While previous studies into polarisation dependent single crystal XAS have focused on the pre-edge region, it is the aim in this work to probe not just the pre-edge region, but also the furthest XANES and EXAFS regions.

- The dichroic behaviour of these target materials is to be modelled using two theoretical approaches with the aims of:

  i) Rationalising the process of X-ray dichroism in terms of the core electron dynamics on absorption of a polarised X-ray photon and identifying the final states.

  ii) Investigating the relative merits of the two theoretical approaches in describing/modelling identical X-ray dichroism events.

- In addition, the appropriate theoretical technique will be employed to predict the spectral features of selected materials as a means of identifying promising candidates to screen experimentally by polarised XAS.

1.15 References

1) N. P. Bannister, K. D. M. Harris, S. P. Collins, A. Martindale, P. S. Monks, G. Solan and G. W. Fraser, *Exp. Astron.*, 2006, **21**, 1.

2) S. Kitamoto, H. Murakami, Y. Shishido, N. Gotoh, T. Shibata, K. Saito, T. Watanabe, J. Kanai, E. Tekanaka, K. Nagasaki, M. Yoshida, D. Takei and M. Morii, *Rev. Sci. Instrum.*, 2010, **81**, 023105.

3) M. C. Weisskopf, E. H. Silver, H. L. Kestenbaum, K. S. Long and R. Novick, *Astrophys. J.*, 1978, **220**, L117.

4) M. C. Weisskopf, G. G. Cohen, H. L. Kestenbaum, K. S. Long, R. Novick and R. S. Wolff, *Astrophys. J.*, 1976, **208**, L125.

5) H. L. Kestenbaum, G. G. Cohen, K. S. Long, R. Novick, E. H. Silver, M. C. Weisskopf and R. S. Wolff, *Astrophys. J.*, 1976, **210**, 805.

6) J. H. Oort and T. Walraven, *Bull. Astron. Inst. Neth.*, 1956, **12**, 285.

7) W. Ku, H. L. Kestenbaum, R. Novick, and R. S. Wolff, *Astrophys. J.*, 1976, **204**, L71.

8) L. Sartori and P. Morrison, *Astrophys. J.*, 1967, **150**, 385.

9) R. Novick, R. Berthelsdorf, R. S. Wolff, M. C. Weisskopf and R. Linke, *Astrophys. J.*, 1972, **174**, L1.

10) M. C. Weisskopf, R. F. Elsner, D. Hanna, V. M. Kaspi, S. L. O'Dell, G. G. Pavlov and B. D. Ramsey, *ArXiv Astrophyics e-prints*, 2006, arXiv:astro-ph/0611483.

11) E. Costa, P. Soffitta, G. Di Persio, M. Feroci, L. Pacciani, A. Rubini, R. Bellazzini, A. Brez, L. Baldini, L. Latronico, N. Omodei and G. Spandre, *ArXiv Astrophyics e-prints*, 2002, arXiv:astro-ph/0207440.

12) F. Mukeri, S. Basso, R. Bellazzini, A. Brez, E. Costa, V. Cotroneo, S. Di Cosimo, S. Fabiani, F. Lazzarotto, G. Matt, M. Minuti, G. Pareschi, M. Pinchera, A. Rubini, P. Soffitta, G. Spandra and G. Tagliaferri, *Mem. Soc. Astron. Ital.*, 2010, **81**, 488.

13) E. Hecht, *Optics*, Addison-Wesley, Reading, MA, 4th edn, 2001.

14) M.-H. Chao, B. M. Kariuki, K. D. M. Harris, S. P. Collins and D. Laundy, *Angew. Chem., Int. Ed.*, 2003, **42**, 2982.

15) S. P. Collins, D. Laundy, K. D. M. Harris, B. M. Kariuki, C. L. Bauer, S. D. Brown and P. Thompson, *J. Phys.: Condens. Matter*, 2002, **14**, 123.

16) H. K. Hughes, *Appl. Opt.*, 1963, **2**, 937.

17) D. Cotton, LU-X-POL-DL-02, *personal communication*, 2009.

18) B. L. Henke, E. M. Gullikson and J. C. Davis, X-ray interactions: photoabsorption, scattering, transmission, and reflection at E=50–30,000 eV, Z=1-92, *Atomic Data and Nuclear Data Tables*, 1993, **54**, 181.

19) R. Novick, in *IAU Colloq. 23: Planets, Stars, and Nebulae: Studied with Photopolarimetry*, ed. T. Gehrels, University of Arizona Press, 1974, p. 262.

20) P. Soffita, L. Baldini, R. Bellazzini, A. Brez, E. Costa, G. Di Persio, L. Latronico, N. Omodei, L. Pacciani and G. Spandre, *Nucl. Instrum. Methods. Phys. Res., Sect. A*, 2003, **510**, 170.

21) E. Costa, P. Soffita, R. Bellazzini, A. Brez, N. Lumb and G. Spandre, *Nature*, 2001, **411**, 662.

22) R. Bellazzini, L. Baldini, A. Brez, E. Costa, L. Latronico, N. Omodei, P. Soffitta and G. Spandre, *Nucl. Instrum. Methods Phys. Res., Sect. A*, 2003, **510**, 176.

23) W. L. Bragg, *Proc. Cambridge Philos. Soc.*, 1914, **17**, 43.

24) R. A. Gowen, B. A. Cooke, R. E. Griffiths and M. J. Ricketts, *Mon. Not. R. Astron. Soc.*, 1977, **179**, 303.

25) R. E. Griffiths, B. A. Cooke and M. J. Ricketts, *Mon. Not. R. Astron. Soc.,* 1976, **177**, 429.

26) H. W. Schnopper and K. Kalata, *Astron. J.*, 1969, **74**, 854.

27) J. R. P. Angel, R. Novick, P. Vanden Bout and R. Wolff, *Phys. Rev. Lett.*, 1969, **22**, 861.

28) R. S. Wolff, J. R. P. Angel, R. Novick and P. Vanden Bout, *Astrophys. J.*, 1970, **160**, L21.

29) M. Hart, *Nucl. Instrum. Methods Phys. Res., Sect. A*, 1992, **316**, 416.

30) J. R. Lemen, G. A. Chanan, J. P Hughes, M. R. Laser, R. Novick, I. T. Rochwarger, M. Sackson and L. J. Tramiel, *Sol. Phys.*, 1982, **80**, 333.

31) A. Martindale, N. P Bannister, K. D. M. Harris, G. A. Solan, S. P. Collins, Y. Champouret, V. K. Muppidi, G. W. Fraser and M. Roy, *Proc. SPIE*, 2007, **6686**, 66860.

32) A. Martindale, *Novel Instrumentation for Astronomy*, Ph.D. Thesis, University of Leicester, 2008.

33) C. Erd, *ESA science missions: Plans of the cosmic vision programme*, ESTEC, 2011, https://escies.org/download/webDocumentFile?id=49230 (accessed 16/01/2012).

34) ESA Assessment Study Report, *IXO: Revealing the Physics of the Hot Universe*, ESA/SRE(2011)2, 2011.

35) J. J. Rehr and R. C. Albers, *Rev. Mod. Phys.*, 2000, **72**, 621.

36) A. Bianconi, J. Garcia, M. Benfatto, A. Marcelli, C. R. Natoli and M. F. Ruiz-Lopez, *Phys. Rev. B*, 1991, **43**, 6885.

37) S. I. Zabinsky, J. J. Rehr, A. Ankudinov, R. C. Albers and M. J. Eller, *Phys. Rev. B*, 1995, **52**, 2995.

38) E. H. Land, *J. Opt. Soc. Am.*, 1951, **41**, 957.

39) S. P. Collins, *Nucl. Instrum. Methods Phys. Res., Sect. B*, 1997, **129**, 289.

40) S. P. Collins, *J. Synchrotron Rad.,* 1998, **5**, 744.

41) T. Yokoyama, K. Kaneyuk, H, Sato, H. Hamamatsu and T. Ohta, *Bull. Chem. Soc. Jpn.*, 1995, **68**, 469.

42) J. P. Auton, *Appl. Opt.*, 1967, **6**, 1023.

43) G. R. Bird and M. Parrish, *J. Opt. Soc. Am.*, 1960, **50**, 866.

44) M. Gruntman, *Appl. Opt.*, 1995, **34**, 5732.

45) A. Martindale, N. P. Bannister, D. Cotton, G. W. Fraser, K. D. M. Harris, B. Kariuki, B. Palmer, S. P. Collins, G. A. Solan, A. Armitage and M. Roy, *SPIE Newsroom*, 2009, DOI: 10.1117/2.1200904.1585.

46) F. Bengen, *Ger. Patent*, OZ 12438, 1940.

47) K. D. M. Harris and J. Thomas, *J. Chem. Soc., Faraday Trans.*, 1990, **86**, 2985.

48) K. D. M. Harris, S. P. Smart and M. D. Hollingsworth, *J. Chem. Soc., Faraday Trans.*, 1991, **87**, 3423.

49) N. P. Bannister, The scientific case for dichroic X-ray polarimetry filters, *personal communication*, 2009.

50) N. P. Bannister, Problems X-ray polarimetry can solve, *personal communication*, 2009.

51) N. P. Bannister, Identifying target energies and materials, *personal communication*, 2009.

52) D. Gondek, A. A. Zdziarski, W. N. Johnson, I. M. George, K. McNaron-Brown, P. Magdziarz, D. Smith and D. E. Gruber, *Mon. Not. R. Astron. Soc*., 1996, **282**, 646.

53) A. Thompson and D. Vaughan, *X-Ray Data Booklet*, University of California, LBNL/PUB-490 Rev 2, 2001.

54) R. de L. Kronig, *Z. Phys.*, 1932, **75**, 191.

55) C. D. Cooksey and S. T. Stephenson, *Phys. Rev.*, 1933, **43**, 670.

56) S. T. Stephenson, *Phys. Rev.*, 1933, **44**, 349.

57) H. Fricke, *Phys. Rev.*, 1920, **16**, 202.

58) D. Z. Coster, *Z. Phys.*, 1924, **25**, 83.

59) H. Hanson and W. W. Beeman, *Phys. Rev.*, 1949, **76**, 118.

60) T. Yamamoto, *X-Ray Spectrom.*, 2008, **37**, 572.

61) R. A. Bair and W. A. Goddard, *Phys. Rev. B*, 1980, **22**, 2767.

62) T. E. Westre, P. Kennepohl, J. G. DeWitt, B. Hedman, K. O. Hodgson and E. I. Solomon, *J. Am. Chem. Soc.*, 1997, **119**, 6297.

63) C. Brouder, *J. Phys.: Condens. Matter*, 1990, **2**, 701.

64) F. Farges, G. E. Brown, Jr and J. J. Rehr, *Phys. Rev. B*, 1997, **56**, 1809.

65) U. C. Srivasta and H. L. Nigam, *Coord. Chem. Rev.*, 1973, **9**, 275.

66) F. Farges, G. E. Brown, Jr and J. J. Rehr, *Geochim. Cosmochim. Acta*, 1996, **60**, 3023.

67) T. Tanaka and S. Yoshida, Metal oxide catalysts, in *X-ray Absorption Fine Structure for Catalysts and Surfaces,* ed. Y. Iwasawa, World Scientific, Singapore, 1996, p. 304.

68) Y. Wang, Y. Ohishi, T. Shishido, Q. H. Zhang, W. Yang, Q. Guo, H. L. Wan, and K. Takehira, *J. Catal.*, 2003, **220**, 347.

69) A. L. Roe, D. J. Schneider, R. J. Mayer, J. W. Pyrz, and J. Widom and L. Que, Jr, *J. Am. Chem. Soc.*, 1984, **106**, 1676.

70) J. A. Rodriquez, S. Chaturvedi, J. C. Hanson, A. Albornoz and J. L. Brito, *J. Phys. Chem. B*, 1998, **102**, 1347.

71) F. Farges, G. E. Brown, Jr, P. E. Petit and M. Munoz, *Geochim. Cosmochim. Acta*, 2001, **65**, 1665.

72) T. Yamamoto, T. Tanaka, S. Suzuki, R. Kuma, K. Teramura, Y. Kou, T. Funabiki, and S. Yoshida, *Top. Catal.*, 2002, **18**, 113.

73) $CuAl_2O_4$ exists as 66.5% tetrahedral and 33.5% octahedral forms.

74) F. A. Cotton, *Chemical Applications of Group Theory,* Wiley and Sons, New York, 2nd edn, 1970.

75) N. Kosugi, T. Yokoyama and H. Kuroda, *Chem. Phys.*, 1986, **104**, 449.

76) J. Wong, F. W. Lytle, R. P. Messmer and D. H. Maylotte, *Phys. Rev. B*, 1984, **30**, 5596.

77) H. G. Bachmann, F. R. Ahmed and W. H. Barnes, *Z. Kristallogr. Mineral*, 1961, **115**, 110.

78) N. Schönberg, *Acta Chem. Scand.*, 1954, **8**, 221.

79) R. E. Newnham and Y. M. de Haan, *Z. Kristallogr.*, 1962, **117**, 235.

80) G. Anderson, *Acta Chem. Scand.*, 1956, **10**, 623.

81) F. Théobald, R. Cabala and J. Bernard, *J. Solid State Chem.*, 1976, **17**, 431.

82) M. Marezio, D. B. McWhan, P. D. Dernier and J. P. Remeika, *J. Solid State Chem.*, 1973, **6**, 419.

83) M. Fernández-García, *Catal. Rev.-Sci. Eng.*, 2002, **44**, 59.

84) T. Yamamoto, *Adv. X-Ray Chem. Anal.*, 2007, **38**, 45.

85) T. A. Smith, J. E. Penner-Hahn, M. A. Berding, S. Doniach and K. O. Hodgson, *J. Am. Chem. Soc.*, 1985, **107**, 5945.

86) A. W. Addison, T. N. Rao, J. Reedijk, J. van Rijn and G. C. Verschoor, *J. Chem. Soc.*, *Dalton Trans.*, 1984, 1349.

87) S. Stizza, M. Benfatto, A. Bianconi, J. Garcia, G. Mancini and C. R. Natoli, *J. Phys. C*, 1986, **8**, 691.

88) B. Poumellec, P. J. Durham and G. Y. Guo, *J. Phys.: Condens. Matter*, 1991, **3**, 8195.

89) R. Brydson, H. Sauer, W. Engel, J. M. Thomas, E. Zeitler, N. Kosugi and H. Kuroda, *J. Phys.: Condens. Matt*er, 1989, **1**, 797.

90) T. Tanaka, H. Yamashita, R. Tsuchitani, T. Funabiki and S. J. Yoshida, *J. Chem. Soc., Perkin Trans.*, 1988, **84**, 2987.

91) T. D. Tullius, W. O. Gillum, R. M. K. Carlson and K. O. Hodgson, *J. Am. Chem. Soc.*, 1980, **102**, 5670.

92) S. Stizza, G. Mancini, M. Benfatto, C. R. Natoli, J. Garcia and A. Bianconi, *Phys. Rev. B.*, 1989, **40**, 12229.

93) H. Nakamatsu, T. Mukoyama and H. Adachi, *Jpn. J. Appl. Phys., Suppl.*, 1993, **32**, 23.

94) S. Wang, G. S. Waldo and J. E. Penner-Hahn, *Physica B*, 1989, **158**, 253.

95) M. A. Berding, S. Doniach, K. O, Hodgson, J. E. Penner-Hahn and T. A. Smith, *EXAFS and near-edge structure - III,* ed. J. E. Penner-Hahn, B. Hedman and K. O. Hodgson, Springer-Verlag, Berlin, 1984, p. 58.

96) T. A. Smith, J. E. Penner-Hahn, M. A. Berding, S. Doniach and K. O. Hodgson, *J. Am. Chem. Soc.*, 1985, **107**, 5945.

97) J. H. Choy, J. B. Yoon and H. Jung, *J. Phys. Chem. B*, 2002, **106**, 11120.

98) S. Wang, G. S. Waldo, R. M. Fronko and J. E. Penner-Hahn, *Physica B*, 1989, **158**, 119.

99) T. Hatsui, Y. Takata and N. Kosugi, *J. Synchrotron Rad.*, 1999, **6**, 376.

100) T. Hatsui, Y. Takata and N. Kosugi, *J. Synchrotron Rad.*, 1999, **6**, 379.

101) J. Yano, J. Robblee, Y. Pushkar, M. A. Marcus, J. Bendix, J. M. Workman, T. J. Collins, E. I. Soloman, S. DeBeer George and V. K. Yachandra, *J. Am. Chem. Soc.*, 2007, **129**, 12989.

102) D. Collinson, C. D. Garner, E. Pidock, J. F. W. Mosselmans and N. A. Young, *J. Synchrotron Rad.*, 1999, **6**, 364.

103) D. H. Templeton and L. K. Templeton, *Acta Cryst.*, 1980, **A36,** 237.

104) D. Collinson. C. D. Garner, G. Grigg, C. M. McGrath, J. F. W. Mosselmans, E. Pidcock, M. D. Roper, J. M. W. Seddon, E. Sinn, G. Thornton, J. F. Walsh and N. A. Young, *J. Chem. Soc., Dalton Trans.*, 1998, 2199.

CHAPTER 2

Bimetallic copper(II) compounds as materials for astronomical X-ray polarimetry: A combined experimental and theoretical study

2.0 Bimetallic copper(II) compounds as materials for astronomical X-ray polarimetry: A combined experimental and theoretical study

In this chapter, the synthesis and structural characterisation of a number of bimetallic and polymeric copper(II) co-ordination compounds will be described, with a view to examining their performance as potential X-ray dichroic materials. An in-depth study of the dichroic behaviour of **1a** will be discussed (*vide infra*) on the basis of results obtained from polarised X-ray Absorption Spectroscopy (XAS). Furthermore, these XAS results will be modelled using two independent theoretical approaches; i) Time Dependent-Density Functional Theory (TD-DFT), a molecular orbital approach and ii) a Multiple Scattering (MS) theory, a scattered wave approach.

2.1 Target oxalate-bridged dicopper(II) bromide compounds

A search of the Cambridge Structural Database (CSD),[1] using the five co-ordinate CuX(Y,Y)$_2$ [X = Cl, Br; Y,Y = N,N or O,O bidentate ligand] unit as the inputted search parameter, has identified bimetallic, square-based pyramidal (SBP) copper(II) chloride complexes, [(2,2′-bipy)$_2$Cu$_2$Cl$_2$(μ-oxalato)]^2 (**A**), [(1,10-phen)$_2$Cu$_2$Cl$_2$(μ-oxalato)]^3 (**B**) and [(DPA)$_2$Cu$_2$Cl$_2$(μ-oxalato)]^{4,5} (**C**) (Figure 2.1) as promising candidates that fulfil the general molecular design criteria (albeit with chloride) outlined in Chapter 1. Surprisingly, their copper(II) bromide analogues have not been crystallographically characterised. Complexes **A**–**C** all feature a ClCu(μ-oxalato)CuCl core in which the two Cu–Cl bonds are approximately held in parallel alignment, facilitated by the influence of a planar *oxalato* bridging ligand. In addition, a high degree of intermolecular ordering is observed in all three compounds, which is particularly evident in **B**. In compound **A**, due to the *cis*-configuration adopted by the adjacent Cu–Cl units and the geometrical requirements of the metal centres, a minor deviation from a mutually parallel alignment is observed (tors: ClCu⋯CuCl = 10.21°). In contrast, in **B** and **C**, where a *trans*-configuration is adopted, the ideal parallel Cu–Cl bond alignment can be achieved (tors: ClCu⋯CuCl = 180.00°).
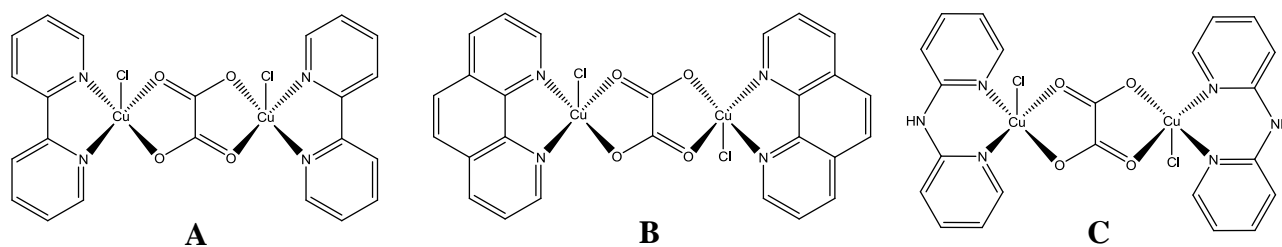
Figure 2.1 Previously reported oxalate-bridged dicopper(II) chloride complexes **A**–**C**.

Closer inspection of these structural motifs has revealed a key role played by the N,N-chelating ligand. In **A** and **B** the N,N-chelates, *viz.* 2,2′-bipy and 1,10-phen, are highly planar, conjugated ligand systems and help promote intermolecular graphitic interactions. Whereas in **C**, the presence of an sp^3 NH unit puckers the N,N-ligand away from planarity, leading to some disorder in the intermolecular packing. As a consequence of the puckering, the τ-value[6] of **C** increases, resulting in a more distorted SBP geometry than that in **A** and **B** [$\tau = 0.48$ (**C**), *cf.* 0.11 (**A**) and 0.44 (**B**)]. Given the more desirable intra- and intermolecular structural characteristics exhibited by **A** and **B**, their copper(II) bromide counterparts have been targeted as potential dichroic filters.

2.2 Synthesis and characterisation of bimetallic copper(II) bromide compounds (1)

(**1a**) N,N = 4,4'-Me$_2$bipy
(**1b**) N,N = 5,5'-Me$_2$bipy
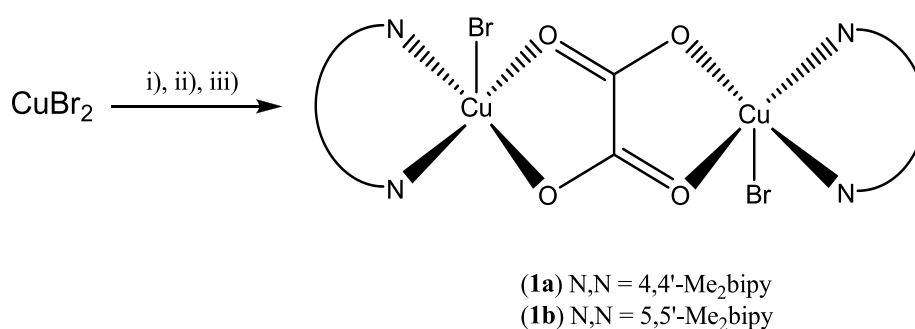
Scheme 2.1 *Reagents and conditions*: i) 4,4′-Me$_2$bipy or 5,5′-Me$_2$bipy, MeOH/DCM, rt; ii) Na$_2$C$_2$O$_4$, H$_2$O; iii) H$_2$O/EtOH, recrystallisation, 100 °C.

Typically, the reactions were performed by treating $CuBr_2$ in methanol with the corresponding diimine in dichloromethane and sodium oxalate in water in a 1:1:0.5 molar ratio. Using 4,4′-Me_2bipy or 5,5′-Me_2bipy as the diimine gave, on recrystallisation, $[(4,4′-Me_2bipy)_2Cu_2Br_2(\mu-C_2O_4)]$ (**1a**) and $[(5,5′-Me_2bipy)_2Cu_2Br_2(\mu-C_2O_4)]$ (**1b**), in moderate yields, respectively (Scheme 2.1).

Unexpectedly, the reaction of $CuBr_2$ with 2,2′-bipy and sodium oxalate under similar conditions gave, in low yield, the polymeric complex, $[(2,2′-bipy)Cu(\mu-C_2O_4)]_n$ (**2a**) as the only crystallisable product which has been reported elsewhere.[7–11] Similarly, attempts to make the bromide derivative of **B** unexpectedly gave, $[(1,10-phen)Cu(H_2O)_2(C_2O_4)]$[12] as the only crystallisable product. Complexes **1a** and **1b** have been characterised by Fast Atom Bombardment (FAB) mass spectrometry, Infra-Red (IR) spectroscopy, magnetic measurements and elemental analysis. In addition, **1a** and **1b** were subject to single crystal X-ray diffraction studies.

Needle-shaped single crystals of **1a** and block-shaped crystals of **1b** suitable for X-ray structure determination were grown from a water/ethanol mixture in a 20:1 volumetric ratio, respectively. The molecular structure of **1a**, as a representative example, is shown in Figure 2.2; selected bond lengths and angles for **1a** and **1b** are given in Table 2.1 along with the previously reported **B**.[7–11] Compounds **1a** and **1b** are structurally related, similar to **B** and consist of an oxalate-bridged bimetallic copper(II) bromide complex with chelating bipyridine ligands. The Cu–Br bonds are *trans*-configured [tors: BrCu···CuBr = 180.00° (**1a**, **1b**)] to complete five co-ordinate geometries at each metal centre. Based on the value of τ [0.121 (**1a**) and 0.151 (**1b**)] the geometries can be best described as distorted SBP with the bromide atom filling the apical position. The Cu···Cu atom distances are 5.221 and 5.225 Å for **1a** and **1b**, respectively. In **1a**, molecules of ethanol are present in the crystal lattice while in **1b** the lattice is solvent-free. In addition, the chloride derivative of **1a**, $[(4,4′-Me_2bipy)_2Cu_2Cl_2(\mu-C_2O_4)]$, has also been synthesised and fully characterised and is isomorphous to **1a** (see Appendix A3.0).

(a)

(b)

(c)
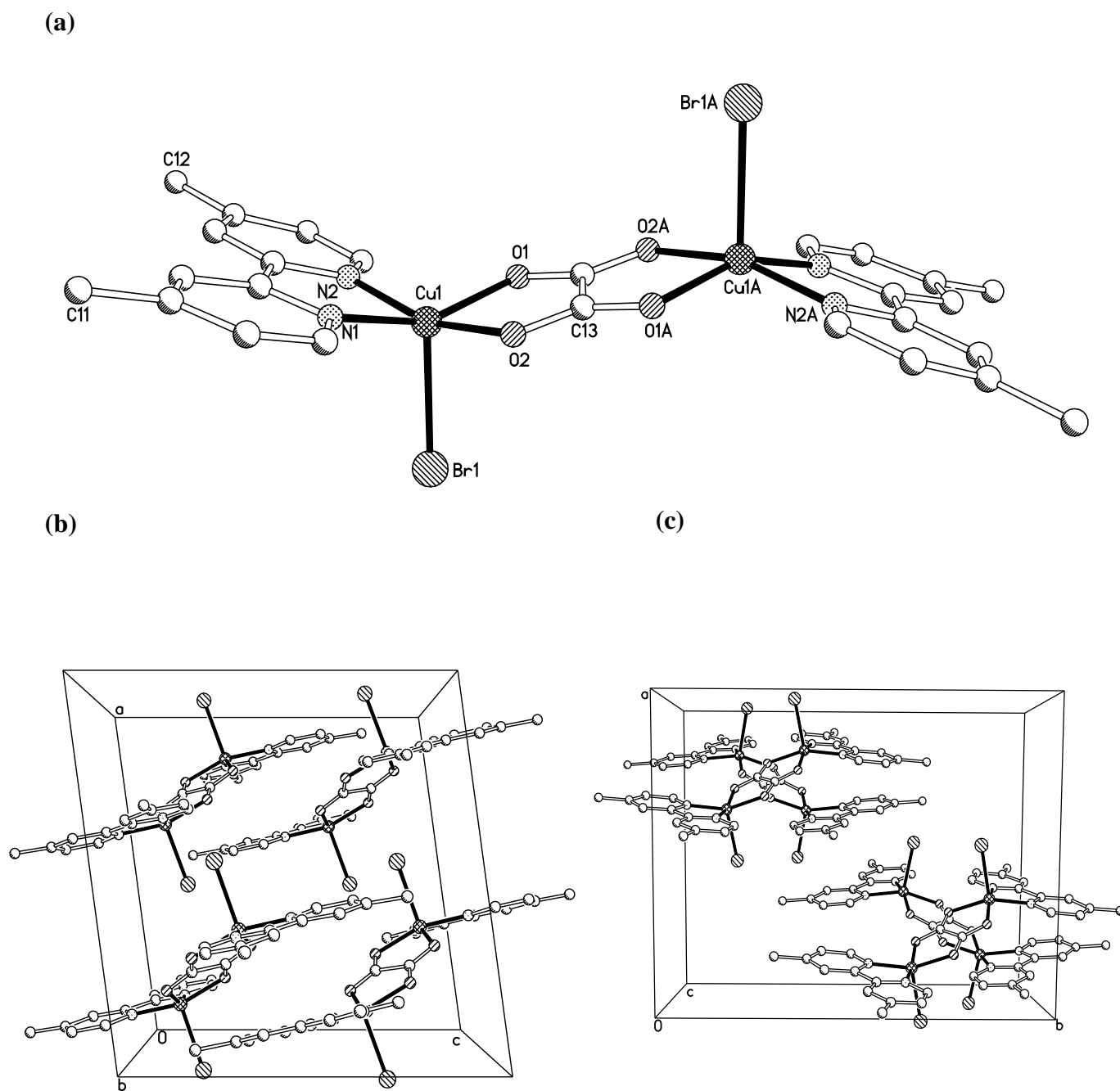
Figure 2.2 (a) The molecular structure of **1a** with partial atom labels; hydrogen atoms and selected carbon labels have been omitted for clarity. Atoms denoted with the letter label 'A' are generated by the symmetry operation $-x+3/2$, $-y+1/2$, $-z+1/2$. Included are the packing diagrams with views down the (b) *b*- and (c) *c*-axis, respectively.

Table 2.1 Selected bond lengths (Å) and angles (°) for **1a**, **1b** and **B**.

	1a (X = Br)	**1b** (X = Br)	**B** (X = Cl)[4]
Cu(1)–N(1)	1.960(3)	1.999(3)	2.041(2)
Cu(1)–N(2)	1.984(3)	1.982(3)	1.999(2)
Cu(1)–O(1)	2.021(2)	1.993(2)	1.960(2)
Cu(1)–O(2)	1.982(2)	2.011(2)	2.194(2)
Cu(1)–X(1)	2.565(10)	2.5516(6)	2.2629(9)
N(1)–Cu(1)–O(1)	92.68(10)	94.28(11)	92.76(10)
N(1)–Cu(1)–O(2)	162.26(10)	154.92(11)	106.41(10)
N(1)–Cu(1)–N(2)	82.29(16)	81.62(12)	91.72(9)
N(1)–Cu(1)–X(1)	99.98(7)	104.16(9)	142.07(10)
N(2)–Cu(1)–O(1)	154.94(9)	163.98(11)	168.53(10)
N(2)–Cu(1)–X(1)	99.85(6)	100.52(9)	96.19(10)
O(2)–Cu(1)–O(1)	83.57(8)	82.04(10)	80.29(8)
O(2)–Cu(1)–N(2)	93.77(9)	93.14(11)	91.57(9)
O(2)–Cu(1)–X(1)	97.74(7)	100.91(8)	111.51(9)
O(1)–Cu(1)–X(1)	99.85(6)	95.51(8)	95.34(10)

The packing diagram of **1a** in two orientations is also depicted in Figure 2.2. The main differences in the packing diagrams of **1a** and **1b** are that in **1a**, two pairs of symmetry related molecules are present within the unit cell, while in **1b**, only one molecule is present. This has the effect that all neighbouring molecules in **1b** are perfectly aligned, while in **1a**, one pair of molecules is inclined by an angle of 22.84° with respect to the second pair [tors: BrCu···CuBr = 157.12° (**1a**) *cf.* BrCu···CuBr = 180.00° (**1b**)] (see view down the crystallographic *c*-axis, Figure 2.2c). The reasons for the differences in the molecular packing are not clear. However, the presence of solvent in the crystal lattice in **1a** is likely to be influential. The distance between the centroids of two aligned bipyridyl layers of neighbouring molecules for **1a** was determined to be 7.080 and 4.501 Å for the maximum and minimum separations, respectively; whilst, **1b** possesses a uniform separation of 3.914 Å.

Neutral complexes **1a** and **1b** all show molecular ion peaks in their FAB mass spectra along with fragmentation peaks corresponding to the sequential loss of bromides. Both complexes were paramagnetic and displayed magnetic moments of 1.57 (**1a**) and 1.51 (**1b**) BM (Evans balance at room temperature) which are typical of oxalate-bridged copper(II) complexes.[11,13,14] The observed values are less than the predicted spin-only value of 2.45 BM [using $\mu_{eff}^2 = \Sigma\mu_i^2$ (μ_i = magnetic moment of individual metal centres)],[15] implying some anti-ferromagnetic coupling.

Attempted characterisation by ^{1}H NMR spectroscopy was limited by the solubility of the complexes in common deuterated solvents. Elemental analysis however, gave results which support the proposed structures.

2.3 Synthesis and characterisation of polymeric copper(II) compounds (2)

Higher yields of polymeric copper(II) compound **2a** could be obtained using the preferred stoichiometry of sodium oxalate; the related polymeric complexes **2b** and **2c** could also be accessed by this route. Thus, the reaction of $CuBr_2$ in methanol with the corresponding bipyridine in dichloromethane and sodium oxalate in water in a 1:1:2 molar ratio, respectively, gave on work-up, $[(2,2'-bipy)Cu(\mu-C_2O_4)]_n$ (**2a**), $[(4,4'-Me_2bipy)Cu(\mu-C_2O_4)]_n$ (**2b**) and $[(5,5'-Me_2bipy)Cu(\mu-C_2O_4)]_n$ (**2c**) in good yields, respectively. Although **2a** has been characterised elsewhere,[7–11] complexes **2b** and **2c** are novel and have been characterised using FAB mass spectrometry, IR spectroscopy, magnetic measurements and elemental analysis. In addition to these techniques, complexes **2b** and **2c** were subject to single crystal X-ray diffraction studies.

Block-shaped single crystals of **2b** and **2c**, suitable for X-ray diffraction were grown by slow evaporation of a water/ethanol mixture in a 20:1 volumetric ratio, respectively. The molecular structure of **2b** is shown in Figure 2.3; selected bond lengths and angles for **2b** and **2c** along with the previously reported **2a**[7] are given in Table 2.2. Like **2a**, **2b** and **2c** exist as zig-zag polymeric structures in which each octahedral metal centre is chelated by a bidentate Me_2-substituted bipy ligand and bridged by two oxalate ligands. The Cu···Cu atom distances within the polymers are 5.498, 5.579 and 5.576 Å for **2a**, **2b** and **2c**, respectively.

The FAB mass spectral data for compounds **2** were inconclusive. However, all of the complexes were paramagnetic and displayed magnetic moments of *ca.* 1.5–1.8 BM (Evans balance at room temperature), which are typical of oxalate-bridged copper(II) polymeric complexes. These values are less than the predicted spin only value of 2.45 BM [using $\mu_{eff}^2 = \Sigma\mu_i^2$ (μ_i = magnetic moment of individual metal centres)] implying some anti-ferromagnetic coupling. Elemental analysis gave

results consistent with the proposed structures. The ready formation of these polymeric complexes

is likely to arise from the lability of the bound halide in **1** and the metal centre's preference to adopt

six co-ordinate geometries.
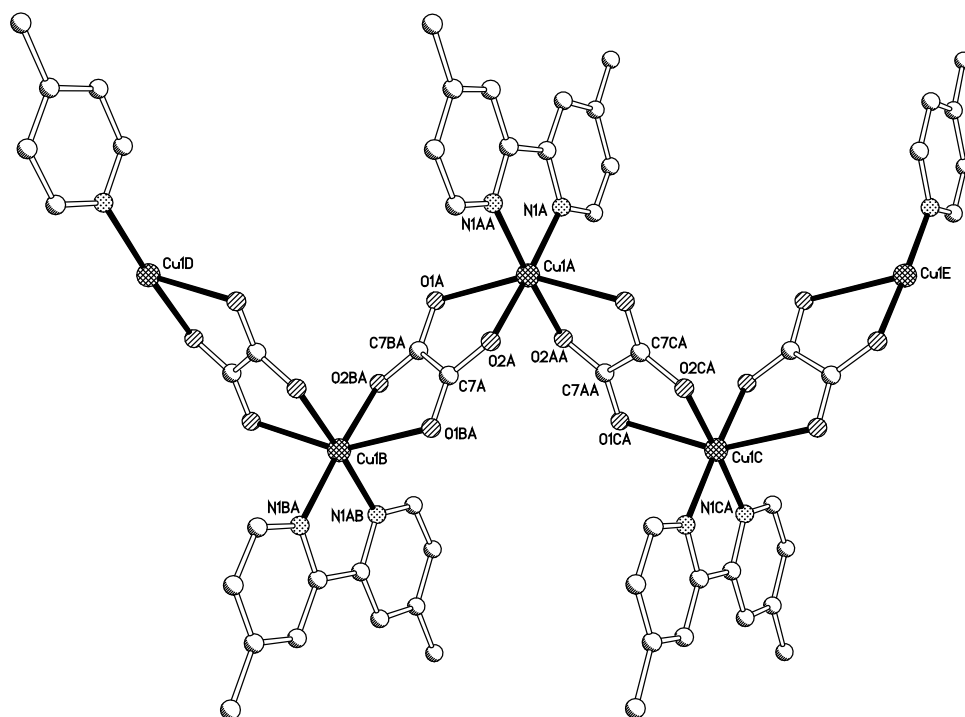
Figure 2.3 A segment of polymeric **2b** with partial atom labels; hydrogen atoms and selected carbon labels have been omitted for clarity. Atoms denoted with a letter label are generated by the symmetry operation -*x*+3/2, -*y*+1/2, -*z*+1/2.

Table 2.2 Selected bond lengths (Å) and angles (°) for complexes **2a**,[7] **2b** and **2c**.

	2a[7]	**2b**	**2c**
Cu(1)–N(1)	2.010 (2)	2.004(16)	2.003(4)
Cu(1)–N(2)	1.994(18)	1.996(10)	1.996(4)
Cu(1)–O(1)	1.981(17)	1.990(14)	1.990(3)
Cu(1)–O(2)	2.313(18)	2.370(14)	2.292(3)
Cu(1)–O(3)	1.994(18)	1.990(14)	1.975(3)
Cu(1)–O(4)	2.317(18)	2.370(16)	2.313(3)
N(1)–Cu–O(1)	93.96(8)	94.76(6)	94.91(13)
N(1)–Cu–O(2)	94.09(7)	96.26(6)	94.27(14)
N(1)–Cu–O(3)	175.66(7)	175.31(6)	172.23(13)
N(1)–Cu–O(4)	104.21(7)	104.63(6)	103.36(13)
N(1)–Cu–N(2)	81.16(8)	80.59(9)	81.29(15)
N(2)–Cu–O(1)	174.27(2)	175.31(6)	174.75(14)
N(2)–Cu–O(2)	99.12(7)	104.63(4)	98.16(13)
N(2)–Cu–O(3)	94.75(8)	94.76(6)	95.71(13)
N(2)–Cu–O(4)	94.53(7)	96.26(6)	93.47(14)
O(1)–Cu–O(2)	78.15(7)	76.33(5)	79.04(12)
O(1)–Cu–O(3)	90.04(8)	89.89(8)	89.04(12)
O(1)–Cu–O(4)	89.55(7)	84.31(8)	89.71(14)
O(2)–Cu–O(3)	85.09(7)	84.31(5)	85.53(12)
O(2)–Cu–O(4)	158.66(7)	152.58(7)	159.07(11)
O(3)–Cu–O(4)	77.46(7)	76.33(6)	77.45(12)

2.4 Determining the molecular alignment in 1a with respect to the crystal morphology

As mentioned in Chapter 1, the anisotropy displayed by the M–X bonds [M = first row transition metal; X = Cl, Br, O] is hypothesised to contribute to the X-ray dichroism. To allow for the most efficient alignment of the incident polarised X-ray beam on a needle-shaped single crystal of **1a**, it was important to establish the orientation of the Cu–Br vector with respect to the longest axes of the crystal faces. By face-indexing,[16] Miller-indices were determined to be (100), (001) and (010), with (010) and (001) being the longest morphological faces. It is evident from inspection of the view down the crystallographic *b*-axis (view into the (010) face) that the Cu–Br vector of both pairs of symmetry related molecules in **1a** are aligned almost parallel (*ca.* + 14° deviation) to the (001) face (see Figure 2.4b). On rotation of the single crystal through a 90º (a goniometer rotation (φ_{90})) about the *a*-axis, however, the symmetry related molecules are now disposed ±14º with respect to the (001) face (view into the (001 face) (see Figure 2.4c), highlighting the importance of which face is presented to the polarised X-ray beam.

2.5 Using polarised X-ray absorption spectroscopy to study 1a

A single crystal of **1a** was subjected to an experimental study to establish its performance as a potential X-ray dichroic filter. The crystal was rotated about a polarisation axis of synchrotron radiation and XAS spectra were recorded in two orientations denoted Chi (χ). In this instance, χ_0 refers to the polarisation axis parallel to the longest crystal axis and χ_{90} being perpendicular to the longest axis (the goniometer rotation of a single crystal of **1a** occurs about the *b*-axis during a χ rotation). It was assumed that the X-ray beam was presented to the (010) face (Figure 2.2b, Figure 2.4b) as slight reductions in the intensity of pre-edge spectral features were observed experimentally upon a φ_{90} rotation about the *a*-axis which were likely to be associated with the observed intermolecular misalignment when the beam is presented to the (001) face (Figure 2.2b, and Figure 2.4c). Polarised XAS spectra were recorded in transmission mode (Daresbury station 16.3) and fluorescence mode (Diamond Light Source, station I16). Raw X-ray data were normalised using the 'step-edge' approach as described by Watts *et al.*[17]

(a)

(b)

(c)
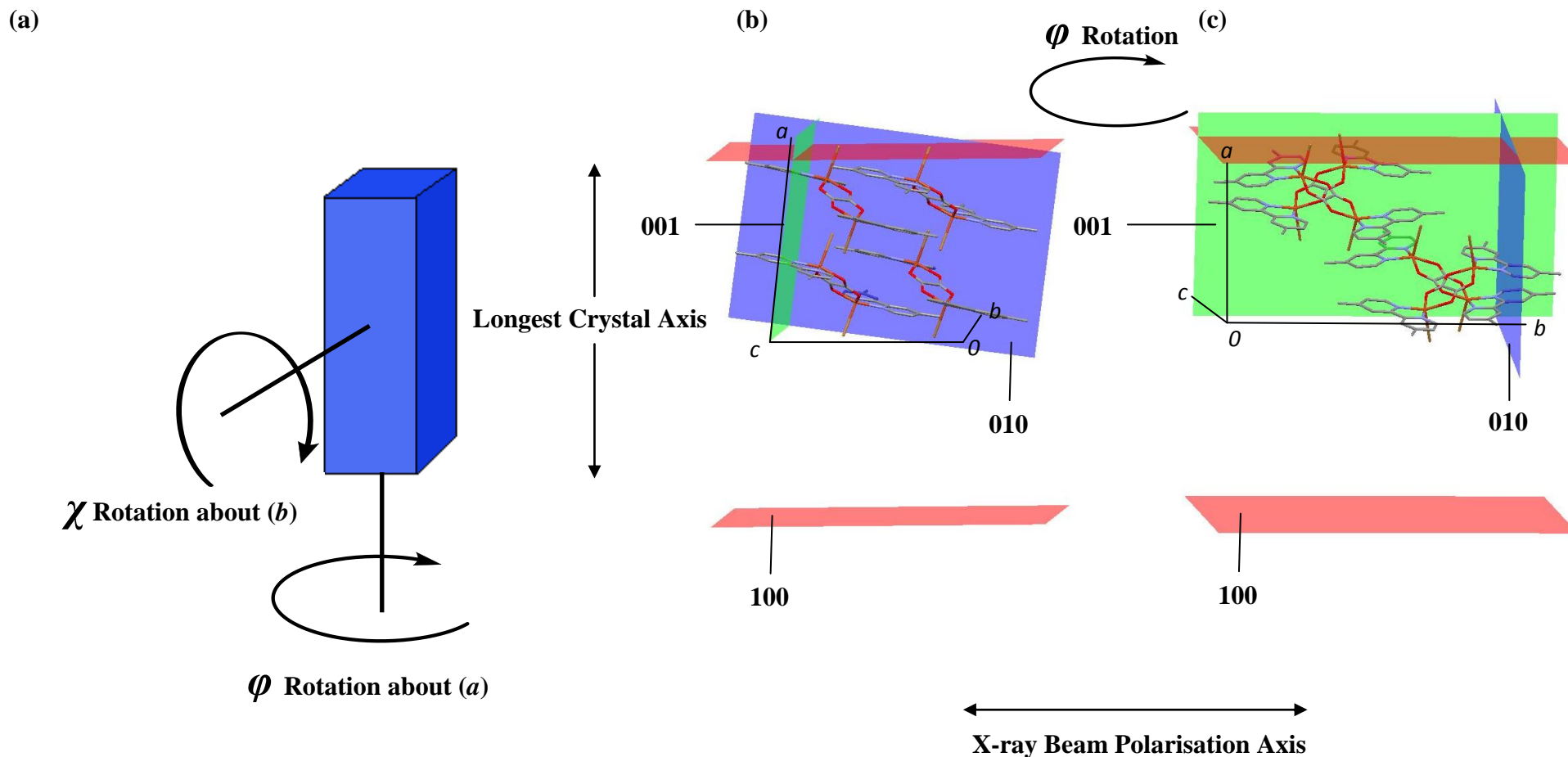
Figure 2.4 An illustration of the goniometer rotations with respect to the crystal morphology showing (a) a schematic of the single crystal morphology in **1a** along with representations of the goniometer rotations (see Chapter 1, Figure 1.18). Note: The depicted crystal orientation is representative of the χ_{90} goniometer position with the X-ray polarisation vector perpendicular to the Cu–Br bond. Also shown are Miller indices overlaid onto the molecular packing diagram of **1a** with the (b) (010) and (c) (001) faces presented to the X-ray beam representing a φ_{90} rotation. Note: The envisaged incident polarised X-ray beam propagates 'into the page' with the polarisation vector fixed horizontally.

$\mathcal{X}_0$ **Orientation**

Single Crystal (Needle)

Goniometer

CuBr Bond vector

(z)

Br—Cu

$\mathcal{X}_{90}$ **Orientation**

(z)

CuBr Bond vector

Single Crystal (Needle)

Br

Cu

Goniometer

90° χ rotation

Electric field vector of incident polarised X-ray beam
(Beam propagates into page)
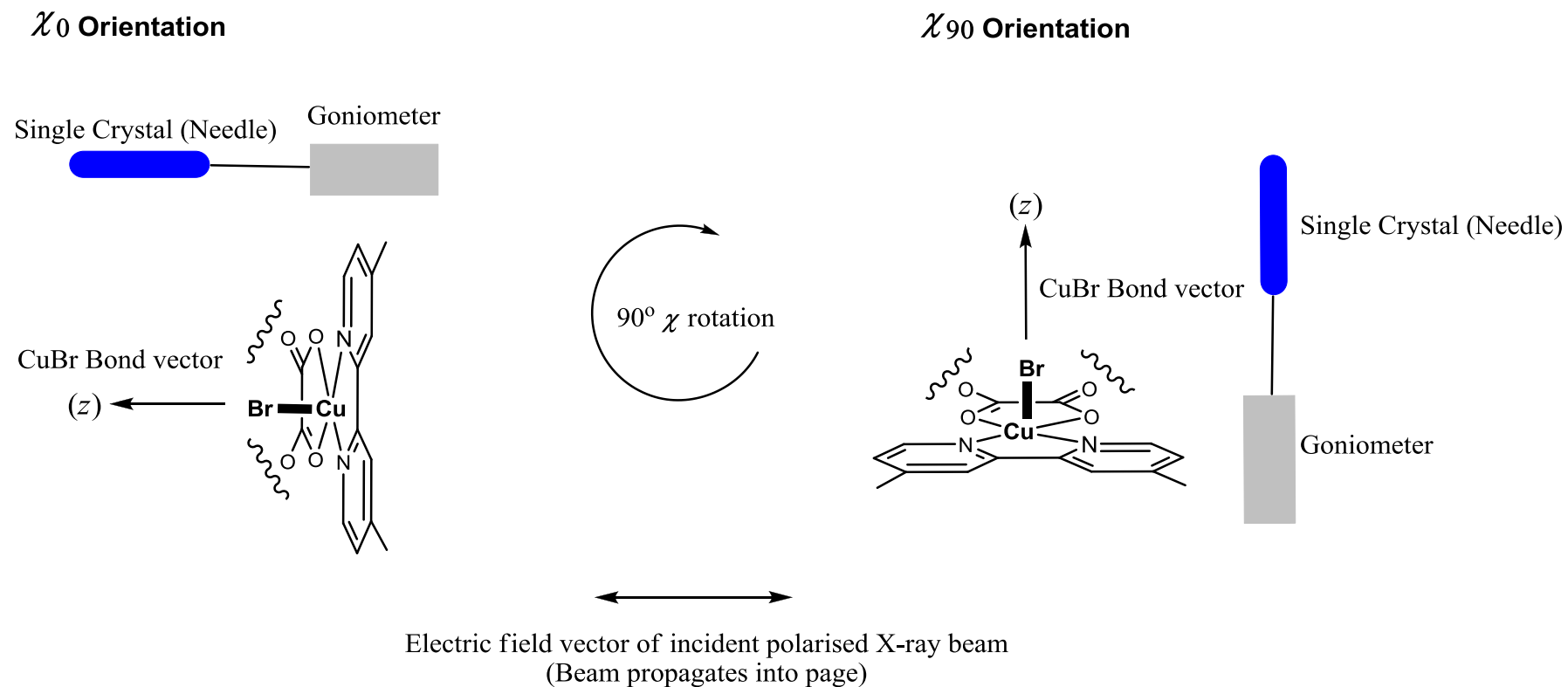
Figure 2.5 A schematic representation of the XAS beamline experimental protocol. A pictoral representation of **1a** is given along with its relationship to the defined rotation axis χ_0 and χ_{90}.

2.5.1 X-ray dichroism of 1a at the Cu K-edge (8979 eV)

Polarised X-ray measurements in transmission mode were performed at the Cu K-edge (8979 eV) on a single crystal of **1a** and the transmission spectra for two orientations χ_0 and χ_{90} are depicted in Figure 2.6. Several points emerge from inspection of the spectra. Firstly, dichroic features can be identified in three principal regions,[18] the pre-edge (8970–8985 eV), the main-edge (8985–9010 eV) and the EXAFS (9010–9080 eV). Within the main-edge, there are sub-regions, namely the main-edge 1 (shoulder; 8984–8988 eV) and the main-edge 2 (8988–9005 eV). Changes in the signal phase are evident at the onset of the main edge at 8983 eV and in the main-edge region more notably through isobestic points occurring at 8997 and 9015 eV. Within the pre-edge region, a feature of greater intensity is evident in the χ_0 orientation at 8979 eV, albeit small in intensity in comparison to the main-edge. Within the main-edge, however, broad intense transitions occur in both orientations with prominent excitations at 8990 eV (shoulder at main-edge 1), 8995 eV in the χ_{90} orientation and 8999 eV in the χ_0 orientation (main-edge 2). In the EXAFS region a subtle difference between the two orientations can be observed at 9026 eV, this feature occurs over a wide energy range (9015–9040 eV) and is shallow in comparison to the main-edge. It is also evident that further dichroic features may be observable in the furthest EXAFS tail (9040–9080 eV); however, these are smaller in comparison.

The fluorescence spectrum for **1a** has also been obtained at the Cu K-edge (8979 eV). This allows a qualitative description of X-ray dichroism which provides evidence of reproducibility and further supports the transmission data. Furthermore, a fit based on the Malus equation[19] allows a prediction of the XAS data for angles of χ which have not been obtained experimentally. In the case of **1a**, angles of χ_0 and χ_{90} have been obtained experimentally and the application of a computational data analysis script[20] has permitted the prediction of XAS spectra for orientations $\chi_{0–360}$ at 15° intervals (Figure 2.7). Using fluorescence data, modulation curves can be generated for all three regions of the spectrum and are shown collectively in Figure 2.8. In addition, points corresponding to the modulation curve for the transmission data at the main-edge 1 (shoulder) are also plotted.
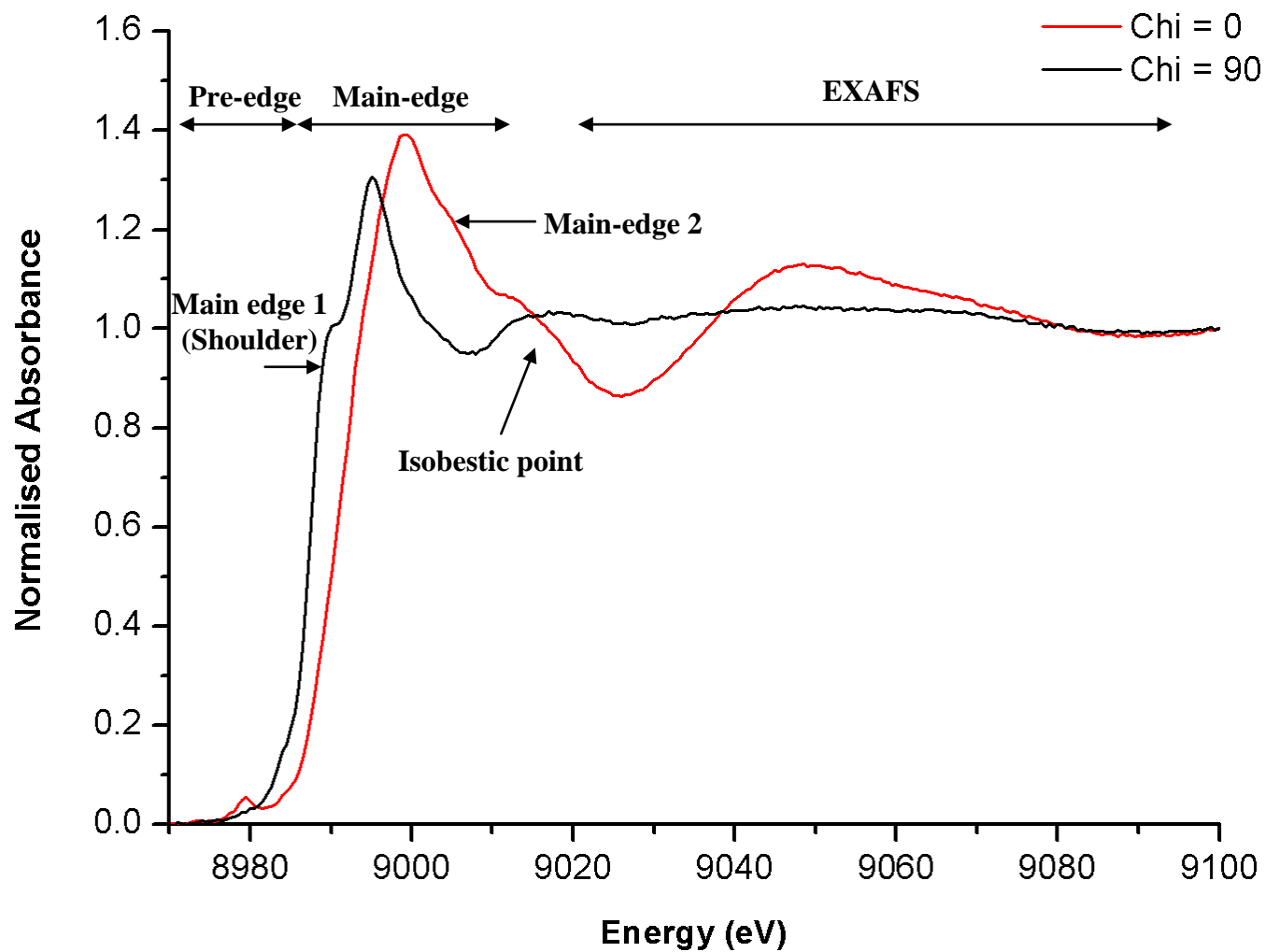
Figure 2.6 Normalised XAS spectra for **1a** at the Cu K-edge at orientations of χ_0 and χ_{90}. These data were obtained using Daresbury station 16.3 and normalised using the 'stepped edge approach' as described elsewhere.[17]
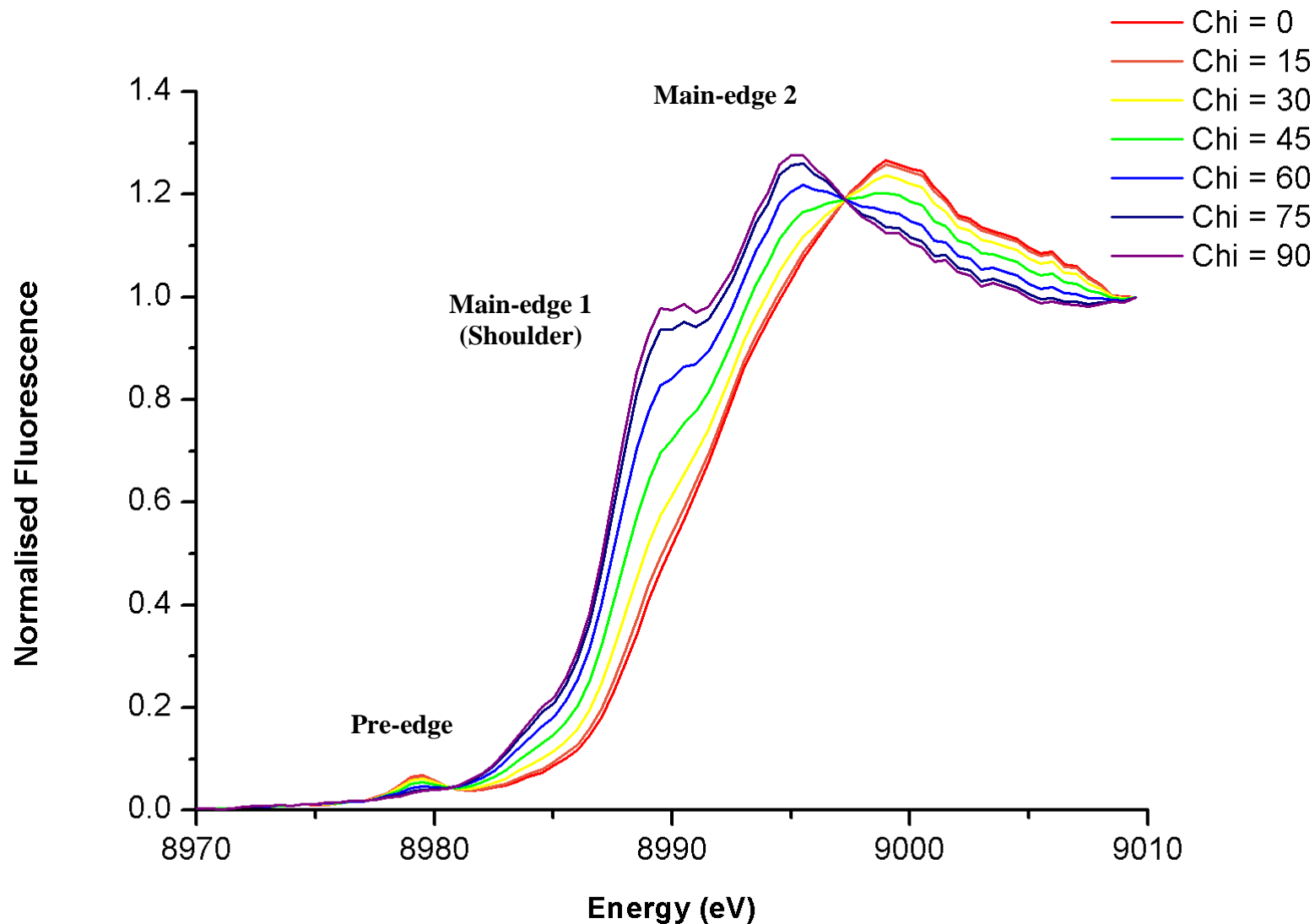
Figure 2.7 Malus' fitted normalised[17] fluorescence XAS spectra for **1a** at the Cu K-edge for orientations χ_0–χ_{90}. The χ_0 and χ_{90} data are experimental and were obtained using Diamond station I16 and only includes only the pre- and main-edge. Angles of χ_{15}–χ_{75} are Malus' fitted and were calculated using the fluorescence data.
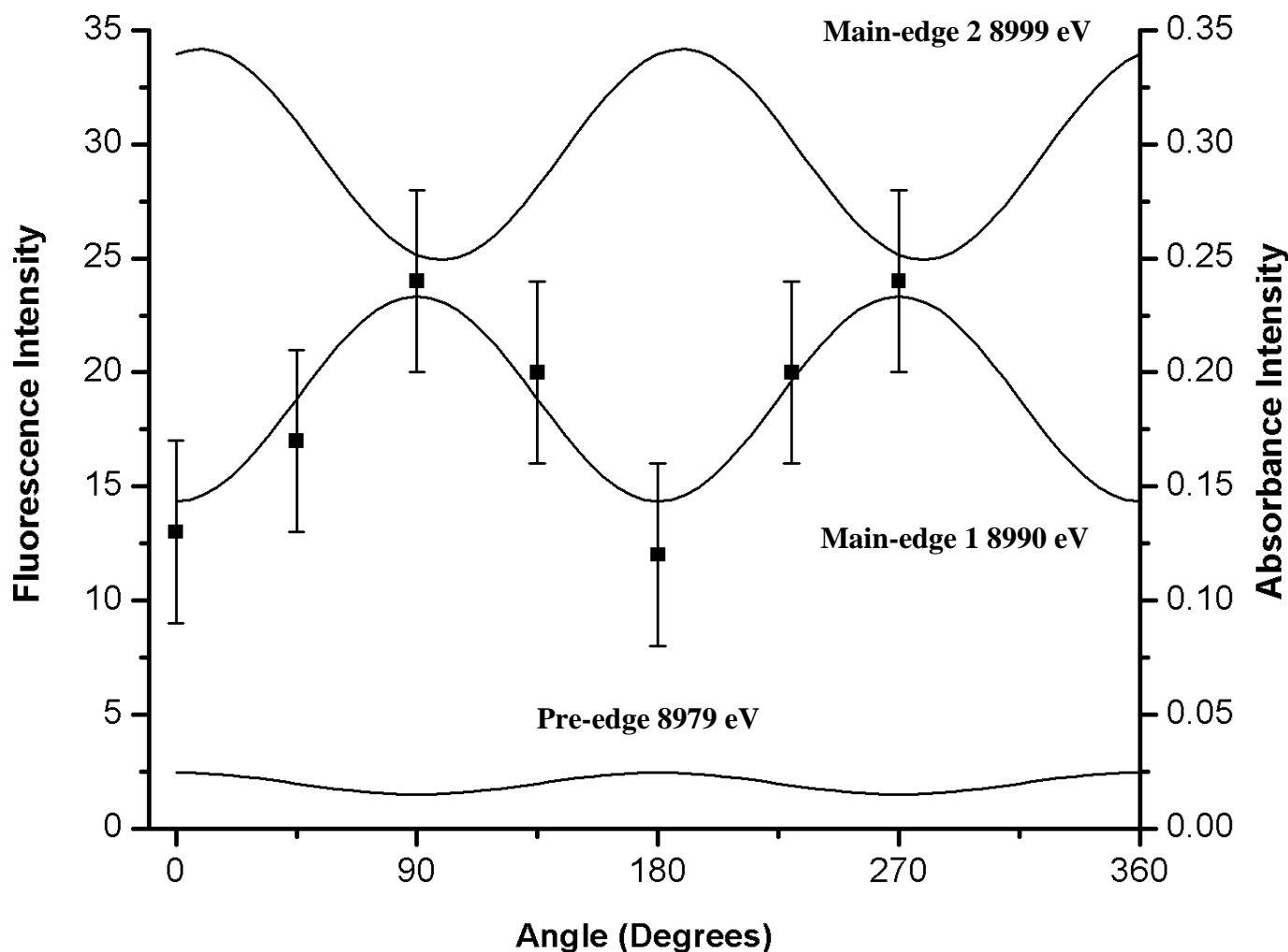
Figure 2.8 Modulation curves for **1a** obtained from Malus' fitted fluorescence data at the pre-edge (8979 eV), main-edge 1 (8990 eV) and main-edge 2 (8999 eV) regions within the XAS spectra at the Cu K-edge. Solid lines represent Malus' fitted fluorescence data (Diamond I16) and points represent absorbance data (obtained from experimental transmission data at the main-edge 1, only for angles of χ_0, χ_{45}, χ_{90}, χ_{135}, χ_{180}, χ_{225}, χ_{270} using Daresbury station 16.3) along with assoicated error bars calculated using a χ^2 statistical analysis. Note: These fluorescence data have not been normalised and were calculated based on a bespoke computational code for the analysis of raw synchrotron data.
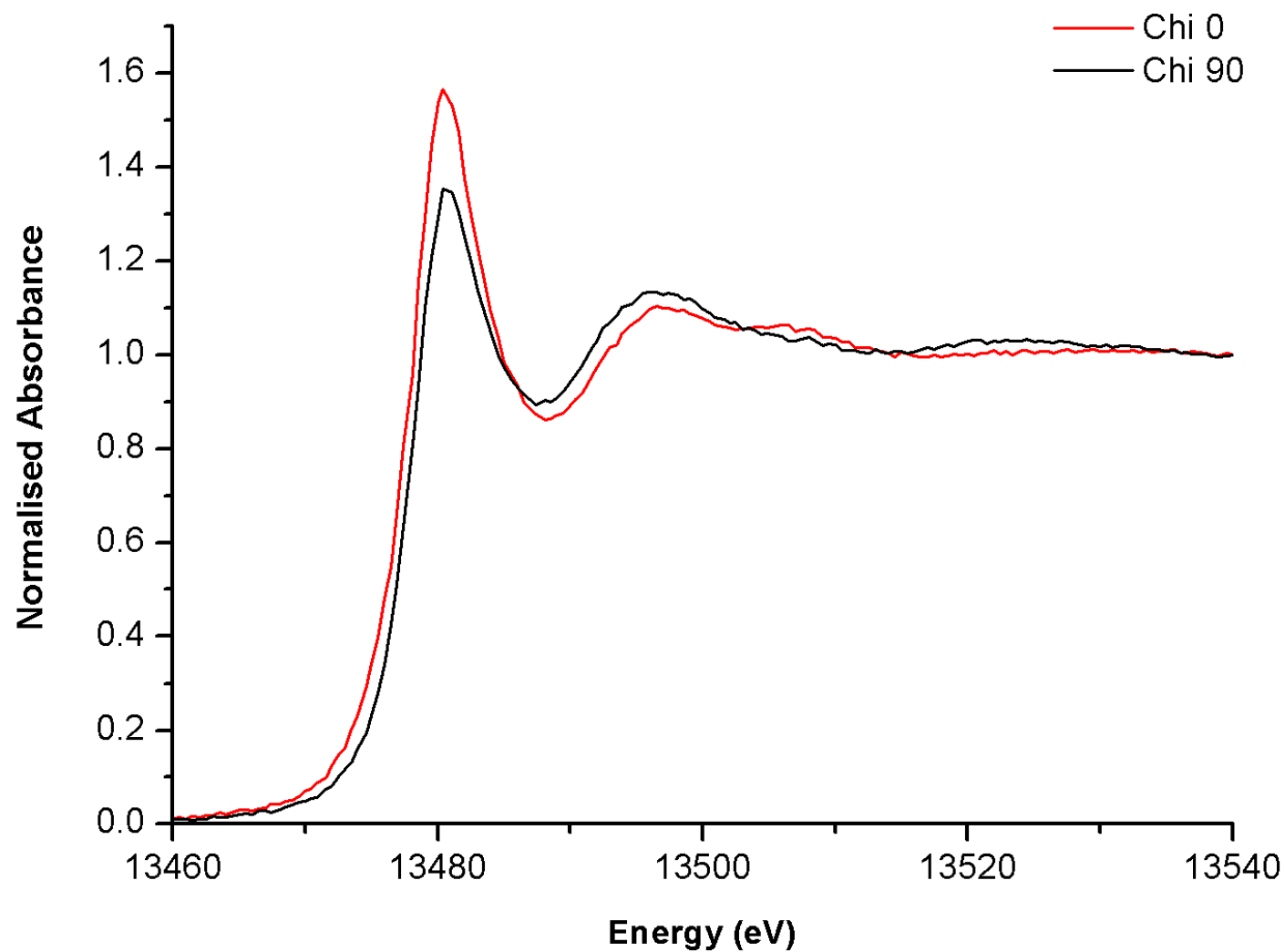
Figure 2.9 Normalised[17] XAS spectra for **1a** at the Br K-edge for orientations χ_0 and χ_{90}. These data were obtained using Daresbury station 16.3.

2.5.2 X-ray dichroism of 1a at the Br K-edge (13473 eV)

A single crystal of **1a** was also subject to an evaluation at the Br K-edge (13473 eV). The polarised XAS spectrum of **1a** at the Br K-edge is illustrated in Figure 2.9 and as expected, there is no pre-edge feature evident in this spectrum (*cf.* **1a** at the Cu K-edge). Dichroic features are apparent in two regions of the spectra, namely the main-edge (13465–13487 eV) and EXAFS (13407–13533 eV). A weak dichroic feature is evident at the main-edge (13480 eV) along with two weaker features in the EXAFS region (13487 and 13522 eV). Furthermore, isobestic points are observed at 13486, 13502, 13513 and 13533 eV.

2.6 Quantification of the performance of 1a as a dichroic filter

Complex **1a** gives an R_γ value of 0.64 at the Cu K-edge (specifically, 8988 eV at main-edge 1) and 0.77 at the Br K-edge (specifically, 13480 eV at the main-edge) (see Chapter 1, section 1.3). Note: R_γ in this context can quantify the usefulness of a material as a potential astronomical dichroic filter. At the Cu K-edge, this is represented in Figure 2.10 by plotting the natural log ratio of the absorption co-efficients *vs.* energy. In comparison, the value of R_γ for the 1-bromoadamantane thiourea inclusion compound of Harris *et al.* is 0.37.[21] It is noteworthy however, that this R_γ value is representative of one feature in the XAS spectrum of **1a**. In 1-bromoadamantane, only one dichroic feature is observed, whereas in **1a** there are multiple dichroic features and the overall collective/summated R_γ may be higher. Nevertheless, some loss of efficiency in the dichroic response may be attributed to the 14° misalignment of the Cu–Br bonds with respect to the (001) crystal face (see Figure 2.4b and 2.4c) and hence the polarised X-ray vector. However, **1a** does possess multiple K-edges (Cu and Br) within the same molecule, a potential advantage over the single K-edge 1-bromoadamantane thiourea inclusion compound. This is considered desirable in astronomical applications where the use of separate filters at different K-edges is constrained by mechanical complexity and weight of a potential flight instrument (see Chapter 4, section 4.11).[22] Furthermore, **1a** offers a metallic K-edge within the preferred 5–10 keV range (see Chapter 1, section 1.8).

The performance of **1a** becomes comparable to 1-bromoadamantane if the ideal figure of merit (μ) is employed. The figure of merit (μ) for **1a** is found to be 0.25 (Cu K-edge) and 0.130 (Br K-edge), *cf*. 0.39 for the 1-bromoadamantane thiourea inclusion compound (Br K-edge) (where one is the idealised value). It is also noteworthy that the ideal thicknesses vary at each K-edge.[21] As a consequence, the observation time of an astronomical source at the Br K-edge is 16 times as long as that needed at the Cu K-edge to achieve the same Minimum Detectable Polarisation (MDP) (see Chapter 1, section 1.3). Ideal thicknesses were obtained from an online computer program[23] using the unit cell empirical formula and density parameter for **1a**.

It is worth mentioning that environmental tests were also performed on **1a**. These revealed that, at ultra-high vacuum (1×10^{-7} Torr), a single crystal of **1a** desolvated. Therefore, a material of this type (where ethanol occupies a proportion of the crystal lattice) may not be suitable for an astronomical application without some kind of passive encapsulation/lamination in place.

A Malus' fitted contour plot obtained from fluorescence data of **1a** using angles of χ_0 and χ_{90} reveals the uniformity of the dichroic behaviour over 360° of rotation (Figure 2.11) which is useful to astronomers to show the angular continuity of this material as a potential dichroic filter. The sinusoidal behaviour of the key features outlined previously (pre-edge, main-edges 1 and 2) as a function of angle can clearly be seen within the plot.
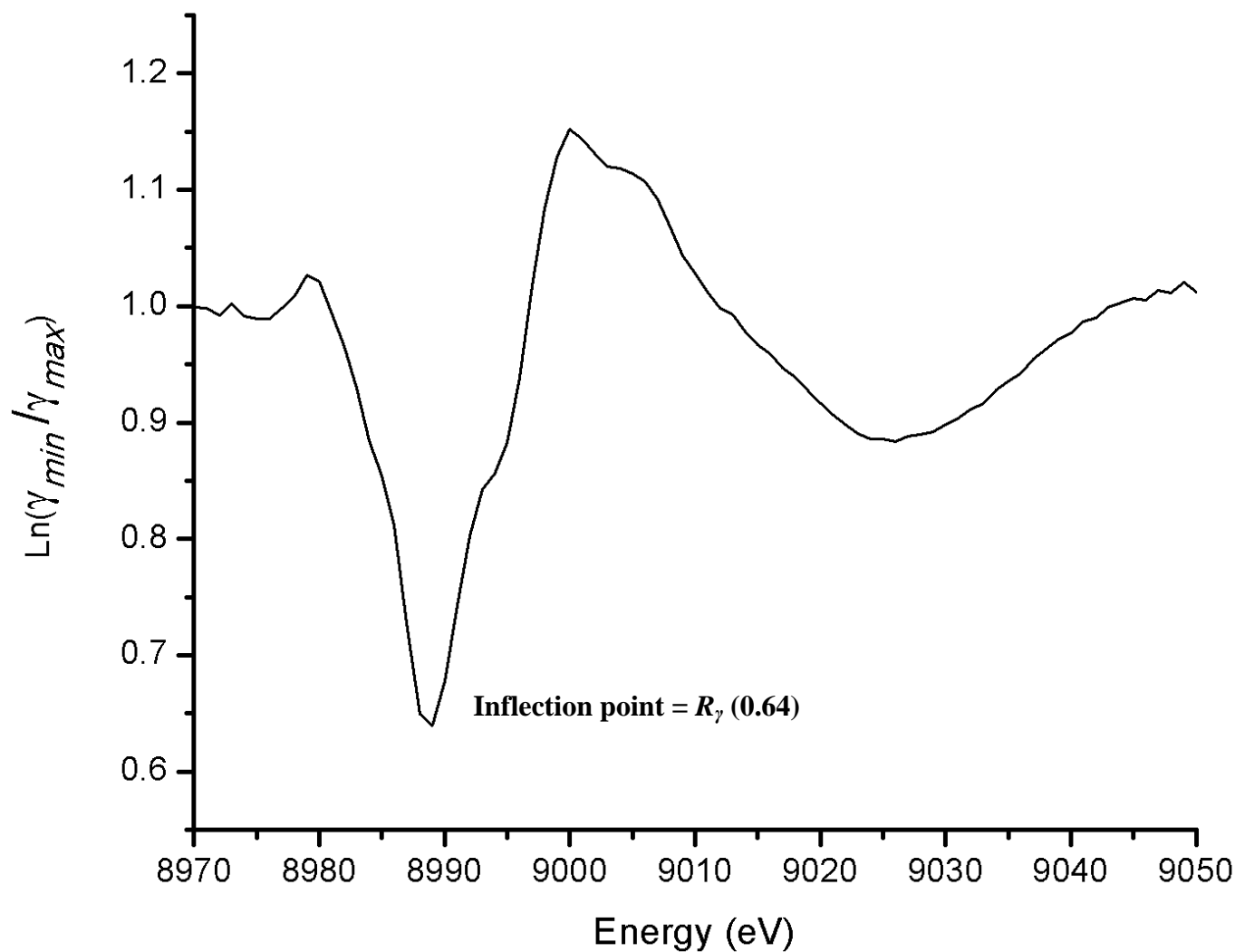
Figure 2.10 A plot of the natural log of the ratio of absorption co-efficients *vs.* energy for **1a** at the Cu K-edge. R_γ can be interpreted from the inflection point. Note: In an astronomical context (R_γ), absorbtion co-efficients are nominated γ as opposed to μ in a more traditional XAS context. Min/max refer to the maxiumum and minimum absorbtions in the experimental spectra.
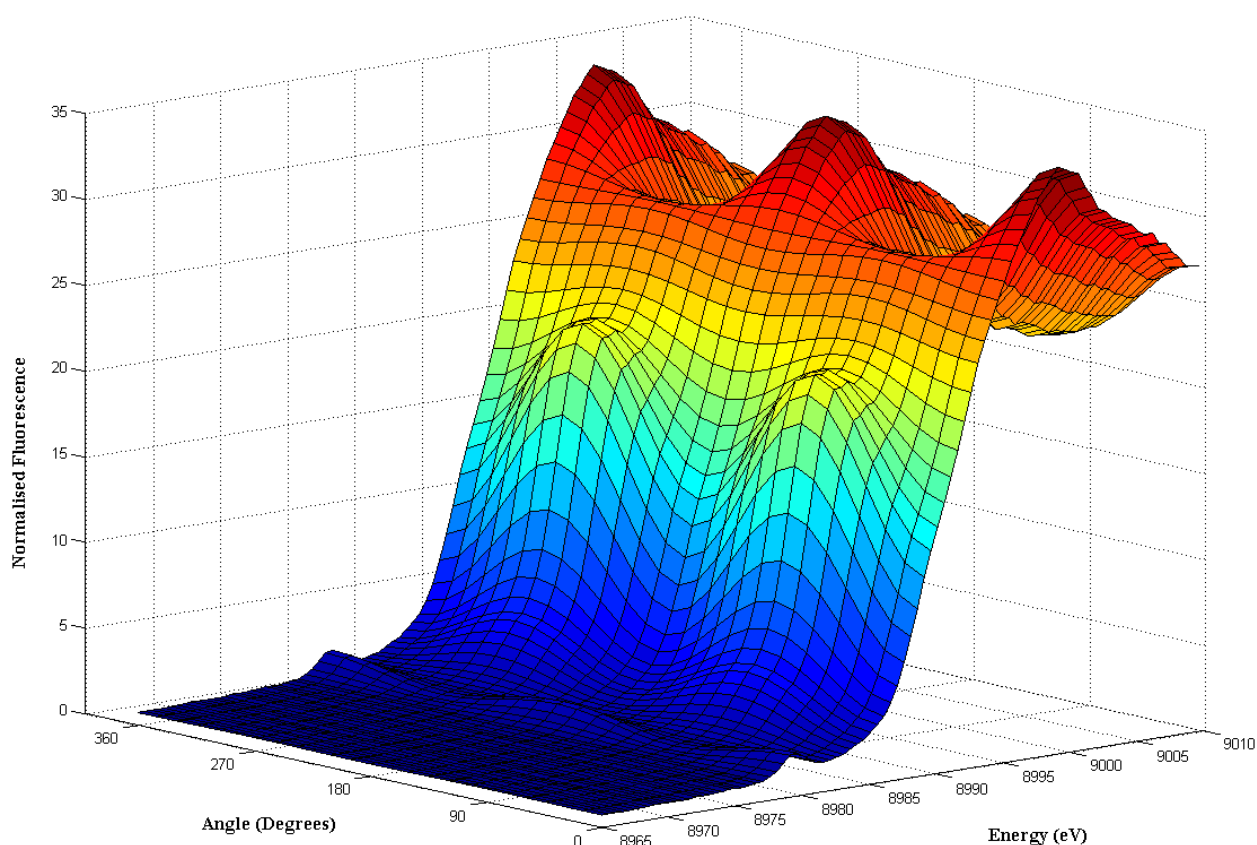
Figure 2.11 A Malus' fitted contour plot of **1a** obtained from experimental fluorescence data based on angles of χ_0 and χ_{90}.

It is noteworthy that polymeric **2a** has also been examined for X-ray dichroism at the Cu K-edge. However, no polarisation dependent features were observed in the XAS spectrum. The absence of highly ordered Cu–Br bonds in **2a** is likely to be responsible.

2.7 Rationalisation of the X-ray dichroism in 1a: Theoretical approaches

The origin of X-ray dichroism in **1a** is envisaged to derive from the relative alignment of the polarisation vector of an incident X-ray beam to the Cu–Br vector. This behaviour can, in principle, be modelled using two commonly used theoretical approaches namely, i) TD-DFT and ii) a real space multiple scattering approach. With the aim of establishing the relative merits of these distinct methods, the following sections are concerned with presenting the relevant background (section 2.7.1 and 2.7.3) along with the results on **1a** obtained using each approach (section 2.7.2 and 2.7.4).

2.7.1 A TD-DFT approach

TD-DFT is a self consistent technique which deals with the molecular orbital description of atoms and molecules. DFT has been used in this context to describe the final excited states resulting from the promotion of an electron from the core [1s] ground state orbital (either at the Cu or Br K-edge). By way of two case studies, the use of DFT to study the core electron dynamics of two related copper(II) complexes is described.

*a) Case study 1: CuCl$_2$·2H$_2$O (**D**) using theoretical approaches*

CuCl$_2$·2H$_2$O (**D**) has previously been synthesised and characterised crystallographically.[24] The neutral molecule exists in a *pseudo*-square planar (D$_{2h}$) geometry with the molecular z-axis defined as being perpendicular to the molecular plane. Two chloride atoms also project perpendicular to the molecular z-axis in a *trans*-arrangement (Figure 2.12). The x- and y-direction are along the O–Cu–O and Cl–Cu–Cl axis, respectively. The distances between the copper atom and neighbouring chloride atoms are *ca.* 3 Å indicating a weak intermolecular interaction.
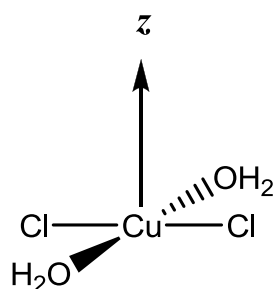
Figure 2.12 A representation of **D** with the molecular *z*-axis overlaid. The *x*- and *y*-axis are parallel to the O–Cu–O and Cl–Cu–Cl axes, respectively.

The X-ray polarisation dependence of **D** has been recorded by Chan *et al.*[25] in 1978 and thoroughly discussed theoretically, first by Bair and Goddard[26] and then subsequently by Kosugi *et al.*,[27] who also independently reproduced the experimental work of Chan *et al*. Interestingly, Kosugi has, in addition, demonstrated the importance of intermolecular anisotropy by obtaining the powder XANES of **D**. The XANES spectrum of **D** is depicted in Figure 2.13 and shows several prominent features. A pre-edge feature can be observed (A) which is most intense when the polarisation vector of synchrotron radiation is perpendicular to the *z*-axis. A shoulder (main-edge 1) (B) can also be observed which is prominent when the polarisation vector is parallel to the *z*-axis. Within the main-edge 2 (C) a broad peak is observed in both orientations. An additional feature (D) is also apparent in the perpendicular orientation. The assignment of these transitions was initially discussed on the basis of orbital splitting patterns. However, these could not explain certain spectral features, such as the shoulder at the onset of the main-edge.[25,28,29] The full assignment of the most prominent transitions for **D** is given in Table 2.3.
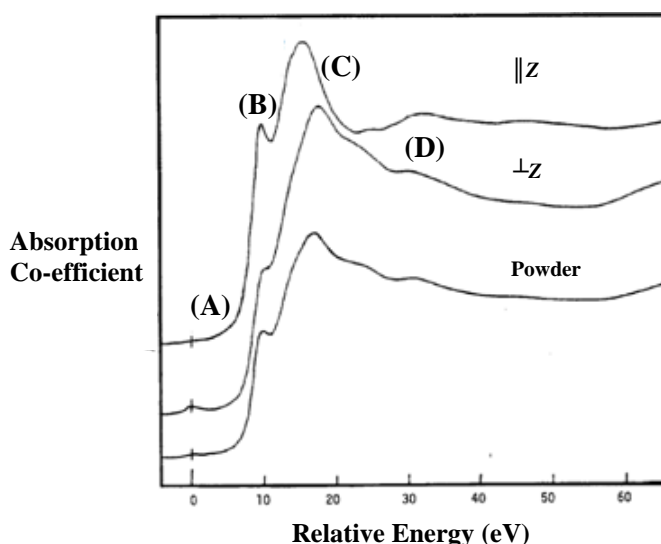
Figure 2.13 Polarised XAS spectra of **D** at the Cu K-edge as reported by Yokoyama. The symbols ∥ and ⊥ refer to the orientations with respect to the *z*-axis in Figure 2.11.[27]

Table 2.3 Calculation of Cu [1*s*] excitations for **D**[27] calculated using HF/double ζ level of theory.

Symmetry[a]	Description	Energy (eV)[b]	Oscillator Strength	Assignment[c]	Observed Energy (eV)[c]
^2A_g	1s→3dz^2	0.0[d]	1.36×10^{-5}	A	0.0
$^2B_{1u}(z)$	1s→4p + LMCT shakedown	10.35	1.35×10^{-4}	B(∥)[e]	9.71
	1s→4p_z	17.75	3.72×10^{-4}	C(∥)	15.20
	1s→5p_z[f]	22.62	1.89×10^{-4}	D(∥)	*ca.* 20 (shoulder)
$^2B_{1u}(y)$	1s→4p_y + LMCT shakedown	11.48	2.51×10^{-5}	B(⊥)	10.21
	1s→4p_y	20.65	5.04×10^{-5}	C(⊥)	
	1s→5p_y	24.73	3.9×10^{-4}	D(⊥)	22.50
$^2B_{3u}(x)$	1s→4p_x + LMCT shakedown	11.20	1.22×10^{-5}	B(⊥)	10.21
	1s→4p_x	20.54	1.64×10^{-4}	C(⊥)	
	1s→5p_x	21.90	2.8×10^{-4}	D(⊥)	22.50

a) The *x*- and *y*-axis are parallel to the O–Cu–O and Cl–Cu–Cl axes, respectively.
b) Refers to the relative energy.
c) Refers to Figure 2.13.
d) In this case, the authors have assigned first excited state (Cu d^{10}) as zero energy.
e) Refers to Figure 2.13, where the symbols ∥ and ⊥ denote parallel and perpendicular orientations, respectively, for the spectra shown within.
f) See reference 33.

To establish the spectral origins of the features observed in the XAS spectra of **D**, Bair and Goddard first calculated the XAS transitions for the Cu^{2+} ion and then a simple linear fragment of **D**, CuCl$_2$ (**D′**), before examining **D** itself.[26] It is noteworthy that the fragment **D′** has, to the knowledge of the author, only been observed experimentally in the gas phase.[30,31] The lowest energy transition in the XAS for **D** originates from the Cu $[1s]^2[3d]^9$ ground state resulting in a Cu $[1s]^1[3d]^{10}$ excited state and is responsible for the pre-edge transition (A). This transition is of quadrupole nature and hence, has intensity much less the main-edge 1 (B) and refers to the occupation of the singly occupied $[3dz^2]$ orbital. Additionally, Bair and Goddard showed that the intensity of the pre-edge did not significantly change with the inclusion of vibrational enhancement due to *p–d* mixing.

The main-edge 1 was elucidated to arise from an intense dipole transition leading to the Cu $[1s]^1[3d]^9[4p]^1$ excited state. The shoulder (main-edge 1) in **D** was originally assigned as a Cu $[1s]^1[3d]^9[4s]^1$ excited state,[25,26] however, this transition is forbidden by symmetry. The creation of a core hole (singularity) causes relaxation of the Rydberg states and thus causes ionisation of the valence ligand electrons in a fashion similar to Ligand-Metal Charge Transfer (LMCT). Although strictly it is not direct ionisation, as any charge separation is minimised by polarisation of the valence orbitals.[32] In **D** it had been envisaged that LMCT into the Cu [3d] hole occured *via* a σ-interaction originating from Cl [3p] valence electrons. This is known as a *shakedown* transition. More recently, Yokoyama has offered a supportive model based on the findings of Bair and Goddard. In their hypothesis, the Cu [1s] core hole (created from the Cu[1s]→[4p] transition) is simultaneously occupied *via* LMCT with σ-character from the Cl [3p] (*cf.* occupation of [3d] hole[26]). A comparison of the two models is shown (Figure 2.14).

(a)

(b)
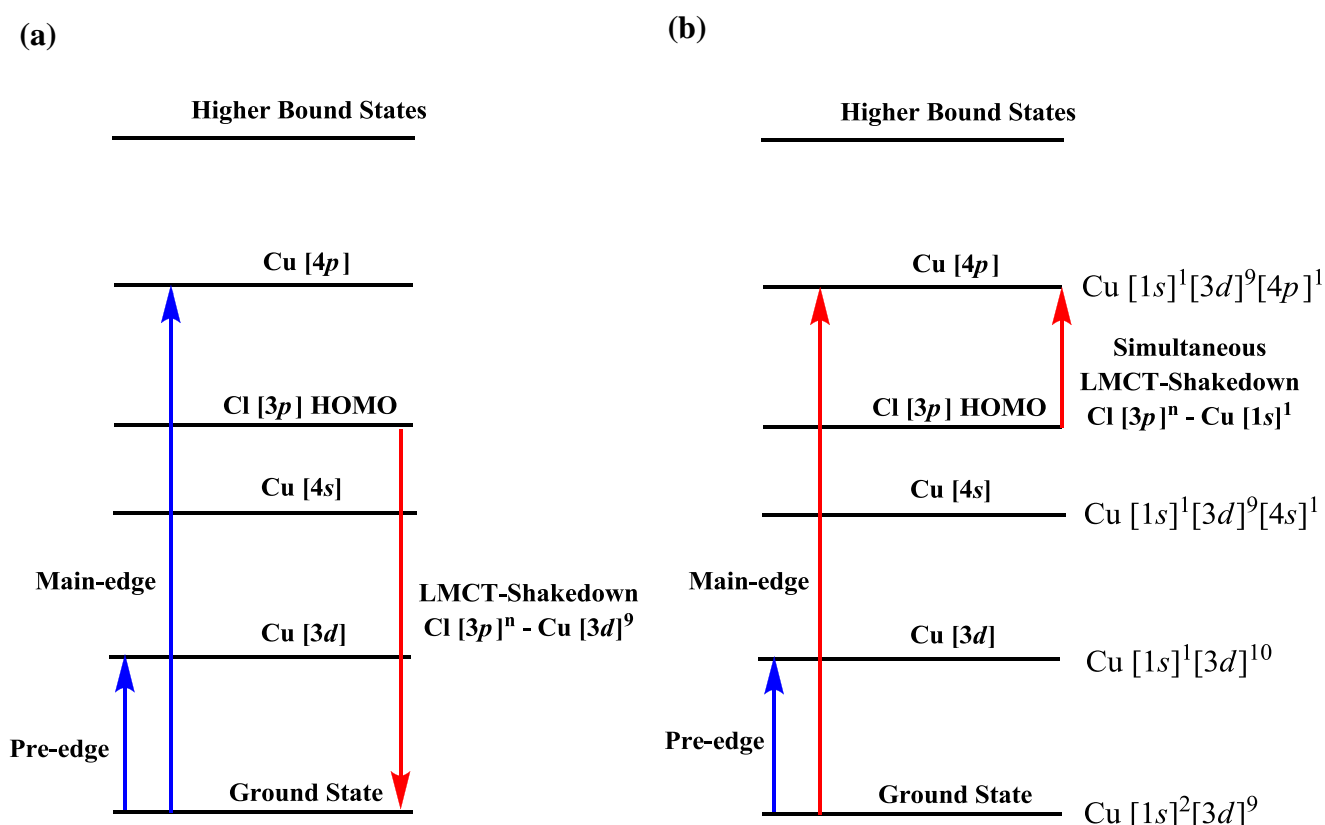
Figure 2.14 A comparative illustration of the electron dynamics of a core Cu [1s] electron in **D** and associated shakedown transitions as suggested by (a) Bair and Goddard, and (b) Kosugi. Note: i) The Cu[1s]→[4s] transition is forbidden. ii) Shakedown transitions originate from the chloride atom whilst the water structure remains unchanged (Cl⁻→Cl + e⁻ = -3.615 eV *cf.* H_2O→H_2O^+ = 12.61 eV).

*b) Case study 2: [Creatinium]$_2$CuCl$_4$ (**E**) using theoretical approaches*

The X-ray structure of [creatinium]$_2$CuCl$_4$ (**E**) (Figure 2.15) was determined by Udupa *et al.*[34] at room temperature. The geometry around the metal centre was revealed to be *pseudo*-square-planar [Cu–Cl bond lengths = 2.233(1) and 2.268(1) Å and Cl–Cu–Cl bond angles = 89.91(4) and 90.09(4)°] and is widely accepted. It is likely, however, that the molecule undergoes thermal motion and hence, the observed geometry is a result of dynamic disorder of a tetragonally distorted ion. The *x*-axis is defined as parallel to the shortest Cu–Cl bond and the *z*-axis is perpendicular to the molecular plane.
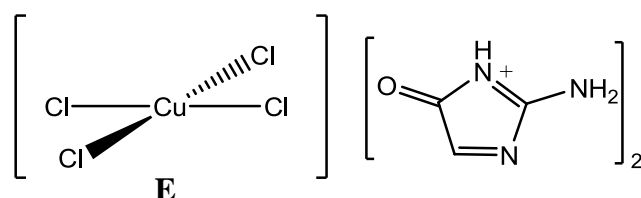
Figure 2.15 A representation of **E** shown with its creatinium counter ions.

The polarisation dependence of **E** was reported by Hahn *et al.*[35] Inspection of the polarised XAS spectrum at the Cu K-edge revealed features that are typical for copper(II) co-ordination compounds of this structural type. The [1*s*]→[3*d$_{x^2-y^2}$*] quadrupole transition cross section (at solely the pre-edge) were plotted as a function of rotation for two differing rotation axis (Figure 2.16) and they display a four-fold sinusoidal configuration (note: a two-fold sinusoidal configuration can be observed for **1a** in section 2.5). Theoretical analysis by Kosugi *et al.*[36] using the HF/double ζ level of the theory also showed a similar spectral assignment to **D** in good agreement with experiment and will not be discussed in detail.

The results of further experimental and theoretical investigations have also been detailed for CuCl$_2$ alone.[37-44] It is apparent based on these observations (and those outlined in previous sections) that the intuitive ordering of orbitals cannot be rationalised by calculations. These apparent inconsistencies have prompted a more detailed set of calculations by the author to gain an insight to the orbital energy orderings of **1a** and further improved rationalisation of experimental specta.
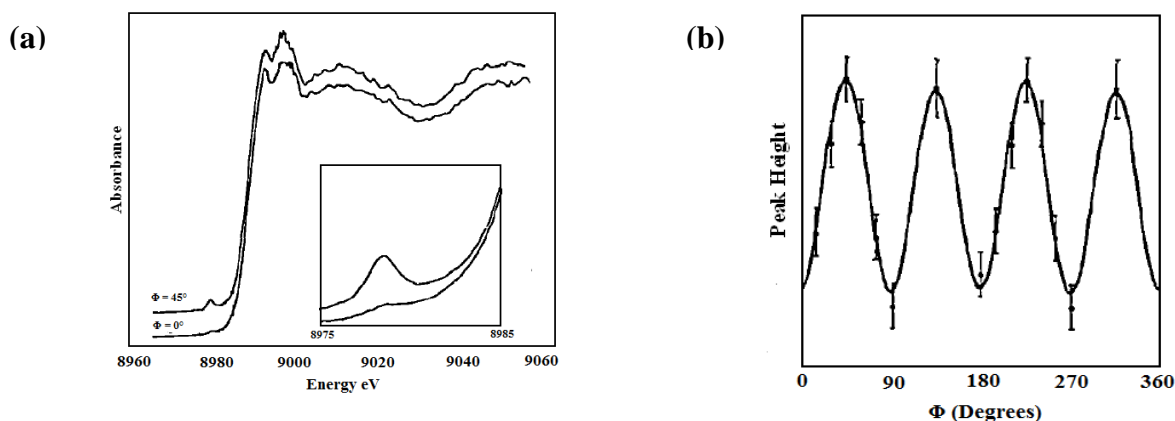
Figure 2.16 (a) Polarised XAS spectra of **E** at the Cu K-edge with (b) the [1*s*]→[3*d*] transition cross-section (pre-edge feature) as a function of rotation.[35] These data were actually collected for *Φ* values of 0–180°.

2.7.2 Using TD-DFT molecular orbital calculations to study 1a

a) Basis set optimisation using an isolated Cu–Br fragment

A series of TD-DFT[45] experiments were initially performed on an isolated Cu–Br fragment (in a fashion similar to Bair and Goddard)[26] using the ORCA software package of Neese[46] which has been used elsewhere to successfully calculate polarised XAS spectra for transition metal complexes[47–50] and ligand K-edge spectra.[48,51] Several basis sets (Table 2.4) were evaluated and the results compared with experimental data. Even using the minimum basis set (STO-3G) with Hartree–Fock theory, polarised XAS spectral features were reproduced to within 0.3–0.8 eV (*ca.* 5% residual error) of experimental data. The main spectral features apparent in the calculated polarised XAS spectra showed very little variation as a function of basis set (with the exception of minor energy scale fluctuations when using the minimal basis set STO-3G). In general, calculations were performed using the BP86[52,53] exchange functional in conjunction with the CP(PPP) basis set of Neese[54] for the copper(II) metal centre and the Ahlrichs' TZVP basis set[55] for all other atoms.

TD-DFT calculations were performed allowing only Cu [1*s*] orbital excitations (unless at the Br K-edge). This approach is similar to that of Neese *et al.* for calculations involving transition metals.[47] Geometry optimisations, where appropriate, were performed using the BP86 exchange functional and 6-311G* basis set.[56] Furthermore, Neese *et al.* found that the inclusion of solvation and scalar

relativistic effects such as COSMO[57] and ZORA[58] respectively, yielded only small improvements in the calculated energies and therefore, have been omitted in this study.

Table 2.4 Level of theory combinations used for calculations involving the isolated Cu–Br fragment.

Functional	Basis set
HF	STO-3G
HF	6-311G
B3LYP	STO-3G
B3LYP	6-311G
B3LYP	6-311G*
B3LYP	TZVP
BP86	6-311G*
BP86	TZVP
BP86	CP(PPP)[a] & TZVP[b]

a)   Basis set used for Cu(II) metal centre.
b)   Basis set used for all other atoms.

On inspection of the ORCA calculated polarised XAS spectrum of the isolated Cu–Br fragment (Figure 2.17a) using the spin unrestricted BP86 level of theory with CP(PPP) basis set for copper atoms and TZVP for all other atoms, several spectral features are evident which are consistent with those described in previous experimental sections and literature discussion (section 2.5 and 2.7). A peak at 8980 eV in the z-orientation corresponds to the quadrupole Cu [1s]→[3d] transition (pre-edge). Specifically, the excited electron transits into the singly occupied Cu [3d_{xz}] orbital of an almost degenerate pair of orbitals, Cu [3d_{xz}] and Cu [3d_{yz}]. This observation can be rationalised by inspecting the d-orbital splitting of Cu–Br in the ground state which shows the Cu [3d_{xz}] to be the SOMO, hence, a d-hole (Table 2.5). Further evidence to support the quadrupole nature of this transition can be found by investigating the pure quadrupole components (Figure 2.17b) where it can be revealed that the quadrupole intensities are *ca.* 1000 times less that of the dipole intensity. Note: in Figure 2.17b, the quadrupole intensites are of the order 10^{-6} A.U. Also apparent (not shown), is the change in the molecular structure of Cu–Br in the excited state, specifically the elongation of the Cu–Br bond by 0.174 Å and the subtle change in the energies of the d-orbitals.

Table 2.5. Cu [3d] orbital energies calculated for the ground state of an isolated Cu–Br fragment. These data were obtained courtesy of Dr. C. Evans (Department of Chemistry, University of Leicester).

Cu 3d Orbital	Energy (Hartree)[a]	Energy (eV)
3d_{xz} (SOMO)	-0.4822	-13.1209
3d_{yz}	-0.4828	-13.1369
3d_{z^2}	-0.5071	-13.7989
3d_{xy}	-0.5152	-14.0205
3$d_{x^2-y^2}$	-0.5177	-14.0860

a) 1 Hartree is equal to 27.21 eV.

a)

Cu-Br fragment

b)
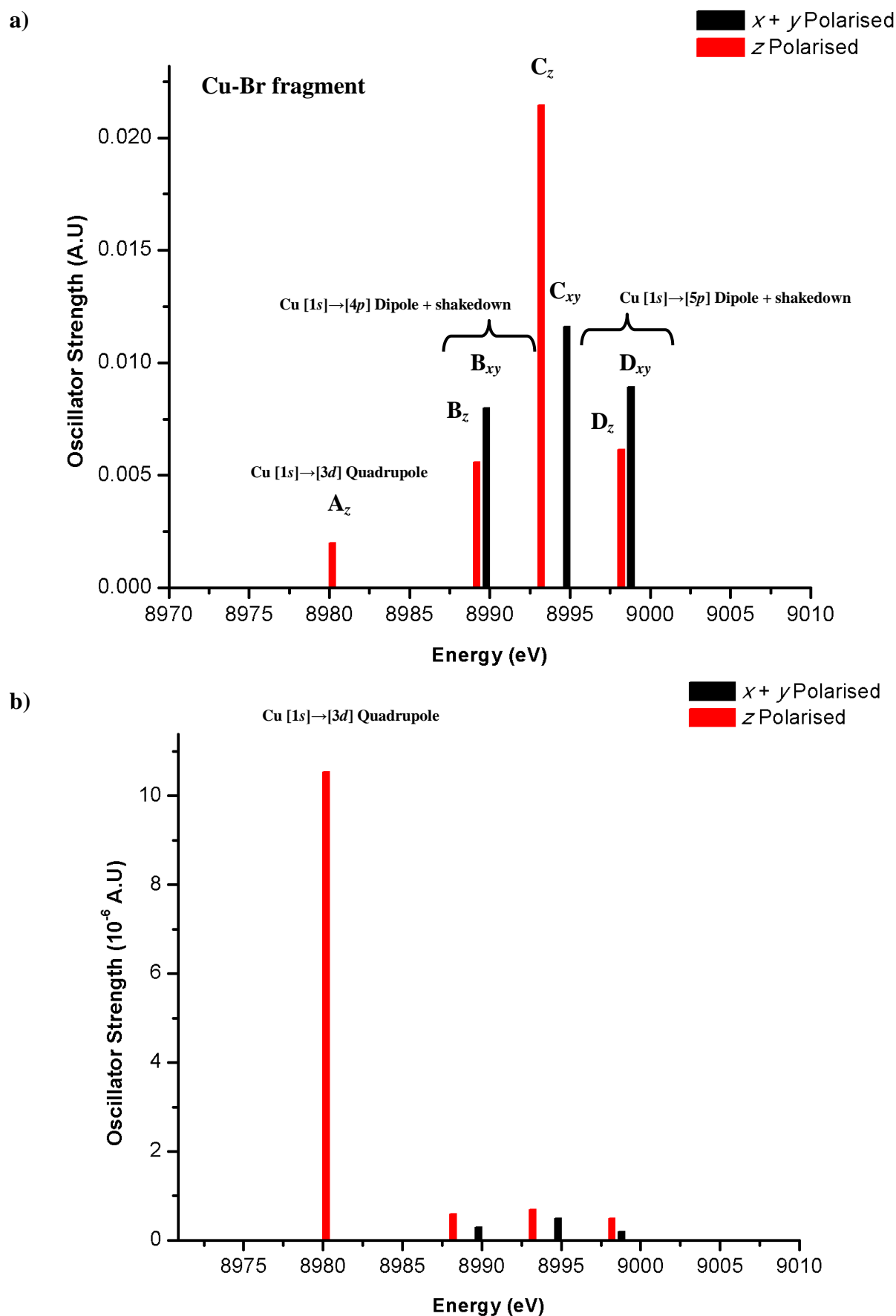
Figure 2.17. Calculated XAS spectrum at the Cu K-edge for the isolated Cu-Br fragment including (a) dipole + quadrupole and (b) pure quadrupole contributions.

Evidence of the *d*-orbital (quadrupole-like) nature of the pre-edge is also presented from inspection of the electron density contour plots which shows admixing with a Br [p_π] component (*ca*. 85% *d*- and 15% *p*-character), a likely result of orbital admixing or a possible interaction facilitating the shakedown transition (*vide infra*). Several peaks are observed in both orientations at 8989 and 8990 eV. A (Mulliken) population analysis reveals that these peaks contain a Cu [4*p*] component as well as significant ligand *p*-character. These are likely to correspond to the Cu [1*s*]→[4*p*] + Br [*np*] (*n* = undefined principal quantum number) shakedown transition (main-edge 1). Interestingly, the most intense shakedown transition appears to be *xy*-polarised. A set of peaks at 8993 and 8995 eV correspond to the main-edge 2, Cu [1*s*]→[4*p*] transition. Investigation of these orbitals suggests that these are purely dipole. Interestingly, molecular orbitals calculated for the Cu [4*p*$_z$] excited state show π admixing with Br [*np*$_z$] orbitals aligned perpendicular to the Cu–Br axis. This interaction may explain the origin of one of the strong *z*-polarised shakedown transition observed in the calculated spectra. Several peaks are evident after the main-edge at 8998 and 8999 eV which could be interpreted as Cu [1s]→[5*p*] + Br [*np*] shakedown transitions in light of previous discussion (section 2.7.1), although the Cu [5*p*] contribution to the total wave function was very small. A summary of the key transitions and oscillator strengths are given in Table 2.6. Overall, this investigation supports the hypothesis that transitions into the orbitals that comprise the Cu–Br bond are responsible for the dichroic response.

Table 2.6 Calculation of Cu [1*s*] excitations for the isolated Cu–Br fragment.

Description	Energy (eV)[a]	Oscillator Strength	Assignment[b]	Observed Energy (eV)[c]
1*s*→3*d*$_{xz}$	8980	0.002	A$_z$	8979
1*s*→4*p*$_z$ + shakedown	8989	0.0056	B$_z$	8987
1*s*→4*p*$_{xy}$ + shakedown	8990	0.008	B$_{xy}$	8987[d]
1*s*→4*p*$_z$	8993	0.022	C$_z$	8995
1*s*→4*p*$_{xy}$	8995	0.012	C$_{xy}$	8999
1*s*→5*p*$_z$ + shakedown	8998	0.0062	D$_z$	9005
1*s*→5*p*$_{xy}$ + shakedown	8999	0.089	D$_{xy}$	9005[d]
1*s*→4*p*$_z$[e]	13127	0.012		13480
1*s*→4*p*$_{xy}$	13129	0.008		13480

a)   Calculated from DFT.
b)   Refer to Figure 2.17a.
c)   Refer to Figure 2.6.
d)   Transitions are indistinguishable due to overlap of broad peaks.
e)   Calculations performed allowing Br [1*s*] excitations using the TZVP basis set.

In addition, ORCA calculations of the Cu–Br fragment at the bromine K-edge using the BP86/TZVP level of theory revealed two prominent transitions corresponding to the Br $[1s] \rightarrow [4p_z]$ at 13127 eV and Br $[1s] \rightarrow [4p_{xy}]$ at 13129 eV and furthermore, electron density plots have been generated which reveal a molecular orbital with substantial *p*-character residing on the bromine atom.

On a related note, calculations performed by the author involving $CuBr_2$ mirror the observations of the isolated Cu–Br fragment and indeed $CuCl_2$ as described in the literature. Therefore, these results will not be discussed further; again, the Cu–Br bonds are revealed to elongate by 0.067 Å on excitation of the core electron.

b) Using TD-DFT molecular orbital calculations to study the hypothetical fragment 1a′

It is worthy of note that ligand *crystal field theory* failed to rationalise the Cu $[3d]$ orbital splitting patterns of the isolated Cu–Br fragment (along with the literature described $CuCl_2$) obtained from the results of theoretical calculations. This is considered to be important an short-comming herein, where the theoretical Cu $[3d]$ orbital assignments and energy ordering will be used, in turn, to aid in the explication of the appearance and orientation of spectral features in polarised XAS.

Due to the complexity of **1a**, TD-DFT calculations were initially performed using ORCA on a hypothetical fragment containing only one copper atom $[(4,4′-Me_2bipy)CuBr(C_2O_2H_2)]$ (**1a′**) using the BP86/CP(PPP) and TZVP level of theory. The geometry of the fragment **1a′** was optimised using an RKS algorithm[59] at the BP86/6-311G* level of theory and shows a good correlation with the structure of **1a** (Figure 2.18 and Table 2.7). The co-ordination geometry and atom configuration was retained and showed a τ-value consistent with a five co-ordinate SBP complex $[\tau = 0.122$ (**1a**) and 0.121 (**1a′**)]. Note: the level accuracy of the atomic positions given in Table 2.8 was obtained by importing the ORCA Cartesian output file into the crystallographic modelling program Mercury; ORCA does not produce its outputs to this level of accuracy.

(a)   **(b)**   **(c)**

1a′   1a′ (optimised)   1a
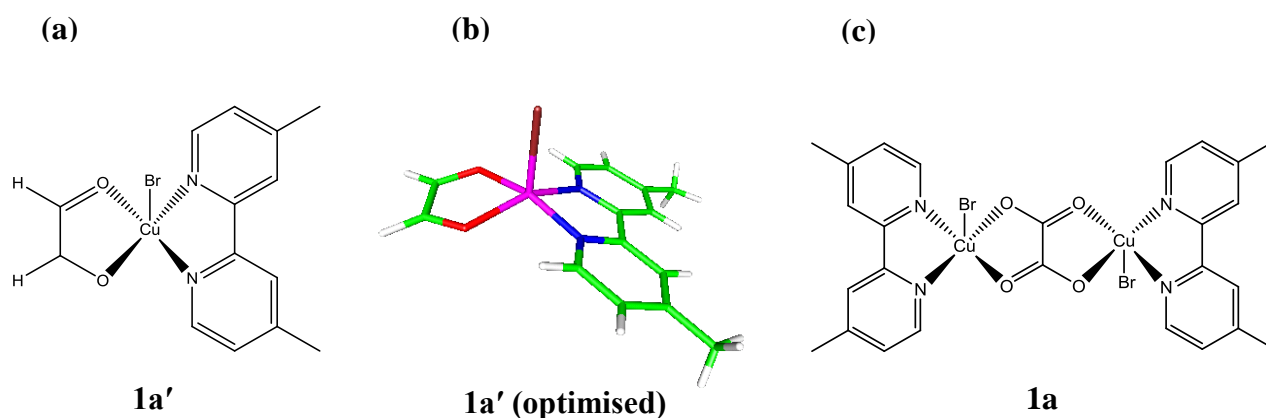
Figure 2.18 (a) Hypothetical fragment **1a′**, (b) its optimised structure (obtained from crystallographic Cartesian co-ordinates for **1a**) along with (c) **1a** itself. Atom colour scheme: copper (pink), bromine (brown), oxygen (red), nitrogen (blue), carbon (green) and hydrogen (white). Geometry optimisation performed using BP86/6-311G level of theory. The *z*-axis is projected along the Cu−Br bond.

Table 2.7 Selected bond lengths (Å) and angles (°) for **1a** along with those for optimised **1a′** and **1a**.

	1a	1a′	Geometry optimised 1a
Cu(1)−N(1)	1.960(3)	1.986	1.985
Cu(1)−N(2)	1.984(3)	1.961	1.961
Cu(1)−O(1)	2.021(2)	2.020	2.020
Cu(1)−O(2)	1.982(2)	1.980	1.981
Cu(1)−Br(1)	2.565(10)	2.567	2.567
N(1)−Cu(1)−O(1)	92.68(10)	93.04	93.03
N(1)−Cu(1)−O(2)	162.26(10)	162.24	162.24
N(1)−Cu(1)−N(2)	82.29(16)	82.27	82.28
N(1)−Cu(1)−Br(1)	99.98(7)	100.01	99.99
N(2)−Cu(1)−O(1)	154.94(9)	154.93	154.94
N(2)−Cu(1)−Br(1)	99.85(6)	99.87	99.91
O(2)−Cu(1)−O(1)	83.57(8)	83.55	83.56
O(2)−Cu(1)−N(2)	93.77(9)	93.75	93.76
O(2)−Cu(1)−Br(1)	97.74(7)	97.76	97.75
O(1)−Cu(1)−Br(1)	99.85(6)	99.87	99.85

With specific regard to **1a′** and **1a**, the identity of the Cu [3*d*] SOMO in the ground state and hence, its angular momentum state, can aid in confirming which orbital is able to accept the excited Cu [1*s*] electron and gives rise to the polarisation-dependent pre-edge feature. Therefore, this can determine which orientation the orbital/state couples with the incident polarised electric X-ray vector. This investigation was performed in a similar fashion to that for isolated Cu–Br fragment discussed previously. For **1a′** the SOMO giving rise to the pre-edge feature is determined to be the

Cu [$3d_{z^2}$] orbital in the ground state (Table 2.8), which is consiststent with experimental and

theoretical observations of a *z*-polarised pre-edge feature.

Table 2.8. Cu [$3d$] orbital populations and energies calculated for the ground state of **1a′**. These data were obtained courtesy of Dr. C. Evans (Department of Chemistry, University of Leicester).

Cu 3d Orbital	Energy (Hartree)[a]	Energy (eV)
$3d_{z^2}$ (SOMO)	-0.1304	-3.5503
$3d_{xy}$	-0.1454	-3.9563
$3d_{xz}$	-0.1671	-4.5484
$3d_{yz}$	-0.1683	-4.5797
$3d_{x^2-y^2}$	-0.1992	-5.4218

a) 1 Hartree is equal to 27.21 eV.

The unorthodox, yet simple method of cleaving **1a** to give **1a′** by replacing bridging oxygen atoms

with hydrogen atoms was borne out of unsuccessful attempts to optimise the structure of a more

chemically realistic fragment consisting of a terminal oxalate-containing motif, [(4,4'-

Me$_2$Bipy)CuBr(OxH)]. However, the resulting unsatisfied valence of a C–O carbon atom in **1a′**

warrents some discussion. The optimised geometries for **1a** and **1a′**, in the first co-ordination sphere

of the metal, are very similar, wherein the asymmetric HC(O)CH(O$^-$) ligand generates asymmetry

in the Cu-N and Cu-O bond lengths. Furthermore, in **1a**, the ground state calculations reveal a

triplet state in which both copper atoms have one unpaired electron as expected for a d^9 copper(II)

metal centre. Attempts to deterimine the spin assignments of these unpaired electrons have, at this

time, been unsuccessful and further work in this area is ongoing. Significantly, the ground state

calculations for **1a′** also reveal a triplet state with an unpaired electron located on the trivalent

carbon atom along with the expected unpaired electron on copper, consistent with the electronic

configuration of a copper(II) metal centre.

Despite the shortcomings of **1a′** as a *chemically reasonable* model, for the purposes of theoretical

calculations, it is deemed adequate and consistent with **1a** itself; the input parameters of the

calculations for both **1a** and **1a′** are both similar. Furthermore, the calculated polarised XAS

spectrum for **1a′** (Figure 2.19 and Table 2.9) generally shows a good agreement with experimental

results (Figure 2.21, *vide infra*).

The calculations indicate that a change in the point group occurs from the ground state to the excited state, resulting in changes to the orbital ordering, suggesting that the excited state is dynamic. Attempts to fully model the excited state state using ORCA in order to numerically determine the exact orbital eneries proved difficult due to this transient nature of the excited state. It is not unreasonable to rationalise this dynamic behaviour, since it is known that electronic transitions can bring about vibrational changes in the molecule due to Born–Oppenhiemer approximations and Frank–Condon related phenomena.

The ORCA calculated polarised XAS spectrum for **1a′** (Figure 2.19) reveals similar features to that of the isolated Cu–Br fragment, namely the weak quadrupole pre-edge, intense dipole main-edge and associated shakedown transitions (Table 2.9). The pre-edge peak (8977 eV) appears in the z-polarised spectrum and can be assigned to the Cu$[1s]\rightarrow[3d_{z^2}]$ transition. Inspection of the molecular orbital for this excited state reveals that the Cu $[3d_{z^2}]$ orbital is projected along the Cu–Br bond vector (Figure 2.20).

Also shown in Figure 2.20, the electron density plot contains a significant proportion of ligand p-character, the majority of which was found to be Br $[p_z]$ (*ca.* 23%), however, a small proportion of mixing from the O $[2p]$ (9 %) was observed. This admixing between the bromine and copper may be the result of an interaction associated with shakedown transitions. At the onset of the edge, peaks assigned to the Cu $[1s]\rightarrow [4p_{x,y}]$ + shakedown are more prominent in the experimental spectrum at 8987 eV (χ_{90}) and this is reflected in the ORCA calculated spectra 8989 eV.

A similar observation can be made for the Cu $[1s]\rightarrow[5p]$ + shakedown which is more prominent in the z-polarised ORCA spectrum (9000 eV). At the main-edge 1, intense peaks are evident at 8994 and 8998 eV and can be assigned to Cu $[1s]\rightarrow[4p_{x,y}]$ and Cu $[1s]\rightarrow[4p_z]$ dipole transitions, respectively. Investigation of the molecular orbitals revealed that the Cu $[4p_z]$ is indeed aligned along the Cu–Br vector.
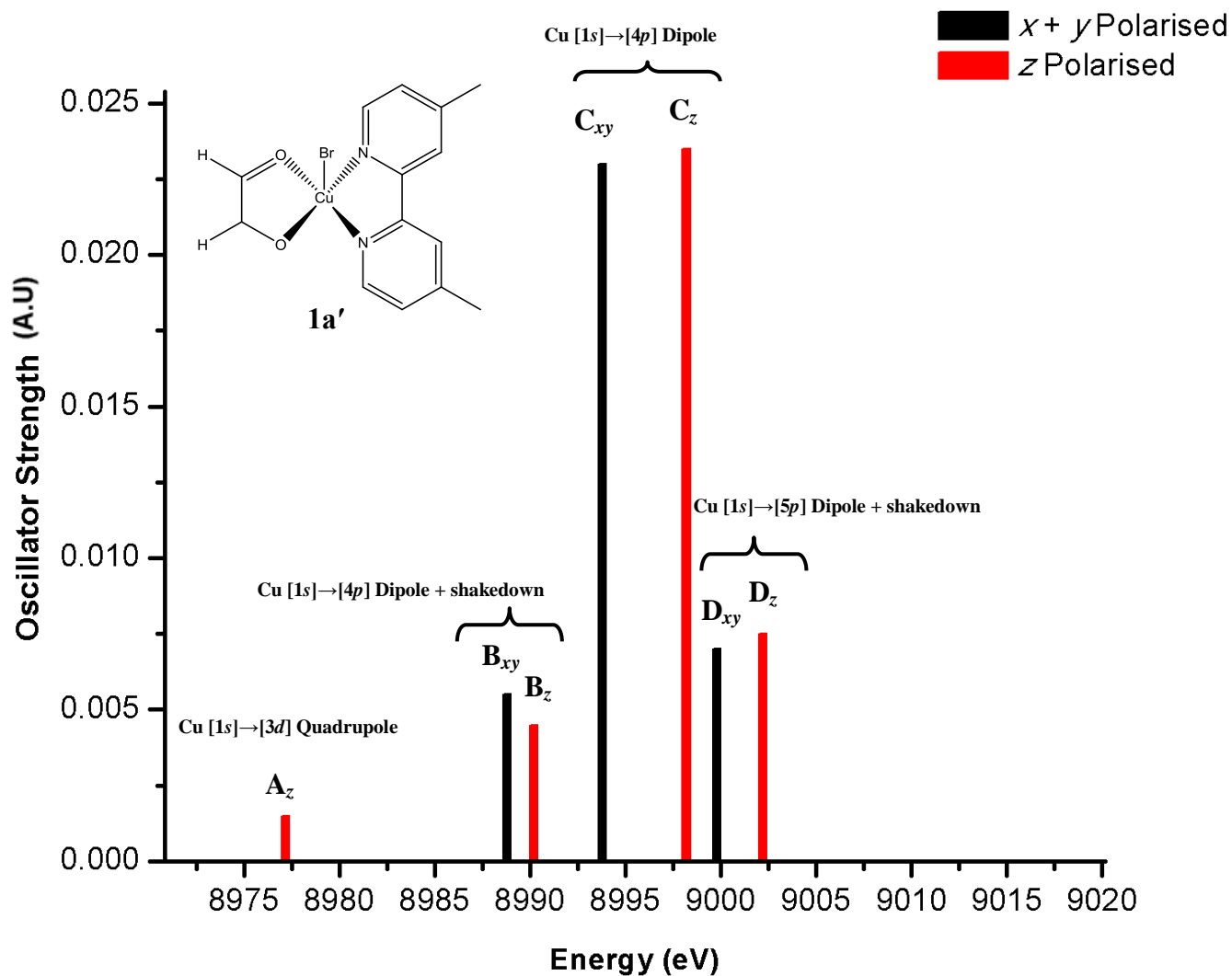
Figure 2.19 Calculated XAS spectrum at the Cu K-edge for the hypothetical fragment **1a′**. Transitions to all other atoms except copper and bromine have been omitted for clarity.

Table 2.9 Calculation of Cu [1s] excitations for the hypothetical fragment **1a′**.

Description	Energy (eV)[a]	Oscillator Strength	Assignment[b]	Observed Energy (eV)[c]
1s→3dz^2	8977	0.0015	A$_z$	8979
1s→4px,y + shakedown	8989	0.0055	B$_{xy}$	8987
1s→4pz + shakedown	8990	0.0055	B$_z$	8987[d]
1s→4px,y	8994	0.023	C$_{xy}$	8995
1s→4pz	8998	0.0235	C$_z$	8999
1s→5pxy + shakedown	9000	0.0065	D$_{xy}$	9005
1s→5pz + shakedown	9002	0.0067	D$_z$	9005[d]

a) Calculated from DFT.
b) Refer to Figure 2.19.
c) Refer to Figure 2.6.
d) Transitions are indistinguishable due to overlap of broad peaks.
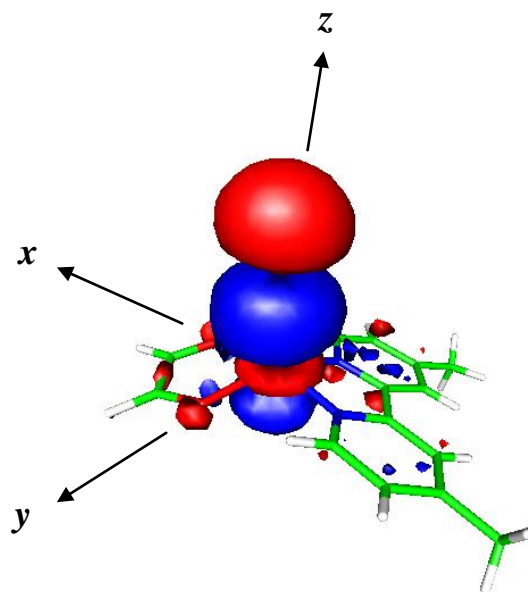
Figure 2.20 Cu [3dz^2] and Br [np_z] molecular orbitals calculated for the hypothetical fragment **1a′** at 60% of the total electron density. Calculations were performed using the BP86 exchange functional with CP(PPP) (copper atom) and TZVP (other atoms) basis sets. Orbital phases are represented with red and blue. Atom colour scheme is consistent with that used in Figure 2.18. Cartesian axis directions are also overlayed.

Figure 2.21 depicts the overlaid experimental specta at the copper K-edge and ORCA generated theoretical spectra (also at the copper K-edge). Inspection of Figure 2.21 reveals a good fit between these experimental and theoretical spectra. In general, the intensity and energy positions of the spectral features have been modelled well.
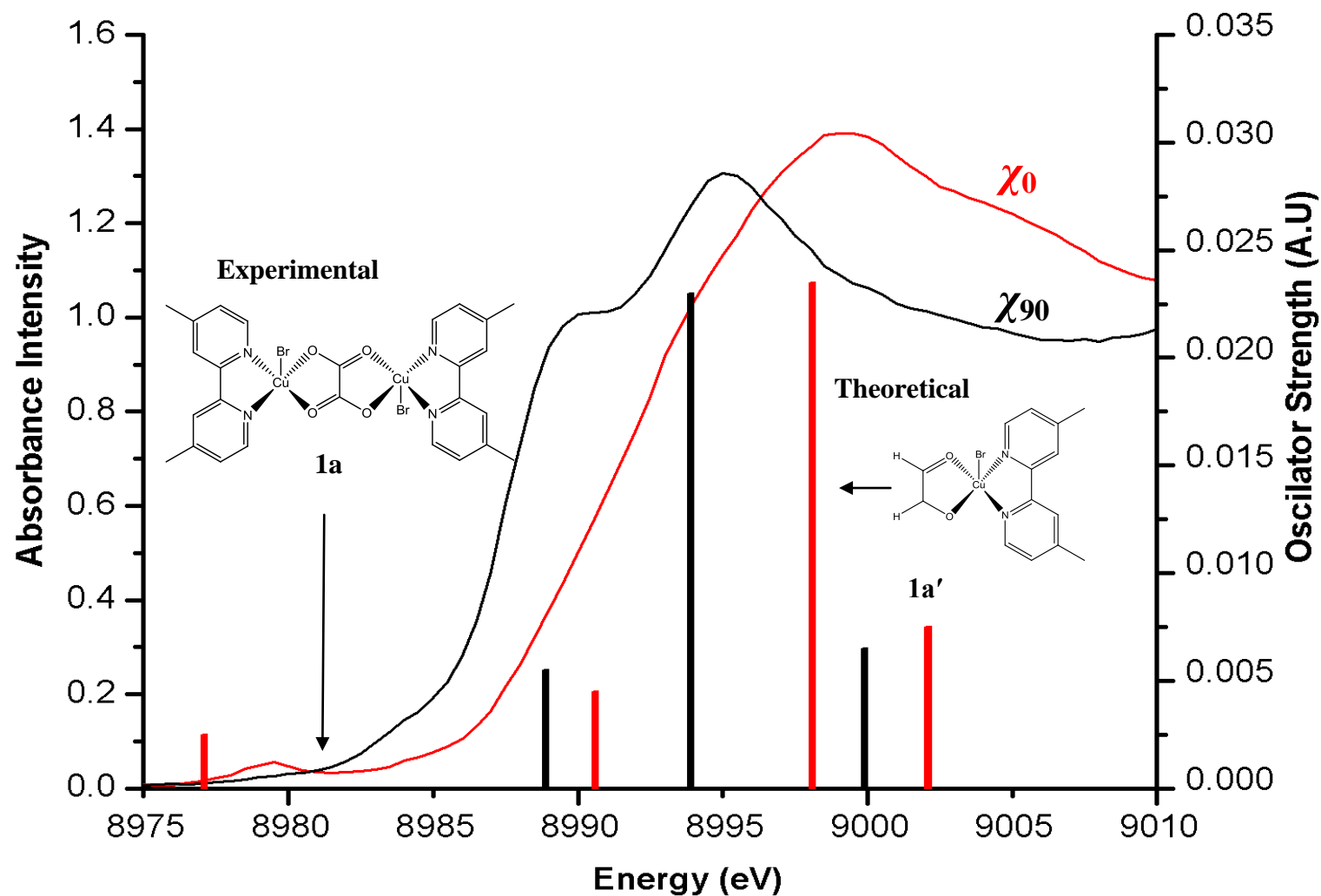
Figure 2.21 A comparison between calculated XAS spectra at the Cu K-edge for the hypothetical fragment **1a′** (column chart) along with experimental XAS spectra for **1a** (line chart) overlaid. In the calculated spectrum transitions to all other atoms except copper and bromine have been omitted for clarity.

*c) Using TD-DFT molecular orbital calculations to study **1a***

Initially, calculations on the full molecular structure of **1a** could only be successfully performed at Hartree–Fock/STO-3G level of theory despite several attempts at geometry optimisation. More recently however, convergence has been achieved using the Newton-Raphson method using the B3LYP/6-211G level of theory.[60] Nevertheless, it proved difficult to extract the precise 3*d* orbital energies and identify the ground state SOMO due to its complexity. The Cu [3*d*] orbiral contribution appeared to be smeared out with numerous other atoms that make up the contribution to a given molecular orbital. However, it is likely that the SOMO ground state is a mixture of Cu [$3d_{z^2}$], Cu [$3d_{xy}$] and Cu [$3d_{x^2-y^2}$].

The calculated polarised XAS spectrum for **1a** generally shows a good agreement with **1a′** and hence, experimental results for **1a** (due to its similarity to **1a′** the spectra for **1a** is not shown). Furthermore, analysis of the molecular orbitals calculated for **1a** (Figure 2.22) using a higher percentage electron density plot shows significant overlap of the π-orbitals within the oxalate ligand to each copper(II) metal centre, suggesting a possible intramolecular communication mechanism.[13,14,61-65] Unfortunately, the molecular orbital contour plots of **1a** are of poor quality due to the solution that the minimal basis sets offer; nevertheless, they show similar interpretable features to **1a′** (Figure 2.21).

(a)　　　　　　　　　　　　　　　　　**(b)**
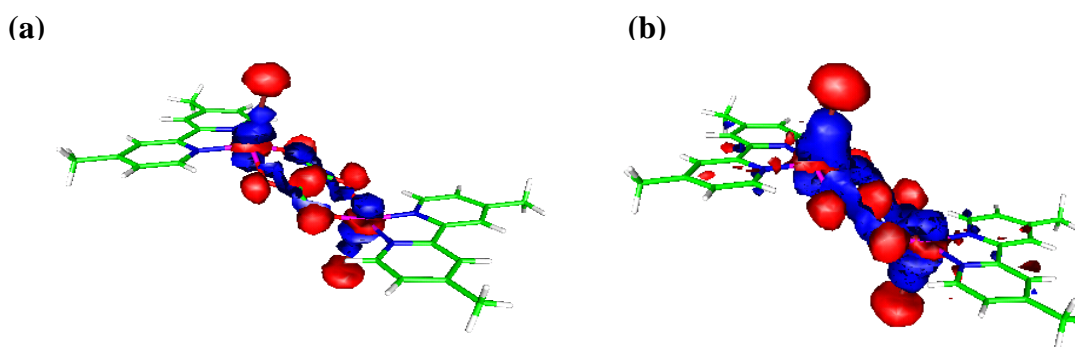
Figure 2.22 Cu [$3d_{z^2}$], Br [*npz*] and O [*2p*] molecular orbitals calculated for **1a** at (a) 40% and (b) 60% of the total electron density. Calculations were performed at HF/STO-3G level of theory for all atoms. Orbital phases are represented with red and blue. Atom colour scheme is consistent with that used in Figure 2.18.

*d) Summary of MO calculations performed on **1a** using ORCA*

The pre-edge and shoulder (main-edge 1) features in the XAS spectra of **1a** at the Cu K-edge have been assigned and show good agreement with previous studies on **D**[27] and **E**.[36] Polarisation dependence of the pre-edge feature arises when the polarisation vector of X-ray radiation is aligned parallel to the Cu–Br bond vector resulting in a Cu [1*s*] electron promotion into the *triplet* Cu [3*d$_{z^2}$*] orbital (3*d* hole) projecting along the bond vector. Admixing between ligand *p*-states (mainly Br with some O) may enhance the intensity of this transition through orbital admixing or spin-orbit coupling.[26] With regard to the main-edge 1 shoulder, a shakedown transition has been similarly assigned, in this case to be the result of shakedown transitions from Br [*p$_{x,y}$*] orbitals into the core hole caused by the main-edge Cu [1*s*]→[4*p*] transition. Furthermore, it has been shown for the first time, for SBP complexes, that the observed main-edge 2 polarisation dependence arises from excitations into the Cu [4*p$_z$*] (χ_0) and Cu [4*p$_{x,y}$*] (χ_{90}) orbitals where the [4*p$_z$*] orbital also projects along the Cu–Br bond vector.[27,36] At the onset of the EXAFS (9005 eV) the hypothesised Cu [1*s*]→[5*p*] transition gives rise to a shoulder (more prominently in χ_0) resulting in further shakedown phenomena. The Cu [5*p$_z$*] orbital is also likely to align with the Cu–Br bond vector. The source of the EXAFS dichroism cannot be adequately described using DFT due to the lack of appropriate basis sets to describe such high energy orbitals. Nevertheless, these DFT determined results highlight the important role played by the Cu–Br bond and its alignment in mediating the X-ray dichroism.

2.7.3 Multiple Scattering (MS) theory

EXAFS phenomena result from the scattering of high energy electrons by surrounding atoms (usually 50 eV above the edge). A formal mathematical description of MS is given by Beeby[66] and is the basis of early computational MS codes[67–69] for the prediction of EXAFS.[70] Early MS calculations for crystalline systems were reliable and accurate, but limited (large basis sets were required and only simple unit cells were considered).[71] More recently however, Rehr and Albers have developed an *ab initio* MS program based on the self consistent effective multiple

scattering amplitude (F_{eff}, referred to as FEFF)[62–74] of a photoelectron from an excited atom within a cluster of atoms. Moreover, the program has demonstrated some reliability.[75–78] A full description of the theoretical approaches to EXAFS is reviewed by Rehr and Albers.[79]

a) Case study 3: [Creatinium]$_2$CuCl$_4$ (E) using MS calculations

Further theoretical studies on **E**[36] (section 2.7.1) by Hahn *et al*. have shown, using a MS approach, that the *z*-oriented main-edge structure in the XANES of several crystalline square-planar copper(II) compounds (*idem.* **E**) can be comparatively (Kosugi) ascribed to the transition of a core electron into empty *bound* Cu [$4p_z$] orbitals (within the main-edge 1 shoulder, albeit a shakedown transition in previous studies) and contrastingly, *continuum* (resonance) states (at the main-edge 2).[80]

2.7.4 FEFF calculations performed on 1a

This apparent conflict in interpretation of **E** (*vide supra*) has inspired the probing of **1a** using a MS approach. Hence, complex **1a** was also subjected to a computational study using FEFF 8.4[81] to elucidate the observed X-ray dichroism phenomenon. The effects of several parameter changes and their influence on the excited Cu [$1s$] photoelectron will be discussed in the following sections. An extensive study was performed on **1a** in a step-wise fashion, using the Hedin-Lundqvist model (*vide infra*), however, only a flavour of the most significant results will be discussed herein. In a typical calculation, an X-ray polarisation vector was aligned parallel and perpendicular to the Cu–Br bond giving the relative orientations χ_0 and χ_{90}, respectively as described previously (see section 2.5). The following outlines the author's MS-based approach to model the experimental behaviour of **1a**.

a) FEFF: Single molecule vs. cluster

A comparison of FEFF calculated polarised absorption spectra for a single molecule of **1a**, and a 10 Å radius spherical molecular cluster (cluster = contents of a spherical segment of the crystallographic packing diagram) centred on an absorbing copper atom within **1a** (Figure 2.23),

revealed comparable features in the χ_0 orientation (Figure 2.24). However, they show a remarkable difference in the χ_{90} orientation in the near-edge-region.

General inspection of these spectra indicated that the cluster model gave the closest fit with experimental data (Figure 2.25) and it could be suggested that the cluster model is a more realistic representation of a single crystal (*cf.* a single molecule in the gas phase with DFT calculations).
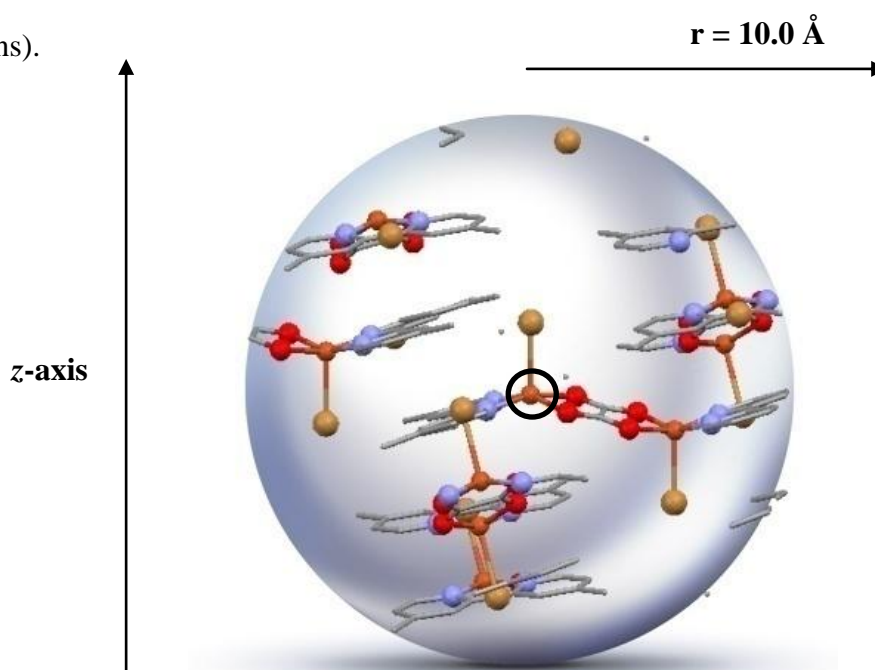
Figure 2.23 A spherical 10 Å radius cluster of atoms aligned along the *z*-axis, generated around the central absorbing copper atom (circled in black). The cluster is the basis for most FEFF calculations involving **1a**; copper atoms are shown in brown and bromine atoms are shown in yellow.
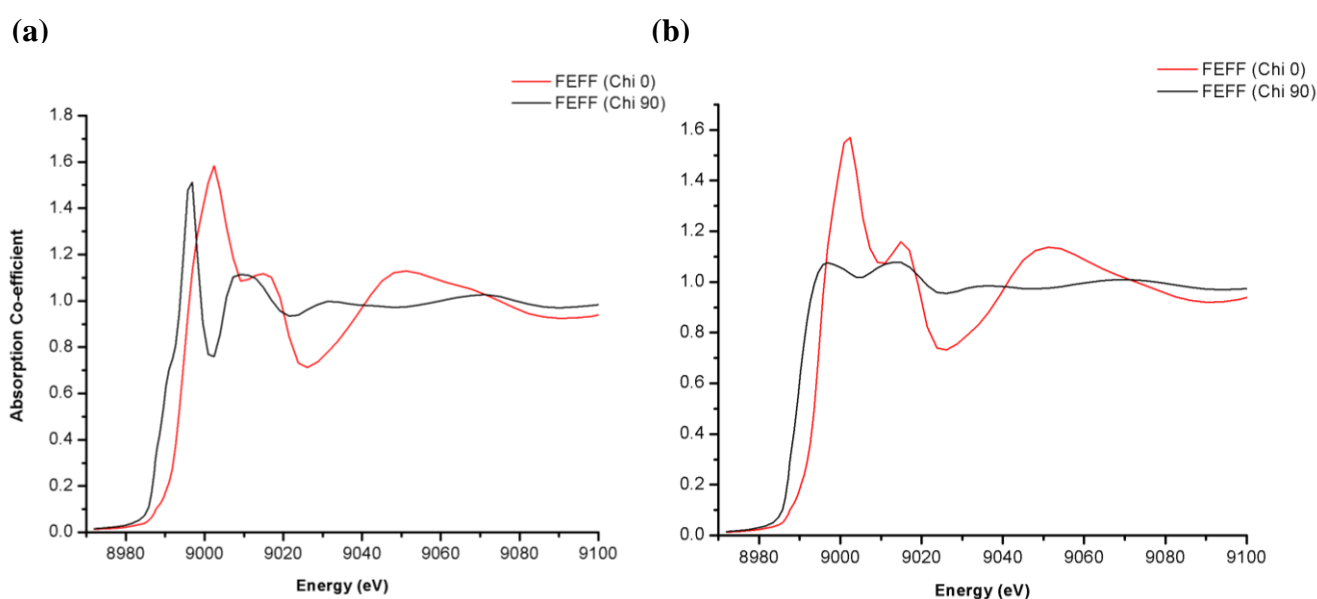
Figure 2.24 FEFF calculated XAS spectra for **1a** at the Cu K-edge for orientations of χ_0 and χ_{90} showing a comparison between (a) a 10 Å radius cluster and b) a single molecule.

(a)

(b)
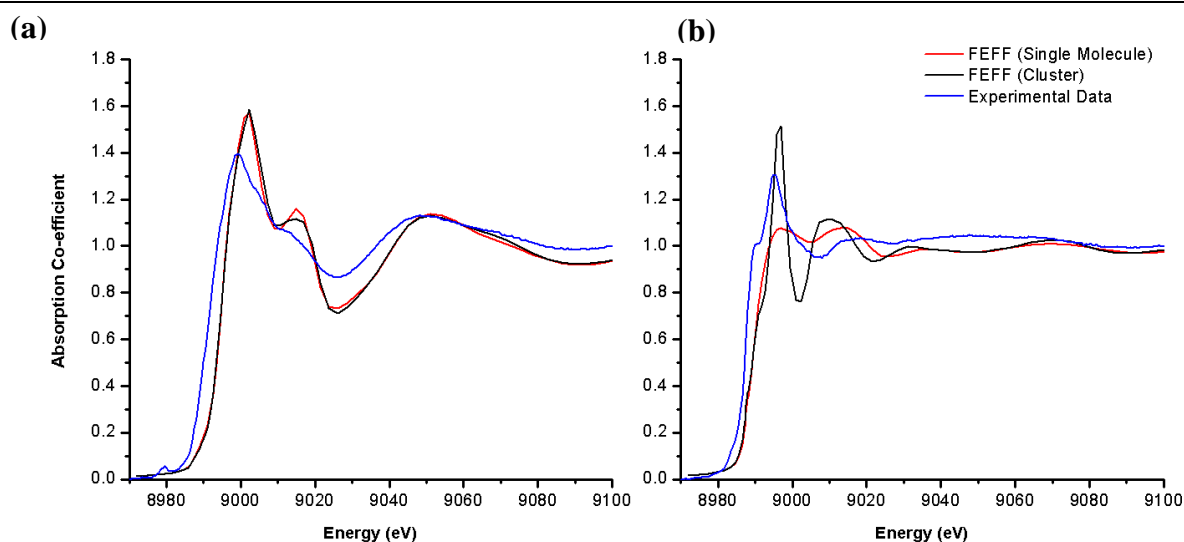
Figure 2.25 FEFF calculated XAS spectra for **1a** at the Cu K-edge comparing a single molecule and a 10 Å radius cluster against experimental data for **1a** for orientations of (a) χ_0 and (b) χ_{90}

b) FEFF: Investigation of the muffin-tin approximation

Practical XANES MS calculations rely on the muffin-tin approximation (Figure 2.26) which has been extensively described mathematically.[89] The model describes a spherical scattering potential centred on each atom with a constant value of the potential in the region between the atoms (interstitial region).[81] Within the muffin-tin, atomic like states exist close to centre while at the surface, the bonding properties of the material determine the distribution of charge over 'resonance states'. The interstitial region is difficult to define for non-periodic materials and typically the muffin-tin potentials can be overlapped by *ca.* 10–15% (minimising the interstitial space).[90] Strictly, this is mathematically incorrect, but has been widely accepted and has produced agreeable comparisons to experimental results.[91]
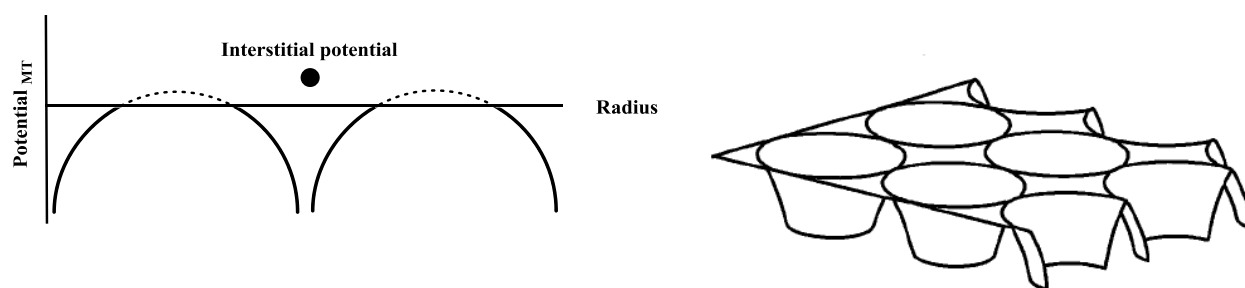
Figure 2.26 A graphical representation of (a) the one and (b) two dimensional muffin-tin potentials.[86] The solid horizontal line in the one dimensional illustration represents the flat constant interstitial potential which truncates the true shape of the potential.

For **1a**, calculations using a non-overlapping muffin-tin potential (applied to the cluster model) correctly predicted the rapid onset of the edge and generally gave results consistent with experiment. However, it was found that the pre-edge was sensitive to overlap and was more pronounced using FEFF's default overlapping parameter. Furthermore, overlap caused dampening of the oscillations at *ca.* 50 eV above the edge.

c) FEFF: Thermal motion and the Debye–Waller factor

The Debye–Waller factor (σ^2)[85,86] accounts for the effects of intra- and intermolecular thermal motion and can be appropriately used here to describe the behaviour of a molecule in a single crystal by introducing static and global structural disorder. In calculations for **1a** (using the cluster model and default muffin-tin overlap), the introduction of heavy disorder $(\sigma^2 = 0.1)$ dampens the oscillations and the loss of definition of many spectral features is apparent. This occurs specifically at the main-edge 2 features at 9005 eV and EXAFS features at 9030 eV and 9050 eV (Figure 2.27a). In contrast, using mild disorder $(\sigma^2 = 0.01–0.05)$ resulted in spectral features being modelled accurately, namely, broadening of the main-edge 2 with slight dampening of the oscillations in the EXAFS region resulting from a reduction in the scattering amplitude (Figure 2.27b). Interestingly however, the definition of the pre-edge is lost. A possible explanation is that the weak transition may have been broadened due to over compensating the amount of thermal disorder (it becomes too broad to be observed). Further evidence to support the above statement is presented when the calculation is run without the influence of any σ^2 and a pre-edge feature is observed at 8987 eV (Figure 2.24).

(a)

(b)

Decreasing

Debye–Waller

factor

(c)
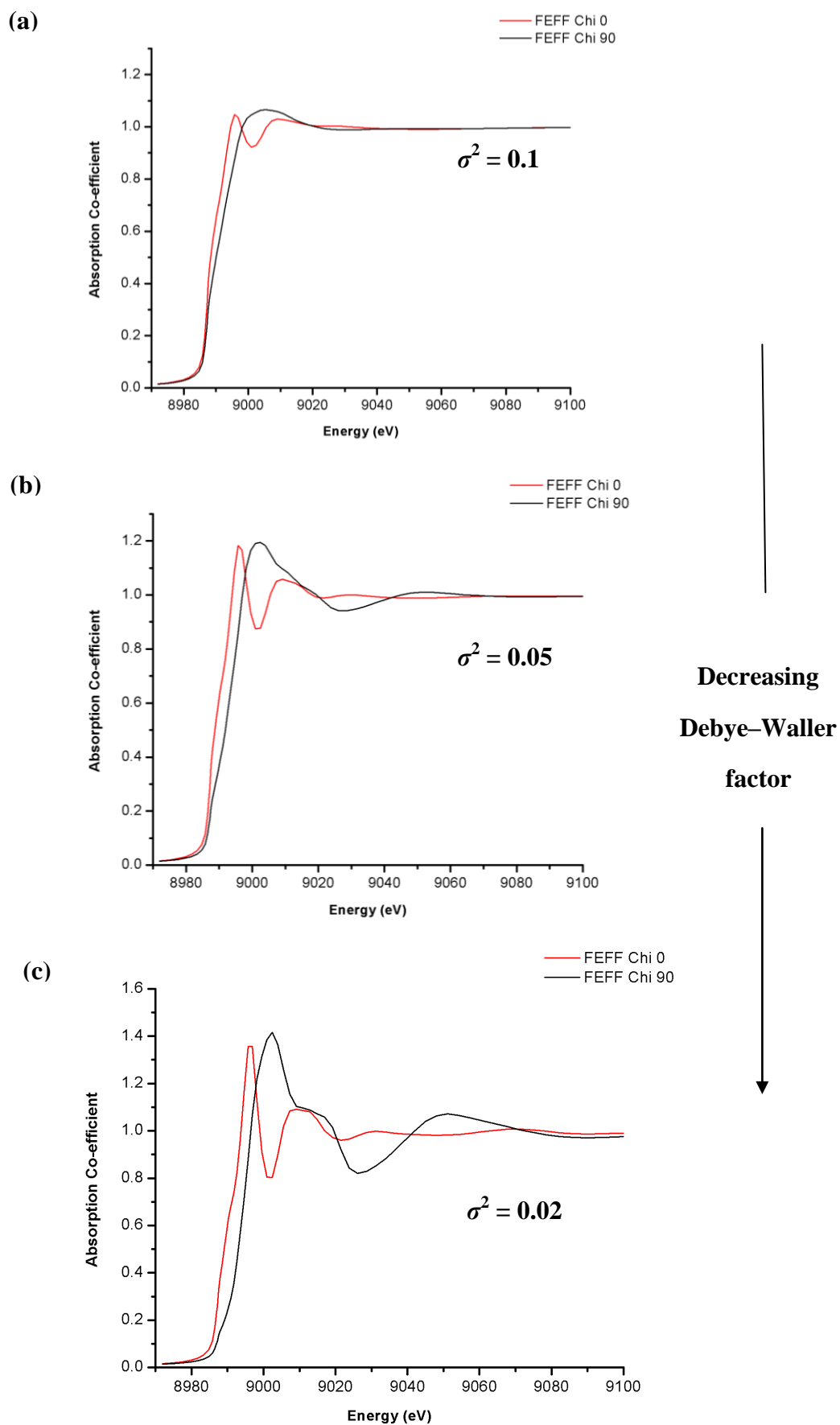
Figure 2.27 FEFF calculated XAS spectra for **1a** at the Cu K-edge for orientations of χ_0 and χ_{90} showing a comparison of Debye–Waller effects (a) $\sigma^2 = 0.1$, (b) $\sigma^2 = 0.05$, (c) $\sigma^2 = 0.02$ with muffin-tin overlap.

d) FEFF: Variation in the exchange potential

Thus far, MS calculations on **1a** using FEFF have been performed using the Hedin–Lundqvist[87] model as described elsewhere.[81] Several other exchange models have been investigated, such as Dirac–Hara and showed very little difference within the calculated spectra. The pre-edge feature in the experimental XAS spectrum could be modelled using FEFF calculations by manipulating the real and imaginary part of the potential within the Hedin–Lundvist model. Inspection of the χ_0 calculated spectrum revealed that a 2 eV Fermi-edge shift in the real part of the potential changes the appearance of the pre-edge feature. It was shown that the pre-edge (8986 eV) was found to be slightly embedded in the shoulder (Figure 2.28). In contrast, a 1 eV change to the imaginary part caused a shift of the pre-edge feature well into the edge with an overall red-shift in energy (*ca.* 10 eV). Furthermore, the EXAFS region appeared to remain unchanged. FEFF calculations were also performed using the <NO HOLE> parameter (which mimics electronic core hole screening) in conjunction with Fermi-level adjustments. In a system where the core-hole is unshielded, the Fermi-states will be attracted to the 'singularity' caused by the core–hole thus lowering the excitation energy and causing an overall red-shift in the lower energy excited states. With core–hole shielding, this attractive interaction is reduced and interestingly, the pre-edge feature was modelled accurately, in so much that its spectral position and intensity was recreated. Hence, this gave the closest fit to experimental data in the χ_0 orientation (Figure 2.29).
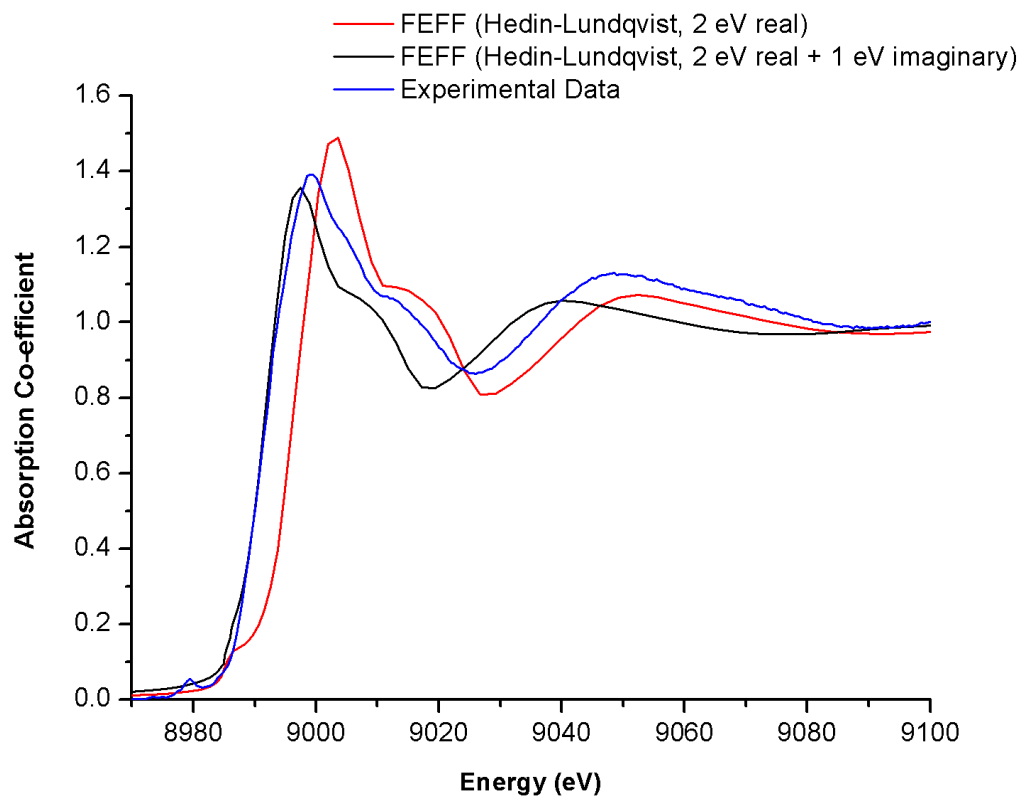
Figure 2.28 FEFF calculated XAS spectra for **1a** at the Cu K-edge showing exchange potential modifications with a comparison to experimental XAS data for **1a** in the χ_0 orientation.
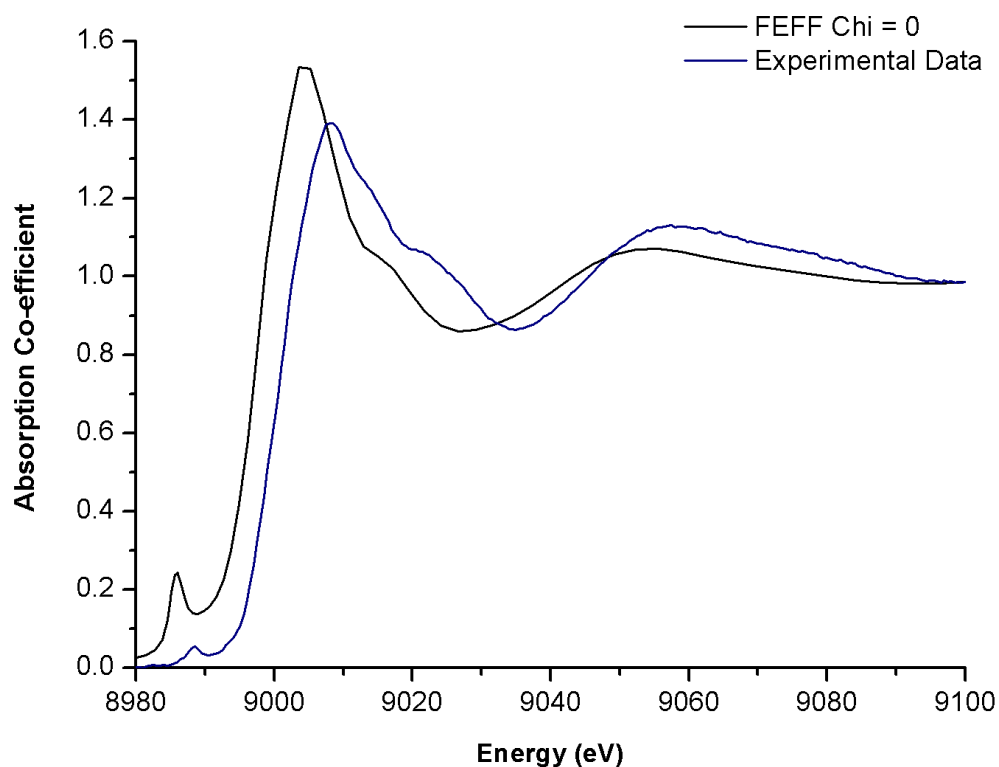
Figure 2.29 Best fit FEFF calculated XAS spectra for **1a** at the Cu K-edge including core–hole screening parameters with a comparison to experimental XAS data for **1a** in the χ_0 orientation overlaid.

e) FEFF: Local Density of States (LDOS)

i) LDOS and quadrupole transitions

It is apparent that the percentage difference between the best fit FEFF calculated XAS spectra for **1a**, where quadrupole terms are present and omitted, is quite small (2–3%); particularly in the pre-edge region. This suggests that the electronic transition that results in the weak pre-edge feature observed in the χ_0 orientation is not of quadrupole origin.[26,27,36] With reference to the interpretation of LDOS data, the local density of states did not reveal any *d*-orbital like states close to the edge (*cf.* DFT in section 2.7.3).

ii) *p*-State DOS

The origin of the pre-edge region in the χ_0 orientation (within experimental and theoretical XAS spectra) is not clear. Significantly, LDOS revealed a large p_z-contribution from the copper, bromine and oxygen atoms at *ca.* 12.6 eV below the vacuum level (corresponding to the same Fermi-energy as the pre-edge feature). Furthermore, the intense main-edge comprises continuum 'resonance' states of significant *p*-character localised on the copper atom. These states reside above the vacuum level between 4–5 eV (Figure 2.31). A graphical representation of these transitions within the muffin-tin potential is depicted in Figure 2.30.
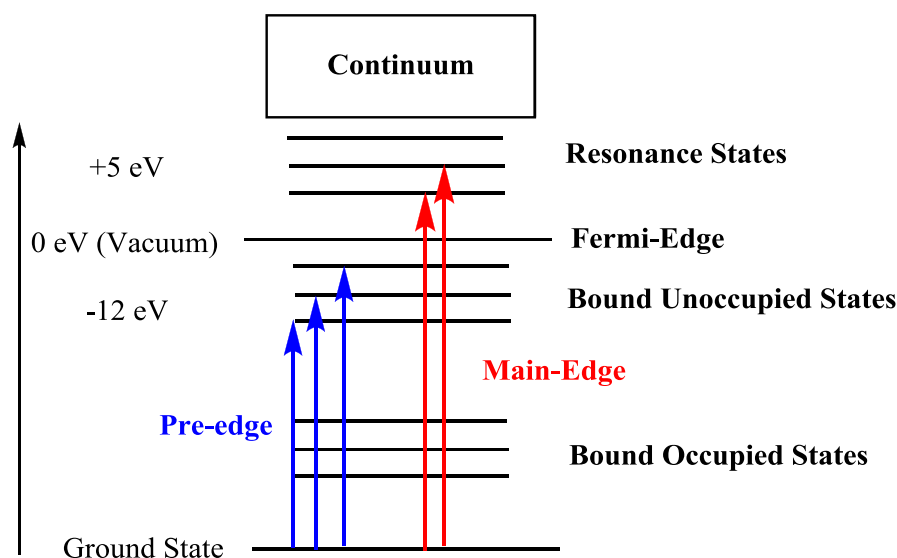
Figure 2.30 A schematic outlining Cu [1*s*] electronic transitions interpreted from FEFF calculations of **1a**.

(a)

(b)
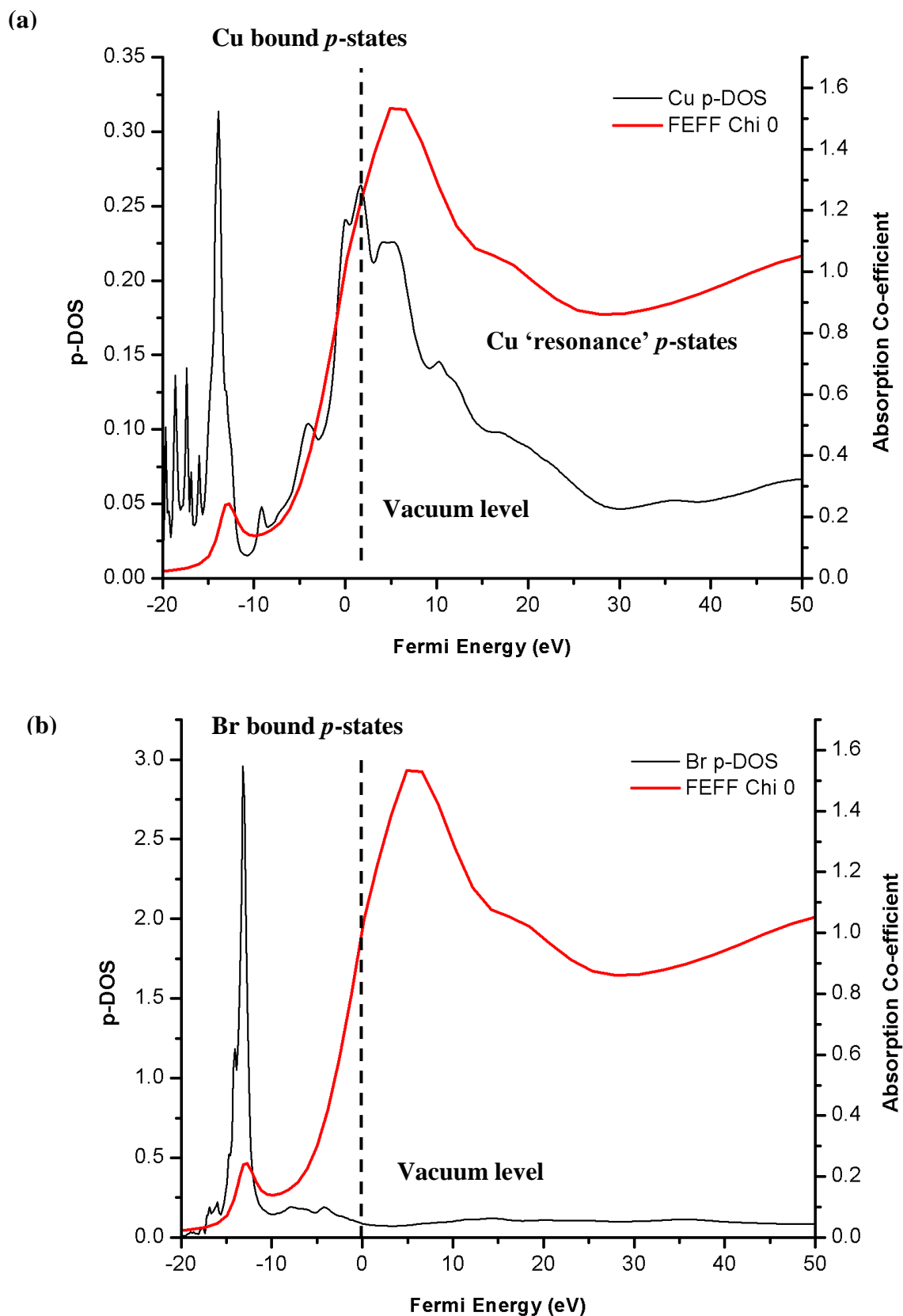
Figure 2.31 (a) Copper and (b) bromine LDOS analysis for **1a** with a FEFF calculated XAS spectrum at the Cu K-edge for the orientation of χ_0 orientation overlaid. These data were obtained courtesy of Dr. M. Roy (Department of Physics and Astronomy, University of Leicester).

*f) Summary of MS calculations performed on **1a** using FEFF*

Using a step-wise methodology, an agreement between experimental and theoretical results has been established using FEFF. Initially, the series of MS calculations performed on **1a** have revealed that a 10 Å radius cluster gave a closer resemblance to experimental XAS spectra than a single molecule of **1a** (*part a*). Interestingly, the pre-edge feature can be enhanced by adjusting the position of the Fermi-edge. Specifically, a 2 eV shift in the real part of the potential gave a notable accentuation in the pre-edge. Interestingly, calculations were performed in which the core [1*s*] hole is shielded by outer-lying electrons and these revealed a significant pre-edge feature within the FEFF generated spectra and indeed very close to experimental XAS spectra (*part d*). The introduction of a significant Debye–Waller factor to the FEFF calculation (involving a cluster of **1a**) revealed broadened spectral features and dampening of the scattering amplitude. These spectral features were resolved using a lower Debye–Waller factor and gave an improved comparison to experimental XAS spectra (*part c*). The origins of the pre- and main-edge were investigated using LDOS and furthermore, no evidence of quadrupole transitions was established (*part e*).

2.7.5 Relative merits of MS *vs.* TD-DFT towards the study of 1a

Theoretical studies of **1a** using TD-DFT (ORCA) and MS (FEFF) modelled well the key features of the experimental XAS spectra. In particular, the pre-edge and main-edges 1 and 2 in the XAS spectra were reproduced accurately while the EXAFS region remains unclear. Furthermore, both approaches reveal intense transitions at the main-edge 2, which correspond to *p*-like states. In TD-DFT these are ascribed to dipole transitions to bound unoccupied states (Cu [4*p*]), while MS suggests transitions into 'resonance' states with *p*-character above the Fermi level. Both approaches also suggest a *p*-contribution from the *bromide* ligand manifests itself at the pre-edge. This can be deduced from the interpretation of FEFF LDOS data and calculated electron density plots obtained from ORCA. However, the electronic origin of the pre-edge can be interpreted differently. Specifically, TD-DFT suggests a weak quadrupole Cu [1*s*]→[3d_{z^2}]

transition (prominent when the X-ray polarisation vector is parallel to the Cu–Br bond vector) for the pre-edge, whilst MS suggests the absence of any quadrupole terms. Indeed, a dipole transition to bound unoccupied *p*-like states on the copper atom and ligand atoms can be rationalised from LDOS analysis of the pre-edge. However, it is interesting to note that re-inspection of the ORCA data using the results of FEFF also suggested that a significant dipole *p*-contribution from the ligand at the pre-edge is apparent. With regard to main-edge 1 (shoulder), the shakedown phenomena identified in DFT were shown to be transitions into bound copper *p*-states using MS with negligible contributions from the bromine atom.

Overall, MS has the means to provide a closer, more realistic description of **1a** within a single crystal environment, namely the cluster approach (*cf.* a single molecule in the gas phase with DFT). In addition, the application of the Debye–Waller factor can simulate thermal motion in a crystal lattice and model structural disorder.

2.8 Conclusions

This chapter has been concerned with a combined experimental and theoretical study of X-ray dichroism in copper(II) complexes. The synthetic routes to several fully characterised, highly ordered dicopper compounds (**1a** and **1b**) have been described. The sensitivity of the reaction pathway to reactant stoichiometry is reported; thus, polymeric **2a**–**2c** could also be prepared in good yields. Complex **1a** was subjected to a thorough study to evaluate its performance as a potential dichroic filter. Polarised XAS spectra were recorded in transmission mode at the Daresbury synchrotron radiation source (station 16.3) and revealed polarisation dependent features at the Cu K-edge (8979 eV) in the pre-edge, main-edge 1 and 2 and EXAFS regions. XAS spectra were also recorded in fluorescence mode at the Diamond Light Source (station I16) and reproduced dichroic features observed in the transmission spectra. Hence, modulation curves showing X-ray dichroism could be generated from both detection modes. Furthermore, an investigation was performed at the Br K-edge (13540 eV) and revealed polarisation dependent features at the main-edge and EXAFS, albeit of lower intensity.

To date, a comparative study of the two theoretical approaches MS and TD-DFT has not been undertaken in the literature for a system exhibiting polarisation dependent features. Authors usually adopt a biased view point based on either quantum chemistry (DFT) approaches[27,28,37,48] or a Multiple Scattered wave theory (MS) approach.[60–74] Herein, the application of the two methodologies has been presented and more significantly, they both reproduce the spectral features in the XAS spectra of **1a** accurately, albeit with a difference in interpretation. Nevertheless, they both provide evidence that X-ray dichroism in **1a** originates from transitions occurring into orbitals/states associated with the Cu–Br bond. Furthermore, the results obtained using FEFF can shed light on the nature of the pre-edge feature that has previously been the subject of some conflict of opinion. Although the DFT model is restricted to a single molecule in the gas phase, it does provide a visual representation of the molecular orbitals (bound states). MS on the other hand is more appropriate to describe the wider aspects of the dichroism phenomenon such as inter- and intramolecular interactions (using the cluster approach). Furthermore, the FEFF package offers the user a choice of a number of manipulations to the construction of the potential which provide a means to better model the experimental XAS spectra.

2.9 General experimental

The FAB mass spectra were performed by Dr. G. Eaton (Department of Chemistry, University of Leicester) and were recorded using a Kratos Concept mass spectrometer using *m*-nitrobenzoic acid (NBA) as a matrix. The electrospray ionisation (ESI) mass spectra were recorded using a Micromass Quattra LC mass spectrometer using a methanolic solvent as the mobile phase. IR spectra were recorded using a Perkin-Elmer Spectrum One FT-IR spectrometer using the universal ATR sampling accessory for solid samples. Magnetic susceptibility measurements were carried out at room temperature using an Evans balance using standard methods[88] and corrections for underlying diamagnetism were applied to the data.[89] Melting points were recorded using Griffin melting point apparatus in open capillary tubes. Elemental analyses were performed by S. Boyer at the Science Technical Support Unit, London Metropolitan University. The reagents 2,2′-bipy, 4,4′-Me$_2$bipy, 5,5′-Me$_2$bipy, sodium oxalate and CuBr$_2$ were purchased from Sigma Aldrich and used as received.

2.9.1 Synthesis of 1

a) 1a: To a solution of CuBr$_2$ (0.446 g, 2.00 mmol) in methanol (50 ml) was added 4,4′-Me$_2$bipy (0.362 g, 2.00 mmol, 1 eq.) previously dissolved in dichloromethane (5 ml). The resulting brown precipitate was stirred for 15 min at room temperature, followed by the addition of sodium oxalate (0.134 g, 1.00 mmol, 0.5 eq.) dissolved in water (3 ml). The mixture was stirred for a further 30 min at room temperature, whereupon a blue precipitate formed which was filtered and dried in an oven at 100 °C for 12 h. The blue solid was recrystallised from a mixture of water and ethanol in a 20:1 ratio, respectively. Slow evaporation of the solvent yielded **1a** as blue needles (0.750 g, 50%). Found: C, 41.85; H, 3.15; N, 7.74. C$_{24}$H$_{24}$N$_4$O$_4$Cu$_2$Br$_2$ (715.88) requires: C, 41.99; H, 3.23; N, 7.53; *m/z* (FAB) 744 (20%) [M + H], 664 (40%) [M - Br], 584 (40%) [M - 2Br]; ν_{max}(ATR)/cm^{-1} 1644, 1613, 1557, 1488, 1446.70, 1412, 1376, 1347, 1304, 1286, 1251, 1025, 914, 839, 730; μ_{eff} = 1.57 BM; mp: >360 °C.

b) 1b: Following a similar approach and molar ratio of reactants to that described for **1a**, **1b** was obtained as blue needles (0.600 g, 40%). Found: C, 41.80; H, 3.12; N, 7.81. C$_{26}$H$_{24}$N$_4$O$_4$Cu$_2$Br$_2$ (743.39) requires: C, 42.01; H, 3.25; N, 7.54; *m/z* (FAB) 744 (20%) [M + H], 664 (40%) [M - Br], 584 (40%) [M - 2Br]; ν_{max}(ATR)/cm^{-1} 1662, 1621, 1508, 1487, 1395, 1295, 1254, 1232, 1165, 1054, 841, 798, 728; μ_{eff} = 1.51 BM; mp: >360 °C.

2.9.2 Synthesis of 2

a) 2a: To a solution of CuBr$_2$ (0.446 g, 2.00 mmol) in methanol (50 ml) was added 2,2′-bipy (0.312 g, 2.00 mmol, 1 eq.) previously dissolved in dichloromethane (5 ml). The resulting brown precipitate was stirred for 15 min at room temperature followed by the addition of sodium oxalate (0.540 g, 4.00 mmol, 2 eq.) dissolved in water (3 ml). The mixture was stirred for a further 30 min at room temperature, whereupon a blue precipitate formed which was filtered and dried in an oven at 100 °C for 12 h. The blue solid was recrystallised from a mixture of water and ethanol in a 20:1 ratio, respectively. Slow evaporation of the solvent yielded **2a** as blue plates (0.250 g, 26%). The product was characterised by X-ray crystallography and gave unit cell parameters consistent with those reported in the literature.[13]

b) 2b: Following a similar approach and molar ratio of reactants to that described for **2a**, **2b** was obtained as blue plates (0.650 g, 65%). Found: C, 46.01; H, 3.11; N, 6.50. C$_{16}$H$_{12}$N$_2$O$_8$Cu (422.99) requires: C, 45.34; H, 2.85; N, 6.01; v_{max}(ATR)/cm^{-1} 1641, 1490, 1476, 1350, 1301, 1154, 1232, 1154, 1104, 1059, 1030, 805, 780, 729 649; μ_{eff} = 1.56 BM; mp: >360 °C.

c) 2c: Following a similar approach and molar ratio equivalents to that described for **2a**, **2c** was obtained as blue plates (0.470 g, 47%). Found: C, 45.50; H, 2.82; N, 6.11. C$_{16}$H$_{12}$N$_2$O$_8$Cu (422.99) requires: C, 45.34; H, 2.85; N, 6.01; v_{max}(ATR)/cm^{-1} 1660, 1483, 1456, 1298, 1232, 1150, 1110, 1067, 1033, 805, 780, 727 660; μ_{eff} = 1.50 BM; mp: >360 °C.

2.10 X-ray crystallography

Crystallographic data analysis was carried out in collaboration with K. Singh (Department of Chemistry, University of Leicester). Data for **1a**, **1b**, **2b** and **2c** were collected on a Brüker APEX 2000 CCD diffractometer. Details of data collection, refinement and crystal data are listed in Tables 2.7 and 2.8. All data were collected using a graphite monochromated Mo-K$_\alpha$ radiation (λ = 0.7107 Å) and the reflections were corrected for Lorentz, polarisation and absorption effects. The structures were solved by full-matrix least squares on F^2 using SHELXTL version 6.10.[90] Carbon bonded hydrogen atoms were included in calculated position (C–H = 0.96 Å) with isotropic displacement parameters set to 1.2 Ueq(C). Non-hydrogen atoms were refined with anisotropic displacement parameters. Disordered molecules of ethanol were removed using the SQUEEZE option in PLATON[91] for **1a**.

Table 2.7 Crystallographic parameters for **1a** and **1b**.

Compounds	1a	1b
Singh code	07045a	08043
Formula	$C_{30}H_{36}Br_2Cu_2N_4O_6$	$C_{26}H_{24}Br_2Cu_2N_4O_4$
Mc	831.54	743.39
Crystal size (mm)	$0.14 \times 0.08 \times 0.05$	$0.16 \times 0.15 \times 0.11$
Temperature (K)	150(2)	150(2)
Crystal system	Monoclinic	Triclinic
Space group	*I*2/*a*	*P*-1
Lattice parameters		
a (Å)	13.4708(18)	8.5015(18)
b (Å)	17.682(2)	8.7132(18)
c (Å)	13.601(3)	9.0564(19)
α (°)	90	91.651(3)
β (°)	98.048	101.099(3)
γ (°)	90	96.541(3)
U (Å^3)	3207.7(9)	653.1(2)
Z	4	1
D_c (Mg/m^3)	1.722	1.890
$F(000)$	1672	368
μ (Mo-K$_\alpha$)	3.863	4.728
Reflections collected	12454	5122
R(int)	0.0816	0.0372
Independent reflections	3154	2539
Parameters/restraints	0/174	0/174
R_1; wR_2[I>2σ(I)]	$R_1 = 0.0420$, $wR_2 = 0.0743$	$R_1 = 0.0362$, $wR_2 = 0.0837$
R_1; wR_2 (All data)	$R_1 = 0.0227$, $wR_2 = 0.0807$	$R_1 = 0.0448$, $wR_2 = 0.0868$
Goodness of fit on F^2 (all data)	0.855	1.003

Table 2.8 Crystallographic parameters for **2b** and **2c**.

Compounds	2b	2c
Singh code	07049	06048
Formula	$C_{14}H_{14}CuN_2O_5$	$C_{28}H_{38}Cu_2N_4O_5$
Mc	353.81	797.70
Crystal size (mm)	$0.16 \times 0.13 \times 0.10$	$0.24 \times 0.22 \times 0.07$
Temperature (K)	150(2) K	150(2) K
Crystal system	Monoclinic	Triclinic
Space group	*C*2/*c*	*P*-1
Lattice parameters		
a (Å)	15.217(3)	9.042(4)
b (Å)	11.815(2)	10.653(4)
c (Å)	8.1342(14)	18.125(7)
α (°)	90	94.791(7)
β (°)	109.510(3)	90.472(7)
γ (°)	90	95.672(7)
U (Å^3)	1378.4(4)	1731.0(12)
Z	4	2
D_c (Mg/m^3)	1.705	1.530
$F(000)$	724	824
μ (Mo-K$_\alpha$)	1.611	1.302
Reflections collected	5208	13561
R(int)	0.0245	0.0490
Independent reflections	1356	6697
Parameters/restraints	0/103	0/446
R_1; wR_2[I>2σ(I)]	$R_1 = 0.0273$, $wR_2 = 0.0726$	$R_1 = 0.0588$, $wR_2 = 0.1382$
R_1; wR_2 (all data)	$R_1 = 0.0289$, $wR_2 = 0.0735$	$R_1 = 0.0829$, $wR_2 = 0.1485$
Goodness of fit on F^2 (all data)	1.088	1.055

2.11 Theoretical calculations

TD-DFT Molecular orbital calculations were performed with guidance from Dr. C. Evans (Department of Chemistry, University of Leicester) using the Magellan computational system (National Service for Computational Chemistry Software, Imperial College, London) employing the ORCA software package of Neese *et al.*[46] In general, calculations were performed using the BP86 exchange functional[52,53] in conjunction with several basis sets, namely the core-potential [CP(PPP)] for the copper atom and triple ζ valence potential (TZVP)[54] for all other atoms. In addition, the Slater type STO-3G[55] and Gaussian 6-311+G[56] (also including the polarised 6-311+G*) basis sets were occasionally used, along with the LYP correlation function B3LYP[92] or the Hartree–Fock[56] configuration. MS calculations were performed with guidance from Dr. M. Roy (Department of Physics and Astronomy, University of Leicester) using the FEFF 8.4 software package[81] on the ULARC and more recently, ALICE computer facilities at the University of Leicester.

2.12 Polarised XAS measurements

The polarisation XAS measurements in this chapter were performed in collaboration with Dr. N. P. Bannister, Dr. A. Martindale and Dr. D. V. Cotton (Space Research Centre, Department of Physics and Astronomy, University of Leicester) also in conjunction with Dr. S. P. Collins (Diamond Light Source LTD). A full technical specification for the Diamond Light Source, I16 beamline can be found elsewhere.[93] Included was a Si(111) channel cut monochromator capable of operating within 3.5–15 keV range along with a diamond phase retarder and parallel double focusing mirrors. Samples were mounted on a Newport six axis N-6050 kappa goniometer (integral sample *xy* stage ±2.5 mm and *z* stage ±13 mm) with full phi rotation. A permanently mounted high resolution polarisation analyser was placed 50 m away from the source capable of 10^{14} photons per second flux at 6 keV. Several remotely interchangeable point detectors [scintilator, APD diode and Pilatus pixel detector (100 K × 172 × 172 micron photon counting detector)] were also used. Technical specifications for Daresbury synchrotron radiation source, station 16.3 can also be found elsewhere.[94]

2.13 References

1) CSD (500,000 entries) January 2011.
2) Z. Smékal, P. Thornton, Z. Šindelář and R. Klička, *J. Coord. Chem.*, 2002, **55**, 259.
3) M. Wang, B. Hu, X.-T. Deng and C.-G. Wang, *Acta Cryst.*, 2007, **E63**, 710.
4) S. Youngme C. Chailuecha and N. Chaichit, *Polyhedron*, 2004, **23**, 1641.
5) S. Youngme, A. Cheansirisomboon, C. Danvirutai, N. Chaichit, G. A. Van-Albada and J. Reedijk, *Inorg. Chem. Commun.*, 2006, **9**, 973.
6) A. W. Addison and T. N. Rao J. Reedijk, J. V. Rijn and G. C. Verschoor, *J. Chem. Soc., Dalton Trans.*, 1984, 1349.
7) R. E. Marsh, *Acta Cryst.*, 2009, **B65**, 782.
8) J.-H. Luo, M.-C. Hong, Y.-C. Liang and R. Cao, *Acta Cryst.*, 2001, **E57**, m361.
9) X.-F. Chen, P. Cheng, X. Liu, B. Zhao, D.-Z. Liao, S.-P. Yan and Z.-H. Jiang, *Inorg. Chem.*, 2001, **40**, 2652.
10) H. Oshio and U. Nagashima, *Inorg. Chem.*, 1992, **31**, 3295.
11) W. Fitzgerald, J. Foley, D. McSweeny, N. Ray, D. Sheahan, S. Tyagi, B. Hathaway and P. O'Brien, *J. Chem. Soc., Dalton Trans.,* 1982, 1117.
12) A. C. Fabretti, G. Franchini, P. Zannini and M. Divaira, *Inorg. Chim. Acta*, 1985, **105**, 187.
13) S. Emori and K. Todoko, *Bull. Chem. Soc. Jpn.*, 1993, **66**, 3513.
14) S. Alvarez, M. Julve and M. Verdaguer, *Inorg. Chem.*, 1990, **29**, 4500.
15) A. Gerli, K. S. Hagen and L. G. Marzilli, *Inorg. Chem.*, 1991, **30**, 4673.
16) Bruker AXS application note SCD 374, *Crystal Face Indexing for Numerical Absorption Correction,* can be found online at Bruker-AXS.
17) B. Watts, L. Thomsen and P. C. Dastoor, *J. Electron. Spectrosc. Relat. Phenom.*, 2006, **151**, 105.
18) H. L. Nigam, *J. Pure Appl. Chem.*, 1988, **60**, 1175.
19) E. Hecht, *Optics*, Pearson Eductation, 4th edn, 2002, ISBN 0-321-18878-0.
20) Courtesy of D. Cotton (Space Research Centre, Department of Physics and Astronomy, University of Leicester) 2010, IDL script for the analysis of XAS data.
21) M.-H. Chao, B. M. Kariuki, K. D. M. Harris, S. P. Collins and D. Laundy, *Angew. Chem., Int. Ed.*, 2003, **42**, 2982.
22) D. Cotton, LU-X-POL-DL-02, *personal communication*, 2009.
23) B. L. Henke, E. M. Gullikson and J. C. Davis, X-ray interactions: photoabsorption, scattering, transmission, and reflection at E=50-30000 eV, Z=1-92, *Atomic Data and Nuclear Data Tables*, 1993, **54**, 181.
24) A. Enberg, *Acta Chem. Scand.*, 1970, **24**, 3510.
25) S. I. Chan, V. W. Hu and R. C. Gamble, *J. Mol. Struct.*, 1978, **45**, 239.
26) R. A. Bair and W. A. Goddard, III, *Phys. Rev. B*, 1980, **22**, 2767.
27) T. Yokoyama, N. Kosugi and H. Kuroda, *Chem. Phys.*, 1986, **103**, 101.
28) F. A. Cotton and H. P. Hanson, *J. Chem. Phys.*, 1956, **25**, 619.
29) W. Seka and H. P. Hanson, *J. Chem. Phys.*, 1969, **50**, 344.
30) C. W. DeKock and D. M. Gruen, *J. Chem. Phys.*, 1966, **44**, 4387.
31) J. C. Person and P. P. Nicole, *J. Chem. Phys.*, 1968, **49**, 5421.
32) G. R. Shulman, Y. Yafet, P. Eisenberger and W. E. Blumberg, *Natl. Acad. Sci. U.S.A.,* 1976, **73**, 1384.
33) E. A. Stern, *Phys. Rev. Lett.*, 1982, **49**, 1353.
34) M. R. Udupa and B. Krebs, *Inorg. Chim. Acta*, 1979, **33**, 241.
35) J. E. Hahn, R. A. Scott, K. O. Hodgson, S. Doniach, S. R. Desjardins and E. I. Solomon, *Chem. Phys. Lett.*, 1982, **88**, 595.
36) N. Kosugi, T. Yokoyama, K. Asakura and H. Kuroda, *Chem. Phys.*, 1984, **91**, 249.
37) P. J. Hodges, A. J. Ross, P. Crozet, H. Salami and J. M Brown, *J. Chem. Phys.*, 2007, **127**, 24309.
38) A. Ramirez-Solis, R. Poteau, A. Vela and P. Daudey, *J. Chem. Phys.*, 2005, **122**, 164306.
39) A. Ramirez-Solis and P. Daudey, *J. Chem. Phys.*, 2005, **122** 14315.
40) A. Ramirez-Solis and P. Daudey, *J. Chem. Phys.*, 2004, **120**, 3221.
41) X. B. Wang, L. S. Wang, R. Brown, P. Schwerdtfeger. D. Schroder and H. Schwarz, *J. Chem. Phys.*, 2001, **114**, 7388.
42) S. G. Wang and H. E. Schwarz, *J. Chem. Phys.*, 1998, **109**, 7252.
43) R. J. Deeth, *J. Chem. Soc., Dalton Trans.*, 1993, 1061.

44) T. K. Ha and M. T. Nguyen, *Zeitschrift Fur Naturforschung Section A – A Journal of Physical Sciences*, 1984, **39**, 175.

45) E. Runge and E. K. U. Gross, *Phys. Rev. Lett.*, 1984, **52**, 997.

46) F. Neese, ORCA: an *ab-initio* DFT and semi-empirical electronic structural package, version 2.6.35; Unversity of Bonn, Germany, 2008.

47) S. DeBeer George, T. Petrenko and F. Neese, *J. Phys. Chem. A*, 2008, **112**, 12936.

48) K. Ray, S. DeBeer George, E. I. Solomon, K. Wieghardt and F. Neese, *Chem. -Eur. J.*, 2007, **13**, 2783.

49) J. Yano, J. Robblee, Y. Pushkar, M. A. Marcus, J. Bendix, J. M. Workman, T. J. Collins, E. I. Solomon, S. DeBeer George and V. K. Yachandra, *J. Am. Chem. Soc.*, 2007, **129,** 12989.

50) R. Sarangi, N. Aboelella, K. Fujisawa, W. B. Tolman, B. Hedman, K. O. Hodgson and E. I. Solomon, *J. Am. Chem. Soc.*, 2006, **128**, 8286.

51) S. DeBeer George, T. Petrenko and F. Neese, *Inorg. Chim. Acta*, 2008, **361**, 965.

52) A. D. Beke, *Phys. Rev. A*, 1988, **38**, 3098.

53) J. P. Perdew, *Phys. Rev. B*, 1986, **33**, 8822.

54) F. Neese, *Inorg. Chim. Acta*, 2002, **337**, 181.

55) A. Schäfer, C. Huber and R. Ahlrichs, *J. Chem. Phys.*, 1994, **100**, 5829.

56) C. J. Cramer, *Essentials of Computational Chemistry*, J. Wiley and Sons Ltd, 2002, ISBN 0-471-48552-7.

57) A. Klamt and G. J. Schüürmann, *J. Chem. Soc., Perkin Trans.*, 1993, **2**, 799.

58) C. J. van Wüllen, *J. Chem. Phys.*, 1998, **109**, 382.

59) W. Kohn and L. J. Shan, *Phys. Rev.*, 1965, **140**, 1133.

60) H. B. Schlegel, Some practical suggestions for optimising geometries and locating transition states, in *New Theoretical Concepts for Understanding Organic Reactions*, ed. J. Bertran, Kulwer Academic, the Netherlands, NATO-ASI series C, 1989, vol. 267, p. 33.

61) A.-L. Zheng, Z.-F. Ju, W. Li and J. Zhang, *Inorg. Chem. Commun.*, 2006, **9**, 489.

62) J. Cano, E. Ruiz, P. Alemany, F. Lloret and S. Alvarez, *J. Chem Soc., Dalton Trans.*, 1999, 1669.

63) J. Shi, G.-M. Yang, P. Cheng, D.-Z. Liao, Z.-H Jiang and G.-L. Wang, *Polyhedron*, 1997, **16**, 531.

64) S. Kitagawa, T. Okubo, S. Kawata, M. Kondo, M. Katada and H. Kobayashi, *Inorg. Chem.*, 1995, **34**, 4790.

65) S. Decurtins, H. Schmalle, P. Schneuwly, J. Ensling and P. Guetlich, *J. Am. Chem. Soc.*, 1994, **116**, 9521.

66) J. L. Beeby and S. F. Edwards, *Proc. R. Soc. London, Ser. A*, 1964, **279**, 82.

67) P. J. Durham, J. B. Pendry and C. H. Hodges, *Comput. Phys. Commun.*, 1981, **25**, 193.

68) J. B. Pendry, *J. Phys. C: Solid State Phys.*, 1972, **5**, 2567.

69) J. B. Pendry, *J. Phys. C: Solid State Phys.,* 1971, **4**, 2501.

70) P. A. Lee and J. B. Pendry, *Phys. Rev. B*, 1975, **11**, 2795.

71) P. J. Durham, B. L. Gyorffy and A. J. Pindor, *J. Phys. F: Met. Phys.*, 1980, **10**, 661.

72) A. L. Ankudinov, B. Ravel, J. J. Rehr and S. D. Conradson, *Phys. Rev. B*, 1998, **58**, 7565.

73) S. I. Zabinsky, J. J. Rehr, A. L. Ankudinov, R. C. Albers and M. J. Eller, *Phys. Rev. B*, 1995, **52**, 2995.

74) J. J. Rehr and R. C. Albers, *Phys. Rev. B*, 1990, **41**, 8139.

75) K. Hatada, K. Hayakawa, J. Chaboy, and C. R. Natoli, *J. Phys.: Conf. Ser.*, 2009, **190**, 012010.

76) J. Chaboy, A. Muñoz-Páez, F. Carrera, P. Merkling and E. Sánchez Marcos, *Phys. Rev. B*, 2005, **71**, 134208.

77) H. Modrow, S. Bucher, J. J. Rehr and A. L. Ankudiniov, *Phys. Rev. B*, 2003, **67**, 35123.

78) J. J. Rehr, R. C. Albers and S. I Sabinsky, *Phys. Rev. Lett.*, 1992, **69**, 3397.

79) J. J. Rehr and R. C. Albers, *Rev. Mod. Phys.*, 2000, **72**, 621.

80) T. A. Smith, J. E. Penner-Hahn, M. A. Berding, S. Doniach and K. O. Hodgson, *J. Am. Chem. Soc.*, 1985, **107**, 5945.

81) FEFF 8.4, Aug. 2006, copyright by A. Ankudinov, B. Ravel and J. J. Rehr. Further information can be found online at: http://leonardo.phys.washington.edu/feff/.

82) W. A. Harrison, *Solid State Theory,* Mcgraw-Hill, New York, 1970.

83) J. G. Norman*, Mol. Phys.*, 1974, **81**, 1191.

84) Y. Joly, *Phys. Rev. B*, 2001, **63**, 125120.

85) A. V. Poiarkova and J. J. Rehr, *Phys. Rev. B*, 1999, **59**, 948.

86) N. Van Hung and J. J. Rehr, *Phys. Rev. B*, 1997, **56**, 43.

87) L. Hedin and B. I. Lundqvist, *J. Phys. C: Solid State*, 1971, **4**, 2064.

88) F. E. Mabbs and D. J. Machin, *Magnetism and Transition Metal Complexes*, Chapman and Hall, London, 1971.

89) C. J. O'Connor, *Prog. Inorg. Chem.*, 1982, **29**, 203.

90) G. M. Sheldrick, SHELX-97, Programs for Crystal Structure Analysis, University of Göttingen, Göttingen, Germay, 1997.

91) A. L. Spek, *Acta Cryst.,* 1990, **A46**, 34.

92) C. Lee, W. Yang and R. G. Parr, *Phys. Rev. B,* 1988, **37**, 785.

93) S. P. Collins, A. Bombardi, A. R. Marshall, J. H. Williams G. Barlow, A. G. Day, M. R. Pearson, R. J. Woolliscroft, R. D. Walton, G. Beutier and G. Nisbet, *AIP Conf. Proc.,* 2010, **1234**, 303.

94) S. P Collins, R. J. Cernik, B. Fell, C. C. Tang, N. W. Harris, M. C. Miller and G. Oszlanyi, *J. Synchrotron Rad.*, 1998, **5**, 1263.

CHAPTER 3

Mononuclear M(II) (M = Cu, Ni, Co, Fe, Mn) bromide complexes bearing mixed α-diimine/β-diketonate *bis*-chelates; potential new materials for X-ray polarimetry

3.0 Mononuclear M(II) (M = Cu, Ni, Co, Fe, Mn) bromide complexes bearing mixed α-diimine/β-diketonate *bis*-chelates; potential new materials for X-ray polarimetry

This chapter is concerned with the synthesis and characterisation of highly ordered materials based on the general monometallic motif, [(α-diimine)MBr(β-diketonate)] (Figure 3.1), with a view to assessing their viability as dichroic filters at the copper (8979 eV), nickel (8333 eV), cobalt (7709 eV), iron (7112 eV) and manganese (6539 eV) K-edges. In Chapter 2, the application of dicopper(II) bromide complexes of the type, [(α-diimine)$_2$Cu$_2$Br$_2$(μ-C$_2$O$_4$)] (**1**), had demonstrated that SBP complexes containing highly aligned Cu–Br bonds could indeed provide the basis for a successful filter. The extension of this latter oxalate-based design to other metal K-edges, *e.g.,* nickel (8333 eV), however, resulted in the formation of insoluble materials; the likely product of uncontrollable oxalate-driven polymerisation reactions.[1] To circumvent these disadvantageous reaction pathways, well-defined neutral, monometallic SBP complexes were targeted in which the bridging oxalate in **1** has been replaced by a chelating β-diketonate ligand; a brief attempt is also given at using chelating pyridonates and benzoates. In support of the proposed target (Figure 3.1), a theoretical study of mononuclear **1a′** (see Chapter 2, section 2.7) has demonstrated the feasibility of a structurally related system.
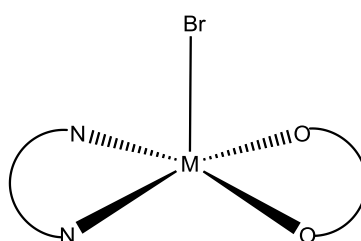
Figure 3.1 Target *bis*-chelates, [(α-diimine)MBr(β-diketonate)] (M = Cu, Ni, Co, Fe, Mn).

3.1 Background to *bis*-chelate M(II) (M = Cu, Ni, Co, Fe, Mn) bromide complexes

Following a review of the literature, crystallographically characterised five co-ordinate complexes of the type, [(α-diimine)M(II)X(β-diketonate)] (M = Cu, Ni, Co, Fe, Mn; X = Cl, Br), are surprisingly rare. For example, only five SBP copper(II) complexes including, [(1,10-phen)CuBr(acac)] (**A**, τ = 0.05),[2] [(1,10-phen)CuCl(acac)] (**B**, τ = 0.10),[3] [(2,2′-bipy)CuCl(bzac)] (**C**, τ = 0.05)[4] and [(1,10-phen)CuCl(bzac)] (**D**, τ = 0.04),[5] have been reported and crystallographically characterised (see Figure 3.2). Complexes **A**–**D** are all highly aligned in the solid state, specifically with respect to the neighbouring Cu–X (X = Cl, Br) bonds [tors: XCu···CuX = 180° (**A**–**D**)]. It is noteworthy that bromide-containing **A** has also been synthesised during the course of this work and will be described herein. On the other hand, there have been no crystallographically characterised examples, to the knowledge of the author, for nickel, cobalt, iron or manganese based on the desired motif (*vide supra*). Indeed, the closest nickel complex is four co-ordinate, [(α-diimine)Ni(acac)][B(C_6F_5)$_4$] (α-diimine = 1,4-diazabutadiene), in which the anion, [B(C_6F_5)$_4$], is non-co-ordinating.[6]
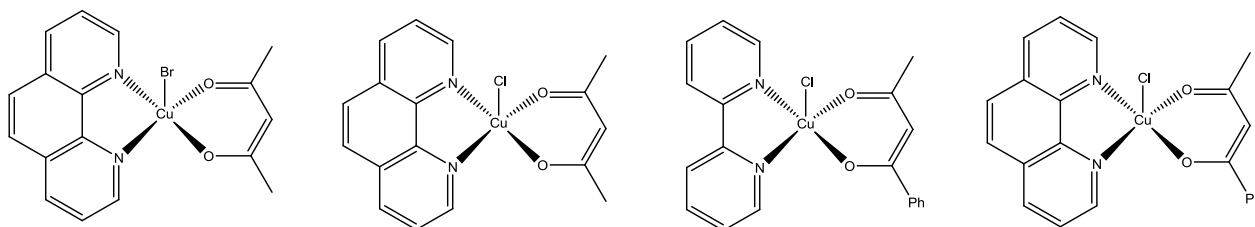
Figure 3.2 Previously reported copper(II) halide complexes of the type, [(α-diimine)CuX(β-diketonate)] (X = Cl, Br) **A**–**D** (from left to right).

The presence of these well-defined five co-ordinate copper(II) examples, **A**–**D**, in the literature is likely due to several contributing factors, including the electronic properties of a copper(II) d^9 metal centre stabilising the observed SBP geometry (see section 3.3.3). In contrast, the absence of examples for the other metal centres (*viz.*, Ni, Co, Fe, Mn) is likely attributed to their preference to adopt six co-ordinate octahedral geometries with *tris*-chelates of the type, [(α-diimine)M(β-diketonate)$_2$][7–16] or [(α-diimine)$_2$M(β-diketonate)][X] (α-diimine = 2,2′-bipy, 1,10-phen; β-diketonate = acac, dbm; X = monoanion, *e.g.*, ClO$_4^-$) prevalent.[17] Surprisingly, no

examples of halide-bridged six co-ordinate bimetallic complexes of the type, [(α-diimine)MX(β-diketonate)(μ-X)]$_2$ (X = Cl, Br), for any first row transition metal have been crystallographically characterised. Conversely, halide-bridged six co-ordinate dimeric *mono*-chelates of the type, [(α-diimine)Ni(H$_2$O)(Cl)(μ-Cl)]$_2$ (α-diimine = 2,2'-bipy)[18] are known, as are their non-solvated five co-ordinate counterparts, [(α-diimine)NiX(μ-X)]$_2$ (α-diimine = neocuprione, pyridylarylimine; X = Cl, Br),[19–22] especially where a more sterically encumbered α-diimine is employed. It is noteworthy that the *bis*-N,N chelated salts, [(α-diimine)$_2$MX][Y] (α-diimine = 2,2'-bipy, 1,10-phen; X = Cl, Br; Y = monoanion, *e.g.,* Cl$^-$, Br$^-$, ClO$_4^-$, PF$_6^-$, BF$_4^-$, NO$_3^-$, OH$^-$, *etc.*) are well known for copper[23–36] which are discrete and five co-ordinate. However, their geometries tend towards TBP or TBPDSBP (Trigonal Bipyramidal Distorted Square-Based Pyramidal), for example, [(1,10-phen)$_2$CuBr][Br] (**E**) (τ = 0.88)[29] and [(2,2′-bipy)$_2$CuBr][Br] (**F**) (τ = 0.86).[31] On the other hand, for metal centres other than copper (*viz.*, Ni, Co, Fe, Mn), five co-ordinate salts of this structural *bis*-N,N type are uncommon, with only one example reported each for cobalt and nickel.[37,38] More generally, these metal centres prefer to adopt solvated octahedral salts of the type, [(α-diimine)$_2$MX(H$_2$O)][Y] (α-diimine = 2,2′-bipy, 1,10-phen; M = Ni, Co, Mn; X = Cl, Br; Y = monoanion].[39–51]

3.2 α-Diimine and β-diketonate libraries

With the intent of studying complexes of the general composition [(α-diimine)MBr(β-diketonate)], for metal centres other than copper, the family of simple α-diimines (*viz.*, 2,2′-bipy, 1,10-phen) will be extended to include a range of substituted pyridylarylimines. It was envisaged that the nature of their substitution pattern would allow a means of systematically introducing steric control, a feature likely to impact upon the co-ordination geometries of complexes based on nickel, cobalt, iron and manganese as the metal centre. In a similar way, the nature of the β-diketonate will also be varied.

3.2.1 From simple α-diimines to pyridylarylimines

The types of pyridylarylimine ligands (**L$_x$**) to be used in this chapter are highlighted in Figure 3.3, along with 2,2′-bipy and 1,10-phen. **L$_x$** all contain the bulky 2,6-diisopropylphenyl group as the *N*-aryl unit and can be grouped by their 2-R-pyridyl substitution patterns, namely, R = H (**L$_1$**), R = Et (**L$_2$**), R = ^{i}Pr (**L$_3$**), R = Ph (**L$_4$**), R = Naphth (**L$_5$**) and R = Anthr (**L$_6$**). Ligands **L$_2$**, **L$_4$**, **L$_5$** and **L$_6$** have been characterised by single crystal X-ray diffraction and the molecular structure of anthracenyl-containing **L$_6$** is illustrated, as a representative example, in Figure 3.4; selected bond lengths and angles for all four **L$_x$** are listed in Table 3.1. **L$_1$** was synthesised in good yields according to a previously reported method.[52] **L$_2$** is novel and has been synthesised *via* an adapted route described for **L$_3$** by Erker *et al*., also in good yield.[53] The ketone precursor to **L$_4$** could be prepared *via* palladium catalysed Stille[54] or Suzuki[55–57] cross-coupling routes and both gave comparable yields. The **L$_5$** and **L$_6$** ketone precursors could also be prepared by Suzuki methods *via* the 1-naphthyl and 9-anthracenyl boronic acids, respectively, which have been previously reported.[58,59] **L$_6$**, to the knowledge of the author, is novel, while synthetic routes to **L$_5$** have only been described within the patent literature.[57]

1,10-phen

2,2'-bipy

(**L$_1$**) R = H
(**L$_2$**) R = Et
(**L$_3$**) R = ^{i}Pr
(**L$_4$**) R = Ph
(**L$_5$**) R = Naphth
(**L$_6$**) R = Anth

2-R-pyridyl(2,6-diisopropylphenyl)imine
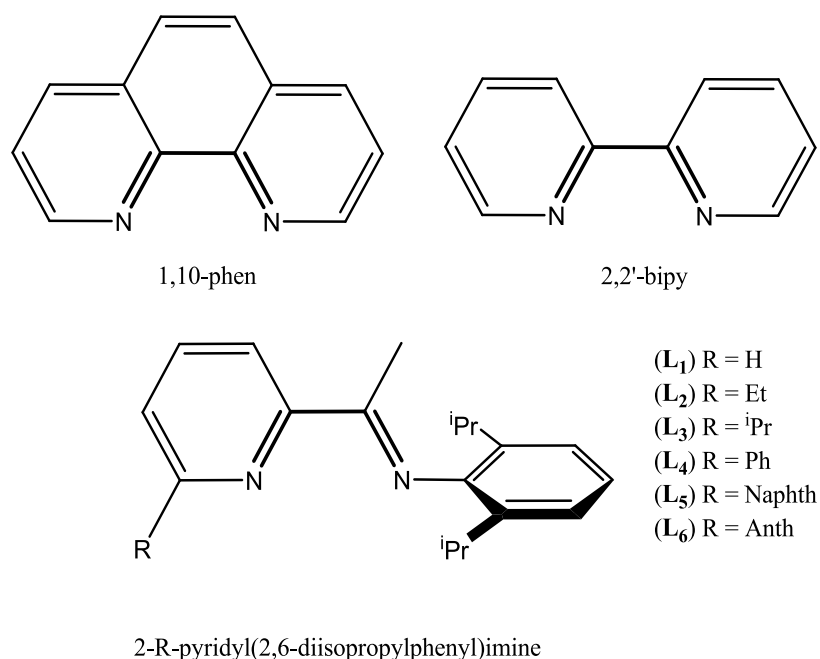
Figure 3.3 α-Diimines to be used in Chapter 3.

The molecular structures of **L₂**, **L₄**, **L₅** and **L₆** consist of a *trans*-configured pyridylarylimine with the *N*-2,6-diisopropylphenyl group being inclined approximately orthogonally to the pyridylimine plane. At the 2-position of the pyridyl ring, is located the hydrocarbyl group which, in the case of the aryl groups is either, nearly co-planar [tors: N(1)C(2)C(21)C(22) = 3.3° (**L₄**)] or inclined at an angle [tors: N(1)C(2)C(21)C(22) = 50.5° (**L₅**), 76.8° (**L₆**)]. Similarly, a minor deviation away from planarity occurs between both the pyridyl and imine nitrogen atoms [tors: N(1)C(7)C(8)N(2) = 1.0° (**L₂**), 1.7° (**L₄**), 5.7° (**L₅**), 3.8° (**L₆**)]. In addition, ligands **L**$_x$ have been fully characterised by IR, ^{1}H and ^{13}C NMR spectroscopy, high resolution mass spectrometry, as well as melting point determinations.

Figure 3.4 Molecular structure of **L₆** shown with partial atom labels; hydrogen atoms have been omitted for clarity.

Table 3.1 Selected bond lengths (Å) and angles (°) for **L₂**, **L₄**, **L₅** and **L₆**.

	L₂	**L₄**	**L₅**	**L₆**
N(1)–C(2)	1.350(3)	1.323(3)	1.340(3)	1.359(4)
N(1)–C(6)	1.341(3)	1.336(3)	1.345(3)	1.343(4)
C(2)–C(21)	1.495(3)	1.488(3)	1.503(3)	1.491(5)
C(6)–C(7)	1.497(3)	1.498(3)	1.488(3)	1.486(5)
C(7)–N(2)	1.266(3)	1.275(3)	1.282(3)	1.281(4)
N(2)–C(8)	1.501(3)	1.421(3)	1.419(3)	1.437(4)
C(7)–C(20)	1.431(3)	1.493(3)	1.496(4)	1.497(5)
C(6)–N(1)–C(2)	118.29(2)	119.42(19)	118.12(2)	116.8(3)
C(7)–N(2)–C(8)	1.21.36(2)	122.34(18)	120.62(2)	121.09(3)
N(1)–C(2)–C(21)	116.14(2)	116.21(2)	116.39(2)	115.74(4)
C(6)–C(7)–N(2)	117.33(2)	117.21(19)	117.05(2)	116.57(4)
N(2)–C(7)–C(20)	125.31(2)	125.32(19)	125.78(2)	125.24(4)
C(7)–C(6)–N(1)	115.92(2)	115.95(19)	115.06(2)	115.86(4)

3.2.2 β-Diketonate ligand families

Three monoanionic β-diketonates namely, acetylacetonato (acac), benzoylacetonato (bzac) and dibenzoylmethanato (dbm), will be employed (Figure 3.5) to probe the impact of differing steric (and electronic properties) on the complex type, as well as any influences in the intermolecular packing. The protonated forms of the β-diketonate are commercially available and can be readily deprotonated in basic media.

$R_1 = R_2 = Me$ (acac)
$R_1 = Me, R_2 = Ph$ (bzac)
$R_1 = R_2 = Ph$ (dbm)
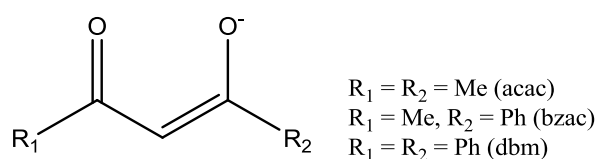
Figure 3.5 β-Diketonates to be employed in Chapter 3.

3.3 Synthesis and characterisation of [(α-diimine)CuBr(β-diketonate)] (3, 4 and 5)

3.3.1 Using 2,2′-bipy and 1,10-phen as the α-diimine

CuBr$_2$ $\xrightarrow{\text{i), ii), iii)}}$

(**3a**) N,N = 2,2'-bipy; $R_1 = R_2 = Me$
(**3b**) N,N = 2,2'-bipy; $R_1 = Me, R_2 = Ph$
(**3c**) N,N = 2,2'-bipy; $R_1 = R_2 = Ph$
(**4a**) N,N = 1,10-phen; $R_1 = R_2 = Me$
(**4b**) N,N = 1,10-phen; $R_1 = Me, R_2 = Ph$
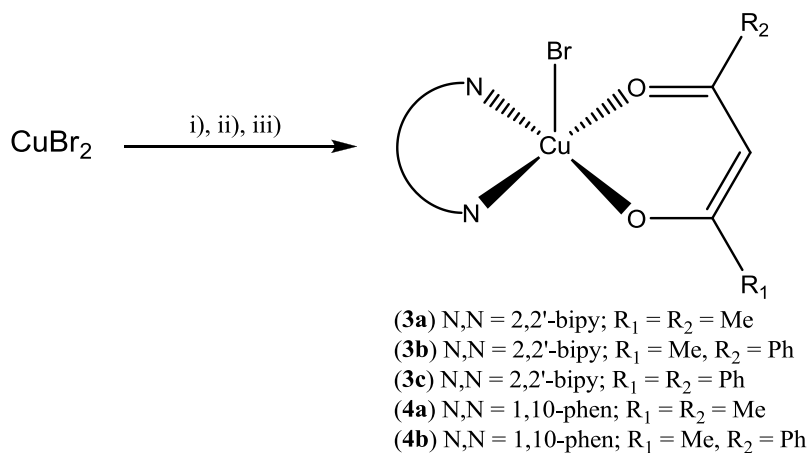
Scheme 3.1 *Reagents and conditions:* i) α-Diimine (2,2′-bipy or 1,10-phen), MeOH, rt, 30 min; ii) β-diketonate (acac, bzac, dbm), NaOH (pH 9), 40 °C, 30 min; iii) MeOH/Et$_2$O recrystallisation.

Treatment of CuBr$_2$ in methanol with 2,2′-bipy or 1,10-phen and the corresponding protonated β-diketonate at pH 9 in a 1:1:1 molar ratio, respectively (Scheme 3.1) gave, on crystallisation, [(2,2′-bipy)CuBr(acac)] (**3a**), [(2,2′-bipy)CuBr(bzac)] (**3b**), [(2,2′-bipy)CuBr(dbm)] (**3c**), [(1,10-phen)CuBr(acac)] (**4a**) and [(1,10-phen)CuBr(bzac)] (**4b**) in good yields, respectively.

Alternatively, **3** and **4** could also be obtained in good yields using the corresponding sodium salt of the β-diketonate at neutral pH. Complexes **3** and **4** have been characterised by FAB mass spectrometry, IR spectroscopy, magnetic measurements and elemental analysis. In addition, **3a**, **3b**, **3c**, **4a** and **4b** were subject to single crystal X-ray diffraction studies.

Crystals of **3a**, **3b**, **3c**, **4a**, and **4b** suitable for the X-ray structure determinations were grown from a slowly evaporating methanolic solution, or by slowly diffusing diethylether into a concentrated methanolic solution of the corresponding complex. Complex **3a** exists as four independent molecules (*A*, *B*, *C* and *D*) differing by slight variations in the bond lengths and angles. The molecular structure of one of the independent molecules of **3a** (*molecule A*), as a representative example, is shown in Figure 3.6a; selected bond lengths and angles for all five complexes are collected in Table 3.2. Complexes **3** and **4** all consist of a CuBr unit with chelating α-diimine [2,2′-bipy (**3**) or 1,10-phen (**4**)] and β-diketonate [acac (**3a**, **4a**), bzac (**3b**, **4b**) and dbm (**4c**)] ligands. In a manner similar to **A**–**D**, the geometries of each complex can be best described as SBP with a bromide atom occupying the apical site [$\tau = 0.06^{60}$ (**3a**), 0.05 (**3b**), 0.29 (**3c**), 0.05 (**4a**), 0.01 (**4b**)]. In all cases, the Cu–O distances are shorter that the Cu–N distances by *ca.* 0.08 Å, consistent with the ionic contribution to the bonding shown by the β-diketonate. In addition, the Cu–Br bonds show some variation, with those in **3a** ranging from 2.7059(9)–2.8131(9) Å (*A*, *B, C* and *D*).

Inspection of the molecular packing diagrams for **3** and **4** revealed that there are two symmetry related molecules in the unit cells of **3b** and **4a**, four symmetry related molecules in **4b** and eight symmetry related molecules in **3c**. Additionally, molecules of methanol are present in the unit cells of **3c**, **4a** and **4b**, whilst a molecule of water is present in **3a** which facilitates a hydrogen-bonding network linking molecules of **3a** (Figure 3.6b). Apart from **3c** and **4b**, all complexes exhibit some degree of intermolecular alignment of the Cu–Br bond. In **3a**, an average BrCu⋯CuBr torsion angle of 4.98° is revealed between neighbouring molecules, however, in **3b** and **4a** a dipole alignment is exhibited between the juxtaposed copper and bromide atoms

ensuring that the BrCu···CuBr torsion angle is 180°. On the other hand, in **4b** it is apparent that adjacent molecules are juxtaposed perpendicular to each other (tors: BrCu···CuBr = 96.29°), while in **3c**, a random distribution of molecular orientations is evident (range tors: BrCu···BrCu = 75.00–54.13°).

Neutral **3** and **4** all show molecular ion peaks in their FAB mass spectra along with fragmentation peaks corresponding to the loss of a bromide atom. All of the complexes were paramagnetic and displayed magnetic moments of 1.79 (**3a**), 1.72 (**3b**) 1.69 (**3c**), 1.72 (**4a**) and 1.76 (**4b**) BM (Evans balance at room temperature), which are consistent with the presence of one unpaired electron and similar to the values previously reported for **A**–**D**.[2–5] Elemental analysis also gave results supportive of the proposed structures.
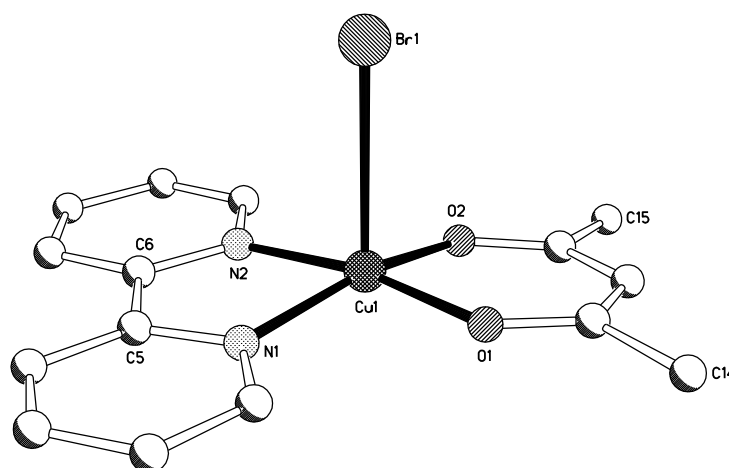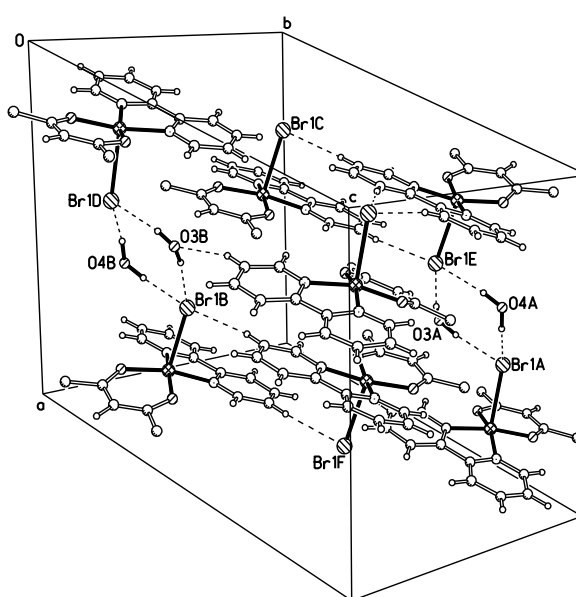
Figure 3.6 (a) Molecular structure of one of the independent molecules of **3a** shown with partial atom labels; hydrogen atoms and selected carbon labels have been omitted for clarity. (b) Molecular packing diagram for **3a**.

Table 3.2 Selected bond lengths (Å) and bond angles (°) for **3** and **4**.

	3a[a]				3b	3c	4a	4b
	Molecule A	*Molecule B*	*Molecule C*	*Molecule D*				
Cu(1)–N(1)	1.996(4)	2.010(4)	1.996(4)	2.009(4)	1.992(9)	2.003(3)	2.027(3)	2.030(2)
Cu(1)–N(2)	1.989(4)	2.009(4)	2.002(3)	1.996(4)	1.987(8)	2.005(3)	2.007(3)	2.014(2)
Cu(1)–O(1)	1.913(3)	1.909(3)	1.920(3)	1915(3)	1.912(7)	1.937(2)	1.916(2)	1.9112(19)
Cu(1)–O(2)	1.919(3)	1.929(3)	1.912(3)	1.925(3)	1.924(7)	1.927(2)	1.923(2)	1.9264(19)
Cu(1)–Br(1)	2.8131(9)	2.7630(9)	2.7451(9)	2.7059(9)	2.718(2)	2.6679(6)	2.6921(7)	2.7280(6)
N(1)–Cu(1)–O(1)	90.58(14)	89.51(14)	92.50(14)	89.55(14)	90.8(3)	172.15(10)	91.11(10)	89.58(9)
N(1)–Cu(1)–O(2)	163.98(13)	168.42(15)	164.33(14)	166.71(15)	167.7(3)	88.51(10)	165.68(11)	164.92(9)
N(1)–Cu(1)–N(2)	80.42(15)	80.72(15)	80.70(14)	80.79(15)	80.3(3)	80.29(10)	81.59(11)	81.40(9)
N(1)–Cu(1)–Br(1)	100.81(9)	86.29(11)	91.75(11)	94.40(11)	94.2(3)	97.74(7)	94.61(8)	97.64(7)
N(2)–Cu(1)–O(1)	169.64(14)	165.57(15)	164.04(15)	160.86(15)	164.5(3)	94.90(10)	162.76(11)	164.45(9)
N(2)–Cu(1)–Br(1)	91.72(11)	94.95(11)	96.67(11)	93.65(11)	99.4(3)	99.40(8)	95.08(8)	95.23(7)
O(2)–Cu(1)–O(1)	94.99(13)	94.49(13)	93.99(13)	95.22(13)	93.9(3)	93.42(9)	94.10(10)	95.65(8)
O(2)–Cu(1)–N(2)	92.42(14)	93.20(14)	89.32(15)	92.14(14)	92.5(3)	154.50(10)	89.67(10)	91.07(9)
O(2)–Cu(1)–Br(1)	93.66(10)	94.04(10)	101.40(10)	97.43(10)	96.6(2)	104.82(7)	97.45(7)	96.05(6)
O(1)–Cu(1)–Br(1)	95.01(10)	96.66(10)	97.96(10)	103.59(10)	93.9(2)	89.24(7)	101.09(8)	98.52(6)

a) Refers to four independent molecules in the unit cell of **3a**.

3.3.2 Using a pyridylarylimine as the α-diimine
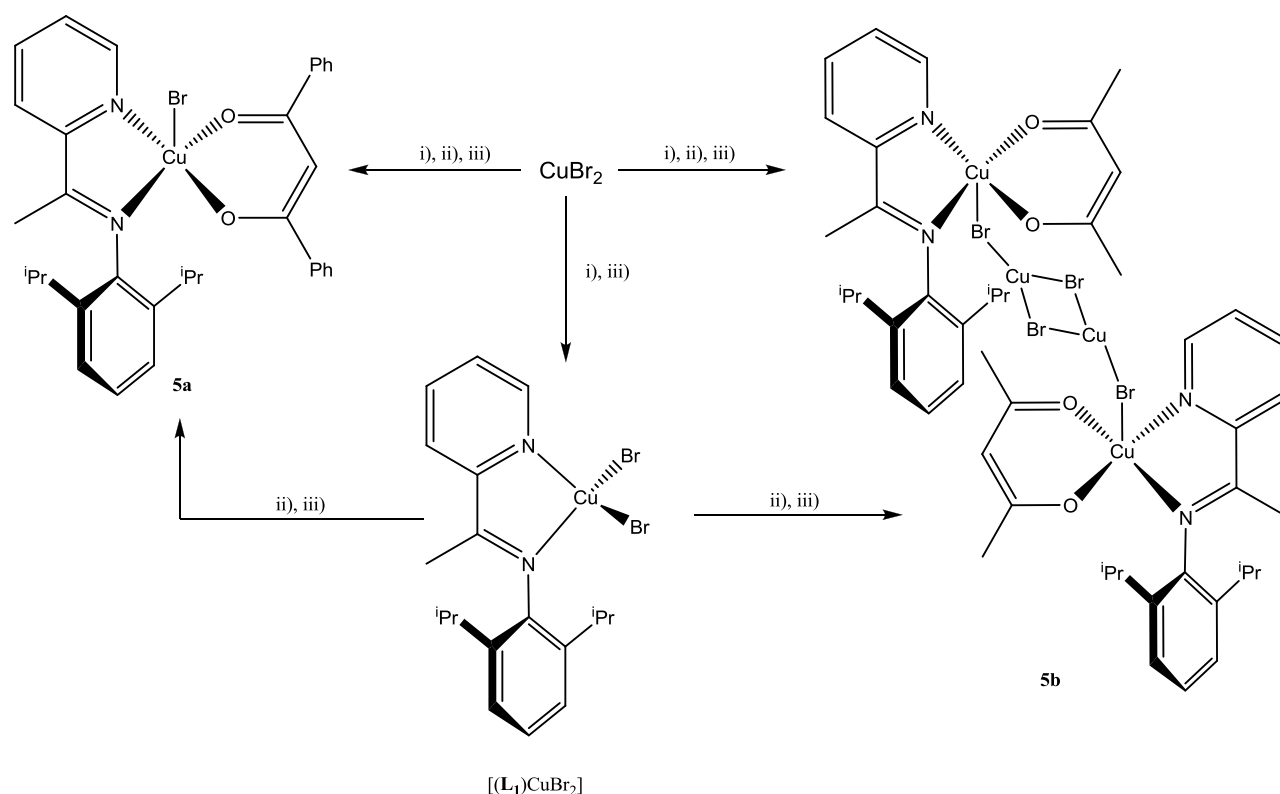
Scheme 3.2 *Reagents and conditions:* i) **L₁**, DCM, rt, 12 h; ii) Na[acac] or Na[dbm], rt, 12 h; iii) DCM/hexane recrystallisation.

The reaction of $CuBr_2$ in dichloromethane with **L₁** followed by sodium dibenzoylmethanato in a 1:1:1.5 molar ratio, respectively, gave on crystallisation [(**L₁**)CuBr(dbm)] (**5a**) in good yield (Scheme 3.2). The intermediate complex [(**L₁**)CuBr₂], could also be synthesised and isolated in good yield by treatment of $CuBr_2$ in dichloromethane with **L₁** in a 1:1 molar ratio, respectively. Interestingly, the reaction of $CuBr_2$ with **L₁**, under similar conditions to that of **5a**, using sodium acetylacetonate as the β-diketonate gave, on recrystallisation, tetrametallic, [{(**L₁**)CuBr(acac)}₂Cu₂Br₂] (**5b**) in low yield along with [Cu(acac)₂]. Complexes **5a**, **5b** and [(**L₁**)CuBr₂] have been characterised by a combination of FAB mass spectrometry, IR, magnetic measurements, elemental analysis and by single crystal X-ray diffraction (see Appendix A4.0 for [(**L₁**)CuBr₂]).

Crystals of **5a** and **5b** suitable for the X-ray determinations were obtained by slowly diffusing hexane into a concentrated dichloromethane solution of the corresponding complex. Their

molecular structures are depicted in Figures 3.7 and 3.8, respectively; selected bond lengths and angles are given in Table 3.3. In **5b**, two independent molecules (*A* and *B*) were present in the unit cell which differ most notably by some variations in bond lengths and angles leading to minor deviations in τ [0.01 (*A*), 0.02 (*B*)].
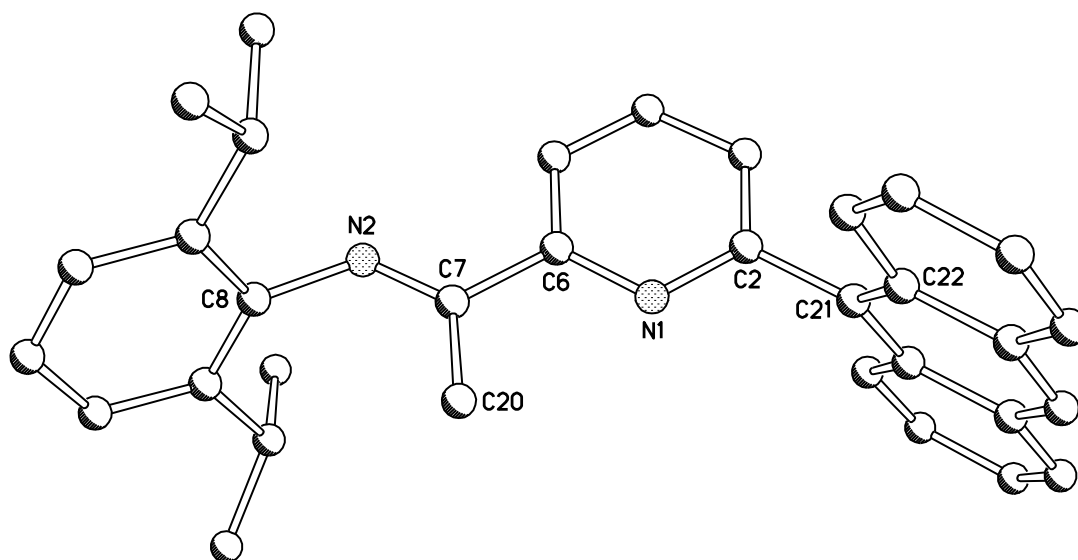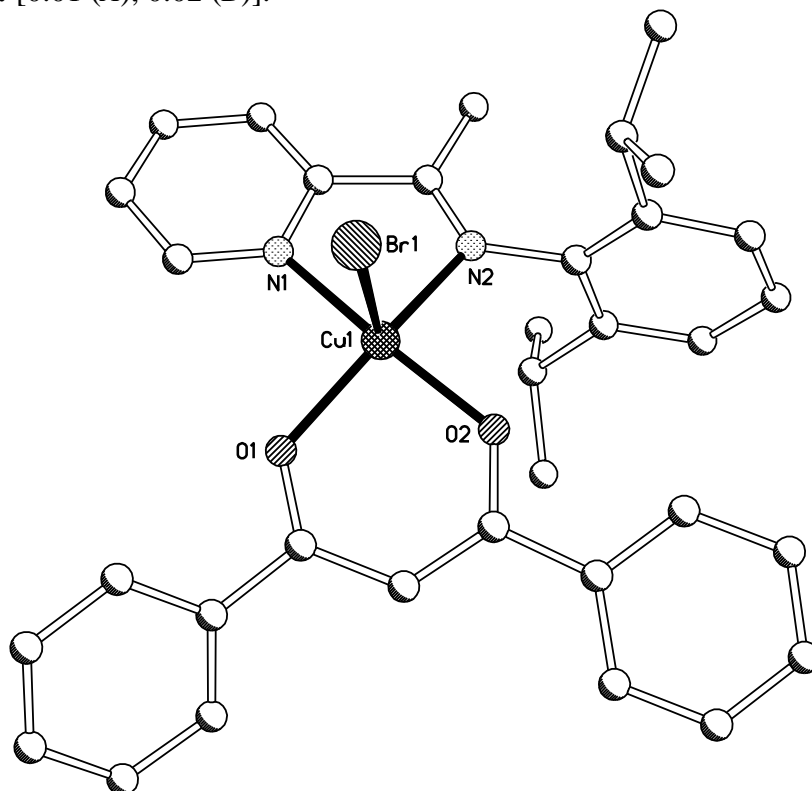

Figure 3.7 Molecular structure of **5a** shown with partial atom labels; hydrogen atoms have been omitted for clarity.
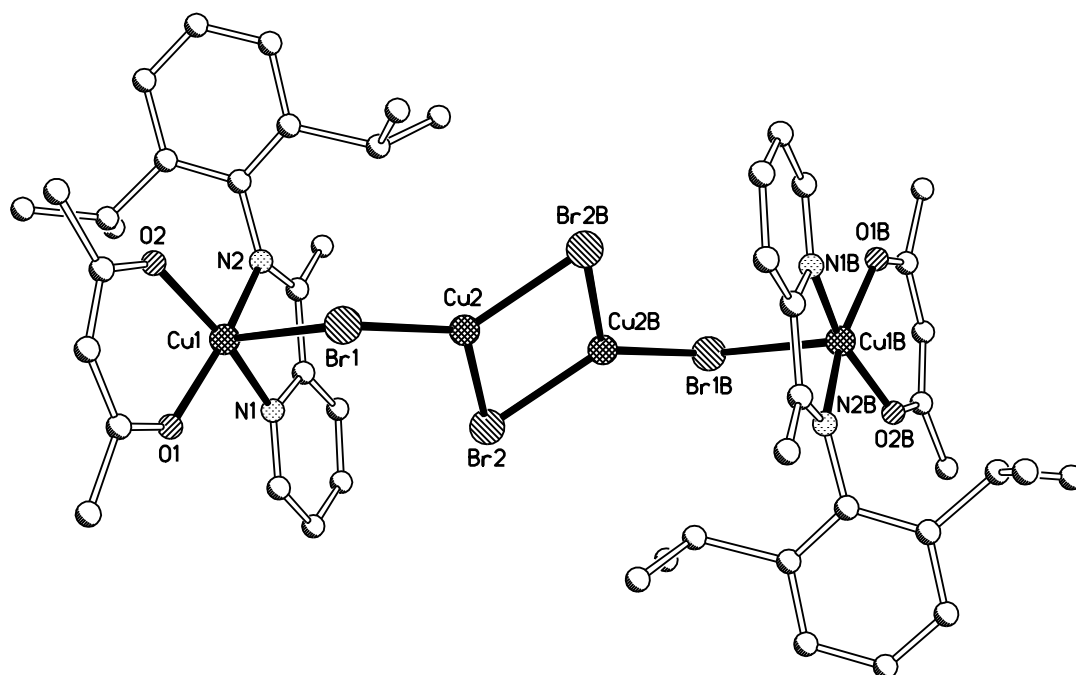
Figure 3.8 Molecular structure of one of the independent molecules of **5b** shown with partial atom labels; hydrogen atoms have been omitted for clarity. Atoms denoted with the letter 'B' are generated by the symmetry operations *x*+1, -*y*+2, -*z* and -*x*, -*y*+1, -*z*.

Table 3.3 Selected bond lengths (Å) and angles (°) for **5**.

	5a	5b[a,b,c]	
		Molecule A	*Molecule B*
Cu(1)–N(1)	2.040(7)	2.066(19)	2.03(2)
Cu(1)–N(2)	1.900(5)	2.745(4)	2.087(18)
Cu(1)–O(1)	1.950(5)	1.908(18)	1.941(18)
Cu(1)–O(2)	2.003(6)	1.979(19)	1.88(2)
Cu(1)–Br(1)	2.6293(15)	2.746(17)	2.752(18)
Cu(2)–Br(1)	–	2.313(4)	2.311(4)
Cu(2)–Br(2)	–	2.398(5)	2.393(5)
Cu(2)–Br(2B)	–	2.411(4)	2.405(3)
Cu(2)···Cu(2B)	–	2.796(7)	2.960(3)
Br(2)–Cu(2B)	–	2.411(4)	2.405(3)
N(1)–Cu(1)–O(1)	91.9(3)	92.5(10)	91.9(8)
N(1)–Cu(1)–O(2)	164.7(3)	162.9(7)	164.8(7)
N(1)–Cu(1)–N(2)	80.2(3)	79.8(8)	97.2(8)
N(1)–Cu(1)–Br(1)	91.83(19)	103.7(4)	99.1(4)
N(2)–Cu(1)–O(1)	156.8(3)	163.8(8)	163.3(7)
N(2)–Cu(1)–Br(1)	103.47(18)	103.4(5)	104.5(9)
O(2)–Cu(1)–O(1)	92.7(3)	90.1(9)	91.2(8)
O(2)–Cu(1)–N(2)	90.0(3)	93.2(8)	91.7(8)
O(2)–Cu(1)–Br(1)	101.97(19)	93.1(5)	95.6(5)
O(1)–Cu(1)–Br(1)	98.49(18)	92.3(5)	91.5(5)
Br(1)–Cu(2)–Br(2)	–	122.33(17)	126.27(15)
Br(1)–Cu(2)–Br(2B)	–	128.6(2)	129.9(2)
Br(1)–Cu(2)–Cu(2B)	–	174.9(2)	178.1(2)
Br(2)–Cu(2)–Br(2B)	–	108.68(11)	103.84(15)
Br(2)–Cu(2)–Cu(2B)	–	54.66(14)	52.10(13)
Br(2)A–Cu(2)–Cu(2B)	–	54.22(14)	52.10(13)
Cu(2)–Br(2)–Cu(1)	–	107.07(15)	110.48(15)
Cu(2)–Br(1)–Cu(2B)	–	71.12(15)	76.16(15)

a) Refers to two independent molecules in the unit cell of **5b**.
b) Atoms denoted with the letter 'B' are generated by the symmetry operations *x*+1, -*y*+2, -*z* and -*x*, -*y*+1, -*z*.
c) Atoms O(1) and N(2) for **5b** were not stable to anisotropic refinement and were therefore refined as isotropic.

As with **3** and **4**, both complexes **5a** and **5b** comprise a copper(II) centre surrounded by a bromide ligand and chelating **L₁** and β-diketonate ligands to complete five co-ordinate SBP metal geometries [τ = 0.13 (**5a**), 0.01 (**5b** *molecule A*), 0.02 (**5b** *molecule B*)] with the bromide atoms occupying the axial site. However, in **5b** the apical bromide atom is linked to a cuprous Cu₂Br₂ unit which acts as a bridge to a second '[(**L₁**)CuBr(acac)]' motif. The Cu(II) metal atoms in **5b** (*molecule A*) are separated by a distance of 10.46 Å [Cu(1)···Cu(1B)], whilst the cuprous distance [Cu(2)···Cu(2B)] is 2.796 Å. In addition, molecules of dichloromethane can be found in the lattice of **5a**, whilst **5b** is solvent free. Unfortunately, monometallic **5a** exhibits significant misalignment between neighbouring molecules [tors: BrCu···CuBr = 70.78°], thus, **5a** does not fulfil the design criteria outlined for a dichroic filter (see Chapter 1).

The FAB mass spectrum of **5a** revealed a peak associated with the loss of a bromide atom from the molecular ion, while in **5b**, fragmentation peaks corresponding to [(**L₁**)Cu(acac)] and [(**L₁**)Cu] could be observed. The IR spectra of **5** revealed peaks at *ca.* 1570–1590 cm^{-1} which are consistent with v(C=N)$_{imine}$ stretches for bound pyridylarylimine ligands; these were shifted *ca.* 40 cm^{-1} to a lower wavenumber when compared with the free **L₁**.[52] Complex **5a** is paramagnetic and displayed a magnetic moment of 1.90 BM (Evans balance at room temperature) consistent with the presence of one unpaired electron. Complex **5b** on the other hand, gave a lower value of 0.96 BM, which is likely due to the mixed oxidation state nature of the complex. Elemental analysis gave results consistent with the proposed structure of **5a** and [(**L₁**)CuBr₂], while **5b**, gave results which were lower than calculated.

It is apparent that partial reduction occurs during the reaction of CuBr₂ with **L₁** and sodium acetylacetonate to give **5b**. Notably, it has been shown elsewhere[61] that, when the more bulky pyridylarylimines (**L₂**–**L₄**) are used in place of **L₁**, reduction is the main reaction pathway, leading to uniquely cuprous [(**L$_x$**)Cu(μ-Br)]₂ (**L$_x$** = **L₂**, **L₃**) and [(**L₄**)CuBr]. Indeed, a preliminary electrochemical study of the comparative reduction potentials of cupric [(**L$_x$**)CuBr₂] (**L$_x$** = **L₁**, **L₂**, **L₃** and **L₄**)[61] revealed reduction to occur more favourably as the pyridyl-2-R steric bulk increases, which has further been demonstrated by their facile chemical reduction upon reaction with sodium acetylacetonate. On a related note, for copper, pyridylarylimine chemistry is relatively unexplored, however some aldimine copper(II) dihalide complexes bearing *N*-alkyl substituents have been reported by Haddleton for application in the area of Atom Transfer Radical Polymerisation catalysis (ATRP).[62,63]

3.3.3 Factors affecting the observed five co-ordinate SBP geometries in 3, 4 and 5

a) Metal centre effects

First row transition metals can form a range of co-ordination geometries in which the octahedral, tetrahedral and square-planar forms dominate. Copper(II) complexes are atypical in this respect as they have a reluctance to adopt regular octahedral or tetrahedral geometries. The d^9 electron configuration of the copper(II) ion lacks symmetry and exhibits distorted forms of these common geometries, where four, five and six co-ordinate geometries predominate.[64] Of the two types of five co-ordinate geometry (TBP and SBP), reasons behind the preference of **A–D** and **3** –**5** to adopt SBP geometries is unclear.[62] Other than the influencing steric factors of the ligands employed,[19] several hypotheses have been suggested.

i) The Jahn–Teller pathway

In copper(II) ions, a distortion of the axial ligands in the regular octahedral geometry is observed due to the Jahn–Teller effect.[65–67] Where equatorial *bis*-chelation is involved, the removal of only one of the axial ligands is energetically favoured. However, the resulting close approach of the fifth ligand may introduce considerable electrostatic asymmetry along the *z*-axis which may result in the asymmetry of the distribution of charge in the Cu [$3dz^2$] orbital, above and below the *x,y*-plane. To minimise electrostatic repulsions, the metal atom is not placed co-planar with the equatorial ligands and hence, raises *ca.* 0.2 Å towards the fifth ligand which has an overall stabilising effect. Typically, the fifth apical ligand exhibits a longer bond than those in the square-planar environment.[64]

ii) Plasticity effects

The two five co-ordinate forms (TBP and SBP) are related by vibrational modes resulting in distortions that lie along the Berry pathway (*vide infra*). These distortions, leading to a geometrical flexibility around the metal centre, are reported to be the result of 'plasticity effects'.[29,68–72] It has been reported that TBP complexes have two vibrational modes in the

equatorial plane, symmetric ($v_{(sym)}$) and asymmetric ($v_{(asym)}$); the dominance of one over the other leads to either TBP or SBP stereo-form. Asymmetric stretches dominate in the SBP form (pathways ±B and -A in Figure 3.9) leading to the axially non-centrosymmetric C_{4v} point group, whilst the TBP stereo-form (D_{3h}) favours the symmetric stretch (pathway +A in Figure 3.9).

In complexes of the type, [(chelate)$_2$CuX][Y] (chelate = 2,2′-bipy, 1,10-phen, DPA; X = Cl, Br; Y = monoanion) the predominating stretches leading to the difference in geometry may be associated with the ligands employed.[29] For example, copper(II) complexes of this type bearing 2,2′-bipy and 1,10-phen tend towards TBP whilst the flexible DPA ligand leads to a more SBP configuration at the metal centre.
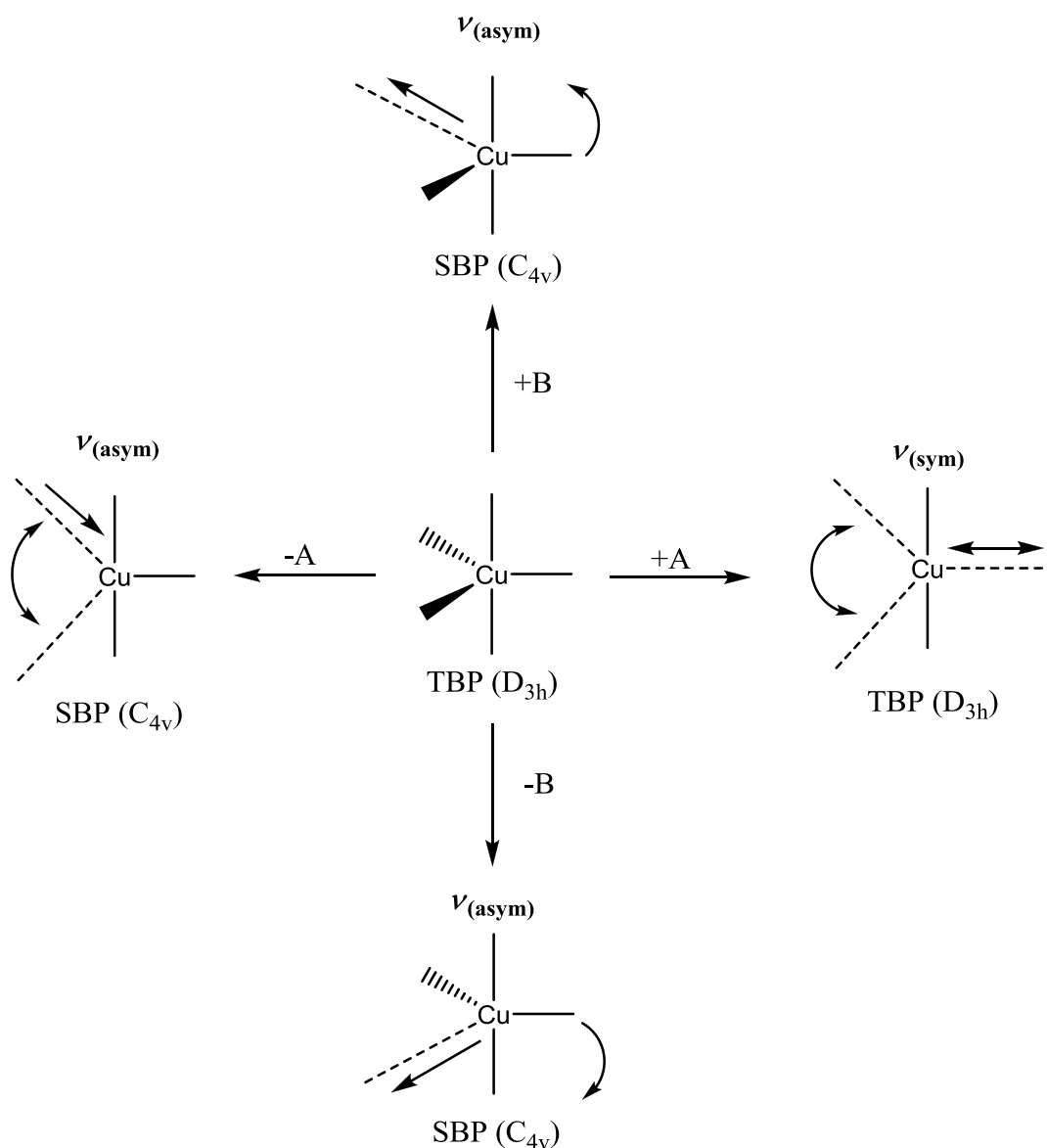
Figure 3.9 A schematic of the equatorial symmetric and asymmetric vibrational forms which exists in five co-ordinate geometries based on copper(II).

b) Hydrogen-bonding effects

Inspection of the inter-ligand distances in **3–5** (Table 3.4 and Figure 3.10) has revealed possible hydrogen-bonding interactions between pyridyl protons and β-diketonate oxygen atoms. Thus, it is conceivable that the presence of such hydrogen-bonding interactions, in conjunction with a copper d^9 electron configuration and associated vibronic preferences before mentioned, may enforce a more rigid SBP geometry, which is reflected in the τ-value. It is noteworthly that **5a** can only hydrogen-bond *via* the single α-pyridyl proton unlike the symmetric α-diimines, 2,2′-bipy and 1,10-phen.

Table 3.4 O···H$_\alpha$ atom distances (Å) of pyridyl α-protons to β-diketonate oxygen atoms in **3-5** along with corresponding τ values.

Compound	Interaction A	Interaction B	τ
3a	2.495	2.411	0.06
3b	2.484	2.409	0.05
3c	2.463	2.561	0.29
4a	2.537	2.516	0.05
4b	2.482	2.625	0.01
5a	2.582	-	0.13
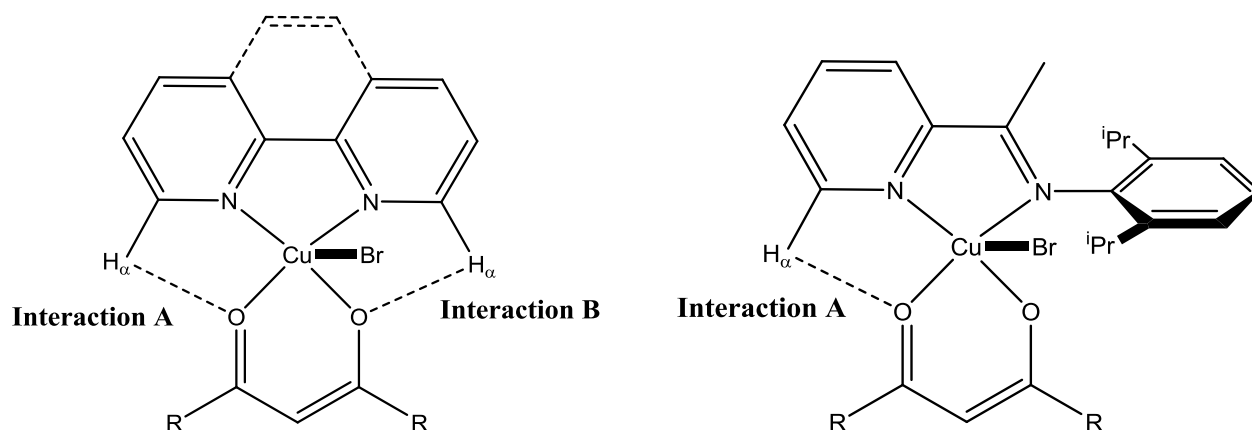
Figure 3.10 Possible hydrogen-bonding interactions in **3**, **4** and **5**.

3.4 Using polarised X-ray absorption spectroscopy to study 3a

As a result of the high degree of intermolecular ordering exhibited by **3a** (Figure 3.6b), along with the low value of τ observed (0.06), X-ray dichroic measurements were performed on a single crystal of **3a** in fluorescence mode at the Diamond Light Source (station B16) in a similar fashion to that described for **1a** (see Chapter 2). Like **1a**, XAS spectra were recorded in two orientations χ_0 and χ_{90}. Single crystals of **3a** were mounted onto a glass capillary secured to a mount which was custom designed to interface with the beam line (see Appendix A14.0).

3.4.1 Determining the alignment of 3a with respect to the crystal morphology

Three crystallographic faces have been identified by face indexing, namely the (100), (010) and (001) faces. It is apparent that the Cu–Br bonds in **3a** are aligned almost orthogonally (deviation = 88°) to the (001) face and at an angle *ca.* 25° to the (010) and (100) faces. Therefore, to achieve an efficient alignment of the incident X-beam, the polarisation vector was incident on the (010) face.
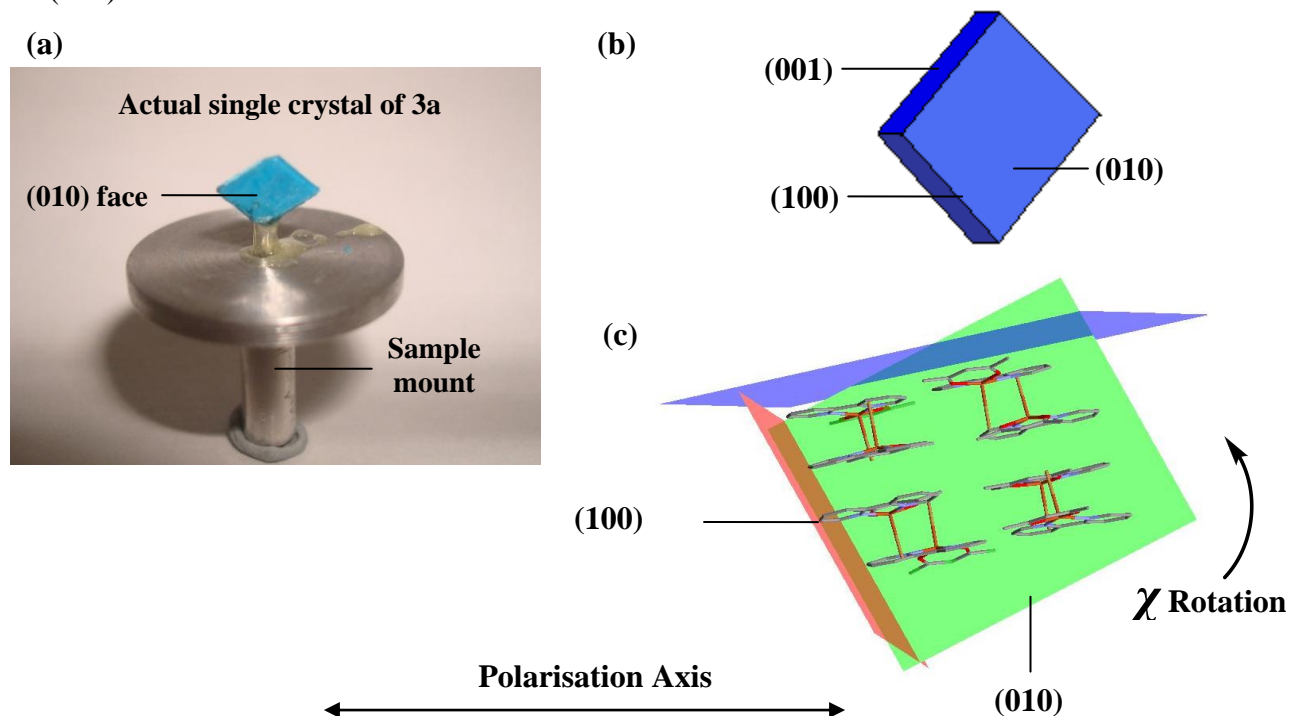
Figure 3.11 (a) An image of the plate-like single crystal of **3a** mounted on a glass capillary. (b) A schematic of the crystal faces. Note: The depicted crystal orientation is representative of the χ_{90} goniometer position with the X-ray polarisation vector perpendicular to the Cu–Br bond. (c) Miller indices overlaid onto the molecular packing diagram with the (010) face presented to the X-ray beam. Note: The envisaged incident polarised X-ray beam propagates 'into the page' with the polarisation vector fixed horizontally.

3.4.2 X-ray dichroism of 3a at the Cu K-edge (8979 eV)

X-ray measurements in fluorescence mode were performed at the Cu K-edge (8979 eV) and inspection of the fluorescence spectra for two orientations (χ_0 and χ_{90}) (Figure 3.12) revealed that dichroic features are apparent in the pre-edge, (8970–8983 eV), the main-edge 1 (shoulder) (8983–8995 eV), the main-edge 2 (8995–9015 eV) and the EXAFS regions (9015–9040 eV). At the main-edge 2 and EXAFS, shallow features occurring over broad energy ranges are revealed. Several phase changes are evident through isobestic points occurring at 8994 and 9012 eV. Modulation curves have been generated using the Malus' law at the three prominent dichroic features at 8989 (main-edge 1), 9005 (main-edge 2) and 9029 (EXAFS) eV (Figure 3.13). Modulation curves for the pre-edge feature are significantly weaker in comparison to the others and are consequently not included in the figure. By comparison to the polarised XAS spectra of **1a** and hypothetical **1a′** (Chapter 2, section 2.5.1, Figures 2.6, 2.7 and section 2.72, Figure 2.21) several noticeable differences are apparent with respect to the dichroic spectral features observed for **3a**. Firstly, that the pre-edge region is much less prominent and appears as a shoulder within the main-edge 1 (8982 eV). Secondly, there is a remarkable difference in the appearance of the main-edge 2 feature. It is apparent, however, that the EXAFS region is very similar for both complexes. Reasons for differences in the XAS spectra for **1a** and **3a** are not clear, however, it is possible that crystal thickness may be a contributing factor (*vide infra*).
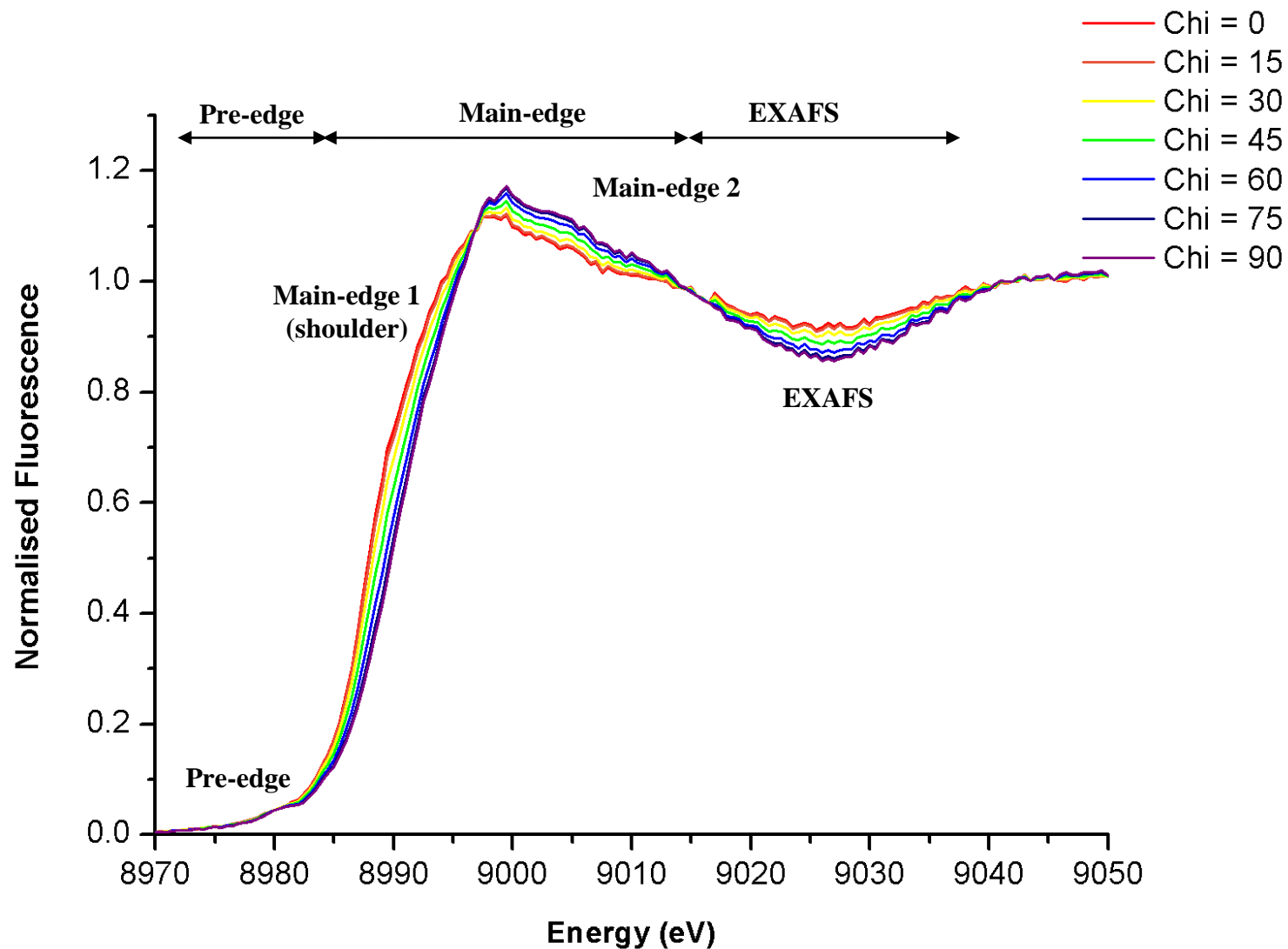
Figure 3.12 Fluorescence XAS spectra for **3a** at the Cu K-edge for orientations χ_0–χ_{90}. These data were obtained using beamline B16 (Diamond Light Source). Angles of χ_0 and χ_{90} have been obtained experimentally. Angles in between these values have been interpolated using Malus' fitting.
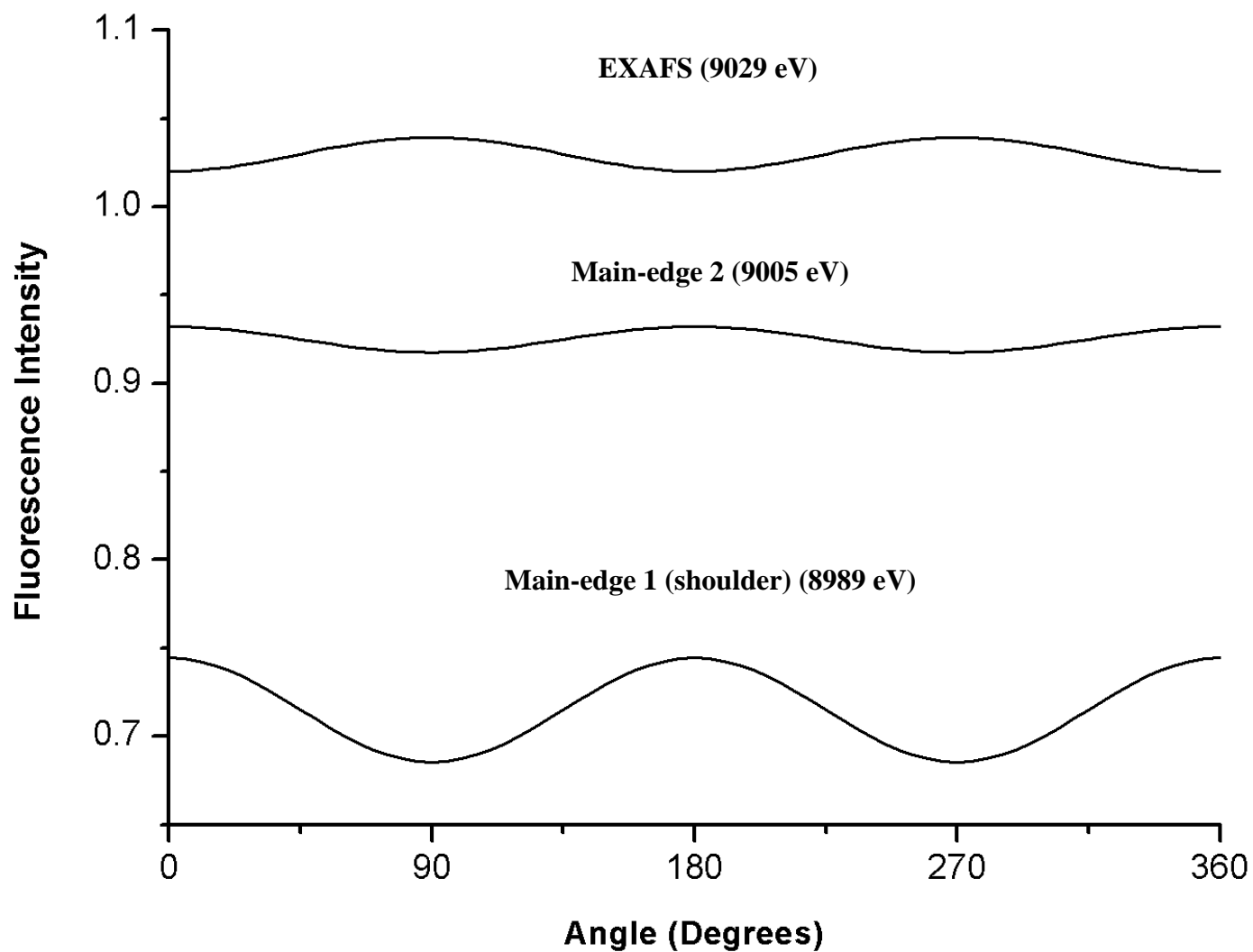
Figure 3.13 Malus' fitted modulation curves for **3a** obtained from the main-edge 1 (8989 eV), main-edge 2 (9005 eV) and EXAFS (9029 eV) regions within the fluorescence XAS spectra.

3.4.3 Attempted quantification of the performance of 3a as a dichroic filter

Unfortunately, the selected single crystal of **3a** was too thick (*ca.* > 1 millimetre) to allow transmission. As a consequence, a reliable figure of merit (R_γ) could not be calculated for **3a**.

3.4.4 Morphological considerations regarding 3a in X-ray astronomical polarimetry

In order to perform efficient synchrotron evaluations, where time is limited, needle-like single crystals (*cf.* **1a**) are preferred in order to align the polarisation vector with the sample quickly. However, from an astronomical point of view, thin plate-like crystals would be desirable to ensure coverage of the focal area of a polarimeter. The inability of plate-like **3a** to allow transmission highlights a further consideration, namely the thickness of the crystal selected, whereby significant attenuation of the incident radiation may result.

3.5 Summary: [(α-diimine)MBr(β-diketonate)] as a platform for copper(II)

In the previous sections, it has been established that SBP copper complexes ($\tau = 0.01$–0.29) of the type, [(α-diimine)CuBr(β-diketonate)] (**3**, **4**, **5**), can be successfully prepared using α-diimines and generally exhibit a high degree of intermolecular alignment in the solid state with respect to the neighbouring Cu–Br bonds. Moreover, it was shown that **3a** displays X-ray dichroism at the Cu K-edge which was predicted on the basis of a theoretical study on **1a** and **1a′**, although the fine structure of the spectral details were not mirrored precisely. Also discussed, was the successful synthesis and characterisation of **5a**, the first example of a SBP copper(II) complex bearing both pyridylarylimine and β-diketonate chelates. Furthermore, a combination of the electronic properties governed by the d^9 metal centre and possible inter-chelate ligand hydrogen-bonding interactions has been postulated as reasons behind the observed SBP geometries of **3**, **4** and **5**.

3.6 Using the [(α-diimine)MBr(β-diketonate)] motif as a general platform for other 3*d* metal centres

Thus far, the focus of this thesis has been on copper-containing complexes and their dichroic behaviour at the Cu K-edge (8979 eV). In this section, emphasis will be placed on the synthesis of other first row transition metal complexes whose metal K-edges fall within the preferred 5–10 keV range. In a preliminary attempt at extending the synthetic methodology described in section 3.3 to prepare five co-ordinate nickel-containing [(α-diimine)NiBr(β-diketonate)] (α-diimine = 2,2′-bipy, 1,10-phen), only octahedral species of the type [(1,10-phen)Ni(acac)$_2$] and [(2,2′-bipy)$_2$NiBr$_2$],[73] could be isolated. In the next section, sterically bulky pyridylarylimines L_x will be employed in an attempt to impede *tris*-chelation or potential halide-bridged dimerisation and deliver the SBP [(α-diimine)MBr(β-diketonate)] (M = Ni, Co, Fe, Mn).

3.6.1 Synthesis and characterisation of [(α-diimine)NiBr(β-diketonate)] (6)
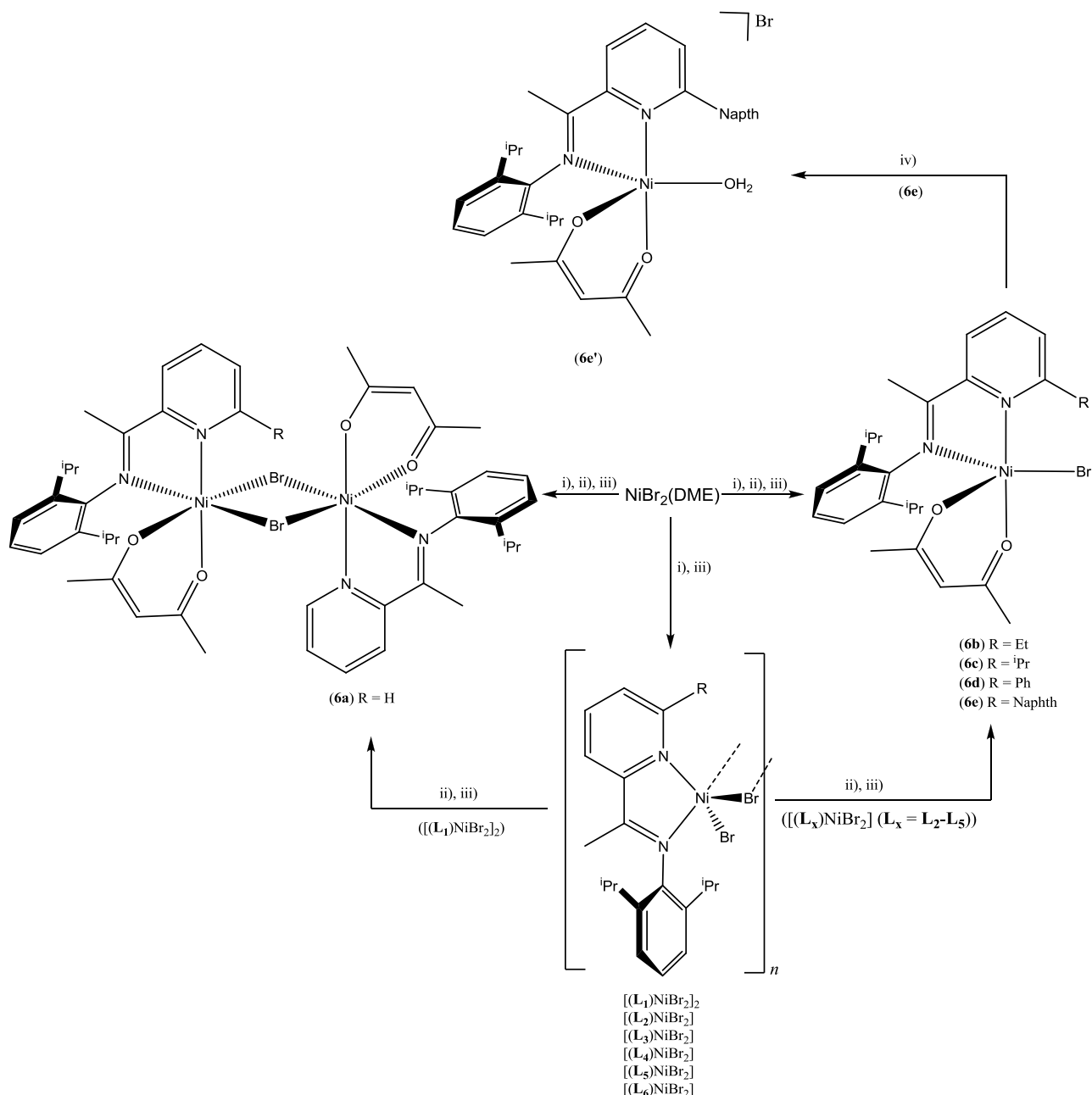
Scheme 3.3 *Reagents and conditions*: i) $\mathbf{L}_x$, DCM, rt, 12 h; ii) Na[acac], rt, 12 h; iii) DCM/hexane recrystallisation; iv) DCM/hexane/H_2O.

Reaction of the NiBr$_2$(DME) adduct with $\mathbf{L}_x$ ($\mathbf{L}_x = \mathbf{L_1}$, $\mathbf{L_2}$, $\mathbf{L_3}$, $\mathbf{L_4}$, $\mathbf{L_5}$) in dry dichloromethane, followed by sodium acetylacetonate in a 1:1:2 molar ratio, respectively, gave on crystallisation, dimeric [($\mathbf{L_1}$)NiBr(acac)(μ-Br)]$_2$ (**6a**) and monometallic [($\mathbf{L}_x$)NiBr(acac)] [$\mathbf{L}_x = \mathbf{L_2}$ (**6b**), $\mathbf{L_3}$ (**6c**), $\mathbf{L_4}$ (**6d**), $\mathbf{L_5}$ (**6e**)] in good yields, respectively (Scheme 3.3). In addition, the attempted recrystallisation of **6e** led, on prolonged standing, to adventitious hydration affording the salt [($\mathbf{L_6}$)Ni(H_2O)(acac)][Br] (**6e′**) in moderate to good yield. On the other hand, the attempted

reaction using anthracenyl-containing **L$_6$** gave only [(**L$_6$**)NiBr$_2$]. Complexes **6** have been characterised by FAB mass spectrometry, IR spectroscopy, magnetic measurements and elemental analysis.

Complexes **6a–6d** and **6e′** have been the subject of single crystal X-ray diffraction studies. As with **5a**, the intermediate complexes [(**L$_x$**)NiBr$_2$] (**L$_x$** = **L$_2$, L$_3$, L$_4$, L$_5$, L$_6$**) could also be isolated (see Appendix A5.0) revealing all species to be monometallic apart from [(**L$_1$**)NiBr$_2$]$_2$, which exists as a bromide-bridged dinickel complex in the solid state.[22]

Crystals of **6a**, **6b**, **6c**, **6d** and **6e′** suitable for the X-ray structure determinations could be obtained by slow diffusion of hexane into a concentrated dichloromethane solution of **6**. The molecular structures of **6a** and **6b** are shown in Figures 3.14 and 3.15, respectively; selected bond lengths and angles for **6a** are given in Table 3.5, while structural data for **6b–6d** are collected in Table 3.6 (a view of the molecular structure of **6e′** can be found within Appendix A9.0).
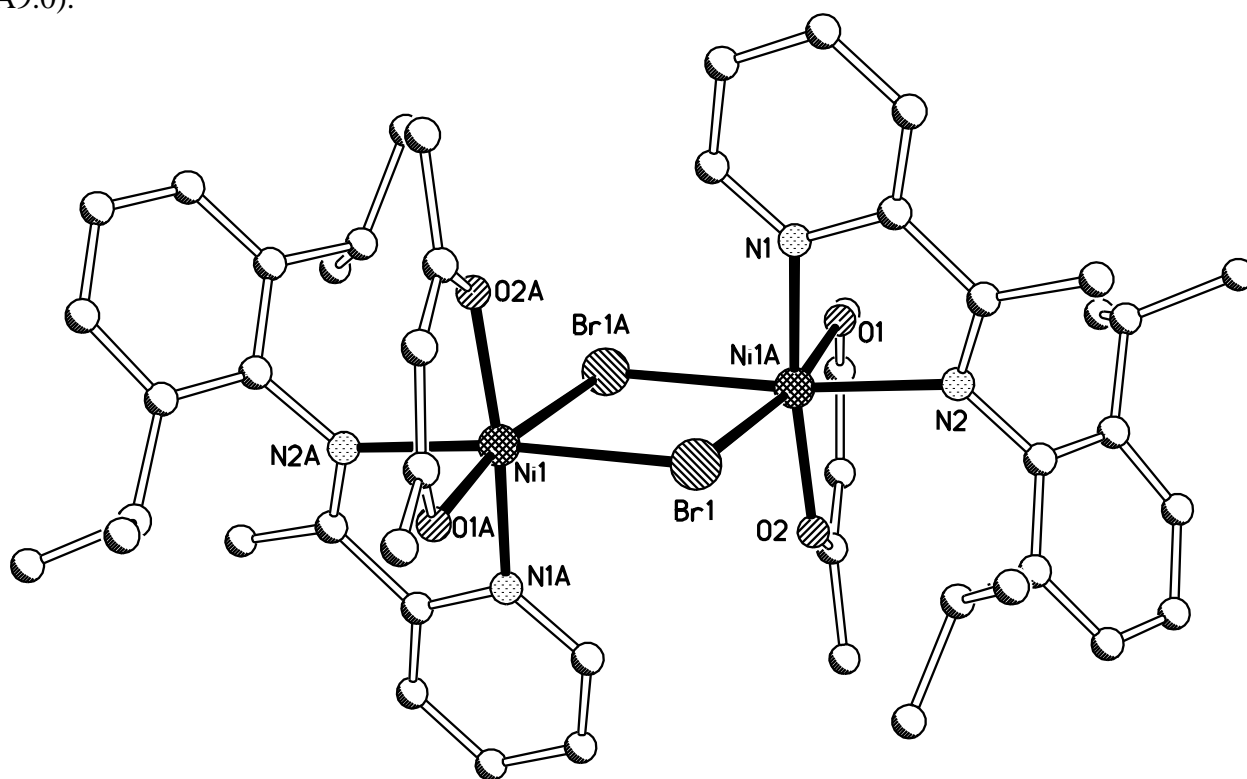
Figure 3.14 Molecular structure of **6a** and along with partial atom labels; hydrogen atoms have been omitted for clarity. Atoms denoted with the letter label 'A' have been generated by the symmetry operation -*x*+1,-*y*+1,-*z*.

Figure 3.15 Molecular structure of **6b** along with partial atom labels; hydrogen atoms have been omitted for clarity.

Table 3.5 Selected bond lengths (Å) and bond angles (°) for **6a**.

	6a[a]
Ni(1)–N(1)	2.058(10)
Ni(1)–N(2)	2.135(11)
Ni(1)–O(1)	2.040(9)
Ni(1)–O(2)	1.970(8)
Ni(1)–Br(1)	2.696(2)
Ni(1)–Br(1A)	2.509(12)
Br(1)–Ni(1A)	2.569(2)
Ni(1)···Ni(1A)	3.900
N(1)–Ni(1)–O(1)	92.7(4)
N(1)–Ni(1)–O(2)	168.8(4)
N(1)–Ni(1)–N(2)	78.8(3)
N(1)–Ni(1)–Br(1)	83.0(3)
N(1)–Ni(1)–Br(1A)	95.5(3)
N(1)–Br(1)–Ni(1)	95.57(7)
N(2)–Ni(1)–O(1)	91.0(4)
N(2)–Ni(1)–O(2)	91.8(4)
N(2)–Ni(1)–Br(1)	96.6(3)
N(2)–Ni(1)–Br(1A)	174.0(3)
O(1)–Ni(1)–O(2)	93.4(30
O(1)–Ni(1)–Br(1)	170.3(3)
O(1)–Ni(1)–Br(1A)	97.4930
O(2)–Ni(1)–Br(1)	92.4(3)
O(2)–Ni(1)–Br(1A)	94.1(3)
Br(1)–Ni(1)–Br(1A)	95.57(7)

a) Atoms denoted with the letter label 'A' were generated using the symmetry operation -x+1,-y+1,-z.

Table 3.6 Selected bond lengths (Å) and angles (°) for **6b**–**6d**.

	6b (X = Br)	**6c** (X = Br)	**6d** (X = Br)
Ni(1)–N(1)	2.0790(19)	2.0886(19)	2.0886(19)
Ni(1)–N(2)	2.0441(19)	2.020(2)	2.020(2)
Ni(1)–O(1)	1.9818(16)	1.9556(17)	1.9556(17)
Ni(1)–O(2)	2.000(16)	2.9587(17)	1.9587(17)
Ni(1)–X(1)	2.4642(7)	2.4739(15)	2.4821(9)
N(1)–Ni(1)–O(1)	87.62(7)	89.0(2)	91.87(7)
N(1)–Ni(1)–O(2)	176.50(7)	175.5(2)	173.15(7)
N(1)–Ni(1)–N(2)	79.42(7)	80.1(3)	79.41(8)
N(1)–Ni(1)–X(1)	90.92(5)	89.94(18)	88.93(5)
N(2)–Ni(1)–O(1)	112.70(7)	104.9(2)	111.38(7)
N(2)–Ni(1)–X(1)	103.03(5)	109.80(18)	101.84(5)
O(2)–Ni(1)–O(1)	89.32(7)	91.5(2)	91.63(7)
O(2)–Ni(1)–N(2)	100.23(7)	95.4(3)	93.83(8)
O(2)–Ni(1)–X(1)	92.55(5)	92.20(17)	91.38(5)
O(1)–Ni(1)–X(1)	143.28(5)	144.59(16)	146.64(5)

The molecular structure of **6a** consists of a halide-bridged, BrNi(μ-Br)$_2$NiBr core,[22] in which each metal centre is bound by chelating **L$_1$** and acetylacetonate ligands to complete six co-ordinate distorted octahedral geometries at each metal centre (Ni$\cdots$Ni distance = 3.900 Å). In contrast, complexes **6b–6d** are all monomeric neutral complexes containing a single nickel bromide unit bound by chelating pyridylarylimine and acetylacetonate ligands. The geometries in **6b–6d** can be best described as five co-ordinate, TBPDSBP [τ = 0.54 (**6b**), 0.51 (**6c**) and 0.44 (**6d**)]. On the other hand, complex **6e′** is based on a cation–anion pair in which the cationic unit is structurally similar to **6b–6d** (**6e′**: τ = 0.38), but with a molecule of water in place of the terminal bromide and the latter now acting as the counter-ion. Furthermore, inter- and intramolecular hydrogen-bonding is present in **6e′**. Comparison of Ni–Br distances **6b**, **6c** and **6d** [Ni(1)-Br(1) 2.4642(7) (**6b**), 2.4739(15) (**6c**), 2.4821(9) Å (**6d**)] reveals a slight increase in bond lengths as the steric properties of the R group increase. It is tempting to suggest that the notional neutral **6e** would have the longest (and weakest) Ni–Br bond distance of the series, perhaps to the point where bromide dissociation is competitive (*c.f* **6e′**) It is apparent that **6b–6d** are all chiral and their molecular structures can be assigned the Λ absolute configuration.

The molecular packing diagrams for five co-ordinate **6b–6d** reveal some misalignment of the neighbouring Ni-Br bonds in the solid state [tors: BrNi$\cdots$NiBr = 15.52° (**6b**), 25.50° (**6c**), 2.53° (**6d**)]. In **6b** and **6d** there are two pairs of symmetry related molecules in the unit cell, whilst in **6c** there are as many as eight pairs. In addition, molecules of dichloromethane are present in the unit cells of **6a**, **6c** and **6d**. Neutral **6b–6e** gave molecular ion peaks in the FAB mass spectra along with fragmentation peaks associated with the successive loss of bromide and acetylacetonate ligands. Bound pyridylarylimine ν(C=N)$_{imine}$ stretches of between 1588–1590 cm^{-1} were also evident in the IR spectra of **6a–6e**, which are lower in magnitude than those displayed in the corresponding free ligands. Magnetic measurements for monomeric **6b–6e** indicated magnetic moments consistent with two unpaired electrons of a nickel(II) metal centre [2.89 (**6b**), 2.84 (**6c**), 2.73 (**6d**), 2.32 (**6e**) BM (Evans balance at room temperature)]. However, dimeric **6a** displayed a magnetic moment of 3.51 BM which is less than the predicted spin-only

value of 3.98 BM [using $\mu_i^2 = \Sigma\mu_i^2$ (μ = magnetic moment of individual metal centres)] suggesting some anti-ferromagnetic coupling.[22] Elemental analysis also gave results consistent with the proposed structures.

3.6.2 Synthesis and characterisation of [(α-diimine)CoBr(β-diketonate)] (7)
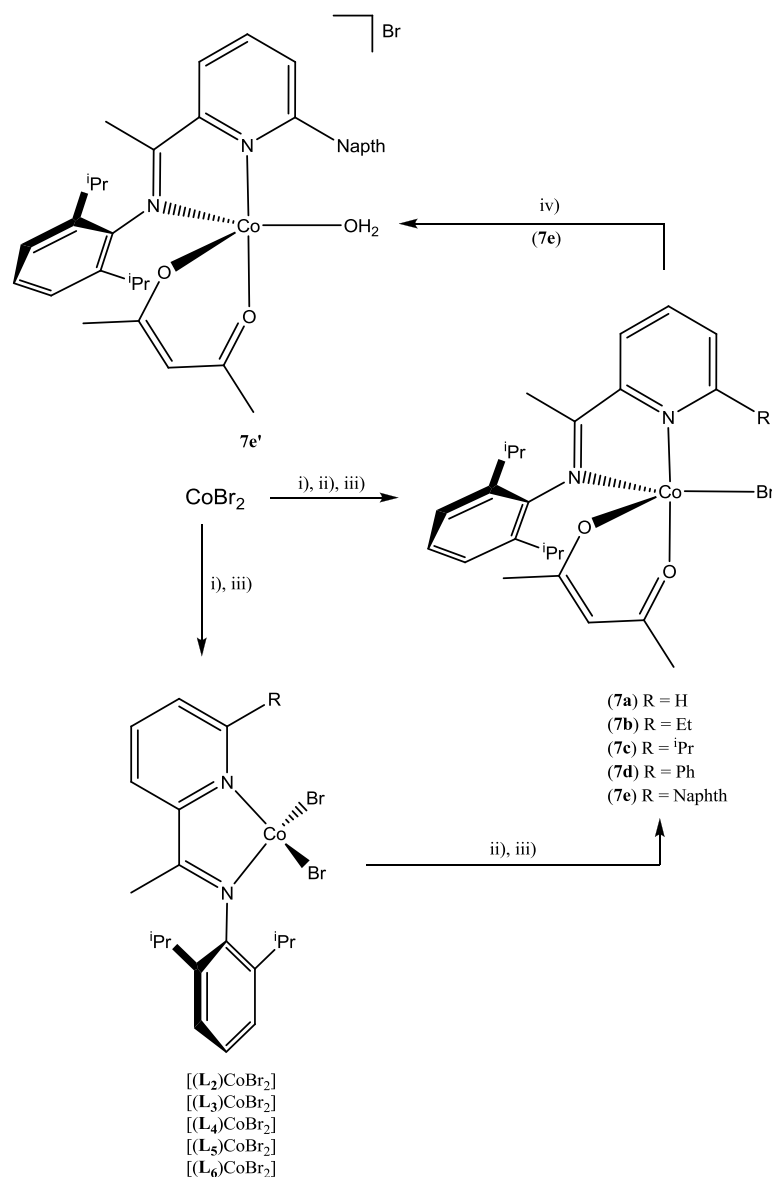
Scheme 3.4 *Reagents and conditions*: i) L_x, DCM, rt, 12 h; ii) Na[acac], DCM, rt, 12 h; iii) DCM/hexane recrystallisation; iv) DCM/hexane/H$_2$O.

Treatment of CoBr$_2$ with the corresponding L_x followed by sodium acetylacetonate in dichloromethane in a 1:1:2 molar ratio, respectively, gave on recrystallisation, monomeric [(L_x)CoBr(acac)] [L_1 (7a), L_2 (7b), L_3 (7c), L_4 (7d), L_5 (7e)], in good yields, respectively

(Scheme 3.4). Complexes **7** have been characterised by FAB mass spectrometry, IR spectroscopy, magnetic measurements and elemental analysis.

As with nickel-containing **6e**, it was found that low levels of water present in the recrystallising solvent were sufficient to allow the formation of the hydrated salt [(**L₅**)Co(H₂O)(acac)][Br] (**7e′**), as the sole product in good yield. In addition, all five neutral complexes of **7** have been the subject of single crystal X-ray diffraction studies; data for **7e′** along with a view of the X-ray structure can be found in the Appendix (A9.0). In all cases, the dibromide intermediate [(**L**$_x$)CoBr₂] could be isolated and characterised by single crystal X-ray diffraction (see Appendix 9). Furthermore, attempts to isolate anthracenyl-containing [(**L₆**)CoBr(acac)] were not successful, instead [(**L₆**)CoBr₂] was isolated along with free **L₆**.

Crystals of **7a**, **7b**, **7c**, **7d** and **7e** suitable for the X-ray structure determinations were obtained by slowly diffusing hexane into a concentrated dichloromethane solution of the corresponding complex. The structure of **7e**, as a representative example, is depicted in Figure 3.16; selected bond lengths and angles for all five complexes are collected in Table 3.8.
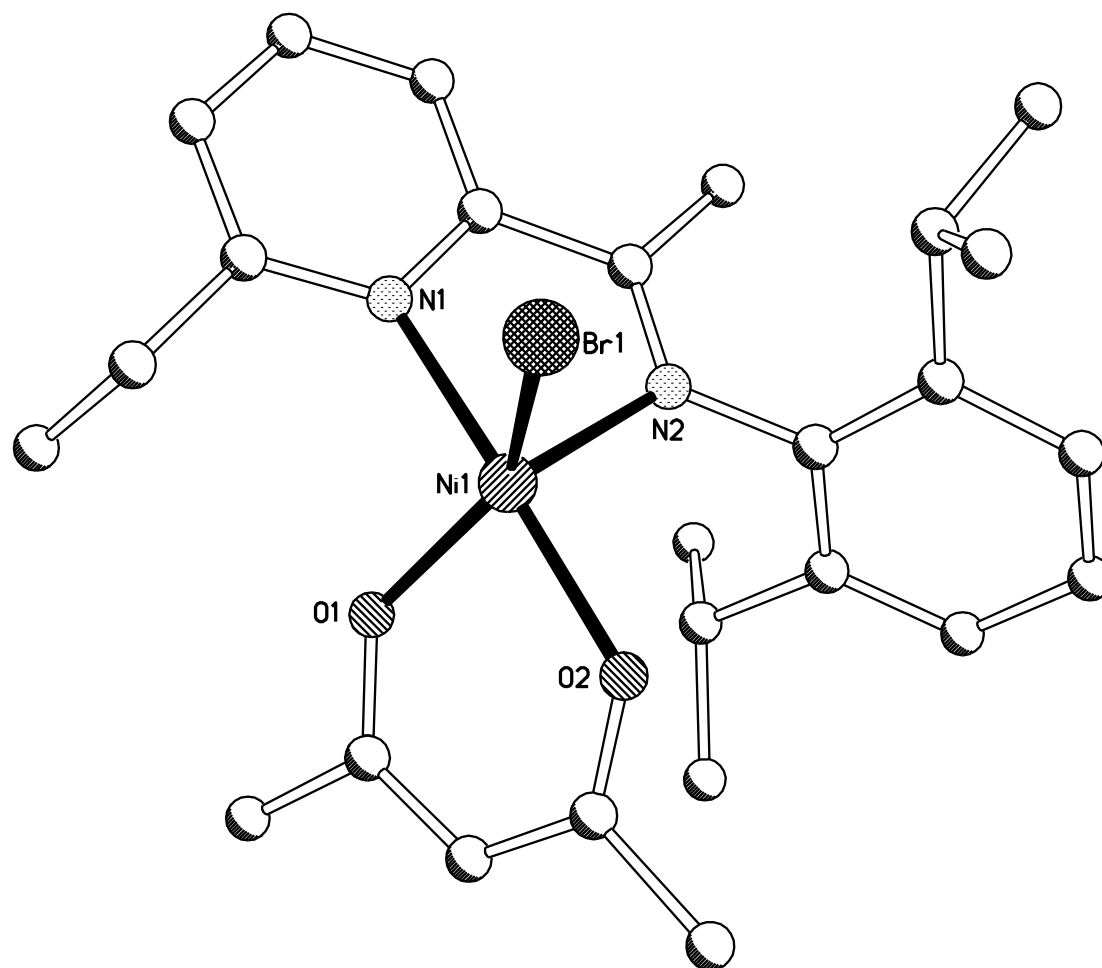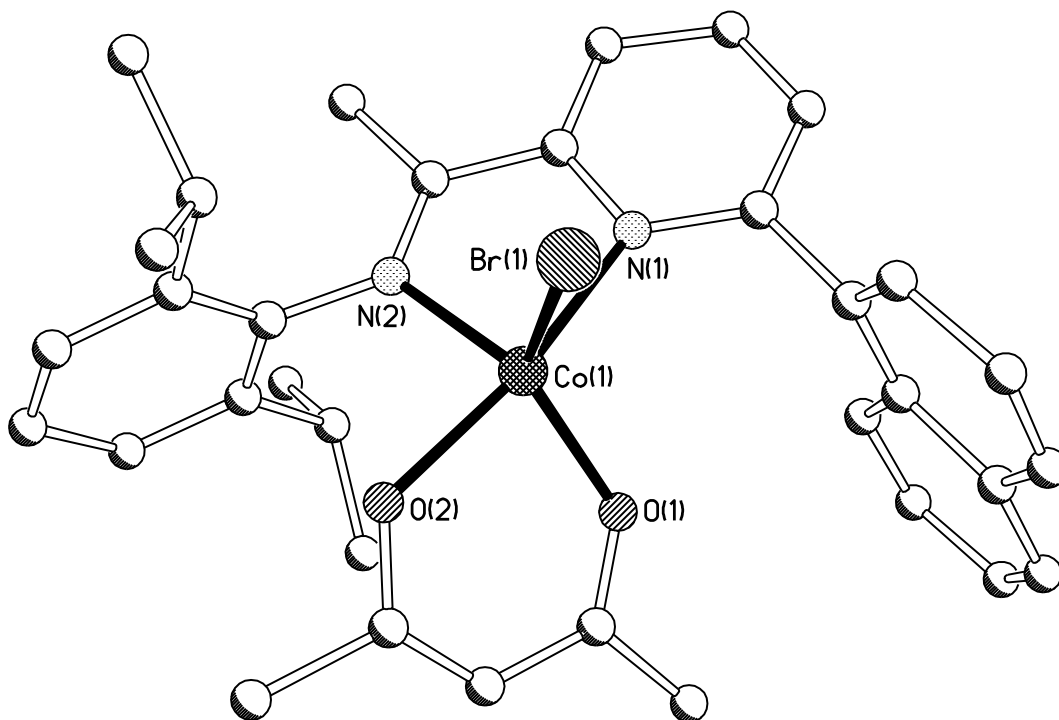

Figure 3.16 Molecular structure of **7e** shown with partial atom labels; hydrogen atoms have been omitted for clarity.

Table 3.8 Selected bond lengths (Å) and angles (°) for **7**.

	7a	7b	7c	7d	7e[a]
Co(1)–N(1)	2.127(4)	2.167(4)	2.174(6)	2.177(4)	2.178(13)
Co(1)–N(2)	2.094(4)	2.096(3)	2.083(6)	2.055(4)	2.087(12)
Co(1)–O(1)	1.991(3)	1.998(4)	1.997(5)	1.971(3)	1.979(11)
Co(1)–O(2)	1.989(3)	1.999(3)	1.990(5)	1.966(3)	2.036(12)
Co(1)–Br(1)	2.4477(10)	2.4666(12)	2.4470(17)	2.4755(17)	2.436(3)
N(1)–Co(1)–N(2)	76.03(16)	76.69(13)	75.7(2)	76.76(15)	76.2(6)
N(1)–Co(1)–O(1)	83.82(14)	85.98(14)	93.2(2)	88.99(14)	92.4(5)
N(1)–Co(1)–O(2)	169.20(16)	172.85(13)	171.2(2)	171.14(14)	166.9(5)
N(1)–Co(1)–Br(1)	90.23(12)	89.97(9)	86.56(15)	88.76(10)	92.1(4)
N(2)–Co(1)–O(1)	125.77(15)	117.22(14)	118.6(2)	114.46(15)	118.7(5)
N(2)–Co(1)–O(2)	100.45(16)	100.97(13)	95.5(2)	95.17(15)	91.4(5)
N(2)–Co(1)–Br(1)	104.43(11)	106.38(10)	116.83(16)	103.47(11)	113.3(4)
O(1)–Co(1)–O(2)	90.27(10)	89.18(13)	90.9(2)	91.12(14)	90.0(5)
O(1)–Co(1)–Br(1)	125.71(13)	133.81(10)	122.62(16)	140.35(11)	127.4(3)
O(2)–Co(1)–Br(1)	100.55(11)	97.18(9)	97.77(16)	96.77(11)	96.7(4)

a) The crystal data for **7e** was very weak, hence a number of atoms were not stable to anisotropic refinement and have been refined as isotropic.

The structures of **7** resemble **6b**–**6d** consisting, in these cases, of a single CoBr unit chelated by pyridylarylimine and acetylacetonate ligands with geometries that can be best described as five co-ordinate, distorted TBPSBP [τ = 0.72 (**7a**), 0.65 (**7b**), 0.81 (**7c**), 0.51 (**7d**), 0.65 (**7e**)]. Interestingly, unlike dimeric nickel-containing **6a** (section 3.6.1), the absolute configuration of **7a**, **7b**, **7d** and **7e** can be assigned Λ while **7c**, as an isolated example, is assigned a Δ absolute configuration and displays a significantly higher value of τ (0.81). Interestingly, unlike dimeric nickel-containing **6a** (section 3.6.1), **7a** is mononuclear, thus highlighting the subtleties of metal centre variation. In addition, both neutral **7e** and salt **7e′** were amenable to crystallisation while only the corresponding salt could be crystallised with nickel (**6e′**).

The molecular packing diagrams for **7a**, **7b** and **7d** reveal two pairs of symmetry related molecules in the unit cells of all six compounds and display some degree of intermolecular ordering between pairs of neighbouring molecules [tors: BrCo···CoBr = 6.52° (**7a**), 4.74° (**7b**)]. However, **7c** and **7e** are quite disordered [tors: BrCo···CoBr = 52.50° (**7c**), 31.04° (**7e**)]. Additionally, molecules of dichloromethane are found in the lattices of **7d** and **7e**.

The FAB mass spectra of **7** reveal peaks corresponding to the sequential loss of bromide atoms and bound acetylacetonate ligands. Also revealed, were prominent $v(C=N)_{imine}$ stretches in the IR spectra occurring between 1565–1590 cm^{-1} resulting from bound pyridylarylimine ligands and were shifted by *ca.* 40 cm^{-1} to lower wavenumbers in comparison to the free ligand. All six complexes were paramagnetic and displayed magnetic moments of 3.9–4.2 BM (Evans balance at room temperature) consistent with high-spin configurations containing three unpaired electrons.

3.6.3 Using dibenzoylmethanato as the β-diketonate chelating ligand; attempted synthesis of [(L$_x$)MBr(dbm)] [M = Ni, Co]

(**8a**) M = Ni, R = Et
(**8b**) M = Ni, R = ^{i}Pr
(**8c**) M = Ni, R = Naphth
(**9a**) M = Co, R = Et
(**9b**) M = Co, R = ^{i}Pr
(**9c**) M = Co, R = Naphth

[(**L$_2$**)NiBr(dbm)]
[(**L$_3$**)NiBr(dbm)]
[(**L$_5$**)NiBr(dbm)]
[(**L$_2$**)CoBr(dbm)]
[(**L$_3$**)CoBr(dbm)]
[(**L$_5$**)CoBr(dbm)]
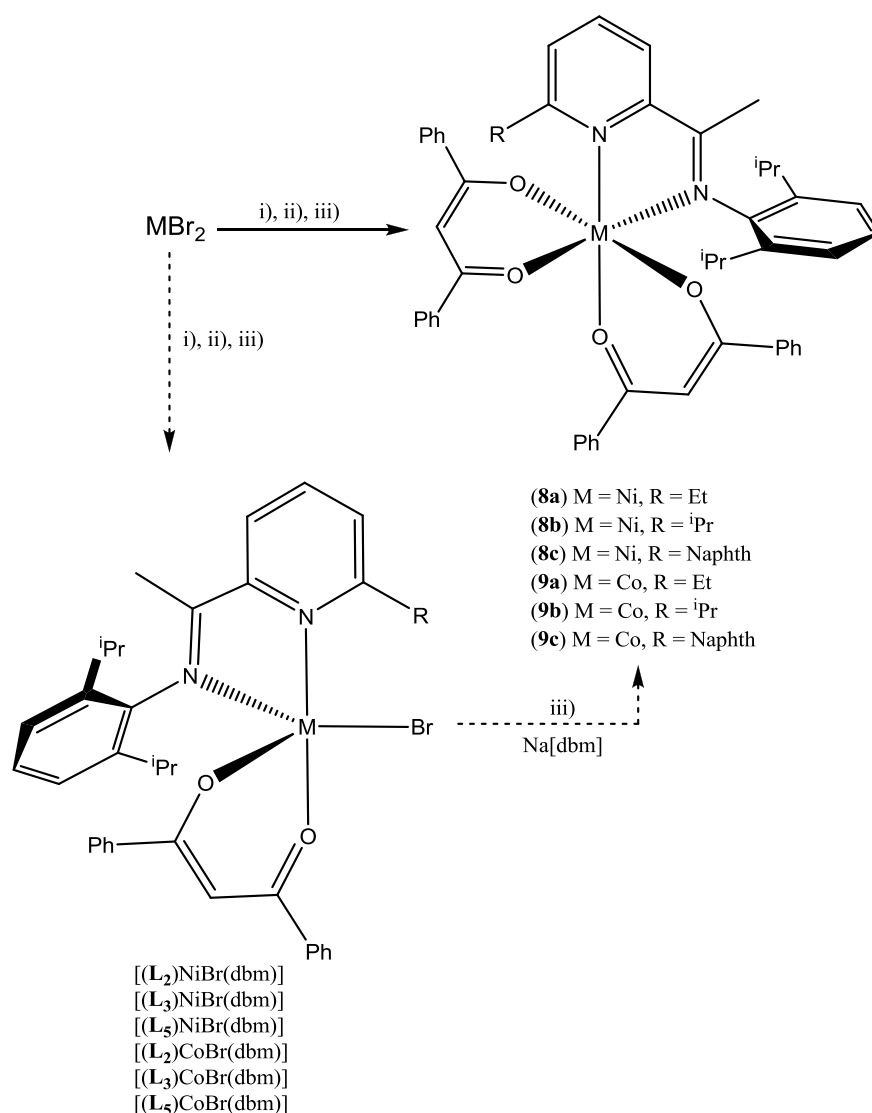
Scheme 3.5 *Reagents and conditions*: i) **L$_x$**, DCM, rt, 12 h; ii) Na[dbm], DCM, rt, 12 h; iii) DCM/hexane recrystallisation.

With a view to influencing the relative M–Br alignment observed in the solid state structures for **6** and **7**, the β-diketonate was modified; it was envisioned that the dibenzoylmethanato derivative could promote phenyl-mediated intermolecular graphitic interactions in [(**L$_x$**)MBr(dbm)] (M = Ni, Co).

However, on treatment of either NiBr$_2$(DME) or CoBr$_2$ with the corresponding **L$_2$** or **L$_3$** followed by sodium dibenzoylmethanato in dichloromethane, in a 1:1:2 molar ratio, the *bis*-dibenzoylmethanato complexes, [(**L$_2$**)M(dbm)$_2$] [M = Ni (**8a**), Co (**9a**)] and [(**L$_3$**)M(dbm)$_2$] [M = Ni (**8b**), Co (**9b**)] were isolated in good yield (Scheme 3.5).

Attempts to reduce the molar equivalents of sodium dibenzoylmethanato and/or performing the reaction at lower temperature, gave either **8a/8b/9a/9b** in lower yield or afforded [(**L$_x$**)MBr$_2$**]** [M = Ni, **L$_x$** = **L$_2$**, **L$_3$**; M = Co, **L$_x$** = **L$_2$**, **L$_3$**]. With the aim of preventing *bis*-dibenzoylmethanato formation, the more sterically bulky **L$_5$** was also employed in the reaction. Once again, however, the *bis*-dibenzoylmethanato [(**L$_5$**)M(dbm)$_2$] [M = Ni (**8c**), Co (**9c**)] were surprisingly formed in good yield.

Complexes **8a**, **8b**, **8c**, **9a**, **9b** and **9c** have all been characterised by FAB mass spectrometry, IR spectroscopy, magnetic measurements and elemental analysis. In addition, these complexes were subject to single crystal X-ray diffraction studies (see Appendix A10.0). Block shape single crystals, suitable for X-ray diffraction were grown by either, slow evaporation of a concentrated dichloromethane solution or by slowly diffusing hexane into a concentrated dichloromethane solution of **8** or **9**. The molecular structures confirm the expected *tris*-chelate motifs with Λ-absolute configurations apparent in both cases. It is uncertain why the desired [(**L$_x$**)MBr(dbm)] [M = Ni, Co] complexes could not be formed, but it is plausible the electron richness of this particular aryl-substituted β-diketonate is influential.

3.6.4 Synthesis and characterisation of [(α-diimine)MBr(acac)] [M = Fe (10), Mn (11)]
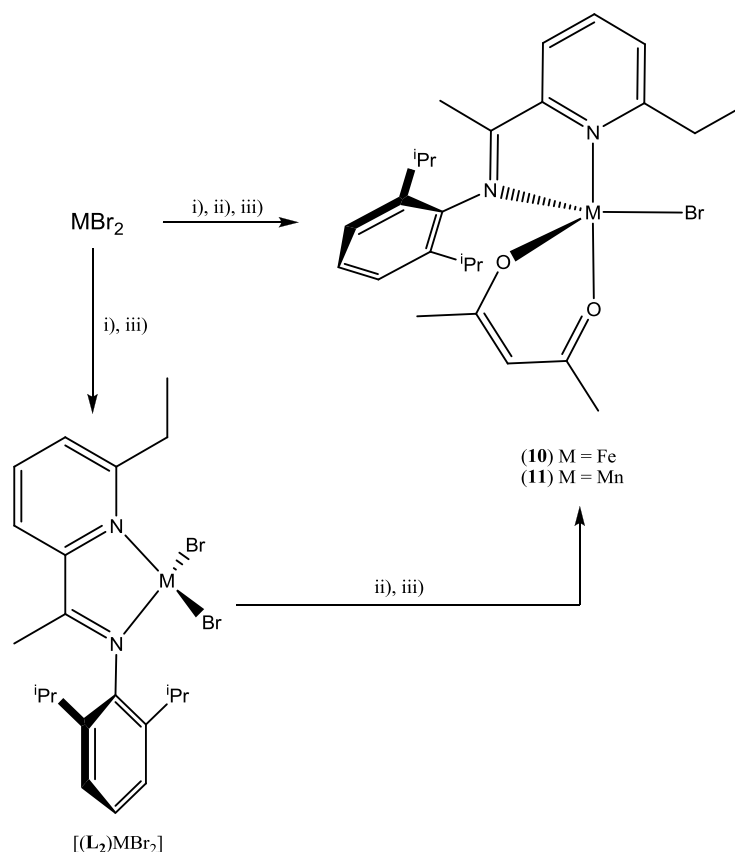
Scheme 3.6 *Reagents and conditions*: i) **L₂**, DCM, rt, 12 h; ii) Na[acac], DCM, rt, 12 h; iii) DCM/hexane recrystallisation.

The sequential treatment of MBr_2 (M = Fe, Mn) with **L₂** and sodium acetylacetonate in dry dichloromethane, in a 1:1:2.5 molar ratio, respectively, gave on recrystallisation under rigorously dry, inert conditions [(**L₂**)MBr(acac)] [M = Fe (**10**), Mn (**11**)] in good yields, respectively (Scheme 3.6). Complexes **10** and **11** have been characterised by FAB mass spectrometry, IR spectroscopy, magnetic measurements and elemental analysis. In addition, single crystals of both complexes have been subject to single crystal X-ray diffraction studies.

Crystals suitable for the X-ray structure determinations were obtained by slowly diffusing dry hexane into a concentrated dry dichloromethane solution of **10** and **11**. The molecular structures are depicted in Figure 3.17; selected bond lengths and angles for both complexes are given in Table 3.9.

Complexes **10** and **11** are isostructural to their nickel and cobalt analogues **6b** and **7b**, containing a metal bromide (M = Fe, Mn) unit supported by chelating $\mathbf{L_2}$ and acetylacetonate ligands to complete five co-ordinate geometries which can be best described as TBPDSPB [τ = 0.57 (**10**) 0.54 (**11**)]. Inspection of the molecular packing diagram reveals four symmetry related molecules of **10** and eight symmetry related molecules of **11** present in the unit cells. Interestingly, **10** shows some degree of ordering in the solid state with respect to the neighbouring M–Br bonds [tors: BrM···MBr = 14.27°]; however, **11** shows a random orientation of M–Br bonds [range tors: BrM···MBr = 5.27–44.35°].

The FAB mass spectra of **10** and **11** reveal peaks corresponding to the molecular ion and loss of a bromide atom. In addition, IR spectra suggest the presence of a bound pyridylarylimine as the ν(C=N)$_{imine}$ stretches are shifted *ca.* 50 cm^{-1} to lower wavenumbers when compared to the free $\mathbf{L_2}$ [ν(C=N)$_{imine}$ = 1579 cm^{-1} (**10**), 1585 cm^{-1} (**11**)]. Both complexes are paramagnetic and display magnetic moments of 5.03 (**10**) and 5.72 (**12**) BM (Evans balance at room temperature) consistent with high-spin d^5 and d^6 electron configurations, respectively.

(a)
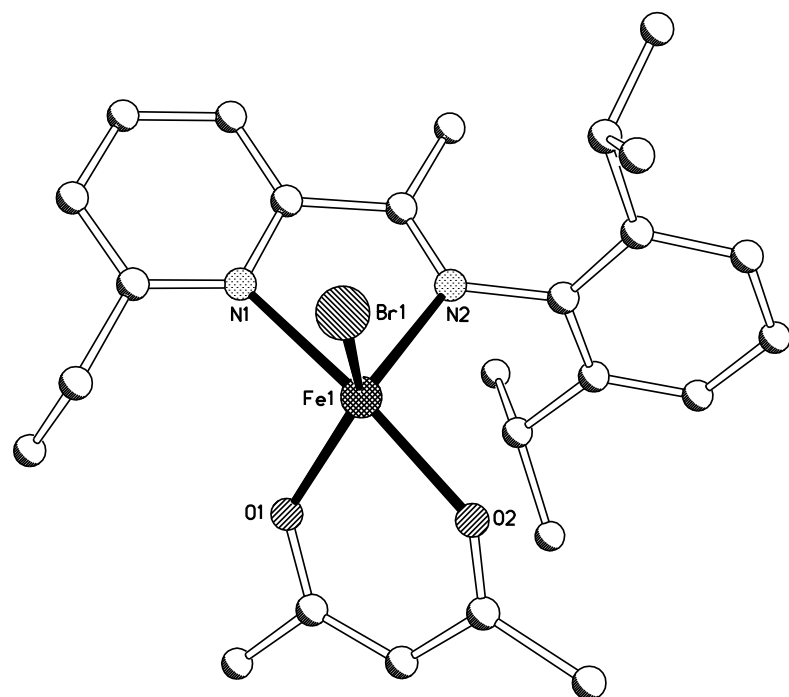
(b)
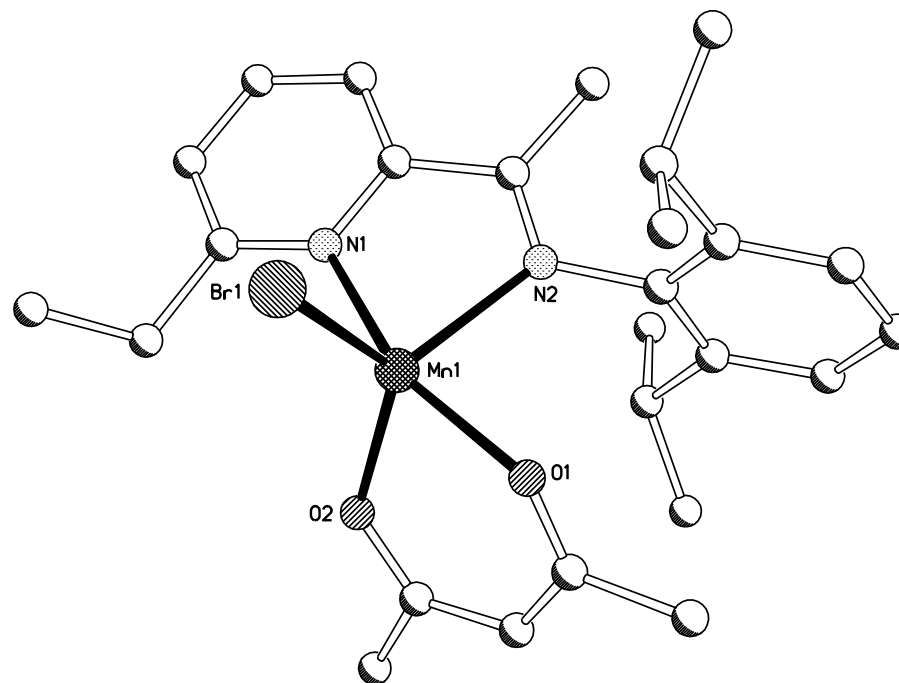
Figure 3.17 Molecular structures of (a) **10** and (b) **11** shown with partial atom labels; hydrogen atoms have been omitted for clarity.

Table 3.9 Selected bond lengths (Å) and bond angles (°) for **10** and **11**.

	10 (M = Fe)	**11** (M = Mn)
M(1)–N(1)	2.213(4)	2.273(3)
M(1)–N(2)	2.128(4)	2.238(2)
M(1)–O(1)	2.021(4)	2.085(2)
M(1)–O(2)	2.020(4)	2.051(2)
M(1)–Br(1)	2.4644(13)	2.5041(11)
N(1)–M(1)–N(2)	75.36(17)	72.20(9)
N(1)–M(1)–O(1)	87.64(17)	158.29(9)
N(1)–M(1)–O(2)	169.69(16)	96.56(9)
N(1)–M(1)–Br(1)	92.17(11)	95.60(6)
N(2)–M(1)–O(1)	116.91(18)	87.49(9)
N(2)–M(1)–O(2)	104.21(18)	117.39(9)
N(2)–M(1)–Br(1)	106.46(12)	116.56(7)
O(1)–M(1)–O(2)	83.41(17)	85.83(9)
O(1)–M(1)–Br(1)	134.98(14)	106.53(7)
O(2)–M(1)–Br(1)	97.76(17)	125.59(7)

3.6.5 Influence of steric bulk and metal centre variation on the five co-ordinate geometries in 6, 7, 10 and 11

From the previous section it can be seen that, while copper exhibits a preference for a regular SBP (τ = 0.01–0.29) geometry, nickel, cobalt, iron and manganese tend towards more distorted geometries between TBP and SBP. In this section, two areas will be discussed, firstly, the effect of the metal centre for a given steric bulk on the value of τ and secondly, the effect of variation in steric bulk for a given metal centre. In addition, an attempt will be made to quantify the magnitude of the steric bulk employed in order to establish a numerical relationship.

*a) Steric effects and metal centre variation in [(**L₂**)MBr(acac)] (M = Ni, Co, Fe, Mn)*

By plotting the τ-value against the metal centre for ethyl-substituted pyridylarylimine derivatives [(**L₂**)MBr(acac)] [M = Ni (**6b**), Co (**7b**), Fe (**10**), Mn (**11**)], it is apparent that there is no significant variation in the τ-values for each metal centre [M = Mn (**11**) (τ = 0.54), Fe (**10**) (τ = 0.57), Co (**7b**) (τ = 0.65), Ni (**6b**) (τ = 0.54)] (Figure 3.18), although the cobalt derivative does appear to display some slightly anomalous behaviour. This suggests that for these metal centres the nature of the metal centre does not contribute to the overall geometry and therefore, the geometry variations are likely to be attributed to the steric properties of the pyridylarylimine ligand (*vide infra*).
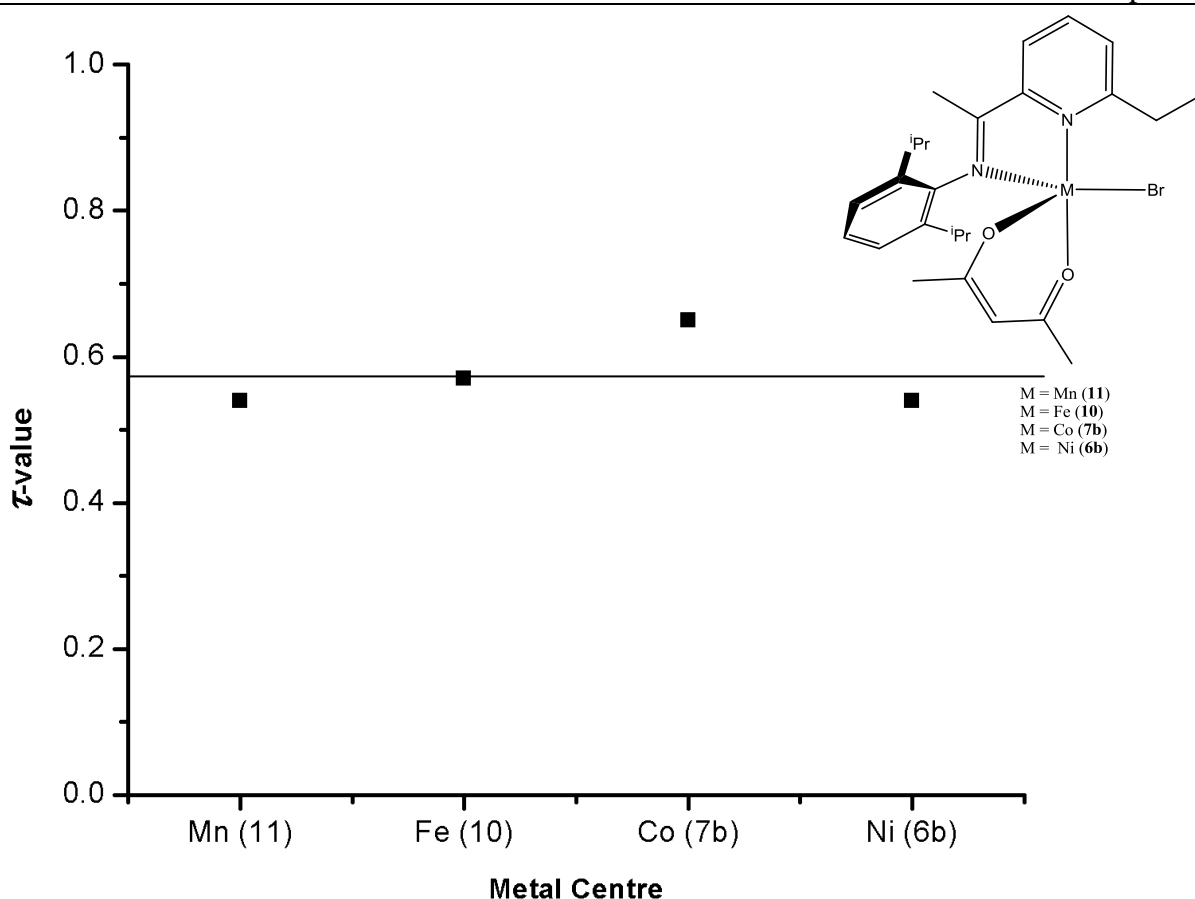
Figure 3.18 A plot depicting the variation of τ as a function of metal centre variations for **11**, **10**, **7b** and **6b**.

b) Steric effects on 6

In contrast, on inspection of Figure 3.19, it is clear that the τ-value decreases with the perceived increase in steric bulk at the 2-R-pyridyl position (H < Et < ^{i}Pr < Ph < Napth). For example, nickel-containing naphthyl-substituted **6e′** displays a τ-value of 0.38 (towards SBP), while the ethyl-substituted **6b** displays a τ-value of 0.54 (towards TBP). In between these two limiting values, the isopropyl- ($\tau = 0.51$) and phenyl-substituted ($\tau = 0.44$) derivatives are found; a similar trend can be observed for the cobalt-containing **7a–7e**.
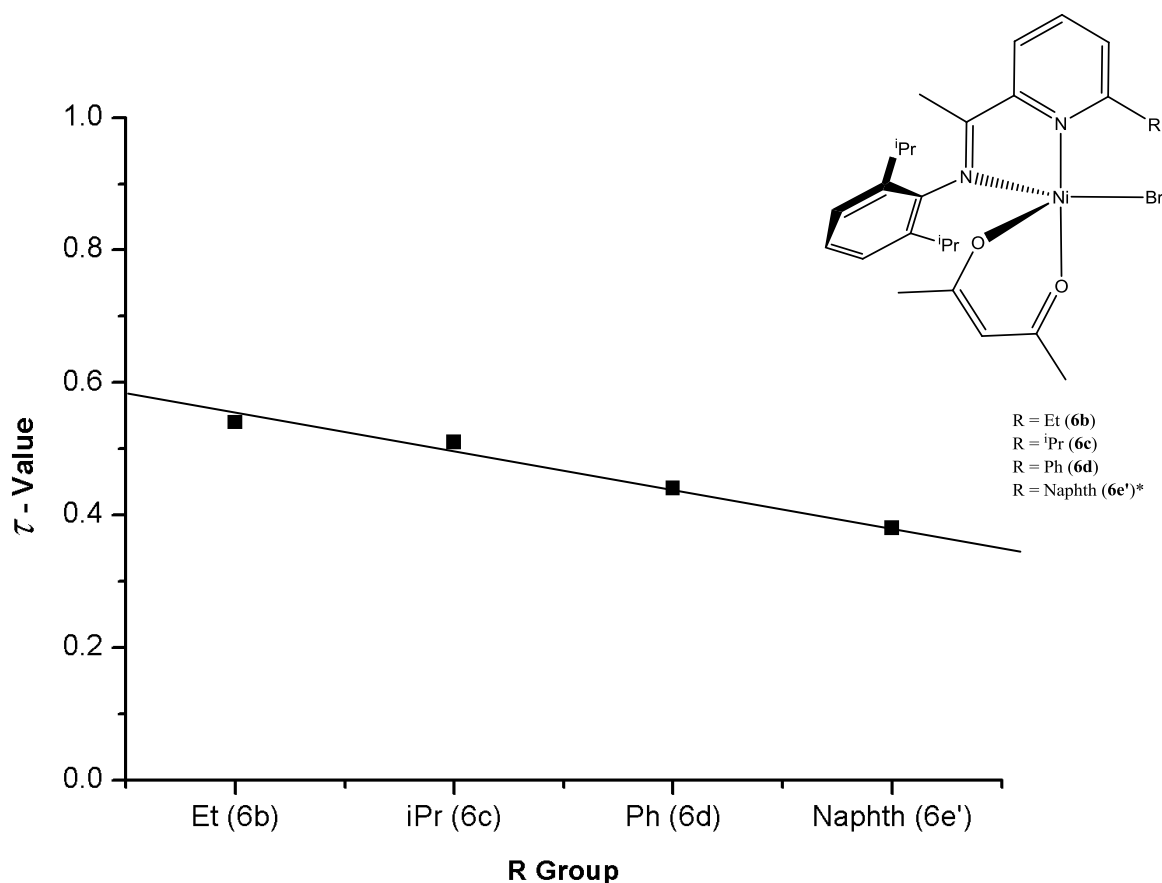
Figure 3.19 τ-Value plotted against the perceived sterically bulky R groups for nickel-containing **6**. Note: For **6e′** the τ-value has been determined from its cationic unit $[(\mathbf{L_6})Ni(OH_2)(acac)]^+$.

In order to quantify this hypothesised relationship between steric bulk at the 2-pyridyl position and the observed transition metal geometries of **6b–6e′**, the steric properties of all hydrocarbyl containing $\mathbf{L}_x$ ($\mathbf{L_1}$–$\mathbf{L_6}$) were examined using the *buried volume* parameter $\%V_{bur}$ described by Nolan *et al.* for *N*-heterocyclic carbenes (NHC's).[74] To the knowledge of the author, this is the first time in which the $\%V_{bur}$ parameter has been calculated for pyridylarylimine ligands (a full description of this procedure is given in the Appendix A13.0). The $\%V_{bur}$ parameter is defined as the total percentage of a co-ordination sphere occupied by the ligand (Table 3.10). The spatial occupation of these pyridylarylimine ligands are calculated using the Salerno Molecular Buried Volume Calculation (sambVca) and can be calculated from crystallographic data by an online program.[75]

Table 3.10 Calculated volume parameters for $\mathbf{L}_x$.

	V_{free} (Å^3)	V_{bur} (Å^3)	V_{tot}(Å^3)^a	%V_{bur}^{b}
R Group				
H ($\mathbf{L_1}$)	343.139	180.335	523.475	34.4
Et ($\mathbf{L_2}$)	315.528	207.947	523.475	39.7
^{i}Pr ($\mathbf{L_3}$)	314.924	208.550	523.475	39.8
Ph ($\mathbf{L_4}$)	307.039	216.436	523.475	41.3
Naphth ($\mathbf{L_5}$)	288.634	234.840	523.475	44.9
Anthr ($\mathbf{L_6}$)	274.727	248.747	523.475	47.5

a) Calculated for a 5 Å radius sphere.
b)%$V_{\text{bur}} = V_{\text{bur}}/V_{\text{free}}$.

Examination of Table 3.10 indicates that as the size of the R group increases, the %V_{bur} increases, with the anthracenyl-substituted $\mathbf{L_6}$ having the largest %V_{bur} and the H-containing $\mathbf{L_1}$ the smallest. Figure 3.20 illustrates the effect of %V_{bur} of $\mathbf{L}_x$ on the τ-value for the nickel falimily $\mathbf{6b}$, $\mathbf{6c}$, $\mathbf{6d}$ and $\mathbf{6e'}$. Once again, a decrease in τ is accompanied by an increase in size of the %V_{bur} parameter.
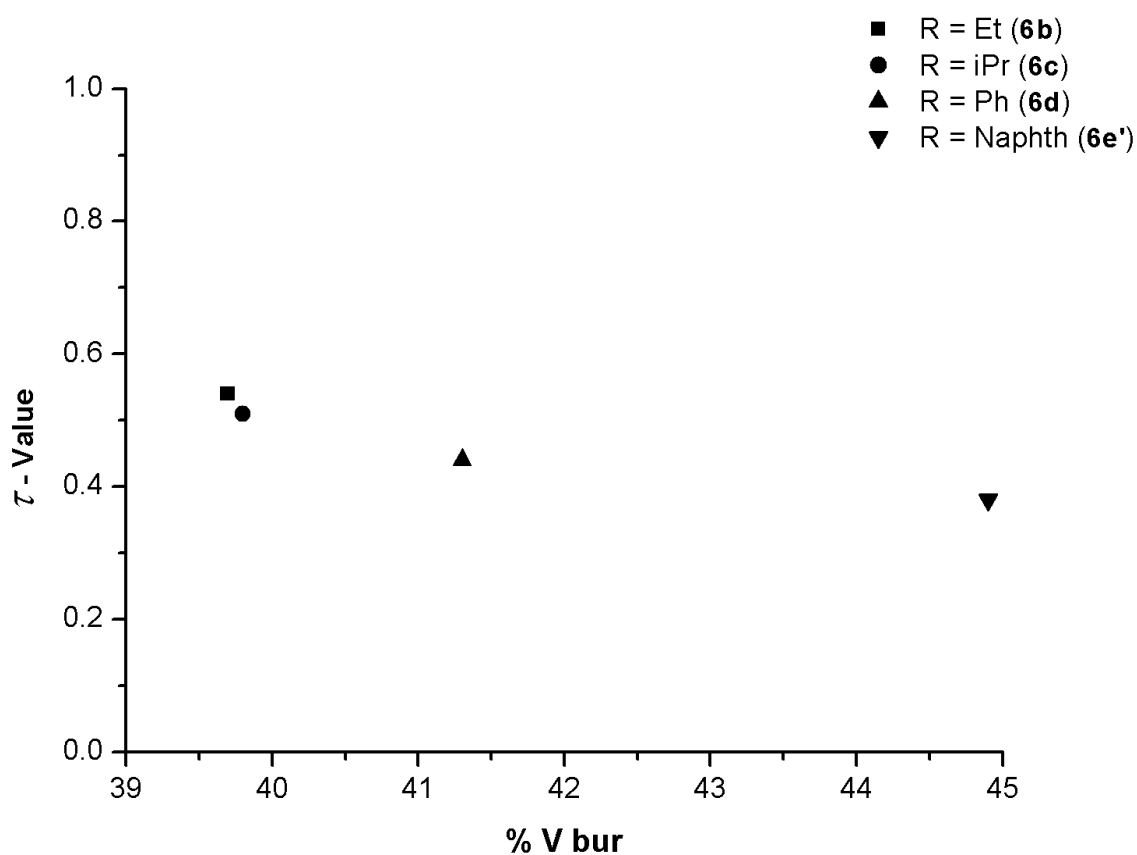
Figure 3.20 τ-Value plotted against the %V_{bur} parameter for nickel-containing $\mathbf{6}$.

However, despite the encouraging effect on the magnitude of τ, closer inspection of the resultant geometries indicates an unexpected result. For example, if phenyl-containing **6d** is regarded as SBP ($\tau = 0.44$), it is apparent that the bromide ligand now occupies a basal site, while the imine nitrogen fills the apical site (Figure 3.21); a configuration quite different from the desired apical occupation for the bromide ligand as seen in copper-containing **5a**.
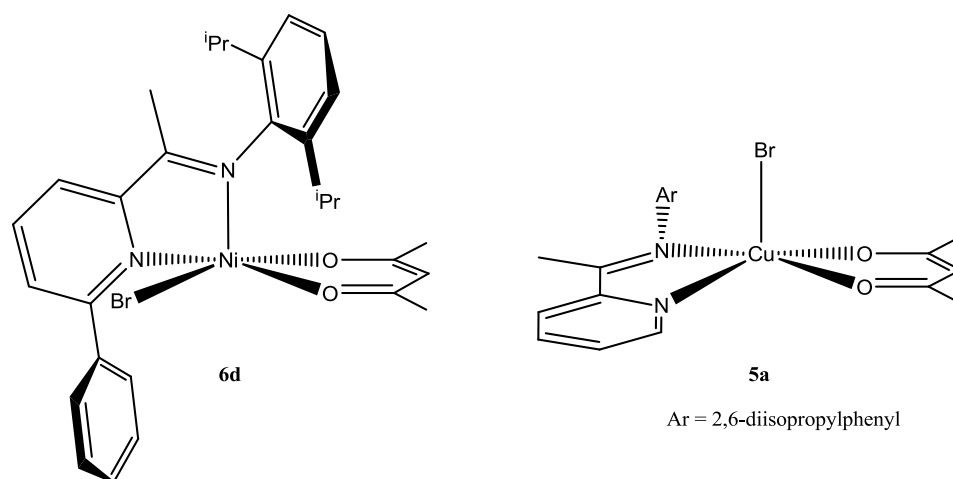
Figure 3.21 Bromide site occupation variations on the SBP geometries found in **6d** and **5a**.

3.6.6 Summary

As with the copper-containing **3–5** (section 3.3), five co-ordinate complexes of the form, [(α-diimine)MBr(β-diketonate)] [Ni (**6**), Co (**7**), Fe (**10**), Mn (**11**)], are all accessible using suitably tailored pyridylarylimine ligands ($\mathbf{L}_x$). Only by appending hydrocarbyl groups at the 2-position of the pyridylimine, could the desired mononuclear complexes be obtained. However, on inspection of the τ-value, geometries anywhere between TBP and SBP were apparent. Notably, a correlation between steric bulk and the observed geometry was identified with a reduction of τ apparent on increasing steric bulk of $\mathbf{L}_x$; but leading to the undesirable basal occupation of the terminal bromide ligand. Furthermore, the molecular packing diagrams revealed intermolecular disorder in some cases, which is in contrast to the copper complexes, despite using richly aromatic groups such as naphthyl and anthracenyl to promote graphitic interactions. In light of

these observations, these materials are not, in principle, suitable for potential X-ray dichroic materials.

The formation of $[(\mathbf{L}_x)MBr(\beta\text{-diketonate})]$ (M = Ni, Co, Fe, Mn) is shown to proceed *via* the intermediate tetrahedral complexes, $[(\mathbf{L}_x)MBr_2]$, which have been isolated and fully characterised as with copper-containing $[(\mathbf{L_1})CuBr_2]$. Furthermore, an attempt was made to improve the intermolecular packing using other β-diketonates such as dibenzoylmethanato. However, in all cases, *bis*-chelation of the β-diketonate was observed to give octahedral $[(\mathbf{L}_x)M(dbm)_2]$ [M = Ni (**8**), Co (**9**)].

3.7 Alternative *bis*-chelates based on α-diimine/pyridonate and α-diimine/benzoate combinations for nickel(II) and cobalt(II) bromides

As highlighted previously, changes in the steric properties of the pyridylarylimine ($\mathbf{L}_x$) can influence the τ-value of the complex, while the nature of the β-diketonate appears to dictate how many O,O chelates are added. In this section, the focus is on replacing the β-diketonate ligand with either a pyridonate or carboxylate, both having some track record for forming N,O or O,O-chelate rings, respectively.

3.7.1 Using N,O = pyridonate; attempted synthesis of [(α-diimine)NiBr(pyridonate)]

2-Pyridonates display a rich variety of bonding modes which have been described by the Harris notation.[76] Whilst bridging modes predominate, there are a number of examples in which the pyridonate acts as a N,O chelate to form discrete mononuclear compounds. For example, [(4,4′-Me$_2$bipy)Ni(chp)$_2$] (**G**),[77] [(DPA)Co(chp)$_2$] (**H**) and [(1-10-phen)Co(hcp)$_2$] (**I**)[78] (with further examples found within reference 78), are all accessible using M(OAc)$_2$ as the starting material. With the aim of using more bulky pyridylarylimines to prevent *tris*-chelation, efforts are outlined at attempting to prepare $[(\mathbf{L}_x)NiBr(pyridonate)]$ from metal halide starting materials.

NiBr$_2$(DME) $\xrightarrow{\text{i), ii), iii)}}$

(**12a**) R = Et
(**12b**) R = ^{i}Pr

Ar = 2,6-diisopropylphenyl
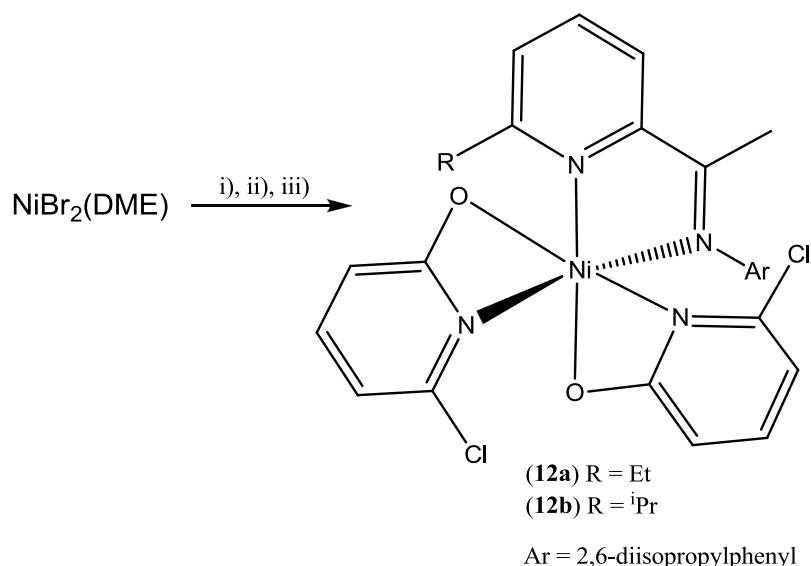
Scheme 3.7 *Reagents and conditions:* i) **L$_2$** or **L$_3$**, DCM, rt, 12 h; ii) Na[chp], DCM, rt, 12 h; iii) DCM recrystallisation.

Thus, the reaction of the NiBr$_2$(DME) adduct with the corresponding pyridylarylimine, **L$_2$** or **L$_3$** followed by sodium 6-chloropyridonate (Na[chp]) in 1:1:2 molar ratio, respectively, gave [(**L$_2$**)Ni(chp)$_2$] (**12a**) and [(**L$_3$**)Ni(chp)$_2$] (**12b**) as the sole products, in good yields, respectively (Scheme 3.7). In addition, the reaction was also performed at lower temperature as well as using a 1:1:1 molar ratio of reactants but, [(**L$_2$**)NiBr$_2$] or [(**L$_3$**)NiBr$_2$] were again the only isolated products. Attempts at using more sterically bulky **L$_5$** gave intractable materials, as did the use of alternative pyridonates, *e.g.*, Na[mhp] (sodium 6-methylpyridonate) and Na[hp] (sodium pyridonate). Complexes **12** have been characterised by FAB mass spectrometry, IR spectroscopy, magnetic measurements and elemental analysis. In addition, **12a** and **12b** were also subject to single crystal X-ray diffraction studies.

Crystals of **12a** and **12b**, suitable for the X-ray determinations were obtained by slowly diffusing hexane into a concentrated dichloromethane solution of **12**. The molecular structure of **12a**, as a representative example, is shown in Figure 3.22; selected bond lengths and angles for **12** are given in Table 3.11.
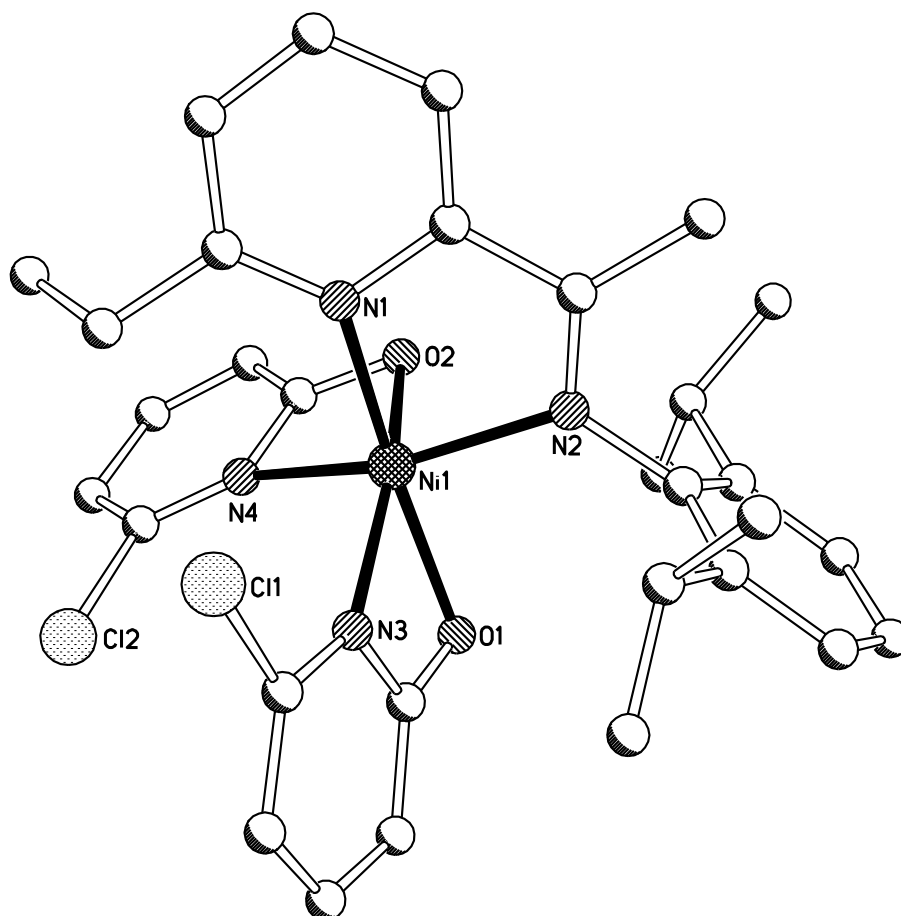
Figure 3.22 Molecular structure of **12a** with partial atom labels; hydrogen atoms have been omitted for clarity.

Table 3.11 Selected bond lengths (Å) and angles (°) for **12**.

	12a	**12b**
Ni(1)–N(1)	2.090(5)	2.119(3)
Ni(1)–N(2)	2.045(5)	2.056(3)
Ni(1)–N(3)	2.067(5)	2.056(3)
Ni(1)–N(4)	2.115(5)	2.112(3)
Ni(1)–O(1)	2.098(4)	2.159(3)
Ni(1)–O(2)	2.068(4)	2.095(3)
N(1)–Ni(1)–N(2)	79.6(2)	79.49(13)
N(1)–Ni(1)–N(3)	107.0(2)	103.10(13)
N(1)–Ni(1)–N(4)	100.80(19)	103.15(13)
N(1)–Ni(1)–O(1)	167.80(17)	165.53(11)
N(1)–Ni(1)–O(2)	89.47(17)	91.32(12)
N(2)–Ni(1)–N(3)	102.09(19)	97.50(12)
N(2)–Ni(1)–N(4)	158.2(2)	161.34(13)
N(2)–Ni(1)–O(1)	93.72(18)	96.10(12)
N(2)–Ni(1)–O(2)	93.83(18)	97.97(12)
N(3)–Ni(1)–N(4)	98.7(2)	99.81(13)
N(3)–Ni(1)–O(1)	64.15(18)	63.56(12)
N(3)–Ni(1)–O(2)	158.78(19)	160.52(12)
N(4)–Ni(1)–O(1)	89.21(17)	85.47(11)
N(4)–Ni(1)–O(2)	64.40(18)	63.69(12)
O(1)–Ni(1)–O(2)	101.25(17)	102.98(11)

Compounds **12a** and **12b** are structurally related and consist of a chelating pyridylarylimine and *bis*-chelated 6-chloropyridonate ligands to complete Δ-configured octahedral geometries about the metal centre. The average N,O chelate bite angles are similar to each other [64.39° (**12a**), 63.71° (**12b**)]. Inspection of the packing diagrams of **12** revealed that eight molecules are present in the unit cell of **12a**, while only four molecules are present in **12b**. FAB mass spectrometry showed molecular ion peaks along with associated sodium ions. Also evident, are peaks corresponding to the sequential loss of 6-chloropyridonate ligands. The IR spectra reveal peaks consistent with a bound pyridylarylimine [v(C=N)$_{imine}$ = 1598 cm^{-1} (**12a**), 1599 cm^{-1} (**12b**)], with peaks corresponding to delocalised C–O stretches of the 6-chloropyridonate [v(C–O) = 1635 cm^{-1} (**12a**), 1642 cm^{-1} (**12b**)]. Both complexes are paramagentic and magnetic measurements confirmed the presence of two unpaired electrons [μ_{eff} = 2.81 BM (**12a**) and 2.92 BM (**12b**)]. In addition, elemental analyses support the molecular structures.

3.7.2 Using O,O = benzoate; attempted synthesis of [(α-diimine)$_2$NiBr(O$_2$CPh)]

(**13a**) M = Ni, R = Et
(**13b**) M = Ni, R = ^{i}Pr

14
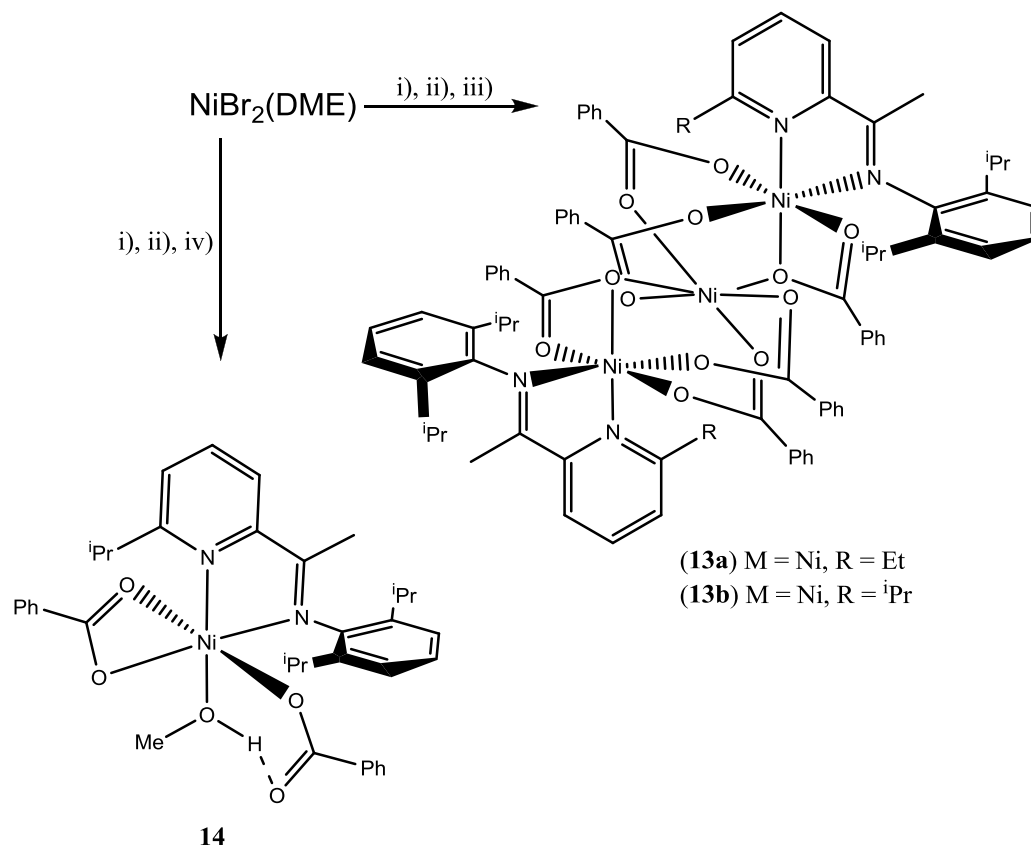
Scheme 3.8 *Reagents and conditions*: i) **L$_2$** or **L$_3$**, DCM, rt, 12 h; ii) Na[O$_2$CPh], DCM, rt, 12 h; iii) DCM/hexane recrystallisation; iv) MeOH recrystallisation.

Treatment of either NiBr$_2$(DME) with the corresponding pyridylarylimine **L$_2$** or **L$_3$** followed by sodium benzoate in dichloromethane in a 1:1:2 molar ratio, respectively gave, on recrystallisation from dichloromethane and hexane, the trimetallic complexes, [(**L$_2$**)$_2$Ni$_3$(O$_2$CPh)$_6$] (**13a**) and [(**L$_3$**)$_2$Ni$_3$(O$_2$CPh)$_6$] (**13b**) in good yields, respectively (Scheme 3.8). Interestingly, attempted recrystallisation of **13b** using methanol as the solvent gave the monometallic [(**L$_3$**)Ni(O$_2$CPh)$_2$(MeOH)] (**14**), in good yield. The isostructural tricobalt counterparts have also been afforded under identical conditions (see Appendix A12.0).

Complexes **13** and **14** have been characterised by FAB and Time of Flight (TOF) mass spectrometry, IR spectroscopy, magnetic measurements, elemental analysis and in addition, they have all been subjected to X-ray structure determinations. Crystals of **13a** and **13b** suitable for X-ray diffraction were obtained from slowly diffusing hexane into a concentrated dichloromethane solution of **13a** or chloroform solution of **13b**, respectively. Likewise, single crystals of **14** suitable for X-ray diffraction, were grown by slow evaporation of a methanolic solution of **14**. The molecular structures of **13b** and **14** are depicted in Figures 3.23 and 3.24 selected bond lengths and angles for both complexes **3a** and **13b** are given in Tables 3.12, with data for **14** listed in Table 3.13.

Nickel-containing **13a** and **13b** consist of discrete trimetallic frameworks with a twofold C$_2$ axis about the central metal atom [Ni(1)] resulting in a perfectly linear arrangement of the metal atoms. At each terminal metal atom [Ni(2) and Ni(2A)], a pyridylarylimine and a benzoate molecule (undergoing a 1,1-bridging interaction to the central nickel atom) are chelated, along with two co-ordinated oxygen atoms from a pair of 1,3-bridging benzoates. The central nickel atom consists of *trans*-arranged 1,3-bridging and 1,1-bridging oxygen atoms which bridge the terminal and central metal centres. The geometry about all the metal centres can best be described as distorted octahedral where the distortion is likely to arise from the small bite angle of the chelating benzoate ligands [O(1)–M(1)–O(2) = 62.35(6)° (**13a**), 61.80(9)° (**13b**)]. In addition, the metal atoms are separated by distances of 3.43 Å (**13a**), 3.478 Å (**13b**).

Furthermore, the benzoate 1,1-bridging mode exhibited by one of the benzoate molecules is rare

for monocarboxylate ligands[79] but is known.[80,83] Following a search of the CSD, it is apparent

that $[Ni_3(L)_2(O_2CPh)_4]$ [L = (2-[3-methylamino-propylimino)-methyl]-phenolate)] (**J**) is the only

reported complex resembling **13** (albeit with a tridentate Schiff-base ligand).[79]
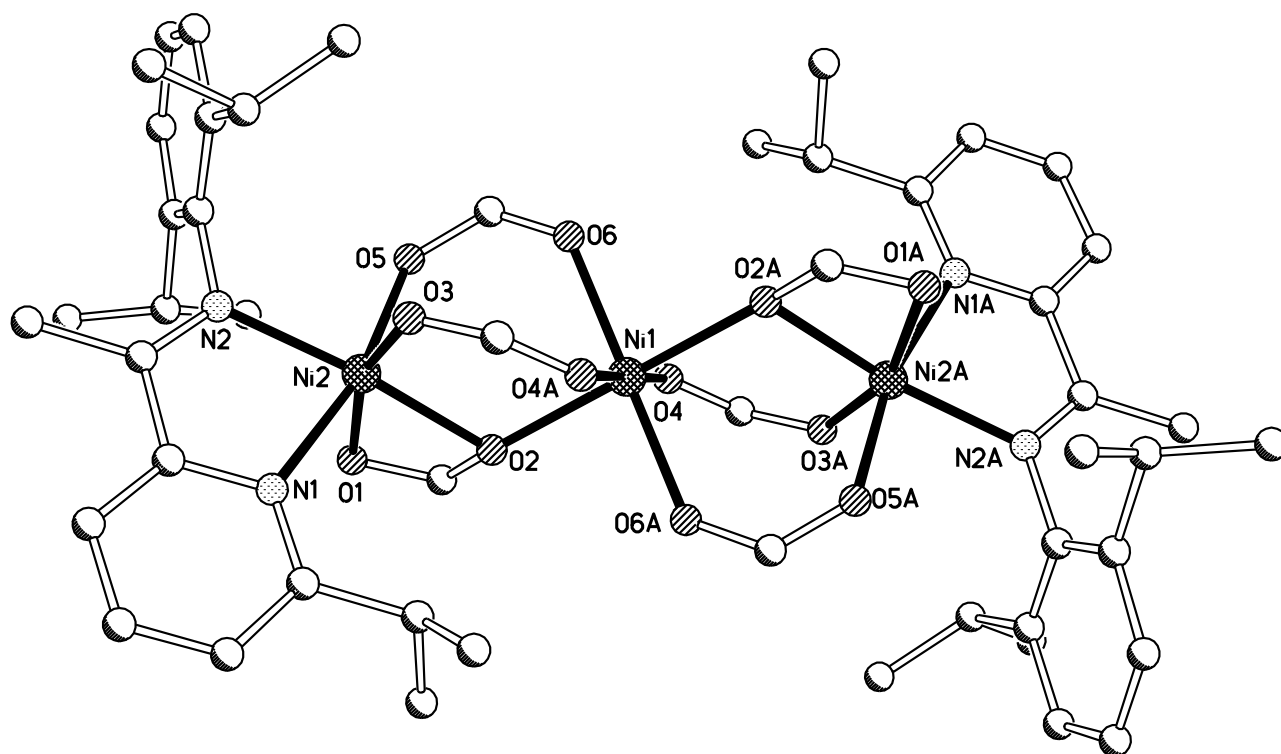
Figure 3.23 Molecular structure of **13b** shown with partial atom labels; hydrogen atoms and phenyl rings of the O_2CPh ligand have been omitted for clarity. Atoms denoted with the letter label 'A' are generated by the symmetry operation -*x*, -*y*+1, -*z*+1.

Table 3.12 Selected bond lengths (Å) and angles (°) for **13a** and **13b**.

13a[a]				13b[b]			
Ni atom 1		*Ni atom 2*		*Ni atom 1*		*Ni atom 2*	
Ni(1)–N(1)	2.167(2)	Ni(2)–O(2)	2.1071(16)	Ni(1)–O(2)	2.118(2)	Ni(2)–N(1)	2.138(3)
Ni(1)–N(2)	2.062(2)	Ni(2)–O(2A)	2.1071(16	Ni(1)–O(2A)	2.118(2)	Ni(2)–N(2)	2.058(3)
Ni(1)–O(1)	2.1225(16)	Ni(2)–O(4)	2.0524(16)	Ni(1)–O(4)	2.030(2)	Ni(2)–O(1)	2.137(2)
Ni(1)–O(2)	2.0872(15)	Ni(2)–O(4A)	2.0524(16)	Ni(1)–O(4A)	2.030(2)	Ni(2)–O(2)	2.112(2)
Ni(1)–O(3)	2.0000(16)	Ni(2)–O(6)	2.0398(16)	Ni(1)–O(6)	2.044(2)	Ni(2)–O(3)	1.993(2)
Ni(1)–O(5)	2.0209(17)	Ni(2)–O(6A)	2.0398(16)	Ni(1)–O(6A)	2.044(2)	Ni(2)–O(5)	2.011(2)
N(1)–Ni(1)–N(2)	78.38(9)	O(2)–Ni(2)–O(2A)	180.00(6)	O(2)–Ni(2)–O(2A)	180.0	N(1)–Ni(1)–N(2)	78.33(2)
N(1)–Ni(1)–O(1)	94.96(7)	O(2)–Ni(2)–O(4)	90.29(6)	O(2)–Ni(2)–O(4)	89.37(0)	N(1)–Ni(2)–O(1)	90.86(10)
N(1)–Ni(1)–O(2)	102.56(7)	O(2)–Ni(2)–O(4A)	89.71(16)	O(2)–Ni(2)–O(4A)	90.63(9)	N(1)–Ni(2)–O(2)	105.66(11)
N(1)–Ni(1)–O(3)	84.67(8)	O(2)–Ni(2)–O(6)	92.92(6)	O(2)–Ni(2)–O(6)	93.14(9)	N(1)–Ni(2)–O(3)	86.79(11)
N(1)–Ni(1)–O(5)	165.25(8)	O(2)–Ni(2)–O(6A)	87.08(6)	O(2)–Ni(2)–O(6A)	89.86(9)	N(1)–Ni(2)–O(5)	166.86(11)
N(2)–Ni(1)–O(1)	104.42(7)	O(2A)–Ni(2)–O(4)	89.71(6)	O(2A)–Ni(2)–O(4)	90.63(9)	N(2)–Ni(2)–O(1)	101.91(10)
N(2)–Ni(1)–O(2)	166.74(7)	O(2A)–Ni(2)–O(4A)	90.29(6)	O(2A)–Ni(2)–O(4A)	89.37(9)	N(2)–Ni(2)–O(2)	163.07(10)
N(2)–Ni(1)–O(3)	90.59(7)	O(2A)–Ni(2)–O(6)	87.80(6)	O(2A)–Ni(2)–O(6)	89.86(9)	N(2)–Ni(2)–O(3)	95.50(11)
N(2)–Ni(1)–O(5)	89.98(8)	O(2A)–Ni(2)–O(6A)	92.92(6)	O(2A)–Ni(2)–O(6A)	93.14(9)	N(2)–Ni(2)–O(5)	88.91(11)
O(1)–Ni(1)–O(2)	62.35(6)	O(4)–Ni(2)–O(4A)	180.00(8)	O(4)–Ni(2)–O(4A)	180.000(1)	O(1)–Ni(2)–O(2)	61.80(9)
O(1)–Ni(1)–O(3)	164.63(7)	O(4)–Ni(2)–O(6)	93.74(7)	O(4)–Ni(2)–O(6)	87.42(10)	O(1)–Ni(2)–O(3)	161.59(10)
O(1)–Ni(1)–O(5)	89.44(7)	O(4)–Ni(2)–O(6A)	86.26(7)	O(4)–Ni(2)–O(6A)	92.58(10)	O(1)–Ni(2)–O(5)	88.74(10)
O(2)–Ni(1)–O(3)	102.67(6)	O(4A)–Ni(2)–O(6)	86.26(7)	O(4A)–Ni(2)–O(6)	92.58(10)	O(2)–Ni(2)–O(3)	101.22(10)
O(2)–Ni(1)–O(5)	89.14(7)	O(4A)–Ni(2)–O(6A)	93.74(7)	O(4A)–Ni(2)–O(6A)	87.42(10)	O(2)–Ni(2)–O(5)	86.29(9)
O(3)–Ni(1)–O(5)	93.95(7)	O(6)–Ni(2)–O(6A)	180.0	O(6)–Ni(2)–O(6A)	180.00(14)	O(3)–Ni(2)–O(5)	97.62(10)

a) Atoms denoted with the letter 'A' are generated by the symmetry operation *-x*+1, *-y*+1, *-z*+1.

b) Atoms denoted with the letter 'A' are generated by the symmetry operation *-x*, *-y*+1, *-z*+1.

Fragmentation peaks associated with the ions [(L_x)Ni] and [(L_x)Ni(O$_2$CPh)] are only evident in the FAB mass spectra of **13a** and **13b**. In contrast, however, the molecular ion peak displaying the expected isotopic distribution is evident in the TOF mass spectra for both compounds, as well as peaks corresponding to the fragmentation of benzoate molecules. The IR spectra of **13** reveal peaks associated with the stretches of co-ordinated pyridylarylimine ligands [ν(C=N)$_{imine}$ = 1572 cm^{-1} (**13a**), 1594 cm^{-1} (**13b**)] which are lower than the corresponding free ligand, as well as likely carbonyl stretches of the benzoate molecules [ν(C=O)$_{benzoate}$ 1612 cm^{-1} (**13a**), 1620 cm^{-1} (**13b**)] which were lower than that observed in sodium benzoate (*ca.* 1640 cm^{-1}). All complexes are paramagnetic displaying magnetic moments of 4.19 (**13a**) and 3.97 (**13b**) BM (Evans balance at room temperature), values that are less than the predicted spin-only value of 4.90 BM [using $\mu^2 = \Sigma\mu_i^2$ (μ_i = magnetic moment of individual metal centres)], implying some anti-ferromagnetic coupling. In addition, elemental analysis supports the molecular structures.

The molecular structure of **14** consists of a nickel atom chelated by **L$_3$**, a tightly biting benzoate chelate [O(3)–Ni(1)–O(4) = 62.20(6)° *cf.* N(1)–Ni(1)–N(2) = 78.81(9)°] and a monodentate benzoate along with a molecule of methanol to complete a heavily distorted octahedral geometry. The molecule of methanol is *trans* to the pyridyl N(1) atom, whilst one of the chelating benzoate oxygen atoms is *trans* to the pendant benzoate oxygen [O(1)]. A hydrogen-bonding interaction exists between the methanol hydrogen atom and the pendant benzoate oxygen (H–O(2) = 1.736 Å). Four symmetry related molecules are present in the unit cell on inspection of the packing diagram. The FAB mass spectrum of **14** reveals peaks corresponding to the sequential loss of methanol and benzoate molecules. IR data gives peaks at 1532 cm^{-1} [ν(C=N)$_{imine}$] and 1609 cm^{-1} [ν(C=O)$_{benzoate}$] which were lower than those observed in **13a** and **13b**. In addition a peak at 2964 cm^{-1} corroborates the presence of a bound methanol (ν_{OH}). The magnetic moment measurement for **14** at room temperature confirms the presence of two unpaired electrons (μ_{eff} = 3.11 BM). Elemental analysis also supports the molecular structure.
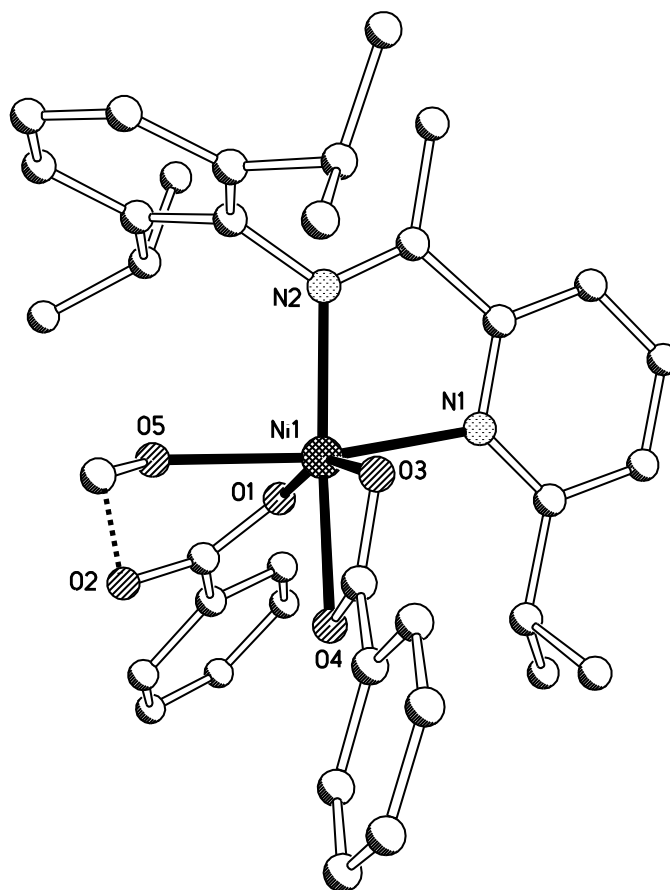
Figure 3.24 Molecular structure of **14** shown with partial atom labels; hydrogen atoms have been omitted for clarity.

Table 3.13 Selected bond lengths (Å)and angles (°) for **14**.

	14
Ni(1)–N(1)	2.122(2)
Ni(1)–N(2)	2.066(2)
Ni(1)–O(1)	2.013(2)
Ni(1)–O(3)	2.102(2)
Ni(1)–O(4)	1.239(2)
Ni(1)–O(5)	2.081(2)
N(1)–Ni(1)–N(2)	78.81(9)
N(1)–Ni(1)–O(1)	86.00(7)
N(1)–Ni(1)–O(3)	96.51(7)
O(4)–Ni(1)–N(1)	105.27(8)
N(1)–Ni(1)–O(5)	169.02(7)
N(2)–Ni(1)–O(1)	101.92(7)
N(2)–Ni(1)–O(3)	98,11(7)
N(2)–Ni(1)–O(4)	160.05(7)
N(2)–Ni(1)–O(5)	92.20(9)
O(1)–Ni(1)–O(3)	159.91(7)
O(1)–Ni(1)–O(4)	97.87(7)
O(1)–Ni(1)–O(5)	89.76(7)
O(3)–Ni(1)–O(4)	62.20(6)
O(3)–Ni(1)–O(5)	90.95(7)
O(4)–Ni(1)–O(5)	85.33(8)

3.8 Conclusions

Highly ordered copper complexes of the type [(α-diimine)CuBr(β-diketonate)] [α-diimine = 2,2′-bipy; β-diketonate = acac (**3a**), bzac (**3b**), dbm (**3c**), α-diimine = 1,10-phen; β-diketonate = acac (**4a**), bzac (**4b**)], were firstly synthesised and fully characterised and provide a general five co-ordinate, SBP platform for copper(II) metal centres. Indeed, **3a** was subject to a successful X-ray dichroism performance evaluation in fluorescence mode [Cu K-edge (8979 eV)] at the Diamond Light Source (station B16) and showed dichroic features at the main-edge 1 (shoulder), main-edge 2 and EXAFS regions. Interestingly, spectral features, namely the pre-edge and main-edge 2 appear different to those displayed by **1a** in Chapter 2. It has been hypothesised herein that a combination of electronic properties and hydrogen-bonding interactions between select α-diimine protons and the β-diketonate ligand may aid in the facilitation of the the metal centres SBP geometry. The more bulky pyridylarylimine ligand, **L₁**, can also be employed and this too leads to a five co-ordinate SBP copper complex (**5a**). On the other hand, attempts to prepare structurally related five co-ordinate complexes for other 3*d* metal centres using **L₁** revealed mixed results, with the cobalt acetylacetonate derivative (**7a**) five co-ordinate, while the nickel analogue (**6a**) a six co-ordinate octahedral, halide-bridged, dimeric species. However, by systematically increasing the steric properties of **L$_x$** (**L$_x$** = **L₂**–**L₆**), well-defined five co-ordinate [(**L$_x$**)MBr(acac)] complexes could indeed be isolated and fully charactersed for nickel (**6b**–**6d**), cobalt (**7b**–**7e**), iron (**10**) and manganese (**11**). Furthermore, the precise nature of the R group in **L$_x$** was found to influence the geometry of the five co-ordinate metal centre, with bulky R groups driving a more SBP geometry (see discussion of **6b**–**6e**), albeit with the halide more basal than the desired apical. Attempts to express this subtle geometry variation in terms of the *τ*-value as a function of the buried space parameter have also been developed. It is also clear that although *τ*-value manipulation is possible, intermolecular packing is more difficult to control, with several complexes of the 3*d* metal centres showing some disorder with respect to neighbouring M–X bonds. Several dibromide intermediate complexes leading to the formation of **6**, **7**, **10** and **11** have also been isolated and fully characterised.

Unexpectedly, using dibenzoylmethanato as the β-diketonate led to the formation of octahedral *bis*-dibenzoylmethanato complexes **8** and **9**. Unfortunately, using alternative O,O and N,O chelates (O,O = O_2CPh, N,O = chp) in place of the β-diketonate did not generate complexes of the desired [(α-diimine)MBr(O_2CPh)] or [(α-diimine)MBr(chp)] type. With regard to pyridonates, the *tris*-chelated **12** were isolated, while for benzoate, benzoate-bridged tri-nuclear clusters **13** were formed.

On a closing note, the modular design of $\mathbf{L}_x$ in terms of the variable steric properties at the pyridyl-2-position allows some control of the five co-ordinate geometry in non-copper based systems. However, it is evident that it is not sufficient to allow the desired apical bromide SBP species. To circumvent this flexible co-ordination geometry, it was decided to target a rigid tetradentate ligand in order to occupy the basal sites of an SBP leading to the desired geometry, an approach which will be developed in the next chapter.

3.9 General Experimental

In addition to the experimental details described in Chapter 2 (section 2.9), all operations, unless otherwise stated, were carried out under an inert atmosphere of dry, oxygen-free nitrogen using standard Schlenk and cannular techniques or in a nitrogen purged glove box. Solvents were dried using appropriate drying agents[84] or were employed directly from a solvent purification system (Innovative Technology Inc). The NMR spectra were recorded using a Bruker DRX400 spectrometer at 400.13 (^{1}H) and 100.61 MHz (^{13}C) at ambient temperature. Chemical shifts (ppm) are referred to the residual protic solvent peaks. Coupling constants are expressed in Hz. The salts, sodium acetylacetonate (acac), sodium benzoylacetonate (bzac), sodium dibenzoylmethanato (dbm), sodium 6-chloropyridonate (chp) were synthesised by treating the corresponding O,O or N,O precursors with a molar equivalent of sodium hydroxide in methanol, followed by rigorous drying under reduced pressure. In addition, 2,6-diisopropylaniline was distilled under reduced pressure prior to use. The metal salts, $CuBr_2$, $NiBr_2(DME)$, $CoBr_2$, $FeBr_2$ and $MnBr_2$ were purchased from Sigma Aldrich chemical company and used without further purification. The compounds *tetrakis*(triphenylphosphine)palladium(0),[87] and 6-tributylstannyl-2-(2-methyl-1,3-dioxolan-2-yl)pyridine[86] along with the pyridylketones (precursors to L_x), 2-isopropyl-6-acetylpyridine,[53] 2-phenyl-6-acetylpyridine,[55] 2-napthyl-6-acetylpyridine[57] were prepared using literature procedures. In addition, 2-ethyl-6-acetylpyridine and 2-anthracenyl-6-acetylpyridine were synthesised by adapted procedures based on structurally similar compounds (see section 3.2.1). All other chemicals were obtained commercially and used without further purification.

3.9.1 Synthesis of L$_2$, L$_5$ and L$_6$

a) L$_2$: A round bottomed flask was charged with 2-ethyl-6-acetylpyridine (2.00 g, 13.422 mmol), 2,6-diisopropylaniline (2.850 g, 16.107 mmol, 1.2 eq.) and absolute ethanol (20 ml). A few drops of formic acid was added and the mixture stirred and heated to 100 °C for 48 h. On cooling to -30 °C, **L$_2$** was obtained as yellow powder which was filtered and washed with cold absolute ethanol (2.400 g, 60%). δ_H (400 MHz, CDCl$_3$, SiMe$_4$); 1.15 (12H, d, *J* = 6.9, CH*Me$_2$*), 1.36 (t, 3H, *J* = 7.9, CH$_2$*CH$_3$*), 2.00 (s, 3H, *Me*C=N), 2.76 (sept, 2H, *J* = 6.9, C*H*Me$_2$), 2.87 (q, 2H, *J* = 7.95. *CH$_2$*CH$_3$), 7.00–7.18 (m, 3H, Ar*H*), 7.20–7.25 (m, 2H, Ar/Py*H*), 7.69 (t, 1H, *J* = 7.3, Py*H*), 8.14 (d, 1H, *J* = 7.4, Py*H*). δ_C (400 MHz, CDCl$_3$, SiMe$_4$); 22.60 (CH*Me$_2$*) 22.91 (CH*Me$_2$*), 23.24 (*C*HMe$_2$), 28.21 (*C*H$_2$CH$_3$), 33.24 (*C*H$_2$CH$_3$), 118.29 (*Me*C=N), 121.63, 122.93, 123.36, 135.87 (Me*C*=N), 136.55, 146.75, 155.35, 166.09, 167.65. ν_{max}(ATR)/cm^{-1} 1644, 1585, 1361, 1089, 821. *m/z* (FAB) 310 [M + H] (100%), Acc. Mass (FAB) 310.2324 (100%). mp: 194–195 °C.

b) L$_5$: A round bottomed flask was charged with 2-(1-naphthyl)-6-acetylpyridine (2.00 g, 8.097 mmol), 2,6-diisopropylaniline (2.719 g, 9.716 mmol, 1.2 eq.) and absolute ethanol (20 ml). A few drops of formic acid was added and the mixture stirred and heated to 100 °C for 48 h. On cooling to -30 °C, **L$_5$** was obtained as yellow powder which was filtered and washed with cold absolute ethanol (2.600 g, 66%). δ_H (400 MHz, CDCl$_3$, SiMe$_4$); 1.10 (12H, t, *J* = 7.6, CH*Me$_2$*), 2.18 (s, 3H, *Me*C=N), 2.73 (sept, 2H, *J* = 6.5, C*H*Me$_2$), 7.0–7.2 (m, 3H, Ar/Py*H*), 7.4–7.8 (m, 5H, Ar/Py*H*), 7.9 (m, 3H, Ar/Py*H*), 8.22 (d, 1H, *J* = 7.0, Ar*H*), 8.33 (d, 1H, *J* = 7.8, Py*H*). δ_C (400 MHz, CDCl$_3$, SiMe$_4$); 22.92 (CH*Me$_2$*) 23.28 (CH*Me$_2$*), 28.29 (*C*HMe$_2$), 119.49, 122.99, 123.54, 125.38, 125.75, 125.91, 126.05, 126.39, 127.82, 128.45, 129.09, 131.18, 135.84, 136.86, 138.31, 146.58, 156.20, 167.45. ν_{max}(ATR)/cm^{-1} 1635, 1566, 1435, 1363, 1318, 1238, 1194, 1110, 823, 772. *m/z* (FAB) 407 [M + H] (100%), Acc. Mass (FAB) 407.2493 (100%). mp: 185–186 °C.

c) L$_6$: A round bottomed flask was charged with 2-(9-anthracenyl)-6-acetylpyridine (1.00 g, 3.36 mmol), 2,6-diisopropylaniline (0.715 g, 4.04 mmol, 1.2 eq.) and absolute ethanol (20 ml). A few drops of formic acid was added the mixture stirred and heated to 100 °C for 48 h. On cooling to -30 °C, **L$_6$** was obtained as yellow which was filtered and washed with cold absolute ethanol (0.800 g, 60%). δ_H (400 MHz, CDCl$_3$, SiMe$_4$); 1.16 (d, 6H, *J* = 6.7, CH*Me$_2$*), 1.20 (d, 6H, *J* = 6.6, CH*Me$_2$*), 2.17 (s, 3H, *Me*C=N), 2.85 (sept, 2H, *J* = 6.6, C*H*Me$_2$), 7.09 (t, 1H, *J* = 7.0, Ar*H*), 7.16 (d, 1H, *J* = 7.0, Ar*H*), 7.4–7.6 (m, 5H, Ar*H*), 7.60 (d,1H, *J* = 7.4, Ar*H*), 7.75 (d, 1H, *J* = 7.0, Ar*H*), 8.0 (m, 3H, Ar/Py*H*), 8.5 (d, 1H, J = 7.7, Py*H*), 8.60 (s, 1H, Ar*H*). δ_C (400 MHz, CDCl$_3$, SiMe$_4$); 22.94 (CH*Me$_2$*) 22.37 (CH*Me$_2$*), 28.29 (*C*HMe$_2$), 119.84, 123.01, 123.58, 125.34, 125.85, 126.17, 127.25, 127.73, 128.07, 128.17, 128.57, 130.14, 131,53, 131.71, 134.71, 135.14, 138.87, 136.62, 146.59, 156.82, 167.63. ν_{max}(ATR)/cm^{-1} 1640, 1580, 1564, 1455, 1428, 1364, 1299, 1110, 891, 815, 775. *m/z* (FAB) 457 [M + H] (100%), Acc. Mass (FAB) 457.2629 (100%). mp: 213–216 °C.

3.9.2 Synthesis of 3, 4

a) 3a: A solution of CuBr$_2$ (0.446 g, 2.00 mmol) in methanol (50 ml) was warmed to 40 ºC followed by the addition of 2,2′-bipy (0.361 g, 2.00 mmol, 1 eq.). The mixture was stirred for 10 min and 2,4-pentanedione (0.200 g, 2.00 mmol, 1 eq.) rapidly added. An aqueous solution of 2 M sodium hydroxide was added dropwise until the pH became 9 and the solution stirred for 30 min. The solution was concentrated under reduced pressure and slow evaporation of solvent gave **3a** as dark blue needles (0.500 g, 65%). Found: C, 43.80; H, 3.95; N, 6.63. C$_{15}$H$_{15}$N$_2$O$_2$CuBr·H$_2$O (416.76) requires: C, 43.31; H, 4.11; N, 6.71; v_{max} (ATR)/cm^{-1} 1581, 1510, 1426, 1320, 1265, 1238, 1216, 1211, 1140, 1120, 1073, 896, 768, 686, *m/z* (FAB) 397 (90%) [M + H], 318 (100%) [M - Br]; μ_{eff} = 1.79 BM; mp: 220–221 ºC.

b) 3b: Using a similar approach and molar ratio of reactants to that described for **3a**, the title complex was obtained as dark green needles from slow diffusion of hexane into a concentrated chloroform solution of **3b** (0.240 g, 29%). Found: C, 44.91; H, 3.66; N, 5.52. C$_{20}$H$_{17}$N$_2$O$_2$CuBr·1.5CH$_2$Cl$_2$ (588.21) requires: C, 44.90; H, 3.43; N, 4.83; v_{max} (ATR)/cm^{-1} 1654, 1540, 1512, 1430, 1213, 1196, 1150, 927, 856, 760, 725, 658; *m/z* (FAB) 461 (40%) [M + H], 381 (100%) [M - Br]; μ_{eff} = 1.72 BM; mp: 294–226 ºC.

c) 3c: Using a similar approach and molar ratio of reactants to that described for **3a**, the title complex was obtained as dark green needles (0.250 g, 17%). Found: C, 56.36; H, 4.16; N, 5.14. C$_{26}$H$_{23}$N$_2$O$_3$CuBr (554.92) requires: C, 56.27; H, 4.18; N, 5.05; v_{max} (ATR)/cm^{-1} 1592, 1545, 1511, 1370, 1308, 1200, 1176. 1030, 994, 780, 776, 728, 660, 605; *m/z* (FAB) 524 (80%) [M + H], 444 (100%) [M - Br]; μ_{eff} = 1.69 BM; mp: 234–235 ºC.

d) 4a: Using a similar approach and molar ratio of reactants to that described for **3a**, the title complex was obtained as blue blocks by slowly diffusing diethyl ether into a concentrated methanolic solution of **4a** (0.350 g, 41%). Found: C, 47.60; H, 4.18; N, 6.09. C$_{18}$H$_{19}$N$_2$O$_3$CuBr (454.61) requires: C, 47.54; H, 4.21; N, 6.16; v_{max} (ATR)/cm^{-1} 3414, 1585, 1518, 1429, 1410, 1381, 1273, 1018, 925, 855, 766, 722, 646; *m/z* (FAB) 421 (30%) [M + H], 342 (100%) [M - Br]; μ_{eff} = 1.72 BM; mp: 203–205 ºC.

e) 4b: Using a similar approach and molar ratio of reactants to that described for **3a**, the title complex was obtained as blue blocks by slowly diffusing diethyl ether into a concentrated methanolic solution of **4b** (0.320 g, 33%). Found: C, 53.47; H, 4.25; N, 5.43 C$_{23}$H$_{21}$N$_2$O$_3$CuBr (516.07) requires: C, 53.45; H, 4.10; N, 5.42; v_{max} (ATR)/cm^{-1} 3410, 1582, 1517, 1460, 1415, 1370, 1270, 910, 815, 760; *m/z* (FAB) 485 (20%) [M + H], 405 (100%) [M - Br]; μ_{eff} = 1.76 BM; mp: 220–225 ºC.

3.9.3 Synthesis of 5

a) 5a: to a solution of CuBr$_2$ (0.223 g, 1.00 mmol) in dichloromethane (10 ml) was added **L$_1$** (0.280 g, 1 mmol, 1 eq.) and the mixture stirred for 12 h. Sodium dibenzoylmethanato (0.369 g, 1.50 mmol, 1.5 eq.) was then added and the mixture stirred for a further 12 h at room temperature. The solvent was removed under reduced pressure and the resulting solid residue recrystallised by slowly diffusing hexane into a concentrated dichloromethane solution of **5a** giving green needles (0.240 g, 37%). Found: C, 63.22; H, 5.89; N, 4.06. C$_{34}$H$_{35}$N$_2$O$_2$CuBr (645.10) requires: C, 63.11; H, 5.45; N, 4.33; v_{max} (ATR)/cm^{-1} 2927, 2343, 1593, 1524, 1313, 1025, 833, 767, 744, 716 685 *m/z* (FAB) 646 (10%) [M + H], 566 (100%) [M - Br]; μ_{eff} = 1.90 BM; mp: 290–295 ºC.

b) 5b: Using a similar approach and molar ratio of reactants to that described for **5a**, the title complex was obtained as light green needles by slowly diffusing hexane into a concentrated dichloromethane solution of **5b** (0.024 g, < 10%). v_{max} (ATR)/cm^{-1} 2961, 1578, 1515, 1381, 1318, 1262, 1189, 1024, 936, 781, 743; *m/z* (FAB) 623 (60 %) [M + H]; μ_{eff} = 0.96 BM; mp: 301–309 ºC.

3.9.4 Synthesis of intermediate [(L$_1$)CuBr$_2$)]

a) [(L$_1$)CuBr$_2$)]: To a solution of CuBr$_2$ (0.223 g, 1.00 mmol) in dichloromethane (10 ml) was added **L$_1$** (0.280 g, 1 mmol, 1 eq.) and the mixture stirred for 12 h at room temperature. The solvent was removed under reduced pressure and the resulting solid residue recrystallised by slowly diffusing hexane into a concentrated dichloromethane solution giving [(**L$_1$**)CuBr$_2$)] as red needles (0.270 g, 57%). v_{max} (ATR)/cm^{-1} 1594, 1459, 1446, 1371, 1321, 1302, 1264, 1178, 1103, 1029, 814, 800, 782, 749; *m/z* (FAB) 423 (100%) [M - Br], 343 (40%) [M - 2Br]; μ_{eff} = 1.85 BM; mp: 256–259 ºC.

3.9.5 Synthesis of 6

a) 6a: A small Schlenk flask was charged with NiBr$_2$(DME) (0.081 g, 0.263 mmol) in a nitrogen filled glovebox. **L$_1$** (0.100 g, 0.263 mmol, 1 eq.) and dry, degassed dichloromethane were then added under nitrogen and the mixture stirred for 12 h at room temperature. Sodium acetylacetonate (0.064 g, 0.526 mmol, 2 eq.) was added under nitrogen and the mixture stirred for a further 12 h. After removal of the solvent under reduced pressure, the solid residue was recrystallised under an inert atmosphere using dry dichloromethane and dry petroleum ether to give **6a** as orange blocks (0.025 g, 40%). Found: C, 55.62; H, 6.09; N, 4.38. C$_{48}$H$_{62}$N$_2$O$_4$Ni$_2$Br$_2$ (1036.23) requires: C, 55.64; H, 6.03; N, 5.41; v_{max} (ATR)/cm^{-1} 1590, 1512, 1400, 1315, 1257, 1188, 1100, 1016, 919, 782, 756; *m/z* (FAB) 437 (100%) [1/2M - Br]; μ_{eff} = 3.98 BM; mp: >350 ºC.

b) 6b: Using a similar approach and molar ratio of reactants to that described for **6a**, the title complex was obtained as green blocks by slowly diffusing hexane into a concentrated dichloromethane solution of **6b** (0.100 g, 56%). Found: C, 57.15; H, 6.61; N, 5.03. C$_{26}$H$_{35}$N$_2$O$_2$NiBr (546.17) requires: C, 57.18; H, 6.46; N, 5.13; v_{max} (ATR)/cm^{-1} 2962, 1583, 1589, 1515, 1456, 1394, 1362, 1260, 1192, 1089, 1014, 924, 796, 766; *m/z* (FAB) 465 (100%) [M - Br], 366 (15%) [M - (Br + acac)]; μ_{eff} = 2.89 BM; mp: 225–227 ºC.

c) 6c: Using a similar approach and molar ratio of reactants to that described for **6a**, the title complex was obtained as green needles by slowly diffusing hexane into a concentrated dichloromethane solution of **6c** (0.110 g, 63%). Found: C, 57.75; H, 6.70; N, 4.90. $C_{27}H_{37}N_2O_2NiBr$ (560.19) requires: C, 57.89; H, 6.66; N, 5.00; v_{max} (ATR)/cm^{-1} 2962, 1588, 1517, 1394, 1362, 1262, 1017, 925, 793, 764; *m/z* (FAB) 480 (100%) [M - Br], 379 (15%) [M - (Br + acac)]; μ_{eff} = 2.84 BM; mp: 191–192 ºC.

6d: Using a similar approach and molar ratio of reactants to that described for **6a**, the title complex was obtained as green blocks by slowly diffusing hexane into a concentrated dichloromethane solution of **6d** (0.100 g, 60%); v_{max} (ATR)/cm^{-1} 1588, 1518, 1398, 1087, 1017, 790, 755, 679; *m/z* (FAB) 514 (100%) [M - Br], 414 (20%) [M - (Br + acac)]; μ_{eff} = 2.73 BM; mp: 227–230 ºC.

6e/6e′

a) 6e: Using a similar approach and molar ratio of reactants to that described for **6a**, the title complex was obtained as green blocks by slowly diffusing dry petroleum ether (b.p 40–60 °C) into a concentrated dichloromethane solution of **6e** (0.113 g, 82%). Found: C, 63.45; H, 5.96; N, 4.26. $C_{34}H_{37}N_2O_2NiBr$ (644.27) requires: C, 63.38; H, 5.79; N, 4.35; v_{max} (ATR)/cm^{-1} 3413, 1587, 1517; *m/z* (FAB) 563 (100%) [M - Br], 464 (20%) [M - (Br + acac)]; μ_{eff} = 2.32 BM; mp: 221–223 ºC.

b) 6e′: Following a similar approach and molar ratio of reactants to that described for **6a**, **6e′** was obtained as green blocks by slowly diffusing bench hexane into a concentrated dichloromethane solution of **6e** (0.125 g, 90%). Found: C, 62.29; H, 5.85; N; 4.06. $C_{34}H_{39}N_2O_3NiBr$ (662.28) requires: C, 61.66; H, 5.93; N, 4.23; v_{max} (ATR)/cm^{-1} 3414, 1581, 1524, 1392, 1255, 1017; *m/z* (FAB) 563 (100%) [M - OH$_2$], 464 (15%) [M - (OH$_2$ + acac)]; μ_{eff} = 2.75 BM; mp: 230–235 ºC.

3.9.6 Synthesis of intermediate [(L$_x$)NiBr$_2$]

a) [(L$_2$)NiBr$_2$]: **L$_2$** (0.100 g, 0.313 mmol), NiBr$_2$(DME) (0.096 g, 0.313 mmol, 1 eq.) and dry degassed dichloromethane (10 ml) were added to a small Schlenk flask under nitrogen and stirred for 12 h at room temperature. The solvent was removed under reduced pressure and the resulting solid recrystallised by slowly diffusing hexane into a concentrated solution of the title complex giving [(**L$_2$**)NiBr$_2$] as red blocks (0.100 g, 63%). Found: C, 47.93; H, 5.27; N, 5.20. $C_{22}H_{28}N_2NiBr_2$ (526.96) requires: C, 47.86; H, 5.30; N, 5.32; v_{max} (ATR)/cm^{-1} 1587, 1520, 1439, 1389, 1367, 1284, 1226, 1195, 1092, 1014, 773, 355; *m/z* (FAB) 447 (100%) [M - Br], 366 (30%) [M - 2Br]; μ_{eff} = 3.67 BM; mp: 317–318 ºC.

b) [(L$_4$)NiBr$_2$]: Using a similar approach and molar ratio of reactants to that described for [(**L$_2$**)NiBr$_2$], the title complex was obtained as green blocks by slowly diffusing hexane into a concentrated dichloromethane solution of [(**L$_4$**)NiBr$_2$] (0.070 g, 66%). Found: C, 52.29; H, 4.95; N, 4.82. $C_{25}H_{28}N_2NiBr_2$ (575.00) requires: C, 52.22; H, 4.91; N, 4.87; v_{max} (ATR)/cm^{-1} 1594, 1583, 1561, 1462, 1367, 1322, 1258; *m/z* (FAB) 495 (20%) [M - Br], 414 (100%) [M - 2Br]; μ_{eff} = 3.76 BM; mp: 325–329 ºC.

*c) [(**L₅**)NiBr₂]*: Using a similar approach and molar ratio of reactants to that described for [(**L₂**)NiBr₂], the title complex was obtained as green blocks by slowly diffusing hexane into a concentrated dichloromethane solution of [(**L₅**)NiBr₂] (0.079 g, 50%). Found: C, 55.72; H, 4.74; N, 5.54. $C_{29}H_{30}N_2NiBr_2$ (625.05) requires: C, 52.72; H, 4.84; N, 4.48; v_{max} (ATR)/cm^{-1} 1587, 1256, 1462, 756; *m/z* (FAB) 545 (20%) [M - Br], 465 (60%) [M - 2Br]; μ_{eff} = 3.79 BM; mp: 297–300 ºC.

*d) [(**L₆**)NiBr₂]*: Using a similar approach and molar ratio of reactants to that described for [(**L₂**)NiBr₂], the title complex was obtained as green blocks by slowly diffusing hexane into a concentrated dichloromethane solution of [(**L₆**)NiBr₂] (0.055 g, 71%). Found: C, 53.66; H, 3.82; N, 3.05. $C_{29}H_{30}N_2NiBr_2 \cdot CH_2Cl_2$ (710.00) requires: C, 53.71; H, 4.51; N, 3.68; v_{max} (ATR)/cm^{-1} 3334, 3922, 1521; *m/z* (FAB) 595 (70%) [M - Br], 515 (100%) [M - 2Br]; μ_{eff} = 3.82 BM; mp: >350 ºC.

3.9.7 Synthesis of 7

a) 7a: **L₁** (0.100 g, 0.355 mmol), CoBr₂ (0.096 g, 0.355 mmol, 1 eq.) and dry, degassed dichloromethane were added to a small Schlenk flask under nitrogen and the mixture was stirred for 12 h at room temperature. Sodium acetylacetonate (0.076 g, 0.710 mmol, 2 eq.) was added under nitrogen and the mixture stirred for a further 12 h. After removal of the solvent under reduced pressure, the solid residue was recrystallised by slowly diffusing dry hexane into a dry dichloromethane solution of **7a** to give red blocks (0.160 g, 88%). Found: C, 56.03; H, 6.12; N, 5.55. $C_{24}H_{31}N_2O_2CoBr$ (518.35) requires: C, 56.61; H, 6.03; N, 5.40; v_{max} (ATR)/cm^{-1} 3410, 1636, 1584, 1512, 1435, 1257, 1101, 1014, 920, 773, 743; *m/z* (FAB) 438 (100%) [M - Br]; 337 (5%) [M - (Br + acac)]; μ_{eff} = 3.89 BM; mp: 294–295 ºC.

b) 7b: Using a similar approach and molar ratio of reactants to that described for **7a**, the title complex was obtained as red needles by slowly by slowly diffusing hexane into a concentrated dichloromethane solution of **7b** (0.150 g, 85%). Found: C, 57.23; H, 6.38; N, 5.06. $C_{26}H_{35}N_2O_2CoBr$ (546.41) requires: C, 57.15; H, 6.46; N, 5.13; v_{max} (ATR)/cm^{-1} 3061, 1565, 1519, 1459, 1380, 1363, 1260, 1194, 1093, 921, 821, 801, 774, 728, 682; *m/z* (FAB) 466 (100%) [M - Br]; μ_{eff} = 3.80 BM; mp: 212–213 ºC.

c) 7c: Using a similar approach and molar ratio of reactants to that described for **7a**, the title complex was obtained as red blocks by slowly diffusing hexane into a concentrated dichloromethane solution of **7c** (0.150 g, 85%). Found: C, 61.00; H, 6.94; N, 5.08. $C_{27}H_{37}N_2O_2CoBr$ (560.43) requires: C, 60.86; H, 6.65; N, 5.00; v_{max} (ATR)/cm^{-1} 3063, 1590, 1517, 1361, 1028, 766; *m/z* (FAB) 480 (100%) [M - Br]; μ_{eff} = 3.75 BM; mp: 209–210 ºC.

d) 7d: Using a similar approach and molar ratio of reactants to that described for **7a**, the title complex was obtained as red needles by slowly diffusing hexane into a concentrated dichloromethane solution of **7d** (0.100 g, 62%). Found: C, 53.41; H, 4.80; N, 3.69. $C_{30}H_{35}N_2O_2CoBr$ (594.45) requires: C, 53.41; H, 5.13; N, 3.88; v_{max} (ATR)/cm^{-1} 3409, 1642, 1616, 1577, 1511, 1457, 1260, 1192, 1057, 926, 819, 764, 710, 762, 679; *m/z* (FAB) 513 (100%) [M - Br], 415 (20%) [M - (Br + acac)]; μ_{eff} = 4.21 BM; mp: 225–227 ºC.

3.9.8 Synthesis of intermediate [(L$_x$)CoBr$_2$]

a) [(L$_2$)CoBr$_2$]: **L$_2$** (0.100 g, 0.313 mmol), CoBr$_2$ (0.096 g, 0.313 mmol, 1 eq.) and dry degassed dichloromethane (10 ml) were added to a small Schlenk flask under nitrogen and stirred for 12 h at room temperature. The solvent was removed under reduced pressure and the resulting solid recrystallised by slowly diffusing hexane into a concentrated solution of the title complex giving [(L$_2$)CoBr$_2$] as red blocks (0.100 g, 63%). Found: C, 48.00; H, 5.46; N, 5.17. C$_{21}$H$_{28}$N$_2$CoBr$_2$ (527.20) requires: C, 47.84; H, 5.35; N, 5.31; v_{max} (ATR)/cm^{-1} 1593, 1459, 1374, 1282, 1020, 795, 777; *m/z* (FAB) 446 (100%) [M - Br]; μ_{eff} = 3.60 BM; mp: 318–320 ºC.

b) [(L$_3$)CoBr$_2$]: Using a similar approach and molar ratio of reactants to that described for [(L$_2$)CoBr$_2$], the title complex was obtained as red blocks by slowly diffusing hexane into a concentrated dichloromethane solution of [(L$_3$)CoBr$_2$] (0.075 g, 70%). Found: C, 45.53; H, 5.32; N, 4.62. C$_{22}$H$_{30}$N$_2$CoBr$_2$·CH$_2$Cl$_2$ (626.16) requires: C, 44.12; H, 5.15; N, 4.47; v_{max} (ATR)/cm^{-1} 1586, 1457, 1367, 1310, 1195, 1056, 1016, 816, 768, 749; *m/z* (FAB) 460 (50%) [M - Br]; μ_{eff} = 3.28 BM; mp: 301–302 ºC.

c) [(L$_4$)CoBr$_2$]: Using a similar approach and molar ratio of reactants to that described for [(L$_2$)CoBr$_2$], the title complex was obtained as orange blocks by slowly diffusing hexane into a concentrated dichloromethane solution of [(L$_4$)CoBr$_2$] (0.100 g, 62%). Found: C, 52.13; H, 4.86; N, 4.84. C$_{25}$H$_{28}$N$_2$CoBr$_2$ (575.24) requires: C, 52.20; H, 4.91; N, 4.87; v_{max} (ATR)/cm^{-1} 1592 1561, 1451, 1368, 1321, 1255, 1096, 1010, 858, 809 765, 699, 657; *m/z* (FAB) 494 (20%) [M - Br], 413 (20%) [M - 2Br]; μ_{eff} = 3.32 BM; mp: 321–322 ºC.

d) [(L$_5$)CoBr$_2$]: Using a similar approach and molar ratio of reactants to that described for [(L$_2$)CoBr$_2$], the title complex was obtained as green needles by slowly evaporating a concentrated acetonitrile solution of [(L$_5$)CoBr$_2$] (0.120 g, 80%). Found: C, 55.56; H, 4.74; N, 4.42. C$_{29}$H$_{30}$N$_2$CoBr$_2$ (625.30) requires: C, 55.70; H, 4.84; N, 4.48; v_{max} (ATR)/cm^{-1} 1586, 1256, 1465, 773; *m/z* (FAB) 544 (100%) [M - Br], 462 (20%) [M - 2Br]; μ_{eff} = 4.22 BM; mp: 293–294 ºC.

e) [(L$_6$)CoBr$_2$]: Using a similar approach and molar ratio of reactants to that described for [(L$_2$)CoBr$_2$], the title complex was obtained as green needles by slowly diffusing hexane into a concentrated dichloromethane solution of [(L$_6$)CoBr$_2$] (0.060 g, 30%). Found: C, 58.49; H, 4.54; N, 4.38. C$_{29}$H$_{30}$N$_2$CoBr$_2$ (675.36) requires: C, 58.69; H, 4.25; N, 4.78; v_{max} (ATR)/cm^{-1} 1639, 1582, 1511, 1259, 797; *m/z* (FAB) 596 (100%) [M - Br]; μ_{eff} = 3.98 BM; mp: 310–312 ºC.

3.9.9 Attempted synthesis of [(L$_x$)MBr(dbm)] [M = Ni, Co]; characterisation of 8 and 9

a) 8a: A small Schlenk flask was charged with NiBr$_2$(DME) (0.081 g, 0.263 mmol) in a nitrogen filled glovebox. **L$_2$** (0.100 g, 0.263 mmol, 1 eq.) and dry, degassed dichloromethane were then added under nitrogen and the mixture stirred for 12 h at room temperature. Sodium dibenzoylmethanato (0.290 g, 0.562 mmol, 2 eq.) was added under nitrogen and the mixture stirred for a further 12 h. The solvent was removed under reduced pressure giving a green powder (0.231 g, 90%). The solid residue was recrystallised by slow vaporation of a dichloromethane solution of **8a** giving green needles (0.190 g 79%). Found: C, 67.92; H, 3.33; N, 2.86. C$_{51}$H$_{50}$N$_2$O$_4$Ni (813.65) requires: C, 67.98; H, 3.74; N, 3.05; ν_{max} (ATR)/cm^{-1} 2853, 1587, 1458, 1410, 1377; *m/z* (FAB) 815 (15%) [M + H], 589 (100%) [M - dbm], 366 (20%) [M - 2dbm]; μ_{eff} = 2.91 BM; mp: 108–113 ºC.

b) 8b: using a similar approach and molar ratio of reactants to that described for **8a**, the title complex was obtained as a green powder (0.098 g, 67%). By slowly diffusing hexane into a concentrated dichloromethane solution of the powder, yellow needles **8b** were obtained (0.060, 38%). Found: C, 75.60; H, 6.30; N, 2.96. C$_{52}$H$_{52}$N$_2$O$_4$Ni (827.67) requires: C, 75.28; H, 6.56; N, 3.18; ν_{max} (ATR)/cm^{-1} 2853, 1589, 1461, 1415, 1379; *m/z* (FAB) 829 (10%) [M + H], 604 (100%) [M - dbm], 381 (20%) [M - 2dbm]; μ_{eff} = 2.46 BM; mp: 234–240 ºC.

c) 8c: Using a similar approach and molar ratio of reactants to that described for **8a**, the title complex was obtained as a green powder (0.150 g, 61%). By slowly diffusing hexane into a concentrated dichloromethane solution of the powder, green blocks of **8c** were obtained (0.060 g, 38%). Found: C, 72.97; H, 5.76; N, 3.59. C$_{59}$H$_{53}$N$_2$O$_4$Ni·CH$_2$Cl$_2$ (996.68) requires: C, 72.29; H, 5.46; N, 3.81; ν_{max} (ATR)/cm^{-1} 2957, 1587, 1544; *m/z* (FAB) 998 (10%) [M + H], 687 (100%) [M - dbm], 465 (20%) [M - 2dbm]; μ_{eff} = 2.10 BM; mp: 254–256 ºC.

d) 9a: A small Schlenk flask was charged with CoBr$_2$ (0.096 g, 0.313 mmol) in a nitrogen filled glovebox. **L$_2$** (0.100 g, 0.313 mmol, 1 eq.) and dry, degassed dichloromethane were then added under nitrogen and the mixture stirred for 12 h at room temperature. Sodium dibenzoylmethanato (0.152 g, 0.626 mmol, 2 eq.) was added under nitrogen and the mixture stirred for a further 12 h. The solvent was removed under reduced pressure giving **9a** as a red powder. The solid residue was recrystallised by slow evaporation of a dichloromethane solution of **9a** to give the title complex as orange needles (0.190 g 79%). ν_{max} (ATR)/cm^{-1} 2853, 1587, 1458, 1410, 1377; *m/z* (FAB) 815 (15%) [M + H], 589 (100%) [M - dbm], 366 (20%) [M - 2dbm]; μ_{eff} = 2.91 BM; mp: 108–113 ºC.

e) 9b: Using a similar approach and molar ratio of reactants to that described for **9a**, the title complex was obtained as a yellow powder (0.098 g, 67%). By slowly diffusing hexane into a concentrated dichloromethane solution of the powder, yellow needles of **9b** were obtained. (0.060, 38%); ν_{max} (ATR)/cm^{-1} 2853, 1589, 1461, 1415, 1379; *m/z* (FAB) 829 (10%) [M + H], 604 (100%) [M - dbm], 381 (20%) [M - 2dbm]; μ_{eff} = 2.46 BM; mp: 234–240 ºC.

g) 9c: Using a similar approach and molar ratio of reactants to that described for **9a**, the title complex was obtained as a yellow powder (0.133 g, 77%). By slowly diffusing hexane into a concentrated dichloromethane solution of the powder, yellow needles of **9c** were obtained (0.040 g, 20%). Found: C, 77.93; H, 5.68; N; 3.19. $C_{59}H_{52}N_2O_4Co$ (911.99) requires: C, 77.70; H, 5.75; N, 3.07; v_{max} (ATR)/cm^{-1} 2961, 1592, 1542, 1513, 1260, 773; *m/z* (FAB) 913 (5%) [M + H], 688 (100%) [M - dbm]; μ_{eff} = 3.46 BM; mp: >350 °C.

3.9.10 Synthesis of 10 and 11

a) 10: **L₂** (0.100 g, 0.313 mmol), FeBr₂ (0.067 g, 0.313 mmol, 1 eq.) and dry, degassed dichloromethane were added to a small Schlenk flask under nitrogen and the mixture stirred for 12 h at room temperature. Sodium acetylacetonate (0.075 g, 0.626 mmol, 2 eq.) was added under nitrogen and the mixture stirred for a further 12 h. After removal of the solvent under reduced pressure, the solid residue was recrystallised by slowly diffusing dry hexane into a dry dichloromethane solution of **10** under an inert nitrogen atmosphere to give red blocks (0.40 g, 23%). Found: C, 54.12; H, 6.11; N, 4.63. $C_{26}H_{35}N_2O_2FeBr$ (543.32) requires: C, 54.38; H, 6.11; N, 4.79; v_{max} (ATR)/cm^{-1} 1579, 1517, 1436, 1366, 1308, 1281, 1193, 1108, 1051, 1014. 921, 800, 774; *m/z* (FAB) 463 (100%) [M - Br]; μ_{eff} = 5.03 BM; mp: 282–283 °C.

b) 11: **L₂** (0.100 g, 0.313 mmol), MnBr₂ (0.066 g, 0.313 mmol, 1 eq.) and dry, degassed dichloromethane were added to a small Schlenk flask under nitrogen and the mixture stirred for 12 h at room temperature. Sodium acetylacetonate (0.074 g, 0.626 mmol, 2 eq.) was added under nitrogen and the mixture stirred for a further 12 h. After removal of the solvent under reduced pressure, the solid residue was recrystallised by slowly diffusing dry hexane into a dry dichloromethane solution of **11** under an inert nitrogen atmosphere to give yellow needles (0.55 g, 32%). Found: C, 57.48; H, 6.51; N, 5.06. $C_{26}H_{35}N_2O_2MnBr$ (542.41) requires: C, 57.57; H, 6.50; N, 5.16; v_{max} (ATR)/cm^{-1} 3412, 1585, 1510, 1457, 1436, 1394, 1256, 1089, 1193, 1014. 918, 820, 795, 765; *m/z* (FAB) 461 (10%) [M - Br]; μ_{eff} = 5.72 BM; mp: 250–255 °C.

3.9.11 Synthesis of intermediate [(L₂)MBr₂] (M = Fe, Mn)

a) [(L₂)FeBr₂]: **L₂** (0.100 g, 0.313 mmol), FeBr₂ (0.067 g, 0.313 mmol, 1 eq.) and dry degassed dichloromethane (10 ml) were added to a small Schlenk flask under nitrogen and stirred for 12 h at room temperature. The solvent was removed under reduced pressure and the resulting solid recrystallised by slowly diffusing dry hexane into a concentrated dry dichloromethane solution containing the complex in an intert atmosphere of nitrogen, giving red blocks (0.25 g, 14%). Found: C, 47.99; H, 5.34; N, 5.28. $C_{21}H_{28}N_2FeBr_2$ (524.11) requires: C, 48.12; H, 5.38; N, 5.34; v_{max} (ATR)/cm^{-1} 1569, 1519, 1418, 1322, 1260, 1085, 1015, 793, 751; *m/z* (FAB) 443 (100%) [M - Br]; μ_{eff} = 4.90 BM; mp: 258–260 °C.

b) [(L₂)MnBr₂]: **L₂** (0.100 g, 0.313 mmol), MnBr₂ (0.066 g, 0.313 mmol, 1 eq.) and dry degassed dichloromethane (10 ml) were added to a small Schlenk flask under nitrogen and stirred for 12 h at room temperature. The solvent was removed under reduced pressure and the resulting solid recrystallised by slowly diffusing hexane into a concentrated dichloromethane solution containing the complex giving yellow blocks (0.35 g, 20%). Found: C, 46.85; H, 5.47; N, 5.55. $C_{21}H_{28}N_2MnBr_2$ (538.14) requires: C, 46.88; H, 5.28; N, 5.15; ν_{max} (ATR)/cm^{-1} 1584, 1458, 1437, 1361, 1261, 1240, 1192, 1098, 1016, 935, 813. 794, 752, 701; *m/z* (FAB) 442 (100%) [M - Br]; μ_{eff} = 5.31 BM; mp: 222–225 °C.

3.9.12 Attempted synthesis of [(L$_x$)NiBr(chp)]; characterisation of 12

a) 12a: A small Schlenk flask was charged with NiBr₂(DME) (0.081 g, 0.263 mmol) in a nitrogen filled glovebox. **L₂** (0.100 g, 0.263 mmol, 1 eq.) and dry degassed dichloromethane were then added under nitrogen and the mixture stirred for 12 h at room temperature. Sodium 6-chloropyridonate (0.067 g, 0.522 mmol, 2 eq.) was added under nitrogen and the mixture stirred for a further 12 h. After removal of the solvent under reduced pressure, the solid residue was recrystallised by slowly diffusing hexane into a concentrated dichloromethane solution of the complex to give green blocks (0.120 g, 74%). Found: C, 59.66; H, 5.39; N, 9.07. $C_{31}H_{34}N_2O_4Cl_2Ni$ (624.23) requires: C, 59.65; H, 5.49; N, 8.98; ν_{max} (ATR)/cm^{-1} 3549, 3473, 3410, 1635, 1598, 1259, 1159, 1091, 1015, 993, 919 779; 731, 694; *m/z* (FAB) 647 (5%) [M + Na], 494 (100%) [M - chp] 365 (50%) [M - 2chp]; μ_{eff} = 2.81 BM; mp: >350 °C.

b) 12b: Using a similar approach and molar ratio of reactants to that described for **12a**, the title complex was obtained as green needles by slowly diffusing hexane into a concentrated dichloromethane solution of **12b** (0.125 g, 80%). Found: C, 60.11; H, 5.74; N, 8.82. $C_{32}H_{36}N_2O_2NiBr$ (638.25) requires: C, 60.22; H, 5.96; N, 8.78; ν_{max} (ATR)/cm^{-1} 3551, 3411, 1599, 1533, 1463, 1362, 1259, 1162, 1092, 995, 916, 972, 726, 690; *m/z* (FAB) 508 (100%) [M - chp], 377 (90%) [M - 2chp]; μ_{eff} = 2.92 BM; mp: >350 °C.

3.9.13 Attempted synthesis of [(L$_x$)NiBr(OCPh)]; characterisation of 13 and 14

a) 13a: A small Schlenk flask was charged with NiBr₂(DME) (0.081 g, 0.263 mmol) in a nitrogen filled glovebox. **L₂** (0.100 g, 0.263 mmol, 1 eq.) and dry, degassed dichloromethane were then added under nitrogen and the mixture was stirred for 12 h at room temperature. Sodium benzoate (0.037 g, 0.522 mmol, 2 eq.) was added under nitrogen and the mixture stirred for a further 12 h. After removal of the solvent under reduced pressure, the solid residue was recrystallised by slowly diffusing hexane into a concentrated dichloromethane solution of **13a** to give green blocks (0.100 g, 33%). Found: C, 63.08; H, 4.57; N, 2.99. $C_{84}H_{86}Ni_3N_4O_{12} \cdot CH_2Cl_2$ (1604.61) requires: C, 63.62; H, 5.53; N, 3.54; ν_{max} (ATR)/cm^{-1} 3413, 1612, 1572, 1533, 1396, 1259, 1089, 1024, 796, 712, 679; *m/z* (FAB) 487 (90%) [Ni(**L₂**)(O₂CPh], 366 (90%) [Ni(**L₂**)]. *m/z* (TOF) 1516 (50%) [M⁺], 1397 (20%) [M - (O₂CPh)]; μ_{eff} = 4.19 BM; mp: >350 °C.

b) 13b: Using a similar approach and molar ratio of reactants to that described for **13a**, the title complex was obtained as green blocks by slowly diffusing hexane into a concentrated dichloromethane solution of **13b** (0.90 g, 60%). Found: C, 66.17; H, 5.68; N, 3.47. $C_{86}H_{90}N_4 Ni_3O_{12}$ (1547.73) requires: C, 66.74; H, 5.86; N, 3.62; v_{max} (ATR)/cm^{-1} 3551, 3411, 1599, 1533, 1463, 1362, 1259, 1162, 1092, 995, 916, 972, 726, 690; *m/z* (TOF) 1547 (10%) [M$^+$], 1525 (10%) [M - (O$_2$CPh)]; μ_{eff} = 3.97 BM; mp: >350 °C.

c) 14 Using a similar approach and molar ratio of reactants to that described for **13a**, the title complex was obtained as green blocks by slow evaporation of a concentrated methanolic solution of **14** (0.56 g, 30%). Found: C, 63.07; H, 6.37; N, 3.56. $C_{38}H_{46}N_2O_4Cl_2Ni$ (740.38) requires: C, 63.05; H, 6.38; N, 3.90; v_{max} (ATR)/cm^{-1} 2964, 1594, 15733, 1532, 1422, 1378, 1259, 1050, 1039, 1023 858, 817, 792, 716, 679; *m/z* (FAB) 501 (100%) [M - (O$_2$CPh)]; μ_{eff} = 3.11 BM; mp: >270–275 °C.

3.10 X-ray crystallography

Crystallographic data analysis was carried out in collaboration with K. Singh (Department of Chemistry, University of Leicester). Data for **L₂**, **L₄**, **L₅**, **L₆**, **3a**, **3b**, **3c**, **4a**, **4b**, **5a**, **5b**, **6a**, **6b**, **6c**, **6d**, **7a**, **7b**, **7d**, **7e**, **10**, **11**, **12a**, **12b**, **13a**, **13b** and **14** were collected on a Bruker APEX 2000 CCD diffractometer. Details of data collection, refinement and crystal data are listed in Tables 3.14 to 3.22. All data were collected using a graphite monochromated Mo-Kα radiation (λ = 0.7107 Å) and the reflections were corrected for Lorentz, polarisation and absorption effects. The structures were solved by full-matrix least squares on F^2 using SHELXTL version 6.10.[87] Carbon bonded hydrogen atoms were included in calculated positions (C–H = 0.96 Å) with isotropic displacement parameters set to 1.2 Ueq(C). Non-hydrogen atoms were refined with anisotropic displacement parameters. Disordered solvent molecules were removed from the unit cells of **3b** (methanol/water), **4b** (methanol), **5a** (dichloromethane), **11a** (hexane), **13a** (dichloromethane/hexane) using the SQUEEZE option in PLATON.[88]

Table 3.14 Structural parameters for **L$_2$**, **L$_4$**, **L$_5$** and **L$_6$**.

Compound	L$_2$	L$_4$	L$_5$	L$_6$
Singh code	09069	10036	10127	10124
Formula	C$_{21}$H$_{28}$N$_2$	C$_{25}$H$_{28}$N$_2$	C$_{29}$H$_{30}$N$_2$	C$_{33}$H$_{32}$N$_2$
Mc	308.45	356.49	406.55	456.61
Crystal size (mm)	$0.39 \times 0.28 \times 0.14$	$0.38 \times 0.20 \times 0.10$	$0.26 \times 0.22 \times 0.19$	$0.38 \times 0.20 \times 0.10$
Temperature (K)	150(2)	150(2)	150(2)	150(2)
Crystal system	Triclinic	Monoclinic	Monoclinic	Monoclinic
Space group	P-1	$C2/x$	$P2(1)/c$	$P2(1)/c$
Lattice parameters				
a (Å)	8.500(4)	21.635(15)	11.490(9)	8.310(2)
b (Å)	11.670(5)	11.519(6)	13.214(9)	27.538(8)
c (Å)	19.328(9)	16.471(9)	15.214(10)	16.471(9)
α (°)	82.067(9)	90	90	90
β (°)	84.957(9)	113.152(17)	95.243(13)	98.424(7)
γ (°)	81.965(9)	90	90	90
U (Å^3)	1875.6(15)	4123(4)	2300(3)	2506(9)
Z	4	8	4	4
D_c (Mg/m^3)	1.092	1.149	1.174	1.210
F(000)	672	1356	872	976
μ (Mo-K$_\alpha$)	0.064	0.067	0.068	0.070
Reflections collected	13551	14413	16270	18092
R(int)	0.0586	0.1260	0.2956	0.886
Independent reflections	6532	3632	3632	4410
Restraints /parameters	0/437	0/249	0/285	0/321
R_1; wR_2[I>2σ(I)]	$R_1 = 0.0749$, $wR_2 = 0.1898$	$R_1 = 0.0637$, $wR_2 = 0.1475$	$R_1 = 0.0754$, $wR_2 = 0.1433$	$R_1 = 0.0772$, $wR_2 = 0.1403$
R_1; wR_2 (all data)	$R_1 = 0.1158$, $wR_2 = 0.2121$	$R_1 = 0.1008$, $wR_2 = 0.1641$	$R_1 = 0.1283$, $wR_2 = 0.1703$	$R_1 = 0.1966$, $wR_2 = 0.1738$
Goodness of fit on F^2 (all data)	1.034	0.988	0.929	0.894

Table 3.15. Crystallographic parameters for **3** and **4**.

Compound	3a	3b	3c	4a	4b
Singh code	08050	08058	08029	08026	08053
Formula	$C_{15}H_{17}BrCuN_2O_3$	$C_{21}H_{23}BrCuN_2O_4$	$C_{26}H_{23}BrCuN_2O_3$	$C_{18}H_{19}BrCuN_1O_3$	$C_{23}H_{31}BrCuN_2O_3$
Mc	416.76	510.86	554.91	454.80	515.87
Crystal size (mm)	$0.26 \times 0.15 \times 0.05$	$0.22 \times 0.18 \times 0.06$	$0.30 \times 0.18 \times 0.13$	$0.21 \times 0.19 \times 0.12$	$0.24 \times 0.16 \times 0.07$
Temperature (K)	150(2)	150(2)	150(2)	150(2)	150(2)
Crystal system	Triclinic	Triclinic	Orthorhombic	Triclinic	Monoclinic
Space group	P-1	P-1	$Pbca$	P-1	$P2(1)/n$
Lattice parameters					
a (Å)	13.605(2)	9.075(6)	13.436(3)	8.9809(16)	12.022(3)
b (Å)	14.673(3)	9.6187(6)	17.505(4)	9.0730(16)	13.790(3)
c (Å)	16.790(3)	12.797(8)	19.801(5)	12.193(2)	13.482(3)
α (°)	86.665(3)	73.334(11)	90	98.255(3)	90
β (°)	73.844(3)	70.896(10)	90	102.699(3)	112.976(4)
γ (°)	87.051(3)	74.254(11)	90	105.642(3)	90
U (Å^3)	3211.8(9)	998.6(11)	4657(2)	911.5(3)	2059.3(8)
Z	8	2	8	2	4
D_c (Mg/m^3)	1.724	1.699	1.583	1.657	1.667
$F(000)$	1672	518	2248	458	1044
μ (Mo-K$_\alpha$)	3.861	3.126	2.685	3.409	3.029
Reflections collected	25310	3870	34807	7114	4042
R(int)	0.0579	0.0000	0.0680	0.0285	0.0000
Independent reflections	12463	3870	4588	3427	4042
Restraints /parameters	0/809	0/174	0/300	0/229	0/254
R_1; $wR_2[I>2\sigma(I)]$	$R_1 = 0.0440$, $wR_2 = 0.0708$	$R_1 = 0.1011$, $wR_2 = 0.2481$	$R_1 = 0.0409$, $wR_2 = 0.0749$	$R_1 = 0.0359$, $wR_2 = 0.0902$	$R_1 = 0.0318$, $wR_2 = 0.0701$
R_1; wR_2 (all data)	$R_1 = 0.0795$, $wR_2 = 0.0786$	$R_1 = 0.1361$, $wR_2 = 0.2676$	$R_1 = 0.0598$, $wR_2 = 0.0800$	$R_1 = 0.0442$, $wR_2 = 0.0938$	$R_1 = 0.0411$, $wR_2 = 0.0721$
Goodness of fit on F^2 (all data)	0.827	1.067	1.029	0.998	0.945

Table 3.16 Crystallographic parameters for **5**.

Compound	5a	5b
Singh code	10043	10079
Formula	$C_{36}H_{39}BrCl_4CuN_2O_2$	$C_{49}H_{62}Br_4Cu\ N_4O_4$
Mc	816.94	13332.82
Crystal size (mm)	$0.17 \times 0.14 \times 0.05$	$0.18 \times 0.10 \times 0.07$
Temperature (K)	150(2)	150(2)
Crystal system	Monoclinic	Triclinic
Space group	$P2(1)/c$	P-1
Lattice parameters		
a (Å)	14.370(3)	8.461(4)
b (Å)	15.429(3)	16.880(7)
c (Å)	16.724(3)	19.068(8)
α (°)	90	78.593(11)
β (°)	106.865(4)	82.291(8)
γ (°)	90	89.552(10)
U (Å^3)	3548.5(11)	2645(2)
Z	4	2
D_c (Mg/m^3)	1.529	1.674
$F(000)$	1668	1332
μ (Mo-K$_\alpha$)	2.078	4.652
Reflections collected	27256	19408
R(int)	0.2919	0.4617
Independent reflections	6951	9210
Parameters/restraints	0/361	0/525
R_1; $wR_2[I>2\sigma(I)]$	$R_1 = 0.0797$, $wR_2 = 0.1644$	$R_1 = 0.1480$, $wR_2 = 0.3163$
R_1; wR_2 (all data)	$R_1 = 0.2076$, $wR_2 = 0.1951$	$R_1 = 0.2861$, $wR_2 = 0.4034$
Goodness of fit on F^2 (all data)	0.803	0.921

Table 3.17 Crystallographic parameters for **6**.

Compound	6a	6b	6c	6d
Singh code	11001	09003	09006	10101
Formula	$C_{50}H_{66}Br_2Cl_4Ni_2N_4O_4$	$C_{26}H_{35}BrN_2NiO_2$	$C_{28}H_{39}BrCl_2N_2NiO_2$	$C_{31}H_{37}BrCl_2N_2NiO_2$
Mc	1206.11	546.18	645.13	679.15
Crystal size (mm)	$0.14 \times 0.10 \times 0.02$	$0.41 \times 0.22 \times 0.19$	$0.31 \times 0.06 \times 0.05$	$0.40 \times 0.22 \times 0.18$
Temperature (K)	150(2)	150(2)	150(2)	150(2)
Crystal system	Triclinic	Monoclinic	Tetragonal	Monoclinic
Space group	P-1	$P2(1)/n$	$I4(1)/a$	$P2(1)/c$
Lattice parameters				
a (Å)	9.368(3)	11.920(4)	36.550(6)	11.764(4)
b (Å)	12.190(4)	15.660(5)	36.550(6)	28.583(11)
c (Å)	13.189(4)	13.860(4)	9.001(2)	9.941(4)
α (°)	108.571(6)	90	90	90
β (°)	92.341(8)	94.515(5)	90	109.077(6)
γ (°)	105.609(6)	90	90	90
U (Å^3)	1361.7(7)	2579.2(13)	12025(4)	3159(2)
Z	1	4	16	4
D_c (Mg/m^3)	1.471	1.407	1.425	1.428
$F(000)$	600	1163	5344	1400
μ (Mo-K$_\alpha$)	2.400	2.326	2.179	2.078
Reflections collected	7176	19566	45677	24401
R(int)	0.211	0.0456	0.4344	0.0471
Independent reflections	5263	5055	5894	6205
Parameters/restraints	0/305	0/297	0/334	0/359
R_1; $wR_2[I>2\sigma(I)]$	$R_1 = 0.1260$, $wR_2 = 0.2835$	$R_1 = 0.0303$, $wR_2 = 0.0664$	$R_1 = 0.0918$, $wR_2 = 0.1455$	$R_1 = 0.0339$, $wR_2 = 0.0704$
R_1; wR_2 (all data)	$R_1 = 0.2191$, $wR_2 = 0.3542$	$R_1 = 0.0428$, $wR_2 = 0.0689$	$R_1 = 0.1996$, $wR_2 = 0.1796$	$R_1 = 0.0469$, $wR_2 = 0.0733$
Goodness of fit on F^2 (all data)	0.952	0.930	0.920	0.967

Table 3.18 Crystallographic parameters for **7**.

Compound	7a	7b	7c	7d	7e
Singh code	10219	08091	08090	10018	10149
Formula	$C_{24}H_{31}BrCoN_2O_2$	$C_{26}H_{35}BrCoN_2O_2$	$C_{27}H_{37}B_2CoN_2O_2$	$C_{31}H_{37}BrCoN_2O_2$	$C_{36}H_{41}BrCl_4CoN_2O_2$
Mc	518.35	546.40	560.43	679.37	814.35
Crystal size (mm)	$0.22 \times 0.17 \times 0.08$	$0.33 \times 0.25 \times 0.07$	$0.27 \times 0.13 \times 0.08$	$0.32 \times 0.18 \times 0.14$	$0.14 \times 0.09 \times 0.04$
Temperature (K)	150(2)	150(2)	150(2)	150(2)	150(2)
Crystal system	Moniclinic	Monoclinic	Monoclinic	Monoclinic	Monoclinic
Space group	$P2(1)/n$	$P2(1)/n$	$P2(1)/c$	$P2(1)/c$	$P2(1)/n$
Lattice parameters					
a (Å)	12.112(3)	11.966(6)	16.134(12)	11.805(8)	10.930(9)
b (Å)	15.632(4)	15.627(8)	10.531(8)	28.66(2)	17.165(15)
c (Å)	13.213(3)	13.903(7)	16.591(13)	9.956(7)	20.086(18)
α (°)	90	90	90	90	90
β (°)	92.704(5)	93.268(9)	102.635	108.932(14)	93.20(3)
γ (°)	90	90	90	90	90
U (Å^3)	2496.4(11)	2594(2)	4830(8)	3186(4)	3763(6)
Z	4	4	8	4	4
D_c (Mg/m^3)	1.379	1.399	1.353	1.416	1.438
$F(000)$	1068	1132	1164	1396	1668
μ (Mo-K$_\alpha$)	2.309	2.226	2.101	1.990	1.836
Reflections collected	8727	19808	20663	24759	29372
R(int)	0.0474	0.1601	0.1379	0.1754	0.7440
Independent reflections	4896	5093	5379	6263	7396
Parameters/restraints	0/278	0/297	0/307	0/359	0/397
R_1; $wR_2[I>2\sigma(I)]$	$R_1 = 0.0666, wR_2 = 0.1199$	$R_1 = 0.0637, wR_2 = 0.126$	$R_1 = 0.0809, wR_2 = 0.1915$	$R_1 = 0.0583, wR_2 = 0.1208$	$R_1 = 0.1278, wR_2 = 0.2324$
R_1; wR_2 (all data)	$R_1 = 0.1071, wR_2 = 0.1351$	$R_1 = 0.0951, wR_2 = 0.143$	$R_1 = 0.1350, wR_2 = 0.2112$	$R_1 = 0.1033, wR_2 = 0.1345$	$R_1 = 0.3701, wR_2 = 0.3581$
Goodness of fit on F^2 (all data)	0.893	0.970	0.952	0.892	0.786

Table 3.19 Crystallographic parameters for **10** and **11**.

Compounds	10	11
Singh code	10069	09077
Formula	$C_{26}H_{35}BrFeN_2O_2$	$C_{26}H_{35}BrMn\ N_2O_2$
Mc	543.32	542.41
Crystal size (mm)	$0.37 \times 0.24 \times 0.06$	$0.28 \times 0.260 \times 0.10$
Temperature (K)	150(2)	150(2)
Crystal system	Monoclinic	Orthorhombic
Space group	$P2(1)/n$	$Pbca$
Lattice parameters		
a (Å)	11.955(4)	16.043(7)
b (Å)	15.722(5)	15.063(7)
c (Å)	13.835(5)	21.805(10)
α (°)	90	90
β (°)	93.477(6)	90
γ (°)	90	90
U (Å^3)	2595.6(15)	5269(4)
Z	4	8
D_c (Mg/m^3)	1.390	1.367
$F(000)$	1128	2248
μ (Mo-K$_\alpha$)	2.144	2.041
Reflections collected	19900	38869
R(int)	0.1020	0.0889
Independent reflections	5091	5173
Parameters/restraints	0/297	0/297
R_1; $wR_2[I>2\sigma(I)]$	$R_1 = 0.0717$, $wR_2 = 0.1735$	$R_1 = 0.0432$, $wR_2 = 0.0924$
R_1; wR_2 (all data)	$R_1 = 0.1148$, $wR_2 = 0.1900$	$R_1 = 0.0718$, $wR_2 = 0.1001$
Goodness of fit on F^2 (all data)	1.020	0.909

Table 3.20 Crystallographic parameters for **12a** and **12b**.

Compounds	12a	12b
Singh code	10057	10050
Formula	$C_{31}H_{34}Cl_2N_4NiO_2$	$C_{32}H_{36}Cl_2N_4NiO_2$
Mc	624.23	638.26
Crystal size (mm)	$0.13 \times 0.08 \times 0.03$	$0.20 \times 0.18 \times 0.05$
Temperature (K)	150(2)	150(2)
Crystal system	Orthorhombic	Monoclinic
Space group	$Pbca$	$P2(1)/n$
Lattice parameters		
a (Å)	18.937(11)	10.005(3)
b (Å)	13.395(8)	21.482(5)
c (Å)	23.924(13)	14.466(4)
α (°)	90	90
β (°)	90	100.033(6)
γ (°)	90	90
U (Å^3)	6069(6)	3061.6(13)
Z	8	4
D_c (Mg/m^3)	1.366	1.385
$F(000)$	2608	1336
μ (Mo-K$_\alpha$)	0.850	0.844
Reflections collected	45402	23902
R(int)	0.3065	0.1477
Independent reflections	5965	6016
Parameters/restraints	0/367	0/377
R_1; $wR_2[I>2\sigma(I)]$	$R_1 = 0.0868$, $wR_2 = 0.1168$	$R_1 = 0.0613$, $wR_2 = 0.0956$
R_1; wR_2 (all data)	$R_1 = 0.2039$, $wR_2 = 0.1456$	$R_1 = 0.1175$, $wR_2 = 0.1115$
Goodness of fit on F^2 (all data)	0.974	0.841

Table 3.21 Crystallographic parameters for **13a** and **13b**.

Compounds	13a	13b
Singh code	08080	10102
Formula	$C_{91}H_{102}Cl_2N_4Ni_3O_{12}$	$C_{94}H_{106}Cl_6N_4Ni_3O_{12}$
M_c	1690.80	1872.66
Crystal size (mm)	$0.20 \times 0.18 \times 0.05$	$0.26 \times 0.16 \times 0.10$
Temperature (K)	150(2)	150(2)
Crystal system	Triclinic	Triclinic
Space group	P-1	P-1
Lattice parameters		
a (Å)	11.342(2)	12.263(2)
b (Å)	13.387(3)	12.689(2)
c (Å)	14.849(3)	14.287(3)
α (°)	105.738(3)	88.067(3)
β (°)	102.453(4)	81.081(3)
γ (°)	93.540(4)	84.974(3)
U (Å^3)	2101.6(7)	2340.4(7)
Z	1	1
D_c (Mg/m^3)	1.336	1.329
$F(000)$	890	980
μ (Mo-K$_\alpha$)	0.792	0.829
Reflections collected	16441	18473
R(int)	0.0323	0.0851
Independent reflections	8151	9073
Parameters/restraints	0/472	0/564
R_1; $wR_2[I{>}2\sigma(I)]$	$R_1 = 0.0414$, $wR_2 = 0.0990$	$R_1 = 0.0613$, $wR_2 = 0.1065$
R_1; wR_2 (all data)	$R_1 = 0.0557$, $wR_2 = 0.1034$	$R_1 = 0.1097$, $wR_2 = 0.1221$
Goodness of fit on F^2 (all data)	0.962	0.912

Table 3.22 Crystallographic parameters for **14**.

Compounds	14
Singh code	10059
Formula	$C_{37}H_{44}NiN_2O_5$
M_c	655.45
Crystal size (mm)	$0.42 \times 0.28 \times 0.25$
Temperature (K)	150(2)
Crystal system	Orthorhombic
Space group	$Pna2(1)$
Lattice parameters	
a (Å)	15.332(10)
b (Å)	12.658(9)
c (Å)	16.658(11)
α (°)	90
β (°)	90
γ (°)	90
U (Å^3)	3488(4)
Z	4
D_c (Mg/m^3)	1.248
$F(000)$	1392
μ (Mo-K$_\alpha$)	0.599
Reflections collected	25823
R(int)	0.0568
Independent reflections	6832
Parameters/restraints	0/414
R_1; $wR_2[I{>}2\sigma(I)]$	$R_1 = 0.0380$, $wR_2 = 0.0746$
R_1; wR_2 (all data)	$R_1 = 0.0452$, $wR_2 = 0.0766$
Goodness of fit on F^2 (all data)	0.987

3.11. Polarised XAS measurements

The polarisation measurements in this chapter were performed in collaboration with Dr. N. P. Bannister, Dr. A. Martindale and Dr. D. Cotton (Space Research Centre, Department of Physics and Astronomy, University of Leicester) also in conjunction with Dr. S. P. Collins, K. Sawhney, I. Dolbnya and M. Tiwary (Diamond Light Source LTD). A full technical specification of the Diamond Light Source, B16 beamline can be found elsewhere.[89] However, also included was a water cooled Si(111) double crystal monochromator capable of operating within 2–20 keV along with a torroidal focusing mirror at 1:1 magnification. It is noteworthy that the beam diameter was recorded at 200 µm. Samples were mounted on a five-circle Huber Diffractometer with chi cradle. Photon detection required a VORTEX 90EX X-ray spectroscopy detector with an active area of 50 mm^2 with a resolution of 150 eV at 5.9 keV.

3.12 References

1) S. Li, X.-L. Yan, S.-B. Wang and Y.-F. Ma, *Acta Cryst.*, 2008, **E64**, m1258.
2) O. O. E. Onawumi, O. O. P Faboya, O. A. Odunola, T. K. Prasad and M. V. Rajasekharan, *Polyhedron*, 2008, **27**, 113.
3) Y. S Wong, C. H. Ng and S. W. Ng*, Acta Cryst.*, 2009, **E65**, m934.
4) O. A. Odunola, M. A. Oladipo, J. A. O. Woods and A. C. Gelebe, *Synth. React. Inorg. Met.-Org. Chem.*, 2003, **33**, 857.
5) Y. Elerman, H. Kara, S. Özcan and E. Kendi, *Acta Cryst.*, 2000, **C56**, 950.
6) D. Meinhard, M.Wegner, G. Kipiani, A. Hearley, P. Reuter, S. Fischer, O. Marti and B. Rieger, *J. Am. Chem. Soc.*, 2007, **129**, 9182.
7) P. Harding, D. J. Harding, W. Phonsri, S. Saithong and H. Phetmung, *Inorg. Chim. Acta*, 2009, **362**, 78.
8) V. A. Dolgikh and L. N. Kholodkovskaya, *Russ. J. Inorg. Chem.*, 1992, **37**, 2006.
9) B. Kaitner, K. Mesarek and E. Meštrović, *Acta Cryst.,* 2008, **E64**, m230.
10) V. Nalbamdyan and I. Sukaev, *Russ. J. Inorg. Chem.*, 1987, **32**, 706.
11) E. Meštrović and B. Kaitner, *J. Chem. Crystallogr.*, 2006, **36**, 599.
12) P. Harding, D. J. Harding, N. Soponrat and H. Adams, *Acta Cryst.*, 2010, **E66**, m1138.
13) F. Stephens, *Acta Cryst.*, 1977, **B33**, 3492.
14) A. Sakane, H. Kumada, S. Karasawa, N. Koga and H. Iwamura, *Inorg. Chem.*, 2000, **39**, 2891.
15) R. van Gorkum, F. Buda, H. Kooijman, A. L. Spek, E. Bouwman and J. Reedijk, *Eur. J. Inorg. Chem.*, 2005, 2255.
16) A. Haikarainen, J. Sipilä, P. Pietikäinen, L. Mutikainen and A. Pajunen, *J. Chem. Soc., Dalton Trans.*, 2000, 991.
17) C.-N. Chen, D.-G. Huang, Q.-T. Liu, C.-B. Ma and X.-F. Zhang, *Acta Cryst.*, 2002, **E58**, m473.
18) R. P. Doyle, O. F. Ikotun, W. Oullette, F. Lloret and M. Julve, *Eur. J. Inorg. Chem.*, 2007, 2083.
19) H. S Preston and C. H. L. Kennard, *J. Chem. Soc. A*, 1969, 2682.
20) A. J. Pallenberg, T. M. Marschner and D. M. Barnhart, *Polyhedron*, 1997, **16**, 2711.
21) T. V. Laine, M. Klinga and M. Leskelä, *Eur. J. Inorg. Chem.*, 1999, 959.
22) D. Meinhard, P. Reuter and B. Rieger, *Organometallics*, 2007, **26**, 751.
23) F. S. Stephens and P. A. Tucker, *J. Chem. Soc.*, *Dalton Trans.*, 1973, 2293.
24) W. D. Harrison, D. M. Kennedy, M. Power, R. Sheahan and B. J. Hathaway, *J. Chem. Soc.*, *Dalton Trans.*, 1981, 1556.
25) R. J. Fereday, P. Hodgson, S. Tyagi and B. J. Hathaway, *J. Chem. Soc.*, *Dalton Trans.*, 1981, 2070.
26) M. Brophy, G. Murphy, C. O'Sullivan, B. J. Hathaway and B. Murphy, *Polyhedron*, 1999, **18**, 611.
27) L. Jia, W. Fu, Q. Yin, M. Yu, J. Zhang and Z. Li, *Acta Cryst.*, 2005, **E61**, m1039.

28) L. Lu, S. Qin, P. Yang and M. Zhu, *Acta Cryst.,* 2004, **E60**, m574.

29) G. Murphy, C. O'Sullivan, B. Murphy and B. J. Hathaway, *Inorg. Chem.*, 1998, **37**, 240.

30) O. J. Parker, G. T. Greiner, G. L. Breneman and R. D. Willett, *Polyhedron*, 1994, **13**, 267.

31) M. A. Kahn and D. G. Tuck, *Acta Cryst.,* 1981, **B37**, 1409.

32) C. O'Sullivan, G. Murphy, B. Murphy and B. J. Hathaway, *J. Chem. Soc., Dalton Trans.,* 1999, 1835.

33) B. J. Hathaway and A. Murphy, *Acta Cryst.,* 1980, **B36**, 295.

34) Y. Sung and H.-H. Zhang, *Acta Cryst.,* 2009, **E65**, m1647.

35) G. Murphy, C. Murphy, B. Murphy and B. J. Hathaway, *J. Chem. Soc., Dalton Trans.*, 1997, 2653.

36) I. Potocnák, Z. Pravcová and D. Rak, *Acta Cryst.,* 2010, **E66**, m1325.

37) S. H. Gou and W. Huang, *J. Struct. Chem.*, 2007, **26**, 541.

38) Z. Gao and F. Li, *Acta Cryst.*, 2009, **E65**, m1664.

39) M. L. Sun, L. Zhang, Q. P. Lin, J. Zhang and Y. G. Yao, *Cryst. Growth Des.*, 2010, **10**, 1464.

40) R. E. Norman and M. Xie, *J. Coord. Chem.*, 2004, **57**, 425.

41) J.-R. Su and D.-J. Xu, *Acta Cryst.*, 2005, **E61**, m1738.

42) C. R. Rice and K. M. Anderson, *Polyhedron,* 2000, **19**, 95.

43) H. Zhong, X.-R. Zeng and Q.-Y. Luo, *Acta Cryst.,* 2006, **E62**, m3429.

44) B. Brewer, N. R. Brooks, S. A-Halim and A. G. Sykes, *J. Chem. Crystallogr.*, 2003, **33**, 651.

45) K. Arun Kumar, A. Dayalan and K. SethuSankar, *Acta Cryst.*, 2009, **E65**, m1300.

46) J. L. Rubin-Preminger, L. Koslov and I. Goldberg, *Acta Cryst.,* 2008, **C64**, 83.

47) X.-M. Chen, K.-L. Shi, T. C. W. Mak and B.-S. Luo, *Acta Cryst.*, 1995, **C51**, 358.

48) T.-G. Xu and D.-J. Xu, *J. Coord. Chem.*, 2005, **58**, 437.

49) C. Ma, W. Wang, H. Zhu, C. Chen and Q. Liu, *Inorg. Chem. Commun.*, 2001, **4**, 730.

50) Z.-P. Deng, S. Gao, L.-H. Huo and H. Zhao, *Acta Cryst.*, 2006, **E62**, m3388.

51) L. Zhang, S. Y. Niu, J. Jin, L.-P. Sun, G. D. Yang and L. Ye, *Inorg. Chim. Acta,* 2009, **362**, 1448.

52) S. Plentz-Meneghetti, P. J. Lutz and J. Kress, *Organometallics*, 1999, **18**, 2734.

53) K. Nienkemper, V. V. Kotov, G. Kehr, G. Erker and R. Frölich, *Eur. J. Inorg. Chem.*, 2006, 366.

54) Y. D. M. Champouret, R. K. Chaggar, I. Dadhiwala, J. Fawcett and G. A. Solan, *Tetrahedron*, 2006, **62**, 79.

55) N. Myaura and A. Suzuki, *Chem. Rev*., 2005, **95**, 2457.

56) D. Lötscher, S. Ruprecht, H. Stoeckli-Evans and A. von-Zelewsky, *Tetrahedron: Asymmetry*, 2000, **11**, 4341.

57) *U.S. Patent*, 2008, WO2008/112113A2.

58) Y. Zhou, T. Kijima and T. Izumi, *J. Heterocycl. Chem.*, 2009, **46**, 116.

59) Q. Dai, D. Xu, R. G. Harvey and K. Lim, *J. Org. Chem.*, 2007, **72**, 4856.

60) τ-Value is an average of all four molecules in the unit cell.

61) A. Armitage, K. Singh and G. Solan, *personal communication*, 2011.

62) D. M. Haddleton, C. B. Jasieczek, M. J. Hannon and A. J. Shooter, *Macromolecules*, 1997, **30**, 2190.

63) D. M. Haddleton, D. J. Duncalf, D. Kukulj, M. C. Crossman, S. G. Jackson, S. A. F. Bon, A. J. Clark, and A. J. Shooter, *Eur. J. Inorg. Chem.*, 1988, 1799.

64) B. J. Hathaway and D. E. Billing, *Coord. Chem. Rev.*, 1970, **5**, 143.

65) M. Bacci, *Chem. Phys*. 1986, **104**, 191.

66) H. A. Jahn and E. Teller, *Proc. R. Soc. London, Sec. A*, 1937, **161**, 220.

67) D. Reinen and M. Atanazov, *Chem. Phys.*, 1989, **136**, 27.

68) J. Gazo, I. B. Berzuka, J. Garaj, M. Kabesova, J. Kohout, H. Langfelderova, M. Melnik, M. Serator and F. Valach, *Coord. Chem. Rev.*, 1976, **19**, 253.

69) S. Youngme, J. Phatchimkun, U. Suksangpanya, C. Pakawatchai, N. Chaichit, P. Kongsaeree, J. Krzystek and B. Murphy, *Polyhedron*, 2007, **26**, 871.

70) V. Chaurin, E. Constable and C. E. Housecroft, *New J. Chem.*, 2006, **30**, 1740.

71) G. Murphy, C. O'Sullivan, B. Murphy and B. J. Hathaway, *Inorg. Chem.*, 1998, **37**, 240.

72) E. C. Constable, C. E. Housecroft, J. R. Price and J. A. Zampese, *CrystEngComm*, 2010, **12**, 3163.

73) F. G. Fontaine, *Acta Cryst.*, 2001, **E57**, m270.

74) H. Clavier and S. P. Nolan, *Chem. Commun.*, 2010, **46**, 841.

75) A. Poater, B. Cosenza, A. Correa, S. Giudice, F. Ragone, V. Scarano and L. Cavallo, *Eur. J. Inorg. Chem.*, 2009, 1759.

76) R. A. Coxall, S. G. Harris, D. K. Henderson, S. Parsons, P. A. Tasker and R. E. P. Winpenny, *J. Chem. Soc., Dalton Trans.*, 2000, 2349.

77) R. E. P. Winpenny, *personal communication*, 2004.

78) A. J. Blake, L. M. Gilby, S. Parsons, J. M. Rawson, D. Reed, G. A. Solan and R. E. P. Winpenny, *J. Chem. Soc., Dalton Trans.*, 1996, 3575.

79) P. Mukherjee, M. G. B. Drew, C. J. Gómez-García and A. Ghosh, *Inorg. Chem.*, 2009, **48**, 5848.

80) H. Adams, S. Clunas, D. E. Fenton, T. J. Gregson, P. E. McHugh and S. E. Spey, *Inorg. Chim. Acta*, 2003, **346**, 239.

81) C. He and S. J. Lippard, *J. Am. Chem. Soc.*, 2000, **122**, 184.

82) H. E. Wages, K. L. Taft and S. J. Lippard, *Inorg. Chem.*, 1993, **32**, 4985.

83) J. Reglinski, M. K. Taylor and A. R. Kennedy, *Inorg. Chem. Commun.*, 2006, **9**, 736.

84) W. L. F. Armarego and D. D. Perrin, *Purification of Laboratory Chemicals*, Elsevier, 4th edn, 1996.

85) F. Tellier, J.-F. Normant and R. Sauvetre, *J. Organomet. Chem.*, 1985, **292**, 19.

86) Y. D. M. Chapouret, R. K. Chaggar, I. Dadhiwala, J. Fawcett and G. A. Solan, *Tetrahedron*, 2006, **62**, 79.

87) G. M. Sheldrick, SHELX-97, Programs for Crystal Structure Analysis, University of Göttingen, Göttingen, Germany, 1997.

88) A. L. Spek, *Acta Cryst.*, 1990, **A46**, 34.

89) K. J. S. Sawhney, I. P Dolbnya, M. K. Tiwari, L. Alianelli, S. M. Scott, G. M. Preece, U. K. Pederson, and R. D. Walton, *AIP Proc., 10th Int. Conf. on Synch. Rad. Instr. 2009*, 2010.

CHAPTER 4

Metallo-porphyrin halides and oxides (M = Co, Fe, Mn, V, Ti) as transmissive filters for X-ray polarimetry

4.0 Metallo-porphyrin halides and oxides (M = Co, Fe, Mn, V, Ti) as transmissive filters for X-ray polarimetry

This chapter focuses on the application of SBP metallo-porphyrin halides and oxides as transmissive filters for X-ray polarimetry at the cobalt (7709 eV), iron (7112 eV), manganese (6539 eV), vanadium (5465 eV) and titanium (4966 eV) K-edges (Figure 4.1). In Chapter 3, it was shown that the five co-ordinate motif [(α-diimine)MBr(β-diketonate)] proved a compatible platform for copper(II) allowing SBP geometries which were highly aligned in the solid state and moreover, gave a dichroic response to polarised X-rays. The extension of this platform to other 3*d* metal(II) centres (*viz.*, Ni, Co, Fe, Mn) was, however, flawed as the *bis*-chelates could readily re-organise about the metal centres leading to geometries anywhere between distorted TBP and SBP, while deviations in the intermolecular alignment were also apparent. To circumvent this chelate flexibility, it was decided to target in this chapter, the ubiquitous dianionic, tetraphenylporphyrinato ligand (TPP^{2-}) as a rigid macrocyclic support that would occupy the basal sites of SBP complexes of the type, [(TPP)MX] (X = Cl, Br) or [(TPP)MO]. These motifs would not only allow the examination of an alternative platform for cobalt, manganese and iron (albeit with a M(III) oxidation state), but also allow a means of probing the lower energy K-edges of vanadium and titanium. A further goal of this chapter is to develop the concept of multi-edge *hybrid filters* discussed in Chapters 2 and 3 by using the macrocyclic periphery as an anchor for additional strategically placed K-edges [*e.g.*, Cl (2282 eV), Br (13473 eV)].
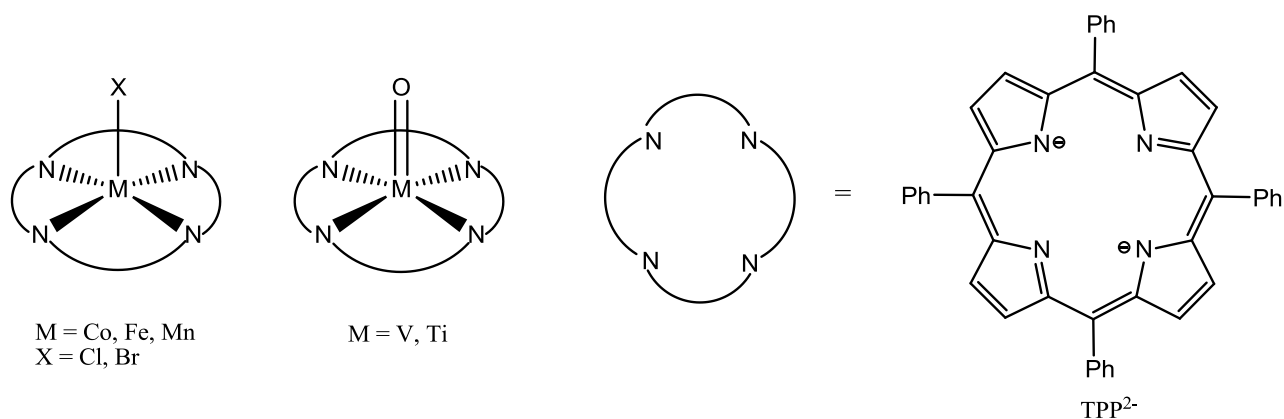

Figure 4.1 Target metallo-tetraphenylporphyrin halides and oxides.

4.1 Background: Metallo-tetraphenylporphyrin halides and oxides

Metallo-porphyrin complexes have been widely studied and have applications in biology,[1,3] molecular building block materials,[4,5] photo-voltaics[6–9] and catalysis.[10] The halide members of the metallo-porphyrin family and in particular, of the tetraphenylporphyrin type, have been widely reported for many of the first row transition metal series, while terminal oxides tend to have been identified for the earlier metals (Ti–Cr) (Table 4.1).

With regard to crystallographically studied terminal oxide complexes, only the vanadium(IV) and chromium(IV) tetraphenylporphyrin-derivatives have been reported. The synthesis of [(TPP)TiO] has been disclosed,[11,12] but unlike its structurally related analogues, *viz.,* [(OEP)TiO][13] [(OEPMe)TiO][14] (OEP = octaethylporphyrin) and the fluorinated tetraphenylporphyrin derivative [(TPP-F$_8$)TiO],[15] its crystal structure has not; on the other hand, EXAFS data for [(TPP)TiO] is known.[16] Complexes [(TPP)CrO][17,18] and [(TPP)VO][19–21] are isostructural and adopt ideal SBP geometries (τ = 0.01 respectively); they also display highly aligned M=O bonds in the solid state. It is worth noting that a number of neutral oxo-bridged species have also been reported for iron(III) metal centres featuring tetraphenylporphyrin[22–25] and its derivatives.[26–37]

In addition to *bis*-halide complexes of titanium(IV),[38,39] structurally characterised trivalent tetraphenylporphyrinato co-ordinated mono-halides have been reported for cobalt, iron, manganese and scandium (Table 4.1). The chromium(III) derivative has only been encountered as a six co-ordinate adduct,[40–45] while the scandium-containing [(TPP)ScCl] is unstable under atmospheric conditions; the X-ray structure of the latter complex however reveals considerable disorder with respect to neighbouring Sc–Cl bonds.[46] On the other hand, for cobalt, iron and manganese highly aligned chloride SBP complexes of the type, [(TPP)MCl] have been reported,[47–54,57–63] while the bromide analogues are known for only iron and manganese.[55,63] With respect to the M(III) chlorides, polymorphism is a key feature with four different forms existing for iron and six forms for manganese. In the case of [(TPP)MnCl], it would seem

apparent that the solvent employed for recrystallisation influences the particular polymorphic outcome, which in turn determines the alignment between neighbouring Mn–Cl bonds. For example, polymorphs obtained from toluene or benzene display intermolecular ClMn···MnCl torsion angles of 180°, whilst polymorphs obtained from acetone or chloroform reveal torsion angles in the range 21.29–57.37°. In this chapter, where polymorphs are present, emphasis has been placed in selecting the most highly aligned form.

4.2 Background: Using XANES to study metallo-porphyrins

XAS has been employed to study high valent chromium, vanadium and titanium-containing metallo-porphyrins, *e.g.*, [(OEP)MO][18,64,65] (M = V, Ti) and [(TPP)MO] (M = Cr, V) (*vide infra*).[17, 66] These species both demonstrate strong pre-edge features, a dichroic handle which has been identified in previous chapters which could be exploited for astronomical polarimetry. Additionally, the XAS spectra of octahedral [(TPP)TiCl$_2$][67] is also known, however, the pre-edge feature is diminished in comparison to the five co-ordinate metal oxide derivatives. Furthermore, there have been no XAS studies on tetraphenylporphyrinato co-ordinated metal halides of cobalt, iron or manganese.

Table 4.1 Metallo-tetraphenylporphyrin terminal halide and oxide compounds of 3d metal centres that have been reported and/or crystallographically characterised.

Complex	a (Å)	b (Å)	c (Å)	α (°)	β (°)	γ (°)	V	Z[b]	Crystal system	Crystallising solvent	Lattice solvent	XM⋯MX torsion angle (°)[c]	Reference
				Unit cell parameters[a]							*Solvation*		
[(TPP)CoCl][d]	13.693	13.693	9.701	90	90	90	1818	2	Tetragonal	Chloroform	–	0	47
[(TPP)FeF]	13.381	13.381	9.761	90	90	90	1709	2	Tetragonal	Chloroform/Et$_2$O	–	0	50
[(TPP)FeCl]	10.254	15.969	20.810	90	90.48	90	3407	4	Monoclinic	–	–	25.61	51
[(TPP)FeCl]	11.341	12.994	13.626	107.96	103.66	111.34	1636	2	Triclinic	Benzene	Benzene	180	52
[(TPP)FeCl]	13.4576	13.4576	9.6853	90	90	90	1695	4	Tetragonal	Dichloromethane	–	180	53
[(TPP)FeCl]	12.720	12.902	22.267	85.756	83.302	63.273	3241	2	Triclinic	Acetone	Acetone	180	54
[(TPP)FeBr]	10.191	16.121	23.223	90	115.34	90	3448	4	Monoclinic	Dichloromethane	–	180	55
[(TPP)FeI]	10.11	10.352	21.11	90	89.36	90	3509	4	Monoclinic	Chloroform	–	52.32	56
[(TPP)MnCl][e]	12.9	12.9	10.2	90	90	90	1697	2	Tetragonal	Benzene	–	180	57
[(TPP)MnCl]	13.463	13.463	9.864	90	90	90	1787	2	Tetragonal	Toluene	Toluene	180	59
[(TPP)MnCl]	9.918	15.395	13.453	90	103.68	90	3997	2	Monoclinic	Toluene	Toluene	180	60
[(TPP)MnCl]	12.1572	21.8985	14.4790	90	102.653	90	3770	4	Monoclinic	Chloroform	Chloroform	23.8	61
[(TPP)MnCl]	14.588	21.765	17.023	90	135.62	90	3780	4	Monoclinic	Acetone	Acetone	57.37	62
[(TPP)MnCl]	12.155	21.763	17.059	90	123.17	90	3777	4	Monoclinic	Acetone	Acetone	21.29	63
[(TPP)MnBr]	9.985	15.453	13.583	90	103.99	90	2033	2	Monoclinic	Toluene	Toluene	180	63
[(TPP)MnI]	22.68	14.466	13.555	76.32	81.74	74.75	4080	4	Triclinic	Acetone	–	56.81	63
[(TPP)CrO]	13.351	13.351	9.749	90	90	90	1738	2	Tetragonal	Chloroform	–	0	18
[(TPP)CrCl][f]	–	–	–	–	–	–	–	–	–	–	–	–	42,43
[(TPP)VO]	13.345	13.345	9.746	90	90	90	1735	2	Tetragonal	Dichloromethane	–	0	19–21
[(TPP)TiO][g]	–	–	–	–	–	–	–	–	–	Dichloromethane	–	–	11,12
[(TPP)TiF$_2$]	13.350	13.350	9.738	90	90	90	1736	2	Tetragonal	HF/Hexane	–	0	37
[(TPP)TiCl$_2$]	13.5956	13.5956	9.8681	90	90	90	1824	2	Tetragonal	HCl/Hexane	–	0	36,67
[(TPP)TiBr$_2$]	13.757	13.757	9.880	90	90	90	1870	2	Tetragonal	HBr/Hexane	–	0	37
[(TPP)ScCl]	9.9530	15.4040	17.7770	86.5190	89.7680	86.720	2717	2	Triclinic	1-Chloronapth	1-Chloronapth	57.56	44

a) Data obtained from the Cambridge Structural Database (June 2011).
b) Refers to the number of molecules in the unit cell.
c) Refers to the torsion angle between neighbouring M–X bonds [tors: XM⋯MX] (M = Metal, X = apical species).
d) Axially solvated analogues [(TPP)CoClPy][48] and [(TPP)CoCl(H$_2$O)][49] are also known.
e) The axially solvated analogue [(TPP)MnClPy][58] is known.
f) Has not been crystallographically characterised, the axially solvated [(TPP)CrCl(H$_2$O)],[38] [(TPP)CrCl(py)][39,40] and [(TPP)CrCl(N-MeImdz)][41] (N-MeImdz = N-methylimidazole) are known.
g) Has not been crystallographically characterised, references refer to synthesis and spectroscopic/analytical characterisation only. For EXAFS data see references 16 and 17.

4.3 Target metallo-tetraphenylporphyrin halides and oxides; aims and objectives

Herein, the aim is to firstly re-synthesise the previously crystallographically characterised species [(TPP)CoCl][47] (**15b**$_{DCM}$) ($\tau = 0.02$), [(TPP)FeBr][55] (**16**$_{DCM}$) ($\tau = 0.04$), [(TPP)MnBr][63] (**17**$_{toluene}$) ($\tau = 0.02$) and [(TPP)VO][19–21] (**18**$_{DCM}$) ($\tau = 0.01$) as these systems all display an almost ideal SBP geometry along with the desired intermolecular alignment in the solid state (Scheme 4.1).

Secondly, the aim is to prepare the bromide analogue of **15b**$_{DCM}$, [(TPP)CoBr] (**15a**$_{DCM}$), as this potentially offers a dual K-edge capability; a similar dual-edge capability has been displayed in **1a** at the Cu and Br K-edges in Chapter 2.

Thirdly, with a view to disrupting the perfect intermolecular Mn–Br bond alignment in **17**$_{toluene}$, disordered polymorphs of **17** will be deliberately targeted by crystallising it from different solvents (*e.g.*, benzene, dichloromethane).

Fourthly, single crystals of the elusive titanium analogue of **18**$_{DCM}$, [(TPP)TiO] (**19**$_{DCM}$) are targeted as this would, in principle, allow access to the lowest K-edge (4966 eV) for a dichroic material developed so far in this work.

Finally, the principal aim is to subject a selection of these systems to an in-depth investigation of their polarised XAS in both transmission and fluorescence mode using exclusively the Diamond Light Source (stations B16 and I18) in order to establish their performance as potential dichroic materials. The use of multiple scattering theory (FEFF) will be used to complement the experimental results. In addition to the above, a separate synthetic section highlights preliminary efforts at developing the concept of multi-edge *hybrid filters* by employing the metallo-porphyrin platform.

4.4 Synthesis and crystallographic characterisation of [(TPP)MX] [M = Co, X = Br (15a_DCM), X = Cl (15b_DCM); M = Fe X = Br (16_DCM); M = Mn, X = Br (17_DCM), (17_benzene), (17_toluene)] and [(TPP)MO] [M = V (18_DCM), Ti (19_DCM)]
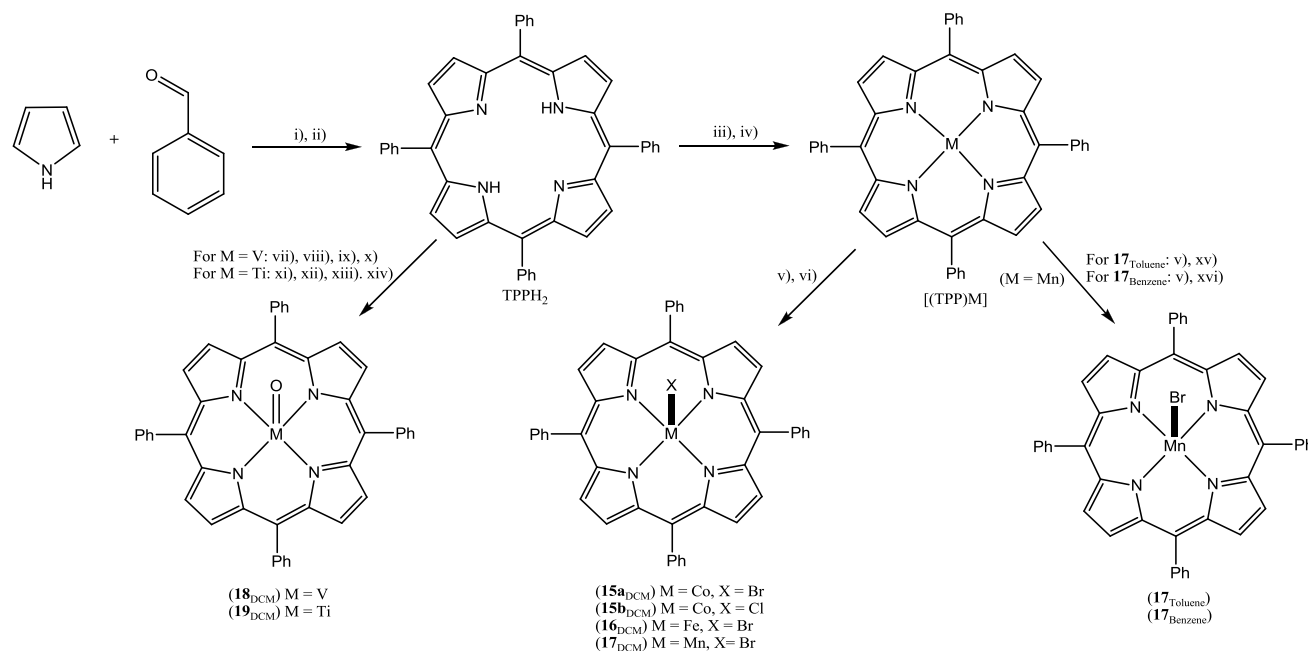

Scheme 4.1 *Reagents and conditions:* i) CH$_3$CH$_2$COOH, 145 °C, 1 h; ii) MeOH; iii) M(OAc)$_2$·nH$_2$O (M = Co, Fe, Mn), CH$_3$COOH, 125 °C, 15 min, 100 W; iv) H$_2$O/toluene; v) Conc. HX (X = Cl, Br), MeOH, rt, 12 h; vi) DCM/hexane recrystallisation; vii) VO(acac)$_2$, quinoline, 130 °C, 72 h; viii) DCM extraction; ix) silica gel chromatography, CHCl$_3$; x) CH$_2$Cl$_2$/hexane recrystallisation; xi) TiCl$_4$, toluene, 110 °C, 12 h; xii) CHCl$_3$, 2 M HCl; xiii) silica gel chromatography, CHCl$_3$; xiv) DCM recrystallisation; xv) toluene/hexane recrystallisation; xvi) benzene recrystallisation.

The synthetic protocol for the preparation of TPPH$_2$ has been previously reported[68–70] and reproduced herein (Scheme 4.1). As an alternative to the reported thermally promoted complexation step,[71] the reaction of the corresponding M(OAc)$_2$.nH$_2$O with TPPH$_2$ in glacial acetic acid in a 5:1 molar ratio, has been performed using microwave assisted conditions, affording [(TPP)M] (M = Co, Fe, Mn) in good yield in considerably decreased reaction times. Treatment of divalent [(TPP)M] with the corresponding concentrated hydro-halous acid in methanol[47,72] gave, on crystallisation from dichloromethane, [(TPP)CoX] [X = Br (15a_DCM), Cl (15b_DCM)], [(TPP)FeBr)] (16_DCM) and [(TPP)MnBr] (17_DCM) in good yields, respectively (Scheme 4.1). Manganese-containing 17_benzene could be obtained by recrystallisation from benzene, while 17_toluene from a combination of toluene and hexane.[63] In addition, the reaction of VO(acac)$_2$ with TPPH$_2$ in quinoline in a 10:1 molar ratio respectively, gave on crystallisation from dichloromethane, [(TPP)VO] (18_DCM), also in good yield.[20] Its titanium analogue [(TPP)TiO]

(19_{DCM}) could be obtained by treating $TPPH_2$ with titanium tetrachloride in toluene, followed by recrystallisation from dichloromethane.[12] Interestingly, the attempted preparation of **19** using the originally reported route[11] gave, in our hands, only divalent [(TPP)Ti] and free $TPPH_2$ (see Appendix A11.0).

Single crystals of the novel $\mathbf{15a_{DCM}}$, $\mathbf{17_{DCM}}$, $\mathbf{17_{benzene}}$ and $\mathbf{19_{DCM}}$ were the subject of X-ray diffraction studies, whilst the unit cells of $\mathbf{15b_{DCM}}$, $\mathbf{16_{DCM}}$, $\mathbf{17_{toluene}}$ and $\mathbf{18_{DCM}}$ were shown to be as previously reported. The molecular structures along with the packing diagrams of $\mathbf{15a_{DCM}}$ and $\mathbf{19_{DCM}}$ are depicted in Figures 4.2 and 4.4 whilst the molecular packing diagrams for polymorphs $\mathbf{17_{DCM}}$, $\mathbf{17_{benzene}}$ and previously reported $\mathbf{17_{toluene}}$ are displayed in Figure 4.3 for comparative purposes.

(a)
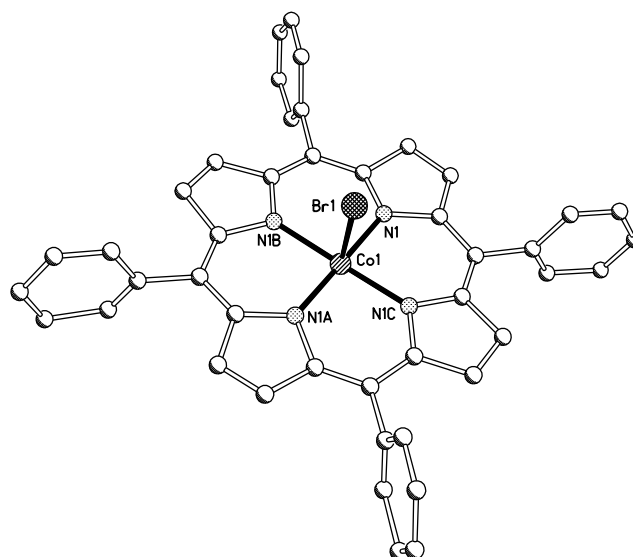
(b)
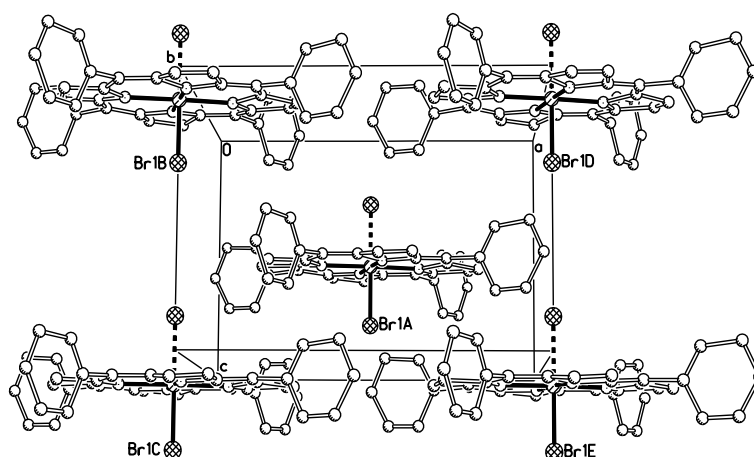
Figure 4.2 (a) Molecular structure of $\mathbf{15a_{DCM}}$ with partial atom labels along with (b) the molecular packing diagram when viewed down the *b*-axis; hydrogen atoms have been removed for clarity. Atoms denoted with a letter label have been generated by the symmetry operations *-x*+1, *-y*+1, *z*, *-y*+1, *x*, *z* and *y*, *-x*+1, *z*. The bromine atoms are disordered *ca.* 60:40 above and below the porphyrin plane.

Table 4.2 Selected bond lengths (Å) and angles (°) for **15a**$_{DCM}$ and **15b**$_{DCM}$.[47]

	15a$_{DCM}$[a] (X = Br)	**15b**$_{DCM}$[a] (X = Cl)[47]
Co(1)–N(1)	1.969(6)	1.974(3)
Co(1)–N(1A)	1.969(6)	1.974(3)
Co(1)–N(1B)	1.969(6)	1.974(3)
Co(1)–N(1C)	1.969(6)	1.974(3)
Co(1)–X(1)	2.187(5)	2.120(8)
Co(1)–X(2)[b]	2.300(5)	2.138(8)
N(1)–Co(1)–N(1A)	178.6(9)	178.1(6)
N(1)–Co(1)–N(1B)	89.992(15)	89.984(12)
N(1)–Co(1)–N(1C)	89.992(13)	89.984(13)
N(1)–Co(1)–X(1)	89.3(5)	89.0(3)
N(1)–Co(1)–X(2)	90.7(5)	91.0(3)
N(1A)–Co(1)–N(1B)	89.992(13)	89.984(13)
N(1A)–Co(1)–N(1C)	89.992(15)	89.0(3)
N(1A)–Co(1)–X(1)	89.3(5)	89.984(12)
N(1A)–Co(1)–X(2)	90.7(5)	91.0(3)
N(1B)–Co(1)–N(1C)	178.6(9)	178.1(6)
N(1B)–Co(1)–X(1)	89.3(5)	89.0(3)
N(1B)–Co(1)–X(2)	90.7(5)	91.0(3)
N(1C)–Co(1)–X(1)	89.3(5)	89.0(3)
N(1C)–Co(1)–X(2)	90.7(5)	91.0(3)
X(1)–Co(1)–X(2)	180.000(1)	180.000(1)

a) Atoms denoted with a letter label are generated by the symmetry operations -x+1, -y+1, z, -y+1, x, z and y, -x+1, z.
b) The atoms X(1) and X(2) are disordered *ca.* 60:40 above and below the porphyrin plane.

The molecular structure of **15a**$_{DCM}$ consists of a CoBr unit co-ordinated by the tetradentate tetraphenylporphyrinato macrocycle which occupies the basal co-ordination sites of a SBP (τ = 0.02). The apical bromine atom is crystallographically disordered across two positions in a similar way to the chloride in **15b**$_{DCM}$.[47] Inspection of the molecular packing diagram revealed that two molecules are present in the unit cell of **15a**$_{DCM}$ and a fully anisotropic alignment of the Co–Br bond vectors with respect to its neighbours is evident [tors: BrCo···CoBr = 180°].

On comparative inspection of the molecular packing diagrams for the three polymorphs of **17** (**17**$_{DCM}$ τ = 0.08), (**17**$_{benzene}$ τ = 0.03) and (**17**$_{toluene}$ τ = 0.02)] (Figure 4.3), it can be noted that for **17**$_{DCM}$ and **17**$_{benzene}$, two pairs of symmetry related molecules are present in the unit cell; molecules of dichloromethane and benzene are also present in the lattice of **17**$_{DCM}$ and **17**$_{benzene}$, the latter of which have been removed using the squeeze option in PLATON.[73] In contrast, **17**$_{toluene}$ has only two symmetry related molecules present which have intermolecular BrMn···MnBr torsion angles of 180°. When compared to **17**$_{toluene}$, the Mn–Br bonds in pairs of symmetry related molecules of **17**$_{DCM}$ are almost aligned perpendicular to each other [tors: BrMn···MnBr = 87.37°], whilst in **17**$_{benzene}$ a slight improvement is apparent [tors: BrMn···MnBr

= 50.73°]. Based on these observations, it is evident that the solvent is indeed having an impact on the observed crystal morphology and intermolecular bond alignment.
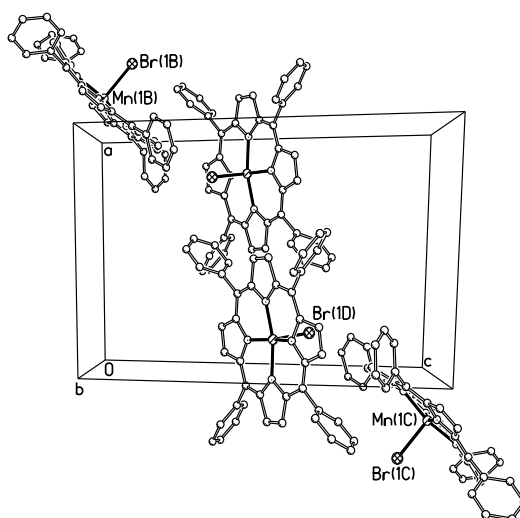
(a)
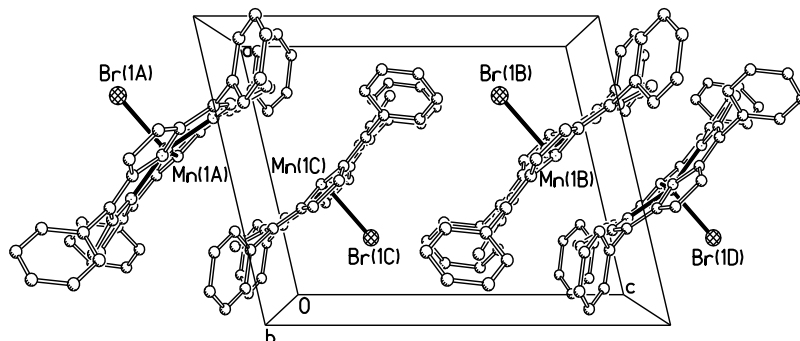
(b)
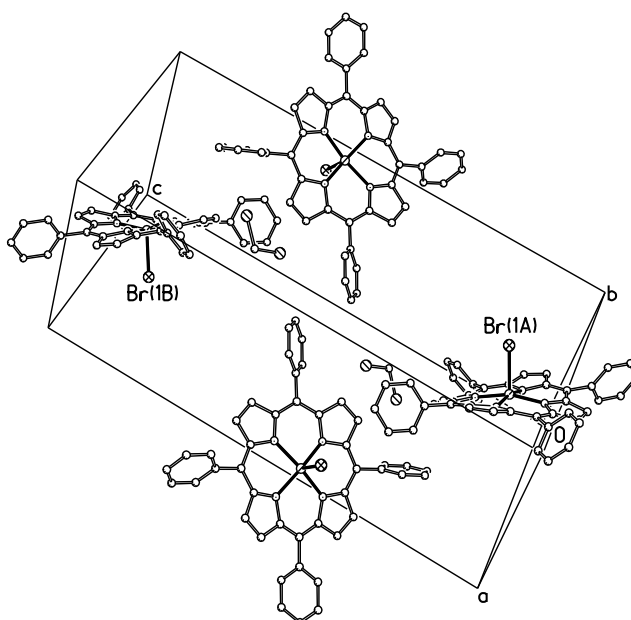
(c)

Figure 4.3 Molecular packing diagrams for **17** when recrystallised from (a) toluene (**17**$_{toluene}$), (b) dichloromethane (**17**$_{DCM}$), and (c) benzene (**17**$_{benzene}$). The unit cells for **17**$_{toluene}$[63] and **17**$_{benzene}$ are viewed down the crystallographic *b*-axis, while the unit cell of **17**$_{DCM}$ is viewed off-axis for clarity.

The structure of the titanium(IV) oxo-containing 19_{DCM} is isostructural and isomorphous to its vanadium(IV)[19] and Cr(IV)[18] oxide counterparts and consists of a TiO core co-ordinated by the tetraphenylporphyrinato macrocycle; its geometry can best be described as SBP ($\tau = 0.01$) with the oxygen atom filling the apical position. Like its vanadium and chromium-containing analogues, the TiO units are crystallographically disordered *ca.* 50% above and below the porphyrin plane. The molecular packing diagram of 19_{DCM} reveals perfect molecular order with respect to the neighbouring Ti–O bonds of the two symmetry related molecules [tors: OTi⋯TiO = 0°].

(a)
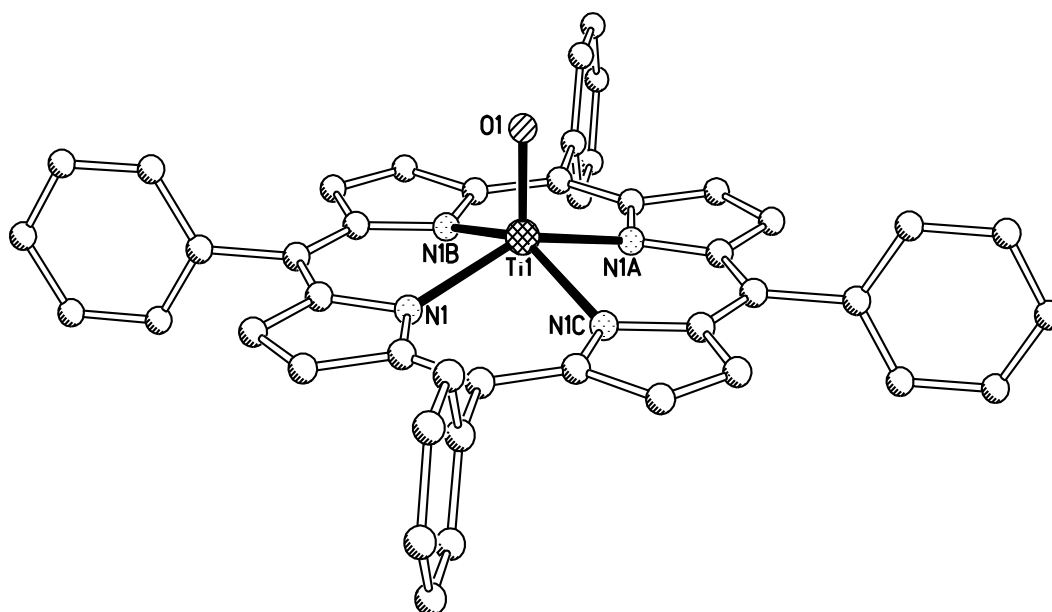
(b)
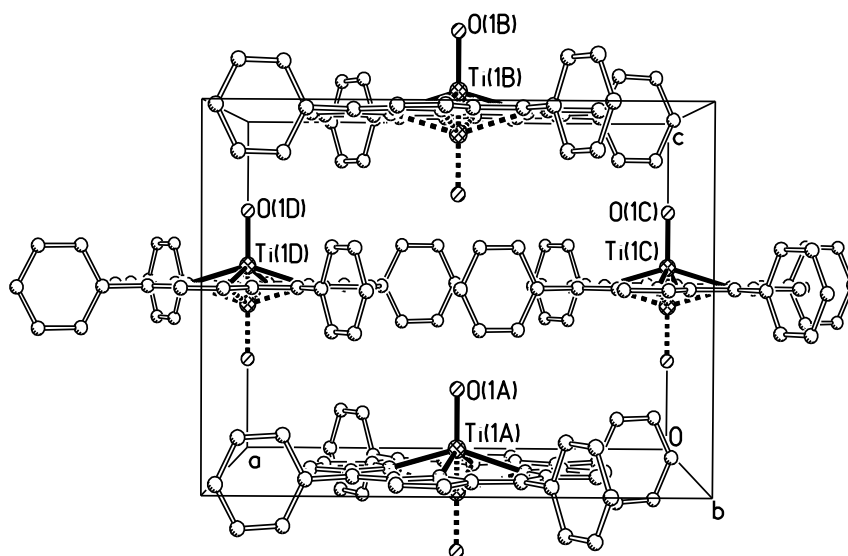
Figure 4.4 (a) Molecular structure of 19_{DCM} with partial atom labels along with (b) the molecular packing diagram when viewed down the *b*-axis; hydrogen atoms have been removed for clarity. Atoms denoted with a letter label have been generated by the symmetry operations -*x*+1, -*y*+1, -*z*, -*y*+1, *x*, z, *y*, -*x*+1, -*z* and *x*, *y*, -*z*. The titanium and oxygen atoms are disordered *ca.* 50:50 above and below the porphyrin plane.

Table 4.3 Selected bond lengths (Å) and angles (°) for **18**$_{DCM}$ and **19**$_{DCM}$.

	18$_{DCM}$[a] (M = V)	**19**$_{DCM}$[b] (M = Ti)
M(1)–M(1A)	1.090(9)	1.969(6)
M(1)–N(1)	2.093(6)	1.969(6)
M(1)–N(1A)	2.093(6)	1.969(6)
M(1)–N(1B)	2.093(6)	1.969(6)
M(1)–N(1C)	2.093(6)	2.187(5)
M(1)–O(1)	1.634(10)	2.300(5)
N(1)–M(1)–N(1A)	148.8(3)	178.6(9)
N(1)–M(1)–N(1B)	86.11(6)	89.992(15)
N(1)–M(1)–N(1C)	86.11(6)	89.992(13)
N(1)–M(1)–O(1)	105.10(13)	89.3(5)
N(1A)–M(1)–N(1B)	86.11(6)	90.7(5)
N(1A)–M(1)–N(1C)	86.11(6)	89.992(13)
N(1A)–M(1)–O(1)	105.10(13)	89.992(15)
N(1B)–M(1)–N(1C)	149.8(3)	89.3(5)
N(1B)–M(1)–O(1)	105.10(13)	90.7(5)
N(1C)–-M(1)–O(1)	149.8(3)	178.6(9)
M(1A)–M(1)–N(1)	74.90(13)	89.3(5)
M(1A)–M(1)–N(1A)	74.90(13)	90.7(5)
M(1A)–M(1)–N(1B)	74.90(13)	89.3(5)
M(1A)–M(1)–N(1C)	74.90(13)	90.7(5)
M(1A)–M(1)–O(1)	180.000(15)	180.000(1)

a) Atoms denoted with a letter label are generated by the symmetry operations -*x*, -*y*+2, -*z*+2, -*y*+1, *x*+1, *z*, *y*-1, -*x*+1, -*z*+2, and *x*, *y*, -*z*+2.
b) Atoms denoted with a letter label are generated by the symmetry operation, -*x*+1, -*y*+1, -*z*, -*y*+1, *x*, *z*, *y*, -*x*+1, -*z* and *x*, *y*, -*z*.
c) The atoms M(1), M(1A) and O(1) are disordered *ca.* 50:50 above and below the porphyrin plane.

4.5 Determining the molecular alignment of 15, 16, 17, 18 and 19, with respect to the crystal morphology

Using cobalt-containing **15a**$_{DCM}$ as a representative example, face indexing has identified three prominent Miller indices, the (001), (010) and (100) faces. It is apparent that the (010) and (100) faces are indistinguishable from each other due to the regular plate-like nature of the single crystal (Figure 4.5). However, it is noteworthy that the Co–Br bonds are perfectly aligned with both the (010) and (100) faces of the crystal of **15a**$_{DCM}$, therefore it could be highlighted that an X-ray beam could be indiscriminately incident on either the (010) or (100) faces with the polarisation vector parallel to the shortest crystal axis and still maintain a parallel alignment with the Co–Br bonds. As expected, isomorphous **15b**$_{DCM}$ exhibits identical morphological features. The Miller indices for all the title complexes were determined in a similar fashion.

(a)
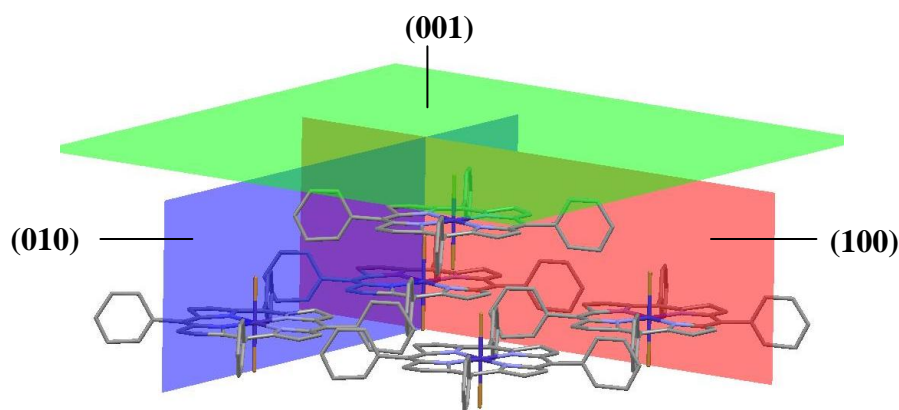
(b)
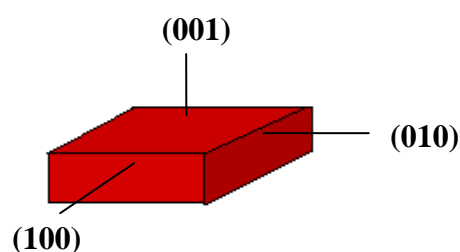
Figure 4.5 (a) Miller indices overlaid onto the molecular packing diagram of **15a**$_{DCM}$ (bromine atoms are disordered above and below the molecular plane) along with (b) a schematic of the single crystal morphology in **15a**$_{DCM}$; **15b**$_{DCM}$ shows identical morphological features.

4.6 Using polarised XAS to study 15a$_{DCM}$ and 15b$_{DCM}$

Single crystals of **15a**$_{DCM}$ and isomorphous **15b**$_{DCM}$ were subjected to an experimental study to establish their performances as potential dichroic filter materials. The crystals were rotated about a polarisation axis of synchrotron radiation and XAS spectra were recorded in two orientations, χ_0 and χ_{90}. Typically, the X-ray beam was assumed to be incident on either the (100) or (010) crystal faces of **15a**$_{DCM}$ or **15b**$_{DCM}$, where the polarisation axis was parallel to the shortest crystallographic axis and hence, aligned with the Co–Br bond (Figure 4.5). The single crystal was rotated through 90° about the shortest axis such that the X-ray vector was now perpendicular to the Co–Br bond (see Figure 4.5).

The polarised XAS spectra were recorded in both transmission and fluorescence modes at the Diamond Light Source (stations I18 and B16, respectively). As previously described, the raw X-ray data were normalised using a 'step-edge' approach (Chapter 2, section 2.5).[74] In addition, the XAS spectra were corrected for the air-path, ion-chamber and Kapton window.[75] Using this experimental set up, both fluorescence and transmission spectra were collected simultaneously.

4.6.1 X-ray dichroism of 15a$_{DCM}$ (and 15b$_{DCM}$) at the Co K-edge (7708 eV)

X-ray measurements were performed at the Co K-edge (7708 eV) on a single crystal of **15a**$_{DCM}$ in transmission mode at both the I18 and B16 beamlines. The transmission spectra of two orientations (χ_0 and χ_{90}) obtained from both beamlines show similar spectral features. The transmission XAS spectra obtained from station I18 only are presented in Figure 4.6. It is noteworthy however, that station I18 is a micro-focus beamline and is only *ca.* 70% polarised. Nevertheless, on inspection of these spectra (Figure 4.6), several points emerge. Firstly, there are three principal dichroic regions, namely the pre-edge (7700–7707 eV), main-edge (7707–7736 eV) and the EXAFS (7736–7810 eV) regions. Within the main-edge, there are two sub-regions, the shoulder (main-edge 1) and the peak maximum (main-edge 2). Shoulders (main-edge 1) occur in both orientations at 7719 eV (χ_0) and 7725 eV (χ_{90}) embedded within the main-edge 2. Intense peaks in both orientations 7727 eV (χ_0) and 7735 eV (χ_{90}) constitute the main-edge 2. Also noticeable, are several isobestic points at 7733, 7737 and 7773 eV resulting in signal phase changes. It is evident that the pre-edge peak (7705 eV) is more prominent in the χ_0 orientation, along with the main-edge 1 shoulder peak in the χ_0 orientations. In the EXAFS region, a shallow feature occurs over a wide energy range (7736–7767 eV) with the maximum intensity separation occurring at 7751 eV. Additionally, a further dichroic feature is notable further along the EXAFS tail between 7777–7802 eV with a maximum intensity separation at 7795 eV. These observable spectral features are very similar to those obtained for **1a** (Chapter 2, section 2.5).

The fluorescence spectra for $15a_{DCM}$ were also recorded at the Diamond Light Source (station B16) and show similar spectral features to the transmission spectra (Figure 4.7a). Due to unforeseen technical difficulties associated with a faulty electrometer measuring the photoelectron current, the fluorescence spectra obtained for $15a_{DCM}$ are noisy. However, the application of the Malus' fit[75] has provided a means of smoothing noisy data and has aided in its interpretation (assuming dichroic behavior follows Malus' law). Hence, the smoothed fluorescence spectra (4.7b) provided a qualitative description of the observed X-ray dichroism for the angles of χ experimentally obtained. Furthermore, modulation curves have been generated for the four most prominent dichroic features of the fluorescence spectra at 7705, 7718, 7729 and 7752 eV (Figure 4.8). In addition, the modulation curve obtained at the pre-edge feature using the Malus' fit (7705 eV) has been supplemented with experimental data (Figure 4.9) and shows a good agreement

A contour plot for $15a_{DCM}$ (Figure 4.10), generated from the fluorescence data, reveals the uniformity of the dichroic response over 360° of rotation. The sinusoidal behavior of the key spectral features (pre-edge, main-edge 1 and main-edge 2) as a function of angle can be clearly seen. Polarised XAS data was also collected for $15b_{DCM}$ at the Co K-edge and revealed similar features for the transmission and fluorescence as expected due to the isostructural and isomorphous nature of the two materials.
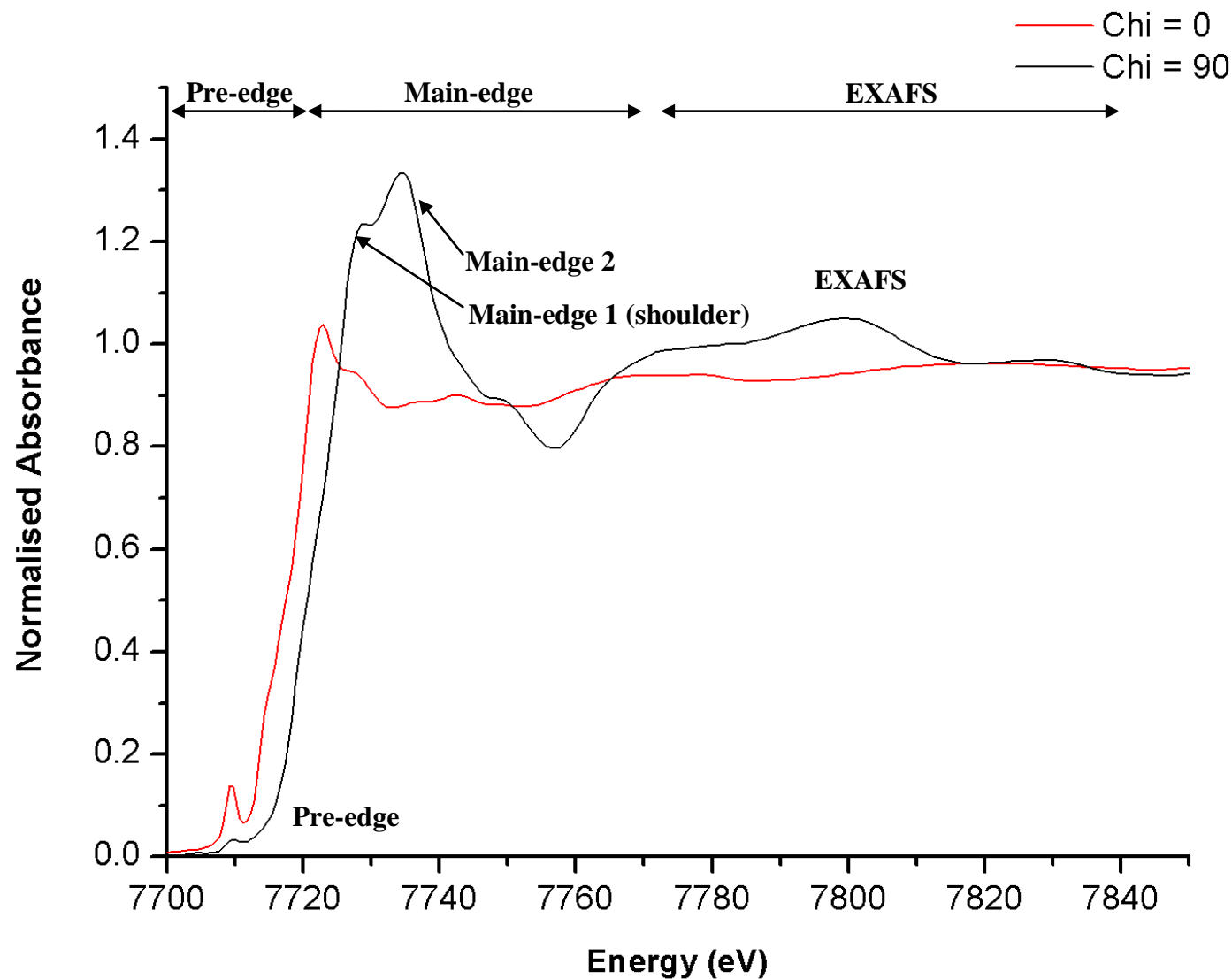
Figure 4.6 Normalised XAS spectra for **15a**$_{DCM}$ at the Co K-edge at orientations of χ_0 and χ_{90}. These data were obtained using the 70% polarised Diamond station I18 and have not been corrected to assume 100% polarisation. These data were normalised using the 'stepped edge approach' as described elsewhere.[74]

(a)

(b)
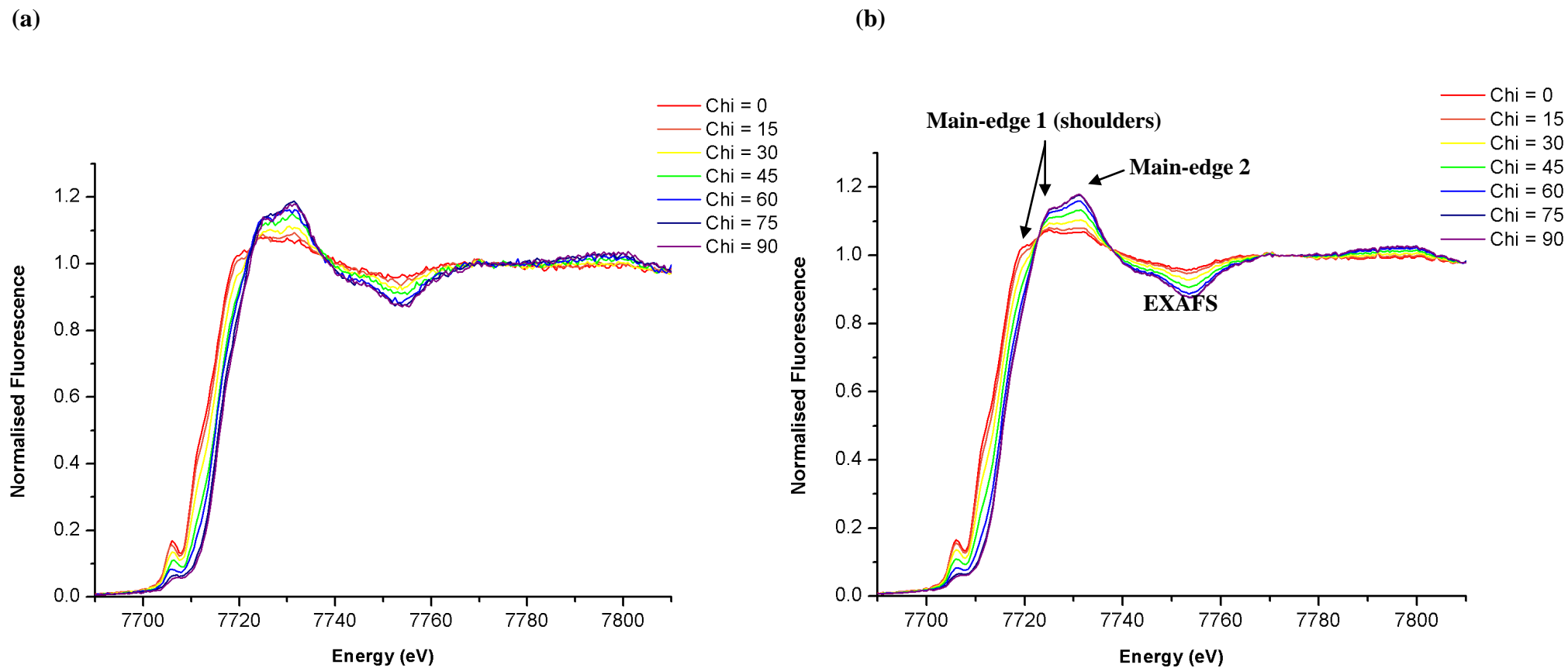
Figure 4.7 (a) Normalised[74] fluorescence XAS spectra for **15a**$_{DCM}$ at the Co K-edge for orientations of χ_0–χ_{90} along with (b) smoothed spectra obtained from using the Malus' fit. These data were obtained using Diamond station B16.
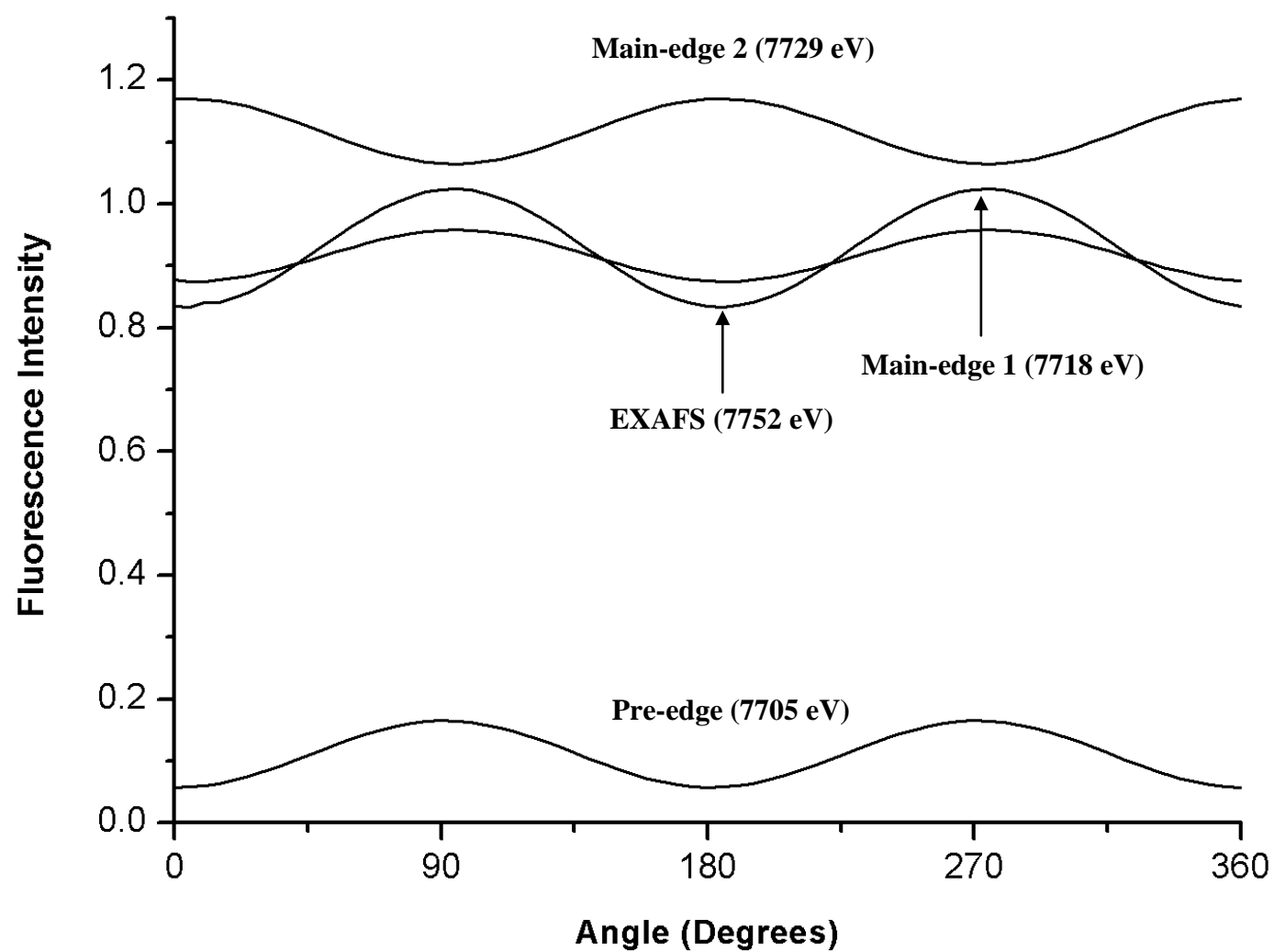
Figure 4.8 Malus' fitted modulation curves for **15a**$_{DCM}$ obtained from the pre-edge (7705 eV), main-edge 1 (7718 eV), main-edge 2 (7729 eV) and EXAFS (7752 eV) regions within the fluorescence XAS spectra at the Co K-edge.
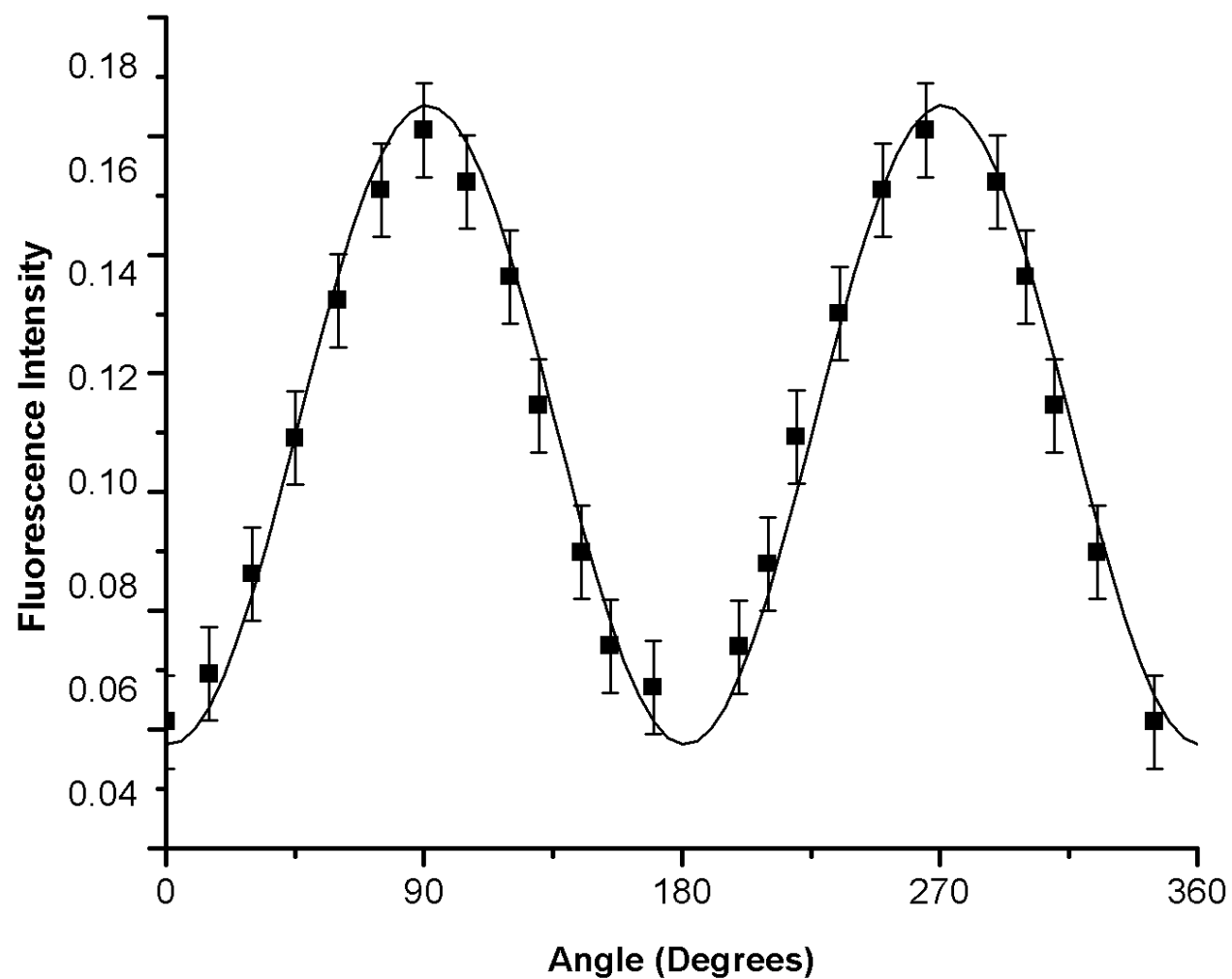
Figure 4.9 Modulation curve for the pre-edge feature (7705 eV) obtained from the XAS spectra of **15a**$_{DCM}$ obtained from from Malus' fitted fluorescence data (solid line) along with selected experimental fluorescence data (points) with associated error bars calculated using a χ^2 statistical analysis.
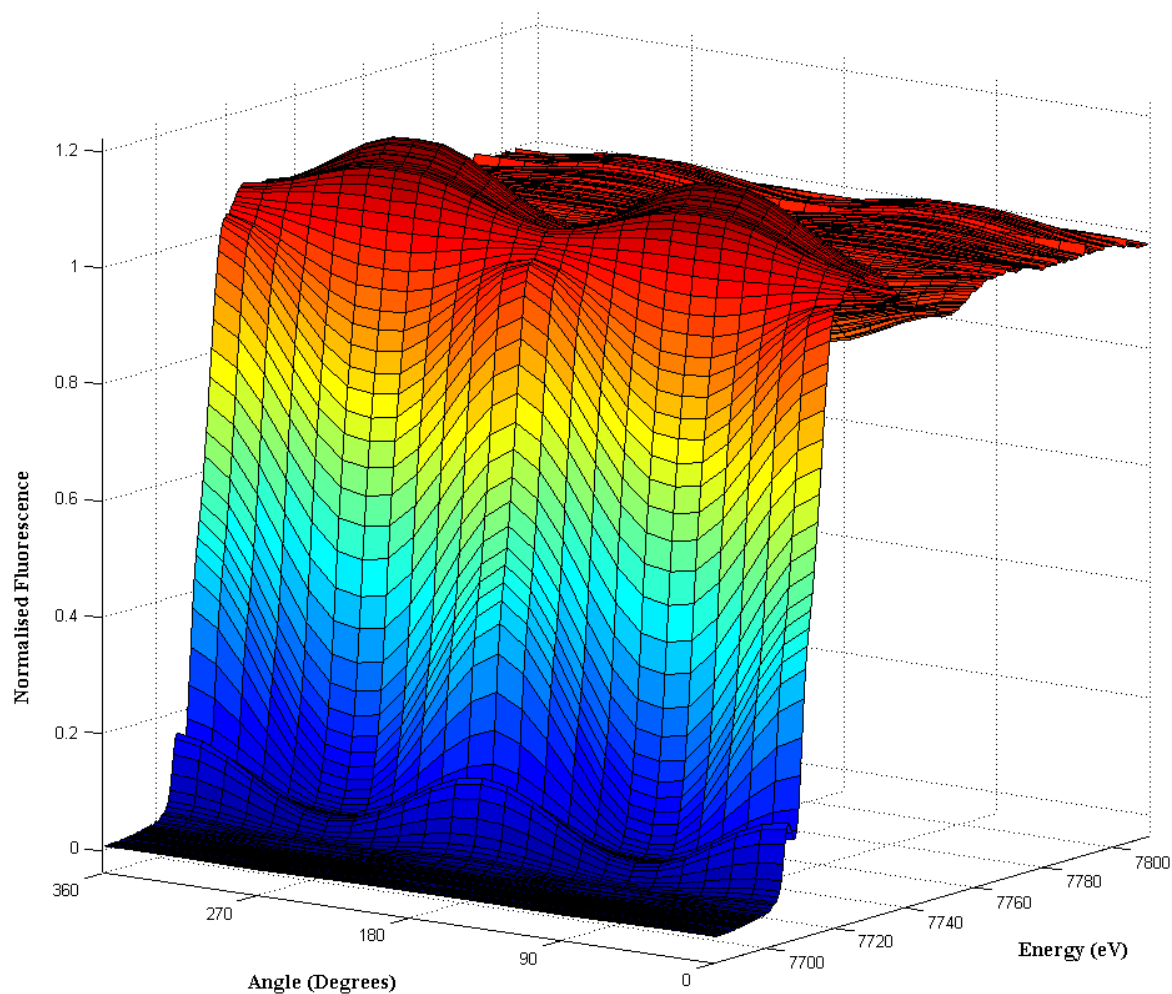
Figure 4.10 Malus' fitted contour plot of **15a**$_{DCM}$ obtained from experimental fluorescence data.

4.6.2 X-ray dichroism of 15a$_{DCM}$ at the Br K-edge (13450 eV)

A single crystal of **15a**$_{DCM}$ was also subject to an evaluation at the Br K-edge (13474 eV) and showed clear dichroic features in the main-edge region (13490–13500 eV), specifically, a shift in energy of the intense main-edge peak (Figure 4.11a). However, due to technical difficulties in recording the spectra, the EXAFS region could not be obtained. A modulation curve has been generated at the specific energy of 13497 eV and shows the expected sinusoidal behaviour (Figure 4.11b).

(a)
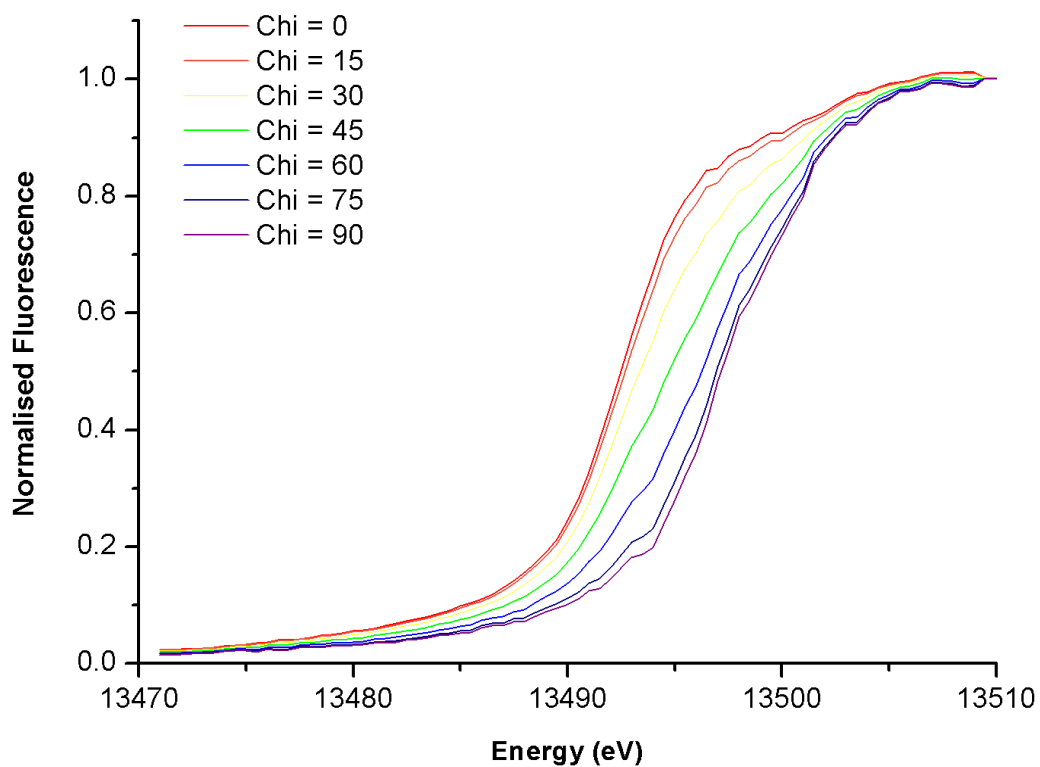
(b)
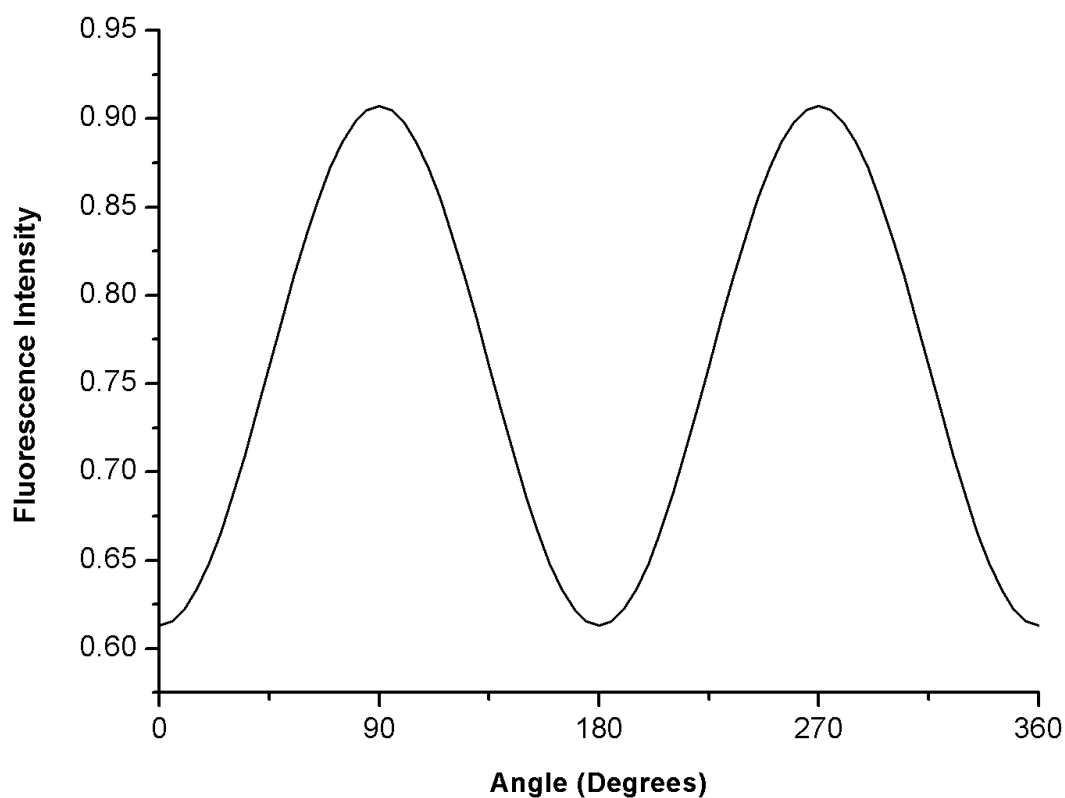
Figure 4.11 (a) Normalised[74] fluorescence XAS spectra for **15a**$_{DCM}$ at the Br K-edge for orientations of χ_0–χ_{90} along with (b) the Malus' fitted modulation curve at a selected energy (13497 eV) within the fluorescence XAS spectra. These data were obtained using Diamond station B16.

4.7 Using polarised X-ray absorption spectroscopy to study 18_{DCM} and 19_{DCM}

4.7.1 X-ray dichroism of 18_{DCM} at the V K-edge (5465 eV)

The transmission spectra (Diamond station I18) for vanadium-containing 18_{DCM} (Figure 4.12) also reveals several dichroic regions, namely the pre-edge (5454–5465 eV), main-edge (5470–5493 eV) and EXAFS (5492–5550 eV) regions. As described previously, the main-edge comprises two features, the main-edge 1 shoulder (5473 eV) and the main-edge 2 (5480 eV). Interestingly, the pre-edge feature (5460 eV) is significantly pronounced in comparison to **1a** and $15a_{DCM}$ and occurs most prominently in the χ_0 orientation when the X-ray polarisation vector is aligned with the V=O bond. With regard to the main-edge 1, a shoulder occurs in both orientations at 5473 eV with a noticeable difference in intensity for the two orientations. The main-edge 2 consists of an intense broad feature with differing energies and intensities for each orientation [5484 eV (χ_0), 5480 eV (χ_{90})]. The EXAFS region contains a much shallower feature occurring over a broad energy range with the maximum intensity separation occurring at 5505 eV. It is also evident that further dichroic features may be observed in the furthest EXAFS tail (*ca.* 5540 eV).

The fluorescence spectra (Diamond station B16) support the transmission spectra but are noisy due to technical problems associated with this beamline (Figure 4.13). It may be feasible that a combination of crystal size and instrument malfunction may be responsible for the lower quality fluorescence data. Nevertheless, similar features are observed using both detection modes. Modulation curves have been generated for the most prominent dichroic features, namely the pre-edge, main-edge 2 and the EXAFS using fluorescence data (Figure 4.14). On inspection of these curves, the pre-edge feature gave the largest modulation curve and may contribute significantly to the overall dichroic response displayed by 18_{DCM}. In addition, modulation curves can also be generated for transmission data (Diamond station I18) and are similar, showing consistency between the two techniques (Figure 4.15). The experimental fluorescence data used to construct the Malus fit also shows good agreement with the transmission data.
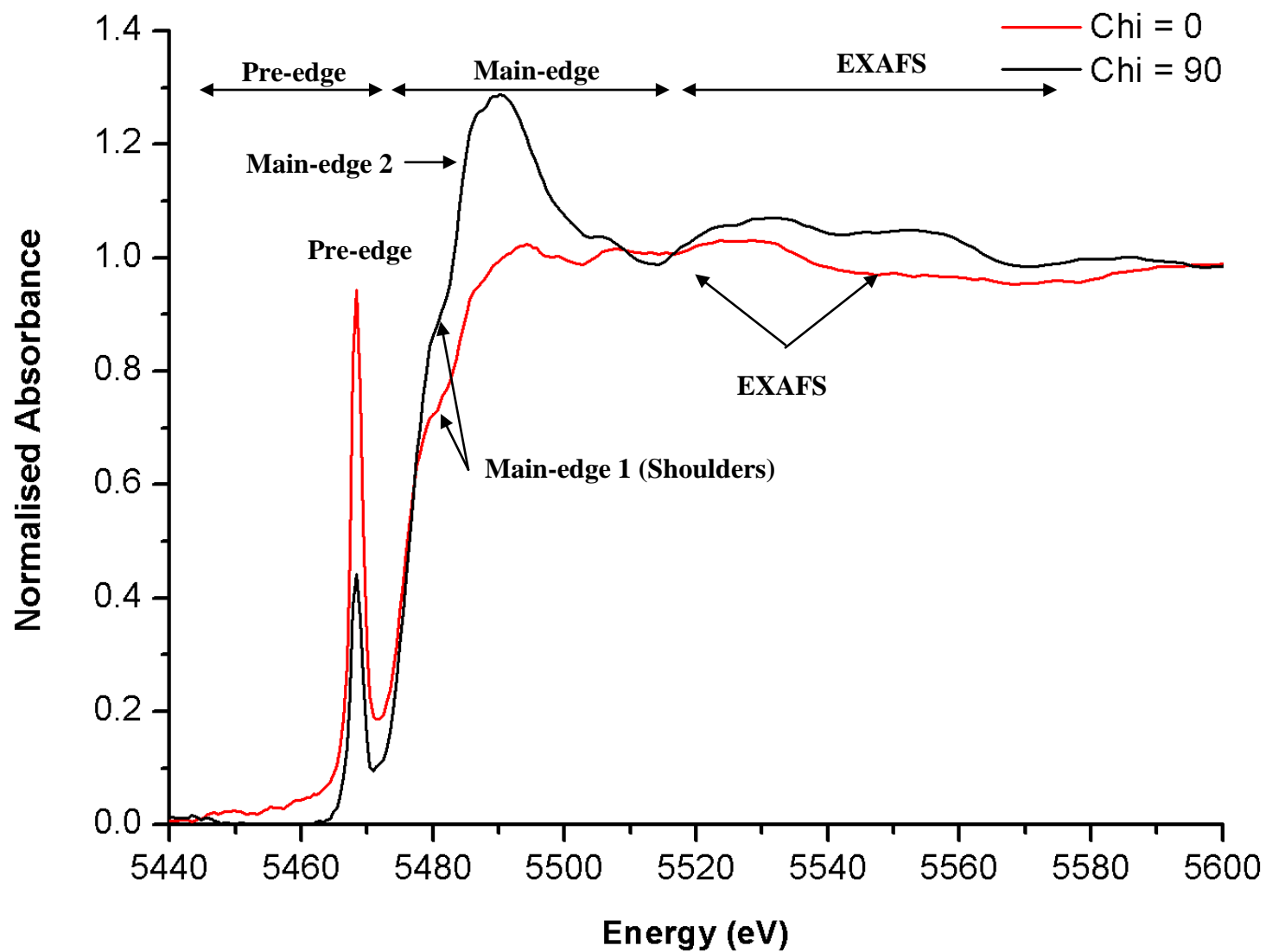
Figure 4.12 Normalised[74] XAS spectra for **18**$_{DCM}$ at the V K-edge for orientations of χ_0 and χ_{90}. These data were obtained using the 70% polarised Diamond station I18 and have not been corrected to assume 100% polarisation.
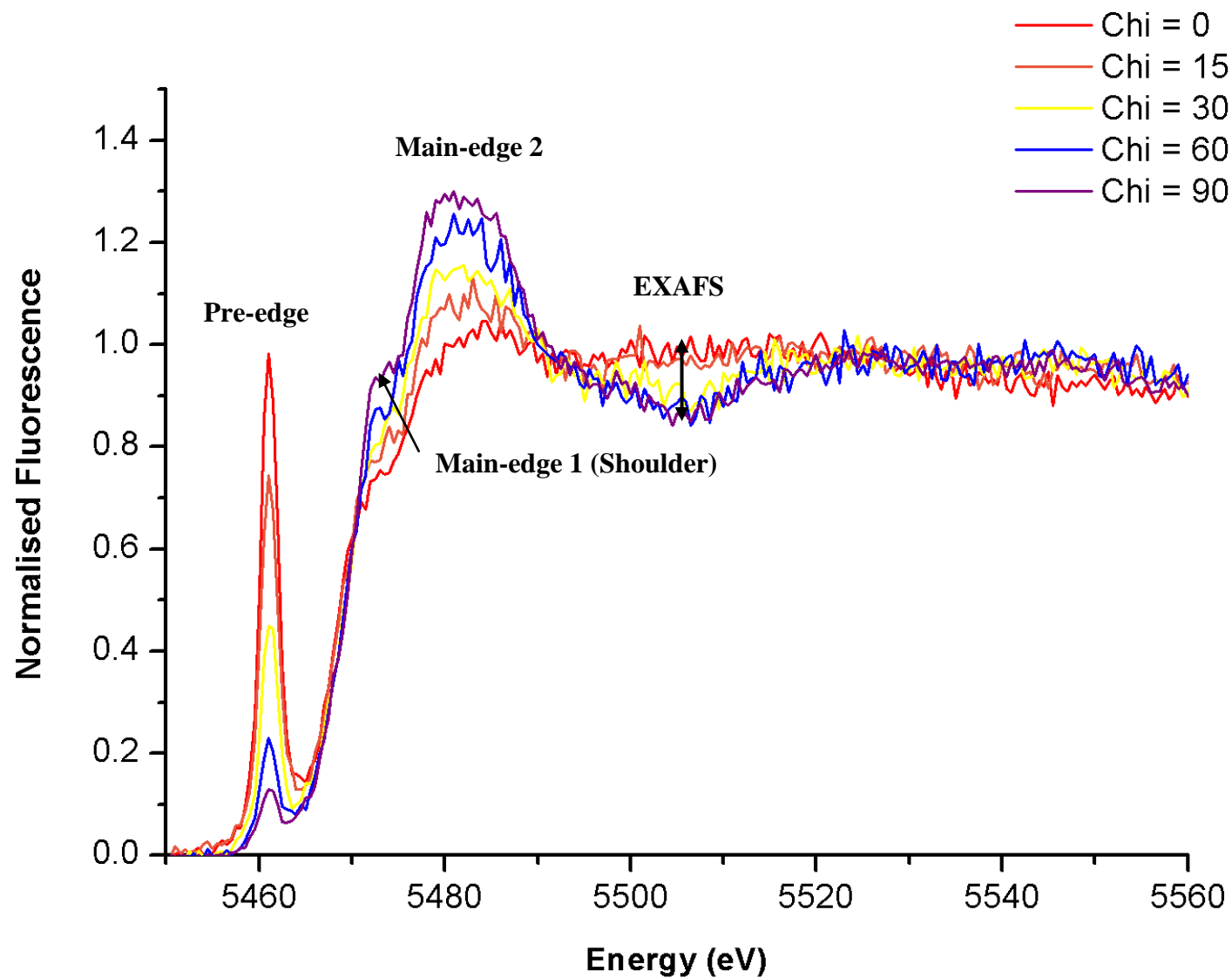
Figure 4.13 Normalised[74] fluorescence XAS spectra for **18**$_{DCM}$ at the V K-edge for orientations of χ_0, χ_{15}, χ_{30}, χ_{60} and χ_{90}. These data were obtained using Diamond station B16.
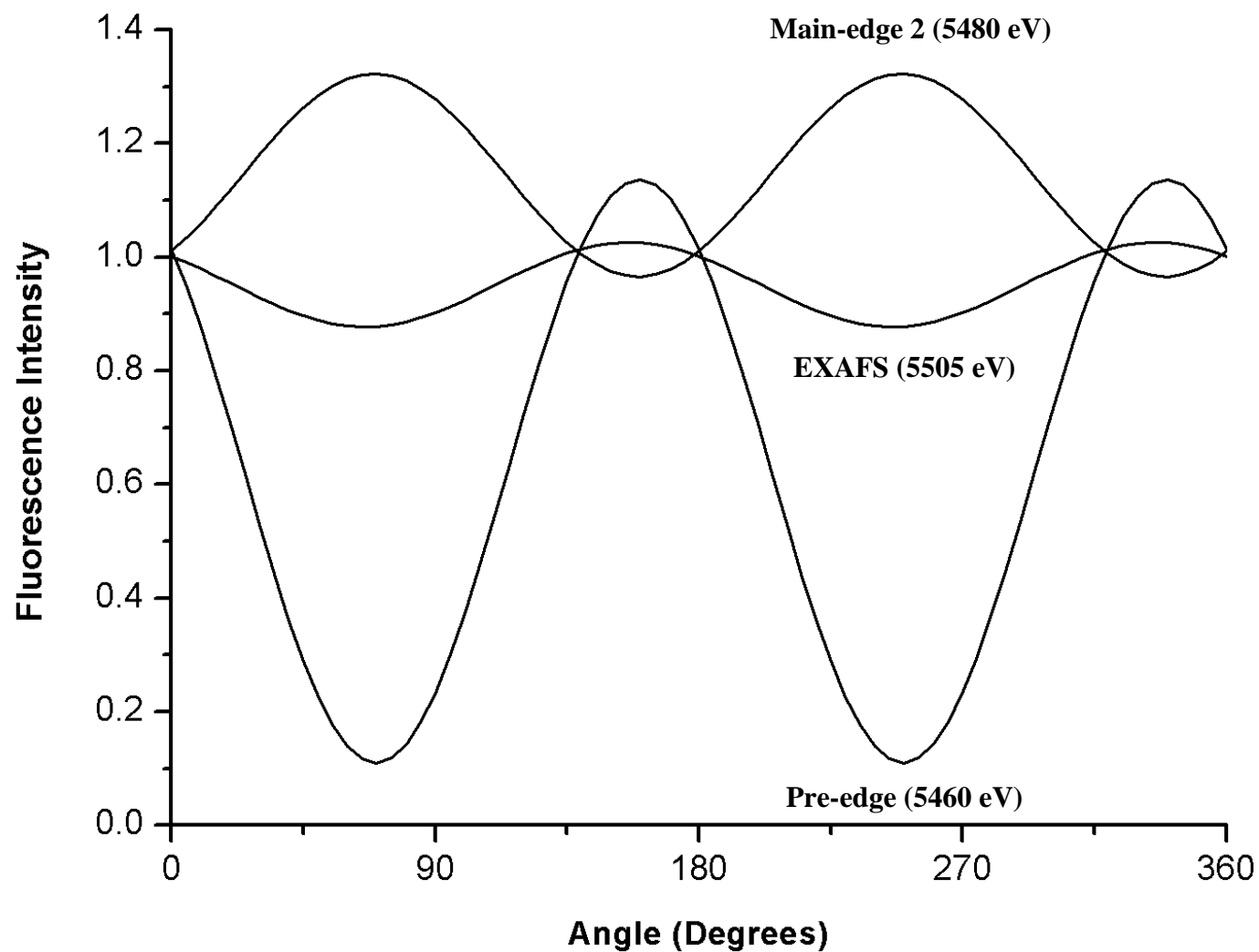
Figure 4.14 Malus' fitted modulation curves for **18**$_{DCM}$ obtained from the pre-edge (5460 eV), main-edge 2 (5480 eV) and EXAFS (5505 eV) regions within the fluorescence XAS spectra.

Figure 4.15 Modulation curves at the selected pre-edge energy (5460 eV) within the XAS spectra of **18**$_{DCM}$ for the Malus' fitted fluorescence (Diamond station B16) and 100% polarisation corrected transmission data (Diamond station I18), along with data points from experimental fluorescence data (Diamond station B16) with associated error bars calculated using a χ^2 statistical analysis.

4.7.2 X-ray dichroism of 19_{DCM} at the Ti K-edge (4966 eV)

The single crystal of titanium-containing 19_{DCM} employed for this study was very small and as a consequence (along with technical difficulties associated with the B16 beamline), only extremely noisy fluorescence data were obtained which could only be reliably interpreted at the pre-edge. Nevertheless, on inspection of the polarised XAS spectrum (Figure 4.16), an intense dichroic feature is evident at the pre-edge (4962 eV), which was more prominent in the χ_0 orientation. The application of the Malus' fit has aided in smoothing the noisy data and a modulation curve has successfully been generated at the energy of the pre-edge feature which generally shows a good agreement between the experimental data and the Malus' fit (Figure 4.17).

Interestingly, on closer observation of the polarised XAS spectra for 19_{DCM}, other spectral features can be speculatively assigned on the basis of previously obtained spectra for related complexes (*e.g.*, 18_{DCM}). These are namely the main-edge 1 shoulder (4975 eV) and broad, intense main-edge 2 region (*ca.* 4980 eV) which are all apparently more prominent in the χ_{90} orientation. Unfortunately, in the χ_0 orientation the main-edge 2 region appears flat. It is noteworthy that work is currently in progress to smooth and further interpret these data.
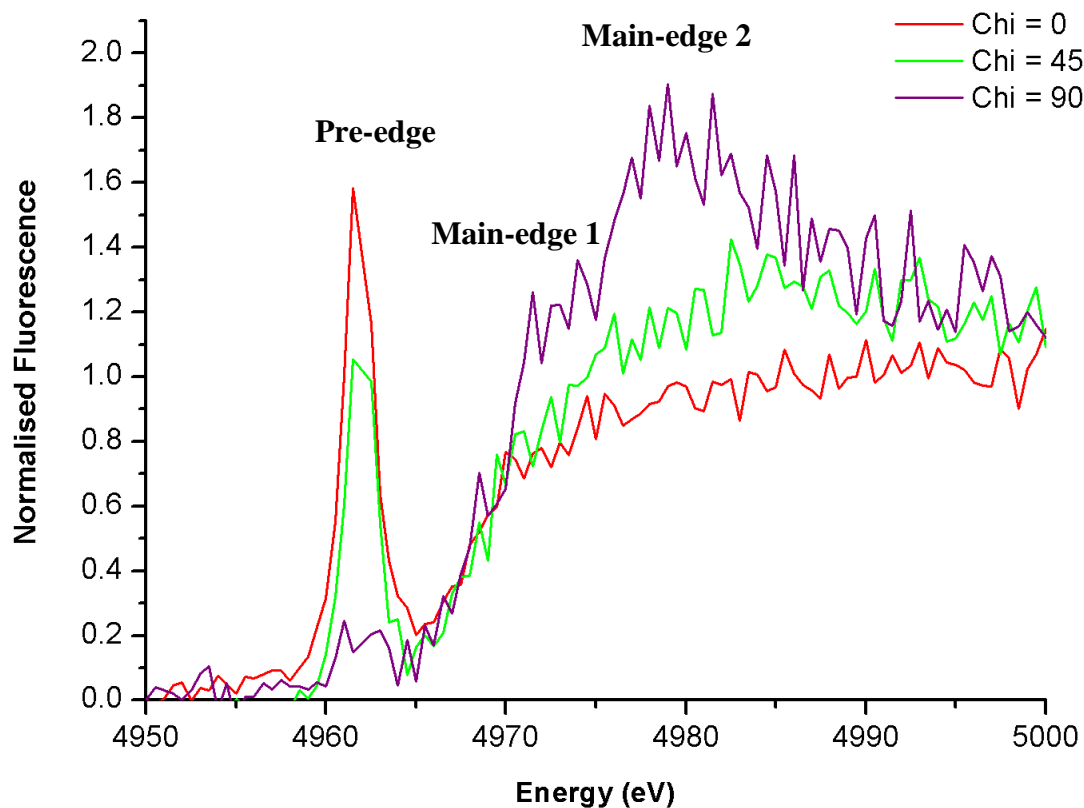
Figure 4.16 Normalised[74] fluorescence XAS spectra at the Ti K-edge for orientations χ_0, χ_{45} and χ_{90} for **19**$_{DCM}$. These data were obtained using the Diamond station B16.
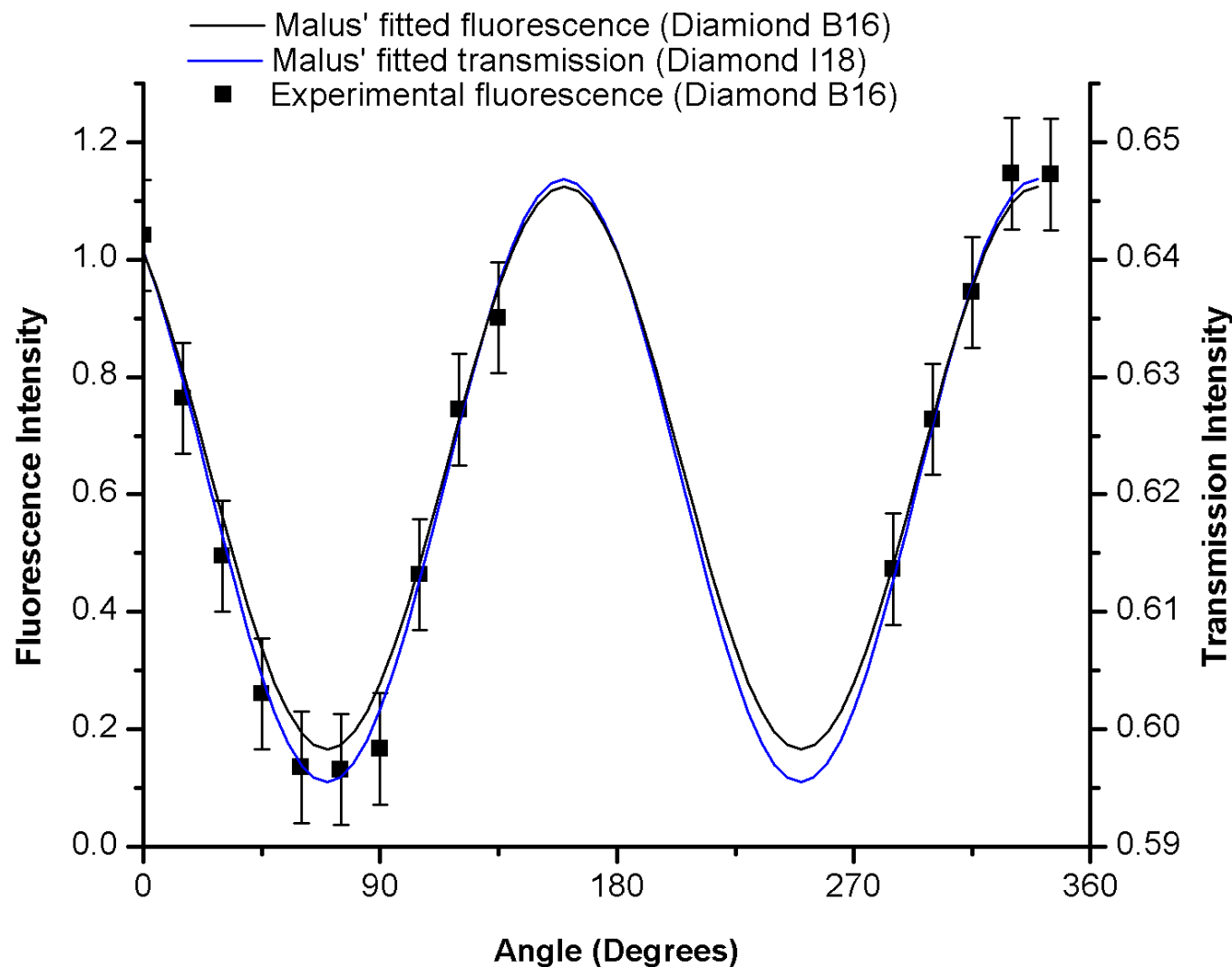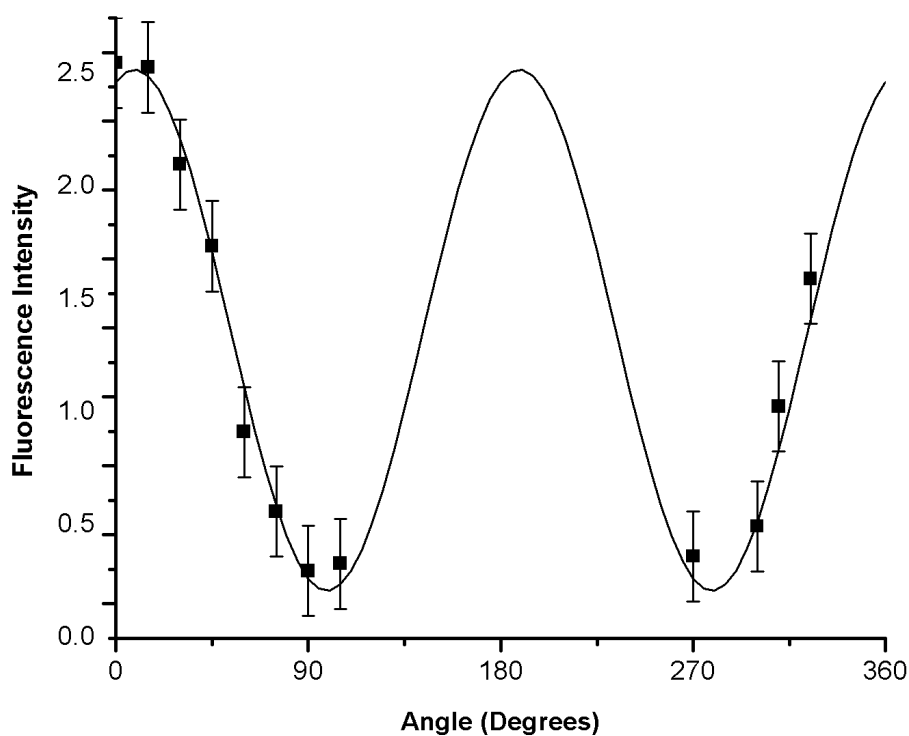

Figure 4.17 Modulation curve for the pre-edge feature (4962 eV) within the XAS spectra of **19**$_{DCM}$ obtained from Malus' fitted fluorescence data (solid line) along with selected experimental fluorescence data (points) with associated error bars calculated from a χ^2 statistical analysis.

4.8 Using polarised X-ray absorption spectroscopy to study 16$_{DCM}$, 17$_{DCM}$ and 17$_{benzene}$

4.8.1 X-ray dichroism of 16$_{DCM}$ at the Fe K-edge (7112 eV)

The polarised XAS fluorescence spectrum (Diamond station B16) for single crystals of iron-containing **16**$_{DCM}$ also revealed dichroic features in the pre-edge (7100–7110 eV), main-edge (7110–7140 eV) and EXAFS (7140–7200 eV) regions like the polarised XAS spectra of previously described complexes in this thesis. The main-edge could also be subdivided into two regions, namely the main-edge 1, appearing as a shoulder in the χ_0 orientation (7120 eV) along with the broad main-edge 2, occurring in both orientations at 7127 eV and 7130 eV, respectively. Additionally, **16**$_{DCM}$ displayed a pre-edge feature at 7107 eV which occurred more prominently in the χ_0 orientations. Isobestic points are manifested within the main edge 1 at 7125 eV as well as in the EXAFS at 7140 eV and 7164 eV. A shallow change in the intensity is prominent in the EXAFS region over a wide energy range between the two aforementioned isobestic points with a maximum difference in intensity occurring at 7151 eV. In addition, modulation curves at the most prominent dichroic energies have been generated for **16**$_{DCM}$ and displays the expected sinusoidal appearance (Figure 4.18).
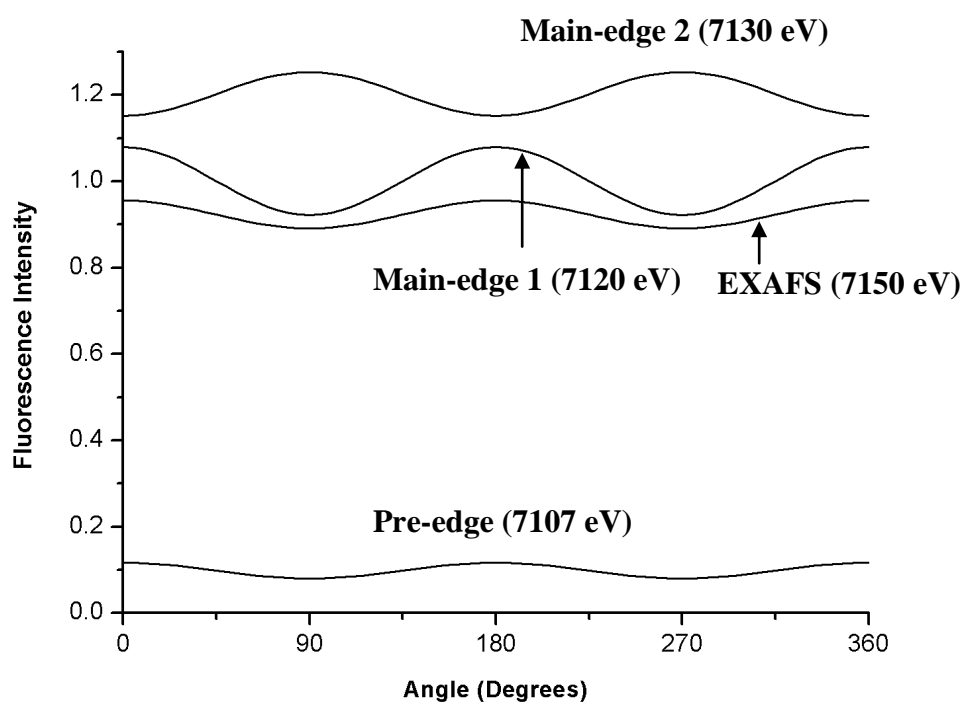
Figure 4.18 Malus' fitted modulation curves obtained from the pre-edge (7107 eV), main-edge 1 (7120 eV) main-edge 2 (7130 eV) and EXAFS (7150 eV) regions within the fluorescence XAS spectrum of **16**$_{DCM}$.

4.8.2 X-ray dichroism of 17$_{DCM}$ at the Mn K-edge (6539 eV)

Intermolecular alignment is considered important for an effective dichroic response (Chapter 1, section 1.7.1 and 1.13). In order to test this hypothesis, **17**$_{DCM}$ was evaluated in order to establish whether it would display any X-ray dichroism. Based on the fact that **17**$_{DCM}$ is disordered in the solid state (section 4.4), it was expected that limited or no dichroism should be evident. The benzene solvate **17**$_{benzene}$, on the other hand, showed some improvement in the intermolecular order, unfortunately however, this material was not subject to an X-ray dichroic evaluation. Moreover, single crystals of highly ordered **17**$_{toluene}$ were not of sufficient quality to allow conformation of its favorable alignment characteristics.

Unlike metallo-porphyrin systems **16**$_{DCM}$ **15a**$_{DCM}$, **15b**$_{DCM}$, **18**$_{DCM}$ and **19**$_{DCM}$ (which show a high degree of intermolecular order in the solid state), X-ray dichroism is not clearly visible at the manganese K-edge for **17**$_{DCM}$. The polarised XAS spectra in fluorescence mode for both orientations of χ are almost identical, with no *significant* changes in energy or intensity of the spectral features apparent between the two. On inspection of these spectra (Figure 4.19) several features are apparent, namely a pre-edge feature occurring at 6534 eV, a main-edge 2 feature with diminished shoulder definition occurring at 6557 eV and interestingly, the expected shallow EXAFS feature is also greatly reduced. Notably however, modulation curves revealed some X-ray dichroism at the pre-edge, main-edge 1 and EXAFS regions that are significantly weaker in comparison to those of the related **15**$_{DCM}$, **16**$_{DCM}$, **18**$_{DCM}$ and **19**$_{DCM}$. It is clear that the minimal X-ray dichroism in **17**$_{DCM}$ is likely due to the observed intermolecular disorder with respect to neighbouring Mn–Br bonds (see Figure 4.3b).

Figure 4.19 Normalised[74] fluorescence XAS spectra for **17**$_{DCM}$ at the Mn K-edge for orientations of χ_0–$\ch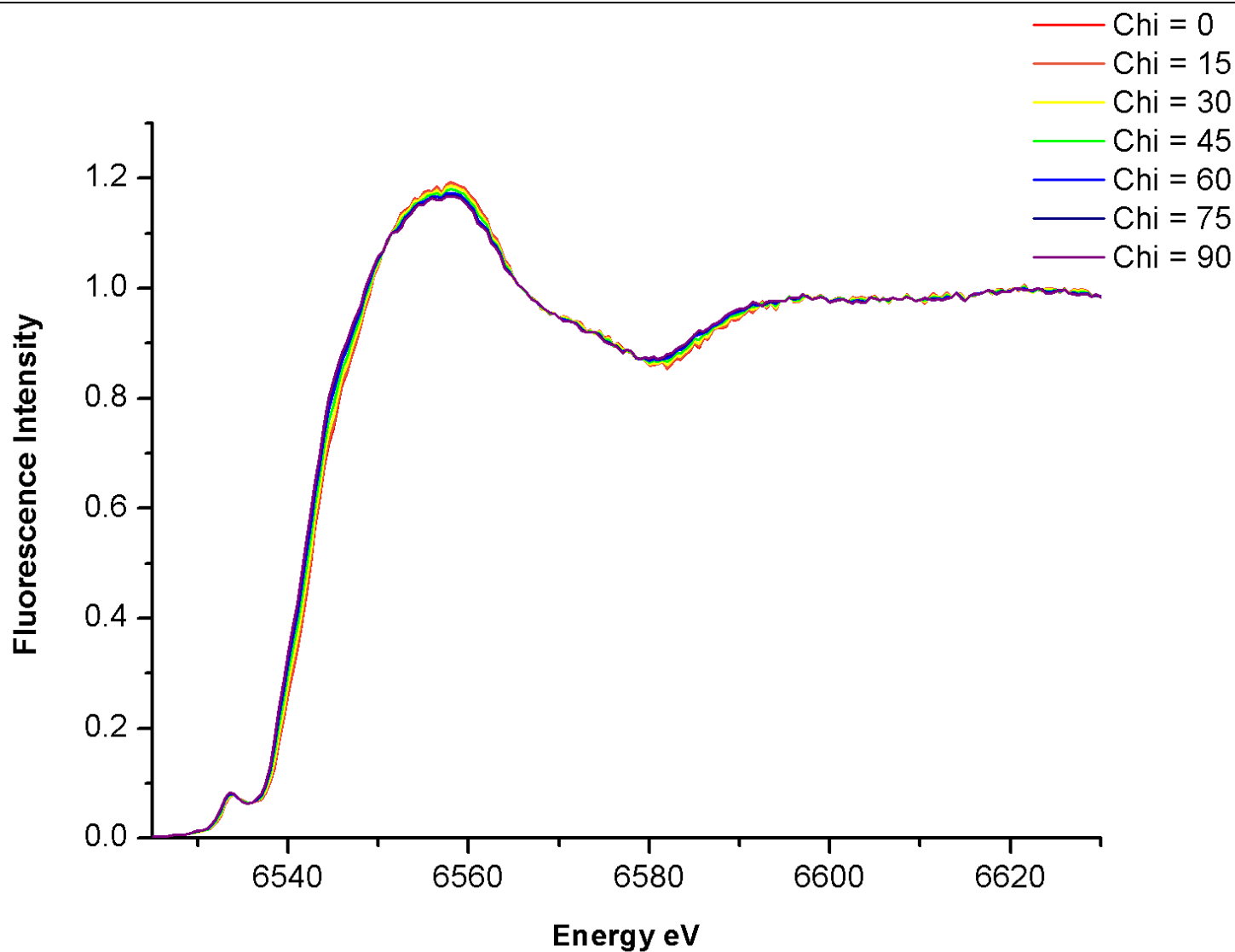i_{90}$. These data were obtained using Diamond station B16. Note: Data for χ_0 and χ_{90} orientations have been obtained experimentally. All other angles have been interpolated using the Malus' fit.

4.9 Quantification of the performance of metallo-tetraphenylporphyrin systems as dichroic filters

The transmission data for cobalt-containing $15a_{DCM}$ and vanadium-containing 18_{DCM} has been used to calculate the figure of merit, R_γ in a similar fashion to that of $1a$ (Chapter 2, section 2.6) as a way of comparatively evaluating their performances as potential X-ray dichroic filter materials. Unfortunately, due to technical difficulties associated with the Diamond Light Source (station B16), namely the faulty electrometer, the transmission data for $15b_{DCM}$, 16_{DCM} and 19_{DCM} could not be obtained, therefore, a figure of merit could not be reliably calculated.

Complex $15a_{DCM}$ has an R_γ value of 0.44 at 7735 eV (main-edge 1), whilst 18_{DCM} has an R_γ value of 0.42 at 5468 eV (pre-edge). Two points emerge from these observations (Figure 4.20). Firstly, the R_γ values for $15a_{DCM}$ and 18_{DCM} are lower than that of $1a$ (0.64, Chapter 2, section 2.6) which suggests that these metallo-porphyrin systems ($15a_{DCM}$ and 18_{DCM}) are improved relative to the dicopper-containing $1a$. This may arise from more efficient molecular packing along with the more regular crystal morphology observed. Note however, that the comparison of R_γ values of these two different chemical systems ($15a_{DCM}$, 18_{DCM} *vs.* $1a$) is only a guide, rather than a definitive comparison of their performances. Secondly, it is evident that the dichroism displayed by $15a_{DCM}$ is most prominent at the main-edge 1, whilst in 18_{DCM} it is greatest in the pre-edge (this observation is also clear from inspection of Figures 4.6 and 4.12).

Interestingly, unlike copper-containing $1a$, single crystals of metallo-porphyrin systems survived ultra-high vacuum conditions (six months to one year at 10^{-7} Torr) and appear to have maintained their crystallinity without apparent desolvation. Efforts are in progress to re-examine their structure and morphology by single crystal X-ray diffraction.
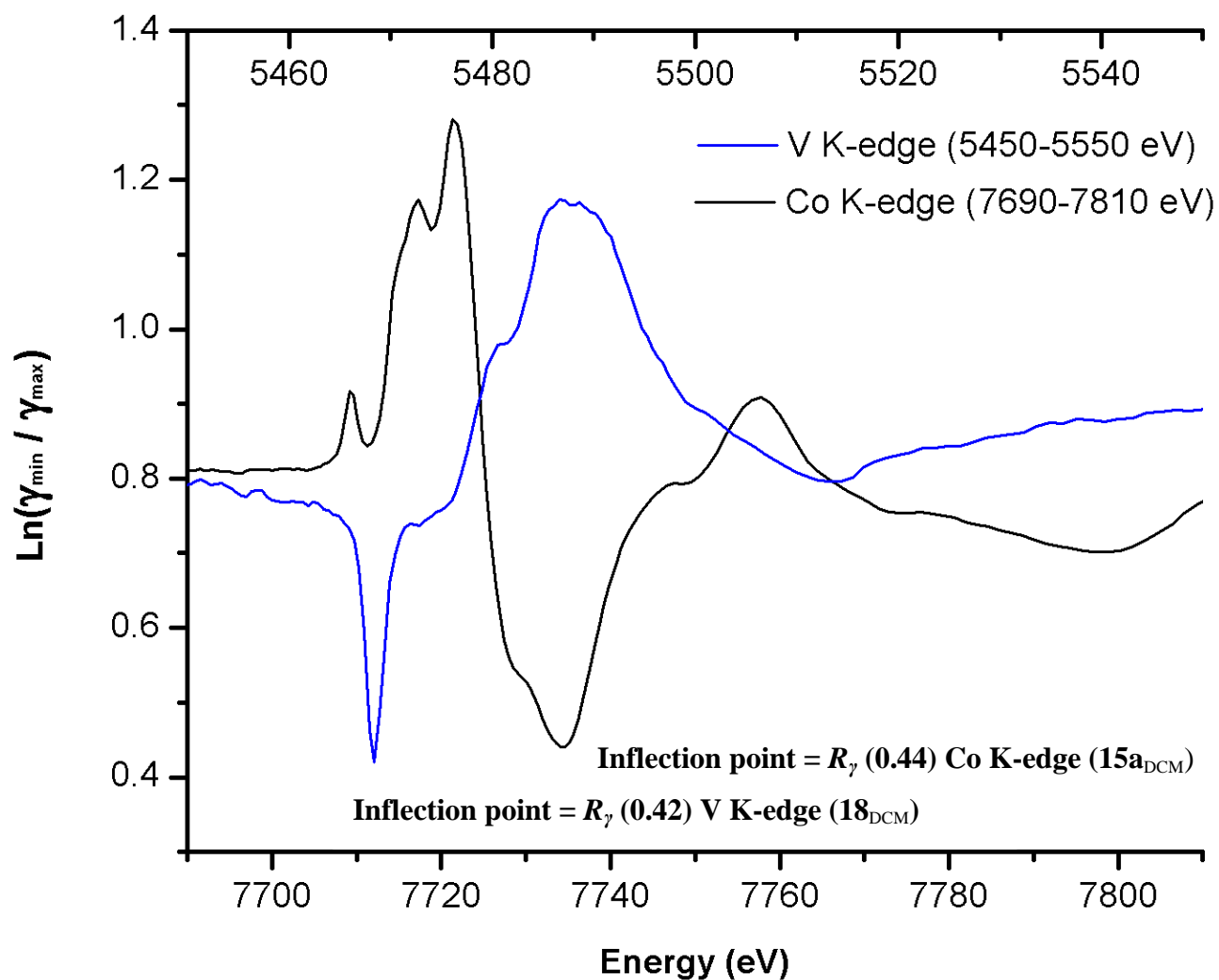
Figure 4.20 A plot of the natural log of the ratio of absorption co-efficient *vs.* energy for **15a**$_{DCM}$ and **18**$_{DCM}$ at the Co and V K-edges, respectively R_γ can be interpreted from the inflection points.

4.10 Using multiple scattering calculations to model 15a$_{DCM}$ and 18$_{DCM}$

Using the stepwise methodology outlined in Chapter 2, **15a$_{DCM}$** and **18$_{DCM}$** were the subject of an investigation to model the polarised XAS spectra using the previously established multiple scattering, FEFF approach. Unlike the detailed description of **1a** given in Chapter 2, only the most significant results for **15a$_{DCM}$** and **18$_{DCM}$** will be discussed in this section, with the presentation of their best fit spectra.

The comparative inspection of the FEFF calculated spectra for **18a$_{DCM}$** in both χ orientations (Figure 4.21) has revealed a good agreement with experimental data. In particular, FEFF has modelled the intense sharp singlet pre-edge feature with accuracy. In addition, the fine-structure within the general main-edge region, including the main-edge 1 shoulder in the χ_{90} orientation has also been reproduced. On the other hand, the FEFF generated XAS spectra of **15a$_{DCM}$** (Figure 4.22) also appeared to model the main-edge 1 and 2 regions well in the χ_{90} orientation, including the spectral detail within the EXAFS region. However, in the χ_0 orientation, the pre-edge region and the appearance of the main-edge 2 did not precisely agree with the experimental data; specifically, the pre-edge feature adopts more of a shoulder definition, with the main-edge 1 appearing flatter than that apparent in the experimental spectrum. Nevertheless, in general, the FEFF calculated spectra for **15a$_{DCM}$** do resemble the significant features displayed in the experimental data. Due to the disorder associated with the bromine atoms in the crystallographic data for **15a$_{DCM}$** (on which the cluster model is based), the metal centre sits artificially located in the porphyrin plane as opposed to either above or below it. Hence, in an attempt to disrupt the symmetry caused by this disorder, the Co-Br bond was deliberately moved 0.5 Å above the porphyrin plane. However, this afforded only minor improvements to the FEFF calculated spectra. In comparison to **1a**, the LDOS analysis of **15a$_{DCM}$** and **18$_{DCM}$** revealed similar information; namely, metal-apical ligand interactions/hybridisation at the pre-edge below the Fermi level (-9 eV) along with transitions into resonance states above the Fermi edge that comprise the main-edge.

(a)

(b)

Figure 4.21 Best fit FEFF calculated polarised XAS spectra for **18**$_{DCM}$ at the V K-edge with a comparison to experimental XAS data for **18**$_{DCM}$ in transmission mode (Diamond Station I18) in (a) the χ_0 orientation and (b) χ_{90} orientation. Experimental data has not been corrected for 100% polarisation.

(a)

(b)

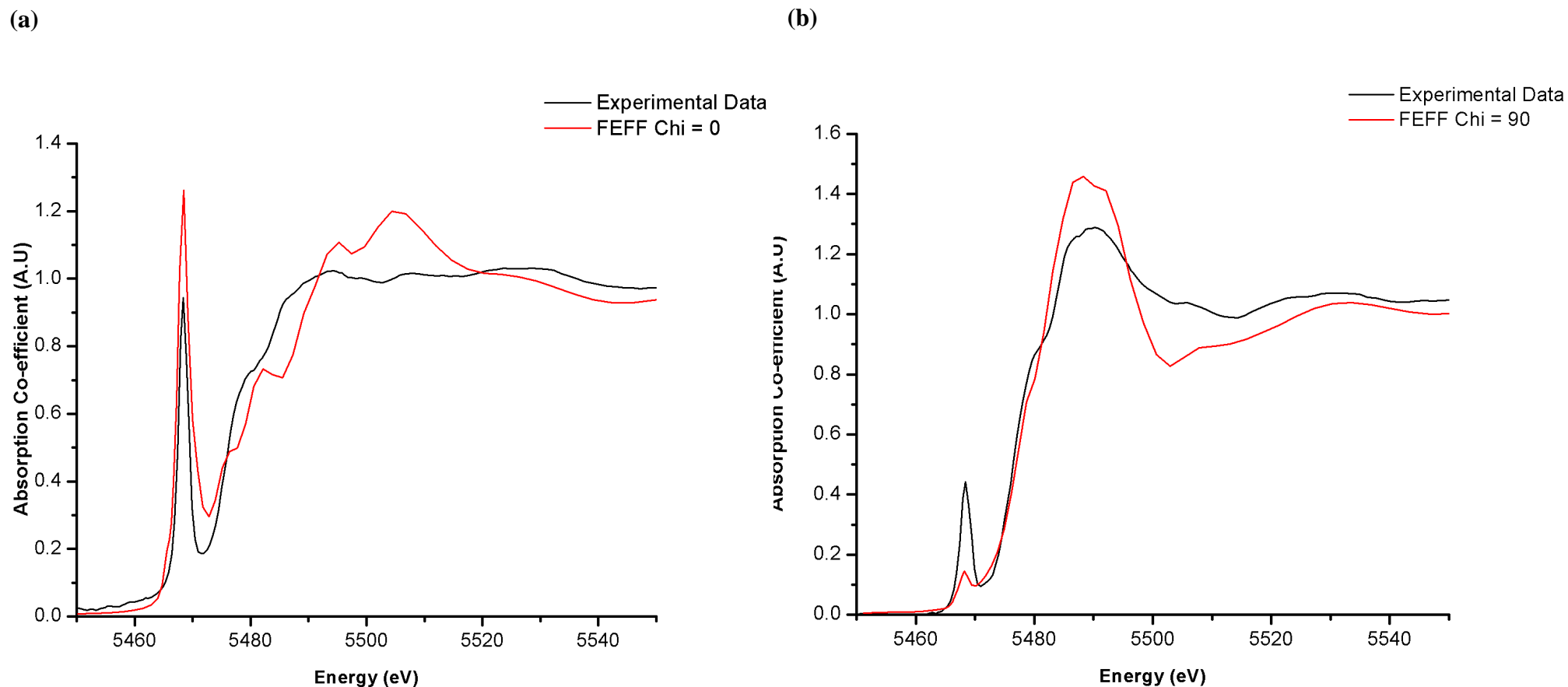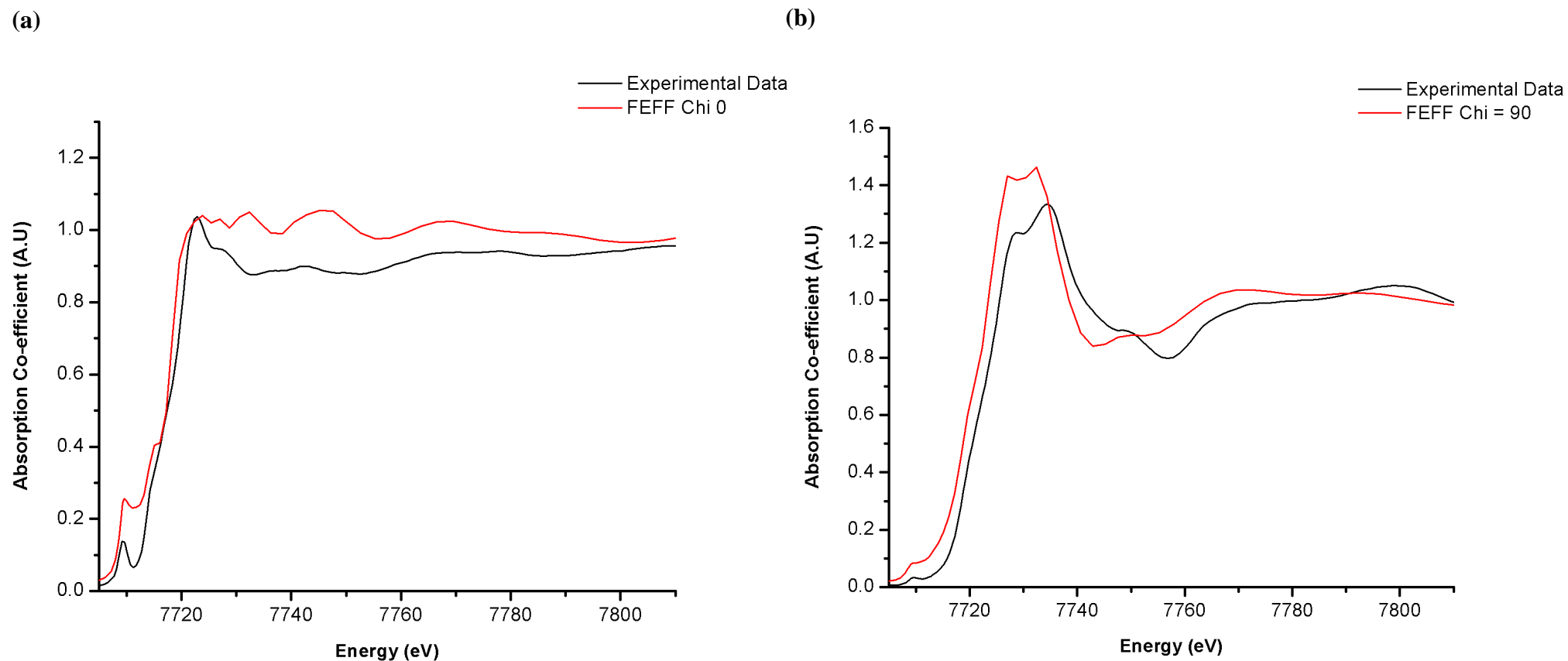**Figure 4.22** Best fit FEFF calculated polarised XAS spectra for **15a**$_{DCM}$ at the Co K-edge with a comparison to experimental XAS data for **15a**$_{DCM}$ in transmission mode (Diamond Station I18) in (a) the χ_0 orientation and (b) χ_{90} orientation overlaid. Experimental data has not been corrected for 100% polarisation.

4.11 Development of multi-edge *hybrid filters*

4.11.1 Background

In Chapter 2, oxalate-bridged **1a** was shown to exhibit X-ray dichroism at the Cu and Br K-edges, and in this chapter it has been shown that cobalto-porphyrin bromide **15a**$_{DCM}$ performs in a similar fashion, thus introducing the concept of *dual-edge* or *hybrid filter* materials. In an X-ray astronomical application, one particular design of a potential filter instrument could involve the use of a revolving wheel with windows in the wheel incorporating materials at different K-edges which could be selected as required. However, a device intended for an astrophysical mission (*e.g.*, IXO, see Figure 4.23) should be lightweight and as mechanically/electronically simple as possible. Therefore, expanding on the *hybrid filter* ideas outlined in Chapter 2, it would be feasible to develop compact, simple materials incorporating multiple K-edges in one molecule, therefore adopting a chemical engineering approach rather than a mechanical engineering solution.
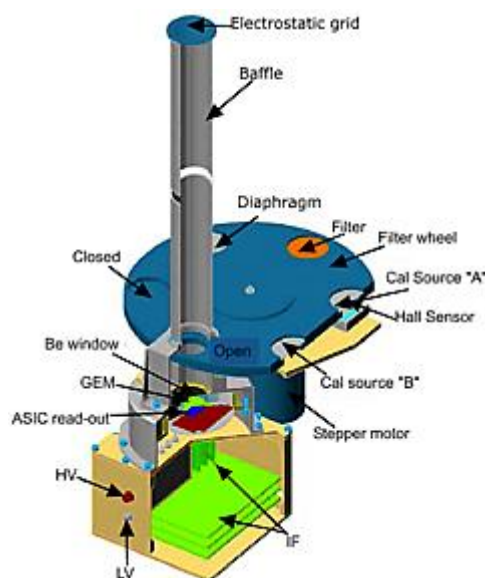
Figure 4.23 A potential filter wheel based X-ray polarimeter design of XPOL for intended use on board IXO.[76]

In this section, the family of A_4 metallo-porphyrins based on the TPP^{2-} ligand will be developed to include A_2B_2 metallo-porphyrins by utilising halogen atoms in *trans*-phenyl rings within the periphery of the metallo-porphin. By varying the halide atom at both the phenyl-ring and the metal centre, a potential tri-edge filter can, in principle, be synthesised. In a recent study, the synthesis of such free halide-substituted A_2B_2 porphyrins have been reported,[77] however, to the knowledge of the author these have never been metallated, or even crystallographically characterised (Scheme 4.2 and 4.3).

4.11.2 Synthesis and characterisation of [(Y$_2$-TPP)FeX] [Y = Cl, X = Br (20a$_{chloroform}$); Y = Br, X = Cl (20b$_{chloroform}$); Y = X = Br (20c$_{chloroform}$)]

a) Preparation of Y$_2$-TPPH$_2$ (Y = Cl, Br)
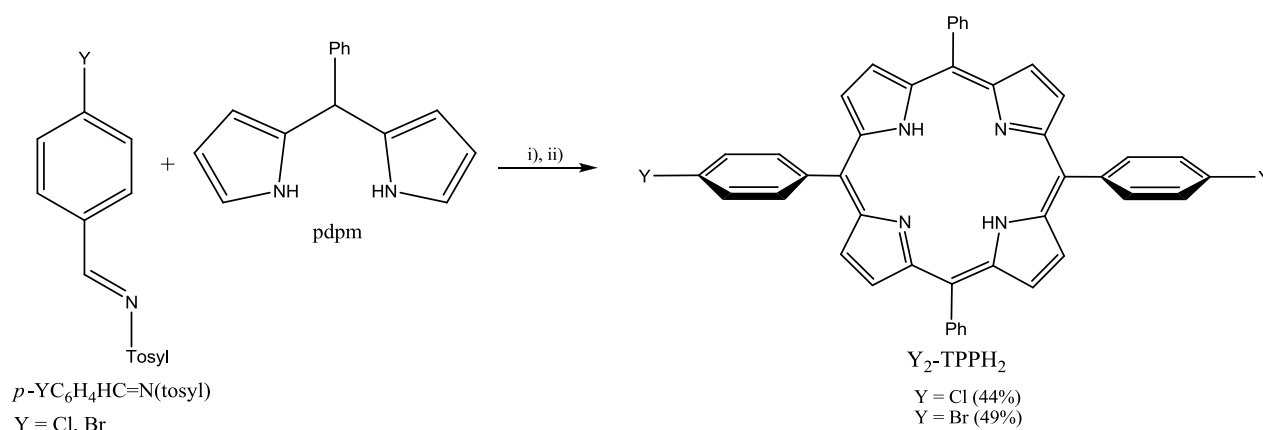
Scheme 4.2. *Reagents and conditions*: i) *p*-YC$_6$H$_4$HC=N(tosyl) (Y = Cl, Br), Cu(OTf)$_2$ (10 mol%), DDQ, 2 h, rt; ii) silica gel chromatography, DCM.

Phenyldipyrrolemethane could be synthesised as described elsewhere[78,79] by condensation of benzaldehyde and pyrrole in the presence of copper(II) triflate. Likewise, the target A_2B_2 porphyrin pro-ligands, Y$_2$-TPPH$_2$ (Y = Cl, Br), could be obtained by treating phenyldipyrrolemethane with the corresponding aryltosylimine[80] in the presence of a catalytic quantity of copper(II) triflate and 2,3-dichloro-5,6-dicyano-1,4-benzoquinone (DDQ) in dichloromethane using the reported methodology (Scheme 4.2).[77]

The X-ray structure of either Cl$_2$-TPPH$_2$ or Br$_2$-TPPH$_2$ could not be obtained, however, treatment of Br$_2$-TPPH$_2$ with concentrated hydrochloric acid in methanol led to the isolation of the salt,

Br$_2$-TPPH$_2$·2HCl which gave single crystals on recrystallisation from chloroform. The molecular structure is depicted in Figure 4.24; selected bond lengths and angles are given in Table 4.4.

The molecular structure of Br$_2$-TPPH$_2$·2HCl consists of a puckered di-protonated porphyrin ring with the two 4-bromophenyl rings located at the periphery of the porphyrin macrocycle and arranged mutually *trans*. Above and below the porphyrin ring are two chloride anions which are held in place by hydrogen bonding interactions from the N-pyrrole-protons [H···Cl(1) = 2.334, 2.401 Å; H···Cl(2) = 2.394, 2.436 Å] and lattice solvent molecules of chloroform.
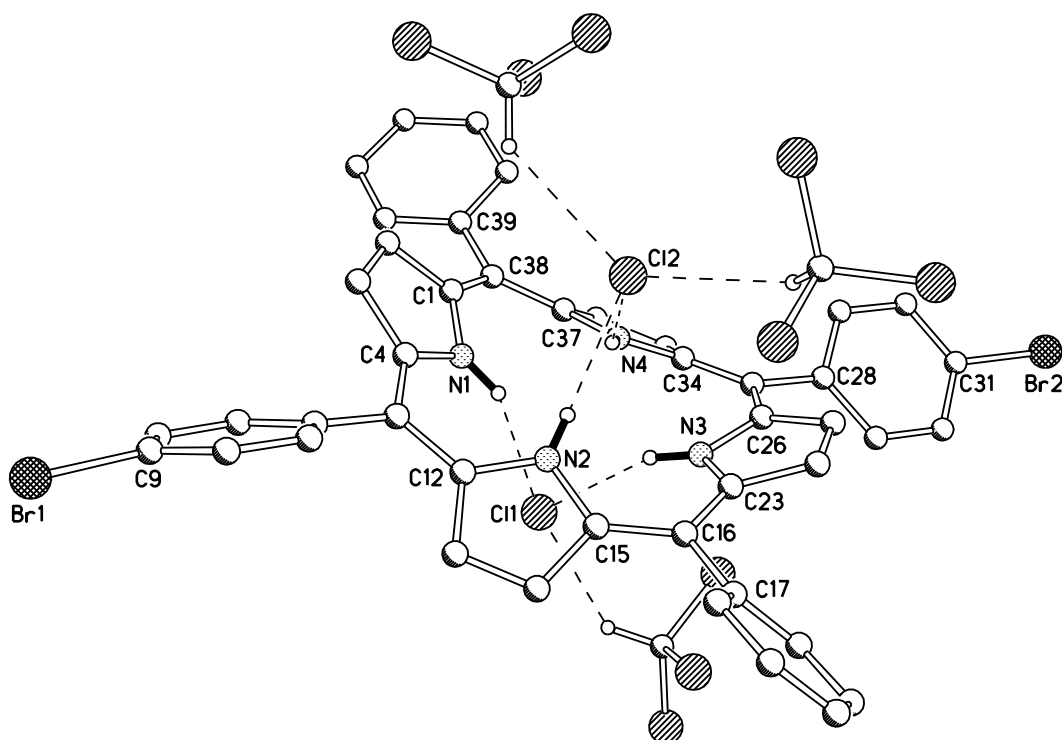
Figure 4.24 Molecular structure of Br$_2$-TPPH$_2$·2HCl with partial atom label schemes and molecules of chloroform. Selected hydrogen atoms have been omitted for clarity.

Table 4.4 Selected bond lengths (Å) and angles (°) for Br$_2$-TPPH$_2$·2HCl.

	Br$_2$-TPPH$_2$·2HCl
C(9)–Br(1)	1.910(9)
C(31)–Br(2)	1.920(9)
C(16)–C(17)	1.476(11)
C(38)–C(39)	1.470(12)
C(4)–N(1)–C(1)	110.6(7)
C(12)–N(2)–C(15)	110.5(2)
C(23)–N(3)–C(26)	110.1(7)
C(34)–N(4)–C(37)	110.2(7)
C(1)–C(38)–C(37)	123.11(8)
C(4)–C(5)–C(12)	123.54(8)
C(15)–C(16)–C(23)	121.80(7)
C(26)–C(27)–C(34)	125.27(7)

b) Preparation of **20a**_{chloroform}, **20b**_{chloroform} and **20c**_{chloroform}

In this section iron(III) derivatives of the type, [(Y$_2$-TPP)FeX] (**20**_{chloroform}), have been the focus of the study, as single crystals suitable for the X-ray determinations were readily accessible. Attempts to generate the cobalt and manganese analogues gave products which were not amenable to single crystal X-ray diffraction.
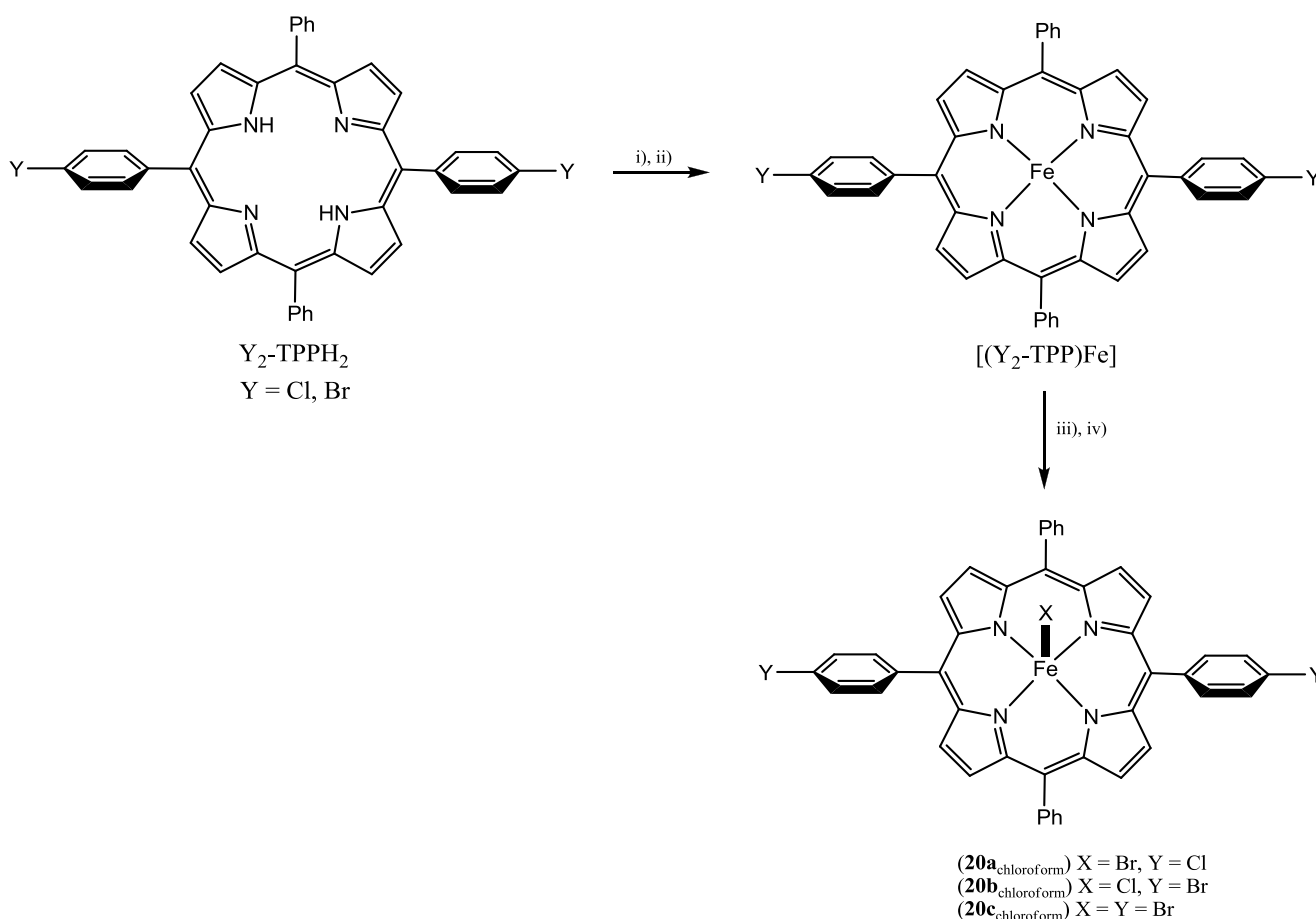
Scheme 4.3 *Reagents and conditions:* i) Fe(OAc)$_2$, CH$_3$COOH, 125 °C, 100 W, 15 min; ii) H$_2$O/toluene; iii) conc. HX (X = Cl, Br), MeOH, rt, 12 h; iv) chloroform recrystallisation.

Reaction of Cl$_2$-TPPH$_2$ or Br$_2$-TPPH$_2$ with iron diacetate in glacial acetic acid in a 1:10 molar ratio respectively, employing microwave heating conditions affords [(Y$_2$-TPP)Fe] (Y = Cl, Br) which were directly treated with the corresponding concentrated hydrohalous acids, HCl or HBr in methanol to give, following crystallisation from chloroform, [(Y$_2$-TPP)FeX] [X = Br, Y = Cl (**20a**_{chloroform}); X = Cl, Y = Br (**20b**_{chloroform}); X = Y = Br (**20c**_{chloroform})] in moderate yields, respectively. Complexes **20a**_{chloroform}, **20b**_{chloroform} and **20c**_{chloroform} have been characterised by IR spectroscopy, FAB mass spectrometry, magnetic measurements and elemental analysis.

In addition, single crystals of all three complexes were the subject of single crystal X-ray diffraction studies. The molecular structure of $20a_{chloroform}$, as a representative example, is depicted in Figure 4.25; selected bond lengths and angles for all three complexes are listed in Table 4.3.

The structures of $20a_{chloroform}$, $20b_{chloroform}$ and $20c_{chloroform}$ consist of an iron(III) metal centre co-ordinated by the tetradentate A_2B_2 porphyrinato macrocycle X_2-TPP^{2-} along with a halide atom which is located at the apical position. The geometry can best be described as SBP [$\tau = 0.03$ ($20a_{chloroform}$), 0.02 ($20b_{chloroform}$), 0.05 ($20c_{chloroform}$)]. The macrocyclic C–Cl bond lengths exhibited by $20a_{chloroform}$ are shorter than the C-Br bond lengths of their bromide counterparts [1.748(6), 1.732(6) Å ($20a_{chloroform}$) *vs.* 1.883(9), 1.847(10) Å ($20b_{chloroform}$) 1.897(7), 1.914(6) Å ($20c$)]. In a similar fashion, the Fe–Cl bond length displayed in $20b_{chloroform}$ is *ca.* 0.1 Å shorter than the corresponding Fe–Br bond lengths displayed in both $20a_{chloroform}$ and $20c_{chloroform}$.

On inspection of the molecular packing diagram for $20a_{chloroform}$, which is a representative example of all three complexes (Figure 4.25), it is apparent that there are two pairs of symmetry related molecules, with each member of the pair disposed at 180° to one another; between pairs there is an inclination of *ca.* 18°. With regard to the aryl C–Y bonds within each pair, there is a intermolecular YC···CY torsion angle approaching 90° [94.90° ($20a_{chloroform}$), 94.83° ($20b_{chloroform}$), 97.33° ($20c_{chloroform}$)]. In addition, the molecules exhibit a modest intramolecular misalignment of the *trans*-aryl halides due to a shallow concave configuration adopted by the metallo-macrocycle [tors: Y(1)C(20)···C(42)Y(2) = 1.46° ($20a_{chloroform}$), 2.20° ($20b_{chloroform}$), 1.77° ($20c_{chloroform}$)].
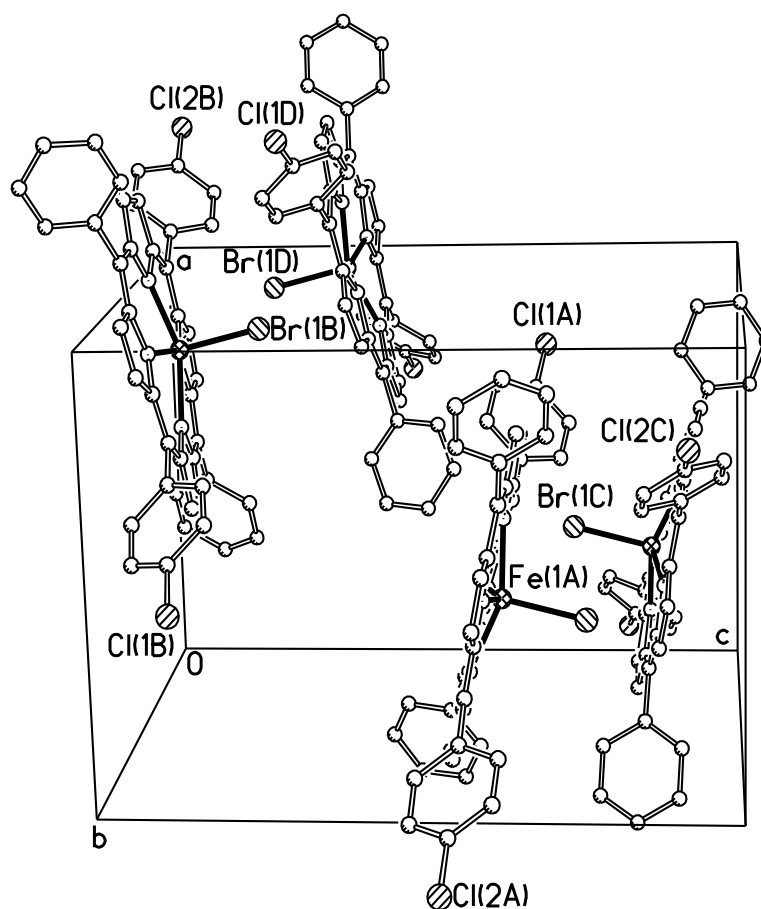
(a)
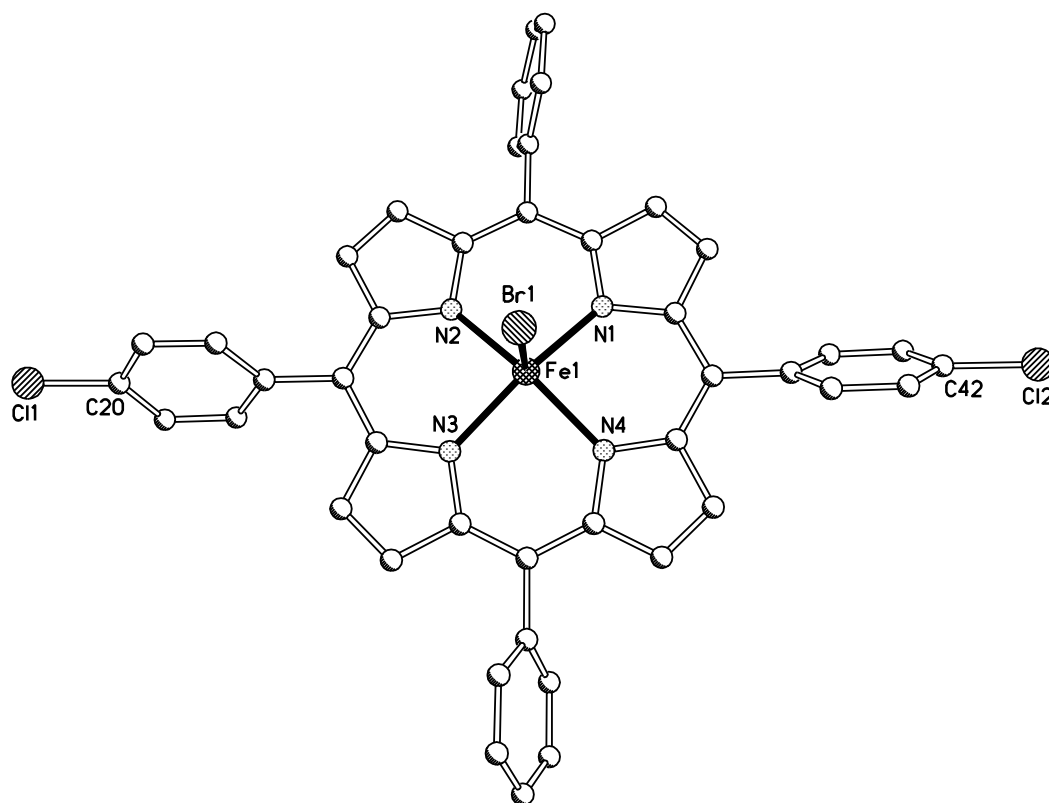
(b)

Figure 4.25 (a) Molecular structure of **20a**$_{chloroform}$ shown with partial atom label scheme; hydrogen atoms have been omitted for clarity. (b) Molecular packing diagram of the four distinct symmetry related molecules viewed down the crystallographic *b*-axis.

Table 4.5 Selected bond lengths (Å) and angles (°) for **20**$_{chloroform}$.

	20a$_{chloroform}$ (X = Br, Y = Cl)	**20b**$_{chloroform}$ (X = Cl, Y = Br)	**20c**$_{chloroform}$ (X = Y = Br)
Fe(1)–(1)	2.3602(11)	2.269(3)	2.3747(13)
Fe(1)–N(1)	2.0631(5)	2.029(8)	2.066(5)
Fe(1)–N(2)	2.066(4)	2.055(8)	2.048(6)
Fe(1)–N(3)	2.059(5)	2.045(9)	2.056(5)
Fe(1)–N(4)	2.062(5)	2.065(7)	2.056(5)
C(20)–Y(1)[a]	1.748(6)	1.883(9)	1.897(7)
C(42)–Y(2)[b]	1.732(6)	1.874(10)	1.914(6)
N(1)–Fe(1)–N(2)	88.28(18)	86.3(3)	88.2(2)
N(1)–Fe(1)–N(3)	155.87(19)	154.9(3)	157.6(2)
N(1)–Fe(1)–N(4)	86.49(19)	88.5(3)	88.8(2)
N(1)–Fe(1)–X(1)	101.73(13)	103.5(3)	11.06(15)
N(2)–Fe(1)–N(3)	86.03(18)	101.6(3)	86.7(2)
N(2)–Fe(1)–N(4)	153.74(19)	155.9(3)	154.8(2)
N(2)–Fe(1)–X(1)	101.73(13)	102.3(3)	103.75(16)
N(3)–Fe(1)–N(4)	88.31(18)	85.8(3)	88.1(2)
N(3)–Fe(1)–X(1)	101.99(14)	101.6(3)	101.91(15)
N(4)–Fe(1)–X(1)	104.53(14)	101.8(2)	101.47(14)

a) In the case of **20c**, Y(1) refers to atom Br(2).
b) In the case of **20c**, Y(2) refers to atom Br(3).

The FAB mass spectra of all three iron complexes reveal the molecular ion peak as well as fragmentation peaks corresponding to the loss of a metal-bound halide atom. Additional fragmentation of the macrocycle is evident in **20b**$_{chloroform}$ and **20c**$_{chloroform}$ with peaks associated with the sequential loss of carbon-bound bromide atoms. All these complexes display magnetic moments in the range 1.4–1.6 BM (Evans balance at room temperature) consistent with one unpaired electron for a low spin d^5 electron configuration.

A word of caution is to be expressed when potentially utilising *hybrid filters* for astronomical polarimetry. Each element is able, in principle, to absorb at a particular K-edge of interest, depending on the astronomical source being observed. However, other atoms in the filter with similar K-edges can also absorb across a wide energy range and in particular, contribute to non-dichroic absorption at the K-edge of interest. In astronomical circumstances, few photons are emitted; therefore the efficiency of a device is lost if one atom absorbs preferentially over the other.

To avoid this preferential, hypothetical absorption, an ideal *hybrid filter* should contain atoms with K-edges of interest in which a significant difference is apparent in their respective absorption co-efficients; however, in practice, this is not possible. In Chapter 2 (section 2.6), the

ideal thicknesses were discussed regarding the *hybrid filter* **1a** where it was outlined that a potential filter material must achieve a balance between sample thickness and source observation time at each K-edge within the molecule. For example, observing at one edge longer than another would minimise absorbance from the relatively stronger absorbing atom.

4.12 Conclusions

This chapter has been concerned with the application of single crystals of new and previously reported, trivalent metal halides and tetravalent metal oxide tetraphenylporphyrinato complexes incorporating metal centres at the titanium (4966 eV), vanadium (5469 eV), manganese (6539 eV), iron (7112 eV) and cobalt (7708 eV) K-edges as potential X-ray dichroic materials. The X-ray structures of [(TPP)CoBr] (**15a**$_{DCM}$) and [(TPP)TiO] (**19**$_{DCM}$) along with two new polymorphs of **17**, namely, **17**$_{DCM}$ and **17**$_{benzene}$, have been reported for the first time. The halide and oxide complexes, [(TPP)CoX], [X = Br (**15a**$_{DCM}$), Cl (**15b**$_{DCM}$)], [(TPP)FeBr] (**16**$_{DCM}$), [(TPP)VO] (**18**$_{DCM}$) and [(TPP)TiO] (**19**$_{DCM}$) all show X-ray dichroism at their respective K-edges and furthermore, **15a**$_{DCM}$ exhibits X-ray dichroism at the Br K-edge with modulation curves for all complexes accessible in fluorescence mode. An in-depth study of the X-ray dichroism displayed by the highly ordered cobalto and vanadyl-porphyrin complexes **15a**$_{DCM}$ and **19**$_{DCM}$ has been undertaken using the Diamond Light Source (station B16) in both transmission and fluorescence modes along with a further examination solely in transmission mode using the micro-focus Diamond Light Source (station I18). Figures of merit have been calculated for **15a**$_{DCM}$ and **18**$_{DCM}$ which show an overall improvement on that of **1a** (Chapter 2). Moreover, it is evident that particular regions of the XAS spectra are weighted in terms of their dichroic response. For example, **15a**$_{DCM}$ has an inflection point at the main-edge 2, whilst **18**$_{DCM}$ has an inflection point at the pre-edge. In addition, the polarised XAS spectra of **15a**$_{DCM}$ and **18**$_{DCM}$ have been modelled using a theoretical multiple scattering approach (FEFF) which has revealed good agreement between experiment and theory.

In an attempt to engineer simple and more compact materials incorporating multiple K-edges, the recently developed A_2B_2 porphyrins $[Y_2\text{-TPP}]^{2-}$ (Y = Cl, Br), bearing *trans*-configured halogen atoms at the ligand's periphery, have been used as a support for an iron(III) halide unit generating $[(Y_2\text{-TPP})FeX]$ [Y = Cl, X = Br (**20a**chloroform); Y = Br, X = Cl (**20b**chloroform); Y = X = Br (**20c**chloroform)]. These materials are aligned in the solid state showing only minor angular deviations with respect to the neighbouring Fe–X bonds, unfortunately, limited intra- and intermolecular order is apparent with respect to the C–Y (Y = Cl, Br) bonds.

It has been shown herein that low energy (K-edge) metal centres bearing apical oxides (*e.g.*, **18**DCM and **19**DCM) display sharp, intense, pre-edge features; a prominent, useful spectroscopic handle. In the next chapter, a framework will be designed to allow the support of complexes bearing exclusively low energy tri- and tetravalent metal centres, *e.g.*, titanium (4966 eV), vanadium (5465 eV) and chromium (5989 eV)

4.13 General experimental

In addition to the experimental details described in Chapters 2 and 3 (Chapter 2 section 2.9; Chapter 3 section 3.9), all operations, unless otherwise stated, were carried out under an inert atmosphere of dry, oxygen-free nitrogen using standard Schlenk and cannular techniques or in a nitrogen purged glove box. Solvents were dried from appropriate drying agents[81] or were employed directly from a solvent purification system (Innovative Technology Inc). Microwave reactions were performed using a CEM discover microwave in sealed standard microwave vials which had been previously degassed using dry nitrogen. The microwave reaction solvent was also degassed using nitrogen prior to use. The reagents $Co(OAc)_2 \cdot 4H_2O$, $Fe(OAc)_2$, $Mn(OAc)_2 \cdot 4H_2O$, $VO(acac)_2$ and $TiCl_4$ were purchased from Sigma Aldrich chemical company and used without further purification. Concentrated HCl was obtained as a 32% aqueous solution (Fischer Scientific) whilst HBr was obtained as a 45% solution in acetic acid (Alfa Aesar). The pro-ligands $TPPH_2$[68–70] and Y_2-$TPPH_2$ (Y = Cl, Br)[77] were synthesised in accordance with previously reported methods. The HCl salt, Br_2-$TPPH_2 \cdot 2HCl$, was prepared by treating Br_2-$TPPH_2$ with conc. HCl in methanol and recrystallised from chloroform.

4.13.1 General procedure for the synthesis of [(TPP)MX] [M = Co, X = Br (15a); M = Co, X = Cl (15b); M = Fe, X = Br (16); M = Mn, X = Br (17)]

The porphyrin pro-ligand $TPPH_2$ (0.100 g, 0.16 mmol) was loaded into a microwave vial along with the corresponding metal acetate (0.80 mmol, 5 eq.) and glacial acetic acid (*ca.* 3 ml) and the reaction mixture degassed by allowing nitrogen to bubble through the solution. The reaction vessel was then sealed and heated with stirring using microwave radiation (125 °C, 100 W, 10 min ramp, 30 min hold). Upon cooling to room temperature the mixture was dissolved in toluene (*ca.* 30 ml) and the organic layer washed with water (3 × 30 ml). The organic layer was then separated and dried over anhydrous magnesium sulphate. Following filtration and the removal of all volatiles under reduced pressure, the solid residue was dissolved in methanol (*ca.* 15 ml) and stirred with the corresponding concentrated hydro-halous acid (HCl or HBr) (*ca.* 10 drops) for 12 h at room temperature. After removal of all volatiles under reduced pressure, the solid residue was thoroughly dried under reduced pressure. The [(TPP)MX] complexes were obtained upon crystallisation from the appropriate solvents.

a) 15a$_{DCM}$: Deep red blocks of the title complex were obtained upon recrystallisation from dichloromethane (0.080 g, 66%). v_{max}(ATR)cm^{-1} 1596, 1439, 1349, 1175, 1071, 1000, 839, 798, 750, 702, 685, *m/z* (FAB) 675 (100%) [M - Br]. See Table 4.6 for crystallographic parameters.

b) 15b$_{DCM}$: Deep red blocks of the title complex were obtained upon recrystallisation from dichloromethane (0.056 g, 50%).

a = 13.391(2) Å, b = 13.391(2) Å, c = 9.651(2) Å, α = 90°, β = 90°, γ = 90°, V = 1730.6(6) Å^3; (*Literature*: a = 13.693 Å, b = 13.693 Å, c = 9.701 Å, α = 90°, β = 90°, γ = 90°, V = 1818 Å^3).[47]

c) 16$_{DCM}$: Purple blocks of the title complex were obtained upon recrystallisation from dichloromethane (0.050g, 47%).

a = 9.994(3) Å, b = 15.945(3) Å, c = 23.564(4) Å, α = 90°, β = 114.87(2)°, γ = 90°, V = 3111.1(3) Å^3; (*Literature*: a = 10.191 Å, b = 16.121 Å, c = 23.223 Å, α = 90°, β = 115.34°, γ = 90°, V = 3241 Å^3).[55]

d) 17$_{toluene}$: Dark green blocks of the title complex were obtained upon by slowly diffusing hexane into a concentrated toluene solution of **17** (0.054 g, 65%).

a = 9.83(2) Å, b = 15.46(2) Å, c = 13.42(2) Å, α = 90.0(1)°, β = 102.79(7)°, γ = 90.1(1)°, V = 1990(5) Å^3; (*Literature*: a = 9.985 Å, b = 15.453 Å, c = 13.583 Å, α = 90°, β = 103.99°, γ = 90°, V = 2033 Å^3).[63]

e) 17$_{DCM}$: Dark green blocks of the title complex were obtained upon recrystallisation from dichloromethane (0.070 g, 60%). See Table 4.6 for crystallographic parameters.

f) 17$_{benzene}$: Dark green blocks of the title complex were obtained upon recrystallisation from benzene (0.053, 44%). See Table 4.6 for crystallographic parameters

4.13.2 Synthesis of [(TPP)MO] [M = V (18$_{DCM}$), Ti (19$_{DCM}$)]

a) 18$_{DCM}$: The complex [(TPP)VO] (**18$_{DCM}$**) was synthesised in accordance with the literature preperation.[20] Dark red crystals of the title complex were obtained upon recrystallisation from dichloromethane (0.070 g, 60%).

a = 13.3045(18) Å, b = 13.3045(18) Å, c = 9.6618(19) Å, α = 90°, β = 90°, γ = 90°, V = 1710.2(5) Å^3; (*Literature*: a = 13.345 Å, b = 13.345 Å, c = 9.746 Å, α = 90°, β = 90°, γ = 90°, V = 1735 Å^3).[19]

b) 19$_{DCM}$: A three neck flask equipped with a reflux condenser and stir bar was evacuated and backfilled with nitrogen. To this flask was added TPPH$_2$ (0.100 g, 0.16 mmol) and dry toluene (300 ml) and the solution stirred and heated to reflux. Under a rigorously maintained atmosphere of nitrogen was added dropwise with caution, titanium tetrachloride (2.00 ml, 18 mmol, 180 eq.) and the solution refluxed further under a gentle stream of nitrogen for 24 h. Upon cooling to room temperature, chloroform (100 ml) followed by 2M hydrochloric acid (250 ml) were added and the mixture stirred for 1 h. The aqueous phase was separated and extracted several times with chloroform and the combined organic phases washed successively with water (3 × 50 ml), saturated sodium hydrogen carbonate (1 × 100 ml) and a further portion of water (1 × 100 ml). The organic phase was dried over magnesium sulphate, filtered and the solvent removed under reduced pressure to give a purple residue. The residue was subjected to silica gel column chromatography employing dichloromethane as the eluent, upon which two distinctly separate bands were observed. The first band gave trace amounts of unreacted TPPH$_2$, and the second purple band gave a bright purple solid on work-up. Lustrous dark red/purple crystals of **19$_{DCM}$** were obtained by slowly diffusing hexane into a concentrated dichloromethane solution of the title complex (0.070 g, 70%). δ_H (400 MHz, CDCl$_3$, SiMe$_4$); 7.8 (m, 20H, Ar*H*), 8.10 (d, J = 8.1, 4H, Pyr*H*), 8.50 (d, J = 8.1, 4H, Pyr*H*). v_{max} (ATR)/cm^{-1} 798 (Ti=O). *m/z* (FAB) 688 (100%) [M + H]. All other data was consistent with that previously reported.[11] See Table 4.6 for crystallographic parameters.

4.13.3 Synthesis of 20a_{chloroform}**, 20b**_{chloroform} **and 20c**_{chloroform}

*a) 20a*_{*chloroform*}: The porphyrin pro-ligand Cl_2-$TPPH_2$ (0.100 g, 0.146 mmol) was loaded into a microwave vial along with $Fe(OAc)_2$ (0.183 g, 1.46 mmol, 10 eq.) and glacial acetic acid (*ca.* 3 ml) and the reaction mixture degassed by allowing nitrogen to bubble through the solution. The reaction vessel was then sealed and heated with stirring using microwave radiation (125 °C, 100 W, 10 min ramp, 30 min hold). Upon cooling to room temperature the mixture was dissolved in toluene (*ca.* 30 ml) and the organic layer washed with water (3 × 30 ml). The organic layer was then separated and dried over anhydrous magnesium sulphate. Following filtration and the removal of all volatiles under reduced pressure, the solid residue was dissolved in methanol (*ca.* 15 ml) and stirred with a solution of 45% hydrobromic acid in acetic acid (*ca.* 10 drops) for 12 h at room temperature. After removal of all volatiles under reduced pressure, the solid residue was thoroughly dried under reduced pressure. Dark purple blocks were obtained by slow evaporation of a dichloromethane solution of the title complex (0.016 g, 62%). Found: C, 64.54; H, 3.36; N, 6.80. $C_{44}H_{26}N_4BrCl_2Fe$ (817.36) requires: C, 64.66; H, 3.21; N, 6.85; ν_{max} (ATR)/cm^{-1} 1598, 1541, 1484, 1350, 1299, 1207, 1178, 1070, 908, 715; *m/z* (FAB) 818 (20%) [M + H], 736 (100%) [M - Br]; μ_{eff} = 1.40 BM; mp: > 300 ºC. See Table 4.8 for crystallographic parameters.

*b) 20b*_{*chloroform*}: Using a similar approach and molar ratio of reactants to that described for **20a** (using Br_2-$TPPH_2$ and conc. hydrochloric acid), the title complex was obtained as purple blocks (0.021 g, 65%). Found: C, 58.37; H, 2.27; N, 5.50. $C_{44}H_{26}N_4Br_2ClFe$ (861.81) requires: C, 58.00; H, 2.90; N, 6.08; ν_{max} (ATR)/cm^{-1} 1588, 1551, 1480, 1353, 1301, 1210, 1171, 1071, 907, 712; *m/z* (FAB) 863 (10%) [M + H], 826 (100%) [M - Cl]; μ_{eff} = 1.66 BM; mp: > 300 ºC. See Table 4.8 for crystallographic parameters.

*c) 20c*_{*chloroform*}: Using a similar approach and molar ratio of reactants to that described for **20a** (using Br_2-$TPPH_2$ and 45% hydrobromic acid in acetic acid), the title complex was obtained as purple blocks (0.016 g, 62%). Found: C, 58.26; H, 2.93; N, 6.09. $C_{44}H_{26}N_4Br_3Fe$ (906.26) requires: C, 58.31; H, 2.89; N, 6.18; ν_{max} (ATR)/cm^{-1} 1584, 1561, 1489, 1359, 1321, 1215, 1169, 1075, 921, 719; *m/z* (FAB) 907 (10%) [M + H], 826 (100%) [M - Br]; μ_{eff} = 1.50 BM; mp: > 300 ºC. See Table 4.8 for crystallographic parameters.

4.14 X-ray crystallography

Crystallographic data analysis was carried out in collaboration with K. Singh (Department of Chemistry, University of Leicester). Data for $\mathbf{15a}_{DCM}$, $\mathbf{17}_{DCM}$, $\mathbf{17}_{benzene}$, $\mathbf{18}_{DCM}$ $\mathbf{19}_{DCM}$ and $\mathbf{20}$ were collected on a Bruker APEX 2000 CCD diffractometer; unit cell parameters for $\mathbf{15b}_{DCM}$, $\mathbf{16}_{DCM}$, $\mathbf{17}_{toluene}$ and $\mathbf{18}_{DCM}$ were also determined using this diffractometer. Details of data collection, refinement and crystal data are listed in Tables 4.6, 4.7 and 4.8. All data were collected using graphite monochromated Mo-K$_\alpha$ irradiation ($\lambda =$ 0.7107 Å) and the reflections were corrected for Lorentz, polarisation and absorption effects. The structures were solved by full-matrix least squares on F^2 using SHELXTL version 6.10.[82] Carbon bonded hydrogen atoms were included in calculated positions (C–H = 0.96 Å) with isotropic displacement parameters set to 1.2 Ueq(C). Non-hydrogen atoms were refined with anisotropic displacement parameters. Disordered benzene molecules were removed from the unit cell of $\mathbf{17}_{benzene}$ using the SQUEEZE option in PLATON.[73]

Table 4.6 Structural parameters for **15a$_{DCM}$**, **17$_{DCM}$**, **17$_{benzene}$** and **19$_{DCM}$**.

Compound	15a$_{DCM}$	17$_{DCM}$	17$_{benzene}$	19$_{DCM}$
Singh code	08093	09009	10092	11035
Formula	$C_{44}H_{28}BrCoN_4$	$C_{45}H_{30}BrCl_2MnN_4$	$C_{56}H_{40}BrMnN_4$	$C_{44}H_{28}N_4OTi$
Mc	751.54	832.48	903.77	676.60
Crystal size (mm)	$0.18 \times 0.17 \times 0.15$	$0.25 \times 0.22 \times 0.18$	$0.30 \times 0.23 \times 0.03$	$0.17 \times 0.16 \times 0.13$
Temperature (K)	150(2)	150(2) K	150(2) K	150(2) K
Crystal system	Tetragonal	Monoclinic	Monoclinic	Monoclinic
Space group	$I4$	$P2(1)/n$	P-1	$I4/m$
Lattice parameters				
a (Å)	13.4987(18)	13.004(2)	13.322(13)	13.3323(16)
b (Å)	13.4987(18)	10.4701(19)	15.042(14)	13.3323(16)
c (Å)	9.6964(19)	27.403(19)	20.769(19)	9.6936(17)
α (°)	90	90	71.782(18)	90
β (°)	90	95.574(4)	84.633(18)	90
γ (°)	90	90	74.72(2)	90
U (Å^3)	1766.8(5)	3713.3(12)	3813(6)	1723.0(4)
Z	2	4	4	2
D_c (Mg/m^3)	1.413	1.489	1.574	1.304
$F(000)$	764	1688	1856	700
μ (Mo-K$_\alpha$)	1.413	1.615	1.444	0.290
Reflections collected	6437	28162	30037	6789
R(int)	0.2065	0.0639	0.1257	0.1004
Independent reflections	1551	7267	14814	905
Restraints /parameters	1/119	0/478	0/901	0/901
R_1; $wR_2[I>2\sigma(I)]$	$R_1 = 0.0911$, $wR_2 = 0.2509$	$R_1 = 0.0476$, $wR_2 = 0.0726$	$R_1 = 0.0701$, $wR_2 = 0.1311$	$R_1 = 0.0684$, $wR_2 = 0.1396$
R_1; wR_2 (all data)	$R_1 = 0.1232$, $wR_2 = 0.2788$	$R_1 = 0.0758$, $wR_2 = 0.1025$	$R_1 = 0.1574$, $wR_2 = 0.1492$	$R_1 = 0.0985$, $wR_2 = 0.1489$
Goodness of fit on F^2 (all data)	1.097	0.928	0.763	1.218

Table 4.7 Crystallographic parameters for Br_2-$TPPH_2 \cdot 2HCl$.

Compound	Br_2-$TPPH_2 \cdot 2HCl$
Singh code	10098
Formula	$C_{51}H_{37}BrCl_{23}N_4$
Mc	1681.02
Crystal size (mm)	$0.21 \times 0.19 \times 0.04$
Temperature (K)	150(2)
Crystal system	Monoclinic
Space group	$P2(1)/c$
Lattice parameters	
a (Å)	12.462(2)
b (Å)	47.706(2)
c (Å)	11.407(2)
α (°)	90
β (°)	103.236(4)
γ (°)	90
U (Å^3)	6601
Z	4
D_c (Mg/m^3)	1.691
$F(000)$	3328
μ (Mo-K$_\alpha$)	1.298
Reflections collected	51774
R(int)	0.2052
Independent reflections	12959
Parameters/restraints	0/721
R_1; $wR_2[I>2\sigma(I)]$	$R_1 = 0.0803$, $wR_2 = 0.1648$
R_1; wR_2 (all data)	$R_1 = 0.2051$, $wR_2 = 0.2012$
Goodness of fit on F^2 (all data)	0.873

Table 4.8 Structural parameters for **20a**$_{chloroform}$, **20b**$_{chloroform}$, and **20c**$_{chloroform}$.

Compounds	**20a**$_{chloroform}$	**20b**$_{chloroform}$	**20c**$_{chloroform}$
Singh code	10020	11013	10114
Formula	$C_{44}H_{26}BrCl_2FeN_4$	$C_{44}H_{26}Br_2ClFeN_4$	$C_{44}H_{26}Br_3FeN_4$
Mc	817.35	861.81	906.27
Crystal size (mm)	$0.33 \times 0.24 \times 0.09$	$0.27 \times 0.19 \times 0.15$	$0.42 \times 0.38 \times 0.33$
Temperature (K)	150(2)	150(2)	150(2)
Crystal system	Orthorhombic	Orthorhombic	Orthorhombic
Space group	$P2(1)2(1)2(1)$	$P2(1)2(1)2(1)$	$P2(1)2(1)2(1)$
Lattice parameters			
a (Å)	12.964(3)	12.998(8)	12.939(3)
b (Å)	14.891(4)	14.938(9)	15.018(3)
c (Å)	18.595(4)	18.461(11)	18.542(4)
α (°)	90	90	90
β (°)	90	90	90
γ (°)	90	90	90
U (Å^3)	3589(15)	3585(4)	3603.0(12)
Z	4	4	4
D_c (Mg/m^3)	1.512	1.597	1.671
$F(000)$	1652	1724	1796
μ (Mo-K$_\alpha$)	1.721	2.764	3.785
Reflections collected	28309	28226	28095
R(int)	0.09208	0.2286	0.0745
Independent reflections	7051	7049	7083
Parameters/restraints	0/469	0/469	0/469
R_1; $wR_2[I>2\sigma(I)]$	$R_1 = 0.0616$, $wR_2 = 0.1444$	$R_1 = 0.0961$, $wR_2 = 0.2435$	$R_1 = 0.0540$, $wR_2 = 0.1320$
R_1; wR_2 (all data)	$R_1 = 0.0812$, $wR_2 = 0.1530$	$R_1 = 0.1241$, $wR_2 = 0.2650$	$R_1 = 0.0735$, $wR_2 = 0.1376$
Goodness of fit on F^2 (all data)	0.990	1.003	0.973

4.15 Polarised XAS measurements

For a description of beamlines B16 see Chapter 3, section 3.11. In addition, transmission measurements on $15a_{DCM}$ and 18_{DCM} were performed using Diamond station I18. A Si(111) monochromator operating within a 2–20 keV range with an energy resolution of 1×10^{-3} eV was employed along with a high rate fluorimeter 9-element detector optimised for energies above 5 keV.

4.16 Theoretical calculations

As described in previous chapters, MS calculations were performed with guidance from Dr. M. Roy (Department of Physics and Astronomy, University of Leicester) using the FEFF 8.4 software package[83] on the ULARC and more recently, ALICE computer facilities at the University of Leicester.

4.17 References

1) K. S. Suslick, *Med. Chem.*, 1989, **32**, 1410.
2) K. M. Kadish, K. M. Smith and R. Guilard, *The Porphyrin Handbook*, Academic Press, 1999, vol. 11.
3) K. M. Kadish, K. M. Smith and R. Guilard, *The Porphyrin Handbook*, Academic Press, 1999, vol. 14.
4) K. S. Suslick, N. E. Rakow, M. E. Kosal and J.-H Chou, *J. Porphyrins Phthalocyanines*, 2000, **4**, 407.
5) C.-T. Chen and K. S. Suslick, *Coord. Chem. Rev.*, 1993, **128**, 293.
6) A. Hines, Z. Liang, M. Woodhouse and B. Gregg, *Chem. Rev.*, 2010, **110**, 6689.
7) L. Guo, D. E. Ellis, K. Mundim and B. M. Hoffman, *J. Porphyrins Phthalocyanines*, 2010, **14**, 759.
8) C. M. Drain, A. Varotto and I. Radivojevic, *Chem. Rev.*, 2009, **109**, 1630.
9) H. Kenneth, K. S. Suslick and R. A. Watson, *New J. Chem.*, 1992, **16**, 633.
10) R. Guilard, K. M. Kadish and K. M. Smith, *The Porphyrin Handbook*, Academic Press, 1999, vol. 6.
11) P. Fournari, R. Guilard, M. Fontesse, J.-M. Latour and J.-C. Marchon, *J. Organomet. Chem.*, 1976, **110**, 205.
12) P. E. Esser, B. Drieβen-Hölscher and W. Keim, *J. Mol. Cat. A*, 1999, **140**, 13.
13) R. Guilard, J. M. Latour, C. Lecomte, J. C. Marchon, J. Protas and D. Ripoll, *Inorg. Chem.*, 1978, **17**, 1228.
14) P. N. Dwyer, L. Puppe, J. W. Buchler and W. R. Scheidt, *Inorg. Chem.*, 1975, **14**, 1787.
15) P. Esser, U. Englert and W. Keim, *Chem. Ber.*, 1996, **129**, 833.
16) J. Fischer, P. Friand, J. Goulon, R. Guilard, J. L. Poncet and L. Richard, in *EXAFS and near edge structure*, ed. A. Bianconi, L. Inoccia and S. Stipcich, Springer Series in *Chem. Phys.*, 1983, vol. 27, p. 100.
17) J. E. Penner-Hahn, M. Benfatto, B. Hedman, T. Takahashi, S. Doniach, T. J. Groves and K. O. Hodgson, *Inorg. Chem.,* 1986, **25**, 2255.
18) J. R. Budge, B. M. K. Gatehouse, M. C. Nesbit and B. O. West, *J. Chem Soc., Chem. Commun.*, 1981, 370.
19) M. G. B. Drew, P. C. H. Mitchel and C. E. Scott, *Inorg. Chim. Acta*, 1984, **82**, 63.
20) S. Bencosme, M. Labady and C. Romero, *Inorg. Chim. Acta*, 1986, **123**, 15.
21) L. M. Berreau, J. A. Hays, V. G. Young, Jr. and L. K. Woo, *Inorg. Chem.*, 1994, **33**, 105.
22) S. H. Strauss, M. J. Pawlik, J. Skowyra, J. R. Kennedy, O. P. Anderson, K. Spartalian and J. L. Dye*, Inorg. Chem.*, 1987, **26**, 724.
23) P. N. Sweptson and J. A. Ibers*, Acta Cryst*, 1985, **C41**, 671.
24) A. B. Hoffman, D. M. Collins, V. W. Day, E. B. Fleischer, T. S. Srivastava and J. L. Hoard, *J. Am. Chem. Soc.*, 1972, **94**, 3620.
25) D. V. Konarev, S. S. Khasanov and R. N. Lyubovskaya, *J. Porphyrins Phthalocyanines*, 2010, **14**, 293.
26) T. Baba, H. Shimakoshi, I. Aritome and Y. Hisaeda, *Chem. Lett.*, 2004, **33**, 906.
27) K.-L. Lay, J. W. Buchler, J. E. Kenny and W. R. Schiedt, *Inorg. Chim. Acta*, 1986, **123**, 91.
28) M. Li, M. Shang, H. F. Duval and W. R. Scheidt, *Acta Cryst.*, 2000, **C56**, 1206.
29) A.-R. Li, H.-H. Wei and L.-L. Gang, *Inorg. Chim. Acta*, 1991, **290**, 51.
30) X.-G. Jiao, J.-W. Huang, L.-N. Ji, B.-S. Luo and L.-R. Chen, *J. Inorg. Biochem.*, 1997, **65**, 229.

31) C. Da Silva, L. Bonomo, E. Solari, R. Scopelliti, C. Floriani and N. Re, *Chem.-Eur. J.*, 2000, **6**, 4518.
32) R. Patra, S. Bhowmik, S. K. Ghosh and S. P. Rath, *Eur. J. Inorg. Chem.*, 2009, 654.
33) E. Vogel, S. Will, A. S. Tilling, L. Neumann, J. Lex, E. Bill, A. X. Trautwein and K. Weigheart, *Angew. Chem.*, Int. Ed., 1999, **33**, 731.
34) B. Cheng, J. D. Hobbs, P. G. Debrunner, J. Erlebacher, P. J. A. Shelnutt and W. R. Scheidt, *Inorg. Chem.*, 1995, **34**, 102.
35) W. P Schaefer, P. E. Ellis, J. E. Lyons and S. N. Shaikh, *Acta Cryst.*, 1995, **C51**, 2252.
36) S. K. Ghosh, R. Patra and S. P. Rath, *Inorg. Chim. Acta*, 2010, **363**, 2791.
37) S. K. Ghosh, R. Patra and S. P. Rath, *Inorg. Chem.*, 2010, **49**, 3449.
38) P. C. Lecomte, J. Protas, J.C. Marchon and M. Nakajma, *Acta Cryst.*, 1978, B**34**, 2856.
39) A. N. Christensen, A. Grand, M. S. Lehmann and D. E. Cox, *Acta Chem. Scand.*, 1990, **44**, 103.
40) M. Inamo, H. Nakaba, K. Nakajima and M. Hoshino, *Inorg. Chem.*, 2000, **39**, 4417.
41) M. Inamo, M. Hoshino, K. Nakajima, S. Aizawa and S. Funahashi, *Bull. Chem. Soc. Jpn.*, 1995, **68**, 2293.
42) K. Oyaizu, A. Haryono, Y. Nishimura, K. Yamamoto and E. Tsuchida, *Bull. Chem. Soc. Jpn.*, 1999, **72**, 1781.
43) K. Fujio*, Bull. Chem. Soc. Jpn.*, 1998, 71, **8**, 83.
44) D. Summerville, R. D. Jones, B. M. Hoffman and F. Basolo, *J. Am. Chem. Soc.*, 1977, **99**, 8195.
45) A. D. Adler, F. R. Longo, F. Kampas and *J*. Kim, *J. Inorg. Nucl. Chem.*, 1970, **32**, 2443.
46) A. S. de Sousa, M. A. Fernandes, W. Nxumalo, J. L. Balderson, T. Jeftic, I. Cukrowski and H. M. Marques, *J. Mol. Struct.*, 2008, **872**, 47.
47) T. Sakurai, K. Yamamoto, H. Naito and N. Nakamoto, *Bull. Chem. Soc. Jpn.*, 1976, **49**, 3042.
48) N. Inamo and K. Nakajima, *Bull. Chem. Soc. Jpn.*, 1988, **71**, 883.
49) T. Sakuri, K. Yamamoto, M. Katsuta and N. Seins, *Acta Cryst*, 1975, **B31**, 2514.
50) K. Anzai, K. Hatano, Y. J. Lee and W. R. Schiedt, *Inorg. Chem.*, 1981, **20**, 2337.
51) W. R. Scheidt and M. G. Finnegan, *Acta Cryst.*, 1989, **C45**, 1214.
52) J. Wojaczynski, M. Stepien and L. L. Grazynski, *Eur. J. Inorg. Chem.*, 2002, 1806.
53) L. M. Grande, B. C. Noll, A. G. Oliver and W. R. Scheidt, *Inorg. Chem.*, 2010, **49**, 6552.
54) C. Hu, C. D. Sulok, F. Paulat, N. Lehnert, A. I. Twigg, M. P. Hendrich C. E. Schulz and W. R. Scheidt, *J. Am. Chem. Soc.*, 2010, **132**, 3737.
55) B. W. Skelton and A. H. White, *Aust. J. Chem.*, 1977, **30**, 2655.
56) K. Hatano and W. R. Scheidt, *Inorg. Chem.*, 1979, **18**, 877.
57) D. V. Behere and S. Mitra, *Inorg. Chem.*, 1980, **19**, 992.
58) J. F. Kirner and W. R. Scheidt, *Inorg. Chem.*, 1975, **14**, 2081.
59) B. Cheng and W. R. Scheidt, *Acta Cryst.*, 1996, **C52**, 361.
60) R. S. Armstrong, G. J. Foran and T. W. Hambley, *Acta Cryst.,* 1993, **C49**, 236.
61) F. Paulat, V. K. K. Praneeth, C. Näther and N. Lehnert, *Inorg. Chem.*, 2006, **45**, 2835.
62) A. Tulinsky and B. M. L. Chen, *J. Am. Chem. Soc.*, 1977, **99**, 3647.
63) P. J. Turner, M. J. Gunter, B. W. Skelton and A. H. White, *Aust. J. Chem.*, 1998, **51**, 835.
64) Y. Watanabe and H. Fujii, *Struct. Bond.*, 2000, **97**, 61.
65) J. Goulon, A. Retournard, P. Friant, C. Goulon-Ginet, C. Berthe, J.-F. Muller, J.-L. Poncet, R. Guilard, J.-C. Escalier and B. Neff, *J. Chem. Soc., Dalton Trans.*, 1984, 1095.
66) M. Loos, I. Ascone, P. Friant, M. F. Ruiz-Lopez, M. J. Goulon, J. M. Barbe, N. Senglet, R. Guilard, D. Faure and T. Des Courieres, *Cat. Today*, 1990, **7**, 497.
67) J.-C. Marchon, J.-M. Latour, A. Grand, M. Belakhovsky, M. Loos and J. Goulon, *J. Inorg. Chem.*, 1990, **29**, 57.
68) A. D. Adler, F. G. Longo, J. D. Finarelli, J. Goldmacher, J. Assour and L. Korsakoff, *J. Org. Chem.*, 1967, **32**, 476.
69) P. Rothermund and A. R. Menotti, *J. Am. Chem. Soc.*, 1948, **70**, 1808.
70) R. E. Falvo, D. F. Marsh and L. M. Mink, *J. Chem. Educ.*, 1999, **76**, 237.
71) G. D. Dorough, J. R. Miller and F. M. Huennekens, *J. Am. Chem. Soc.*, 1951, **73**, 4315.
72) K. Yamamoto and S. Tonomura, *Sci. Papers Inst. Phys. Chem. Res.*, 1964, **58**, 122.
73) A. L. Spek, *Acta Cryst.*, 1990, **A46**, 34.
74) B. Watts, L. Thomsen and P. C. Dastoor, *J. Electron. Spectrosc. Relat. Phenom.*, 2006, **151**, 105.
75) B. L. Henke, E. M. Gullikson and J C. Davis, X-ray interactions: photoabsorption, scattering, transmission, and reflection at *E*=50-30000 eV, *Z*=1-92, *Atomic Data and Nuclear Data Tables*, 1993, **54**, 181.

76) ESA Assessment Study Report, *IXO: Revealing the Physics of the Hot Universe*, ESA/SRE(2011)2, 2011, http://sci.**esa**.int/science-e/www/object/doc.cfm?fobjectid=48361.

77) B. Temelli and C. Unaleroglu, *Tetrahedron*, 2009, **65**, 2043.

78) B. Temelli and C. Unaleroglu, *Tetrahedron*, 2006, **62**, 10130.

79) R. Naik, P. Joshi, S. P. Kaiwar and R. K. Deshpande, *Tetrahedron*, 2003, **59**, 2207.

80) K. Y. Lee, C. G. Lee and J. N. Kim, *Tetrahedron Lett.*, 2003, **44**, 1231.

81) W. L. F. Armarego and D. D. Perrin, *Purification of Laboratory Chemicals*, Elsevier, 4th edn, 1996.

82) G. M. Sheldrick, SHELX-97, Programs for Crystal Structure Analysis, University of Göttingen, Göttingen, Germay, 1997.

83) FEFF 8.4, Aug. 2006, copyright by A. Ankudinov, B. Ravel and J. J. Rehr. Further information can be found online at: http://leonardo.phys.washington.edu/feff/.

CHAPTER 5

Mononuclear M(III) chloride and M(IV) oxide (M = Cr, V, Ti) complexes bearing mixed β-diketiminate/β-diketonate *bis*-chelates for X-ray polarimetry

5.0 Mononuclear M(III) chloride and M(IV) oxide (M = Cr, V, Ti) complexes bearing mixed β-diketiminate/β-diketonate *bis*-chelates for X-ray polarimetry

In this chapter, emphasis will be placed on the synthesis and structural characterisation of potential low energy K-edge [*viz*., Cr (5989 eV), V (5469 eV), Ti (4966 eV)] X-ray dichroic materials that are based on the five co-ordinate motifs, [(β-diketiminate)MCl(β-diketonate)] and [(β-diketiminate)MO(β-diketonate)] (Figure 5.1). Chapter 4 highlighted the enhanced pre-edge feature displayed by porphyrinato-supported vanadium and titanium oxides which has in turn contributed to a more significant dichroic feature at this particular energy bin. Herein, the *bis*-chelates [(β-diketiminate)MO(β-diketonate)] are employed as an alternative platform for vanadium(IV) and titanium(IV) oxides and, in addition, their vanadium(III) and titanium(III) chloride counterparts, [(β-diketiminate)MCl(β-diketonate)] have been targetted; the bound chloride in the latter may serve as an additional low energy K-edge (Cl K-edge 2822 eV). Furthermore, chromium-based materials of the oxide- and chloride-type will be targeted, the latter already having some track record at forming highly ordered mixed β-diketiminate/β-diketonates in the solid state (see **21** in section 5.1).
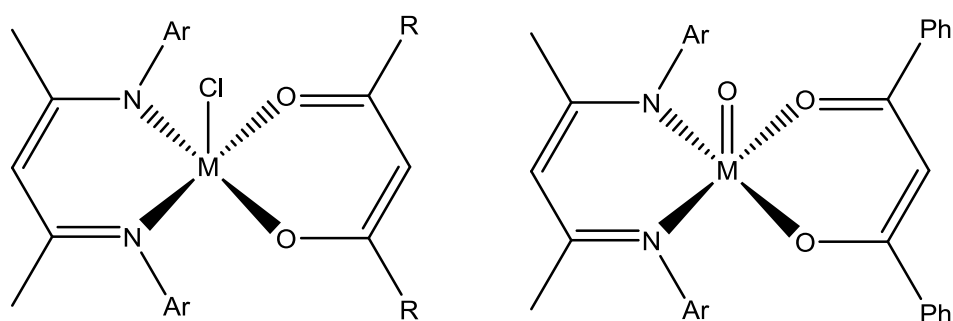
Figure 5.1 Target *bis*-chelate metal halides and oxides (M = Cr, V, Ti; Ar = aryl; R = Ph, Me).

5.1 Background to [(β-diketiminate)MCl(β-diketonate)] and [(β-diketiminate)MO(β-diketonate)] (M = Cr, V, Ti) compounds; aims and objectives

β-Diketiminates have received considerable interest in recent years due, in part, to their connection with polymerisation catalysis.[1] In particular, 4-(2,6-diisopropylamino)pent-3-en-2-ylidine)-2,6-diisopropylanilide (nacnac) has been widely use as a bidentate N,N spectator ligand allowing access to a variety of low co-ordination number 3*d* metal-containing complexes. This

ability of *mono*-anionic nacnac to restrict the co-ordination number of a complex can be attributed to the steric properties of the two *N*-aryl groups.[2–4] Surprisingly, there has only been one metal halide complex bearing both chelating β-diketiminate and β-diketonate ligands that has been crystallographically characterised, namely, five co-ordinate [(nacnac)CrCl(dbm)] (**21**).[5]

On the other hand, no examples of the oxide family [(β-diketiminate)MO(β-diketonate)] have been disclosed for any of the first row transition metals, while only one example of a five co-ordinate *bis*-nacnac species exists, [(nacnac)$_2$TiCl] (τ = 0.3).[6] With regard to **21**, the geometry of the complex can be best described as almost perfectly SBP (τ = 0.01) with the chloride ligand occupying the axial site. Moreover, the packing features of **21** reveal considerable order in the solid state with the intermolecular ClCr···CrCl torsion angle being 180° (see Figure 5.2). In terms of synthetic strategy, **21** can be readily accessed by firstly preparing the *mono*-nacnac chromium(III) species [(nacnac)CrCl(μ-Cl)]$_2$[5,7] followed by its treatment with the dibenzoylmethanato anion. A similar strategy could be envisaged for preparing the vanadium(III) and titanium(III) analogues of **21** and indeed the synthesis of *mono*-nacnac intermediates [(nacnac)TiCl$_2$(THF)$_2$][8,9] and [(nacnac)VCl$_2$(THF)$_2$][9] have been previously reported along with their non-solvated counterparts.[11–13] In contrast, the only reported neutral nacnac-containing manganese chloride species are divalent [(nacnac)Mn(μ-Cl)]$_2$[13] and [{(nacnac)Mn(μ-Cl)$_2$}$_2$Mn(THF)$_2$];[14] the lithiate [(nacnac)MnCl$_2$][Li(OEt$_2$)$_2$] and imidazolium salts [(nacnac)MnCl$_2$][imdz] are also known.[15]

Given the desirable characteristics exhibited by **21**, its synthesis has been repeated in this work and the synthetic methodology extended to its acetylacetonate derivative. Furthermore, in Chapter 4, the oxidation of porphyrinato-bound early transition metal halides to give the corresponding metal oxides proved a facile transformation. Herein, a similar reaction methodology is outlined to oxidise [(β-diketiminate)MCl(β-diketonate)] to give [(β-diketiminate)MO(β-diketonate)] for chromium(III), vanadium(III) and titanium(III). Whilst the emphasis on this chapter is placed on these three early transition metal centres, a brief section is

also included which discusses attempts to prepare manganese(III)-containing *bis*-chelates, [(nacnac)MnCl(β-diketonate)] from manganese(II) starting materials.

In Chapters 2 and 4, the reliability of using multiple scattering theory (FEFF) to model the experimental XAS data was demonstrated. In this chapter, this theoretical approach has again been applied, in this case, to *predict* spectral features for selected compounds in order to ascertain their potential usefulness as dichroic materials.

5.2 Synthesis and characterisation of [(nacnac)MCl(β-diketonate)] and [(nacnac)MO(β-diketonate)] (M = Cr, V, Ti)

5.2.1 Preparation of [(nacnac)CrCl(β-diketonate)] (21 and 22) and attempted oxo formation
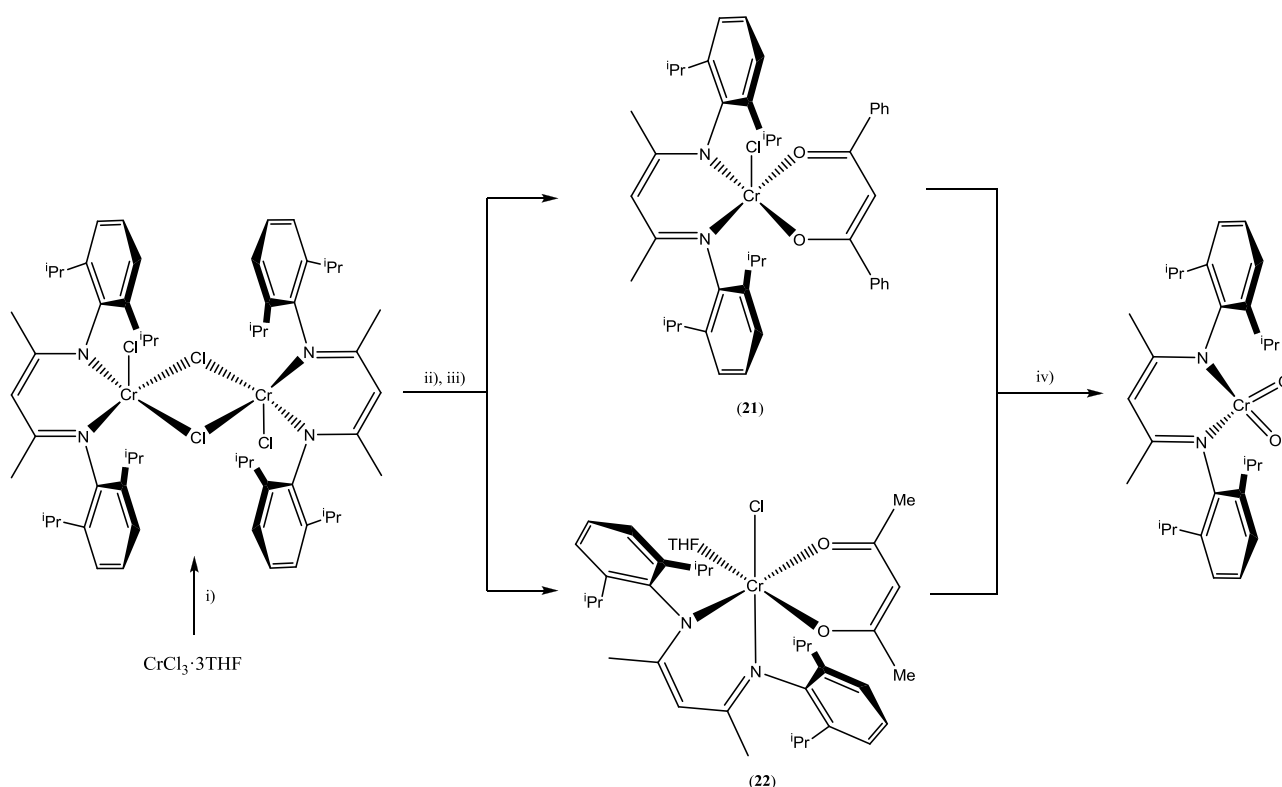
Scheme 5.1 *Reagents and conditions*; i) Li[nacnac], THF, -78 °C, 12 h; ii) Li[acac] or Li[dbm], -78 °C, 12 h; iii) dry petroleum ether (b.p. 40–60 °C), -30 °C, N₂; iv) petroleum ether (b.p. 40–60 °C)/H₂O, -30 °C.

The successive treatment of CrCl₃·3THF with lithium nacnac and the corresponding lithium β-diketonate (dibenzoylmethanato or acetylacetonate), afforded upon recrystallisation with dry petroleum ether at -30 °C, [(nacnac)CrCl(dbm)] (**21**) and [(nacnac)CrCl(THF)(acac)] (**22**) as orange and brown blocks, in good yields, respectively (Scheme 5.1).

The *mono*-nacnac intermediate [(nacnac)CrCl(μ-Cl)]$_2$ was not isolated in either reaction. Both **21** and **22** have been previously characterised using spectroscopic and analytical methods and in the case of **21** by single crystal X-ray diffraction.[5] A unit cell determination on a crystal of **21** grown in this study was consistent with the reported data; a full data collection was performed on **22**. The molecular structures of **21** and **22** are illustrated in Figures 5.2 and 5.3; selected bond lengths and angles are listed in Table 5.1.
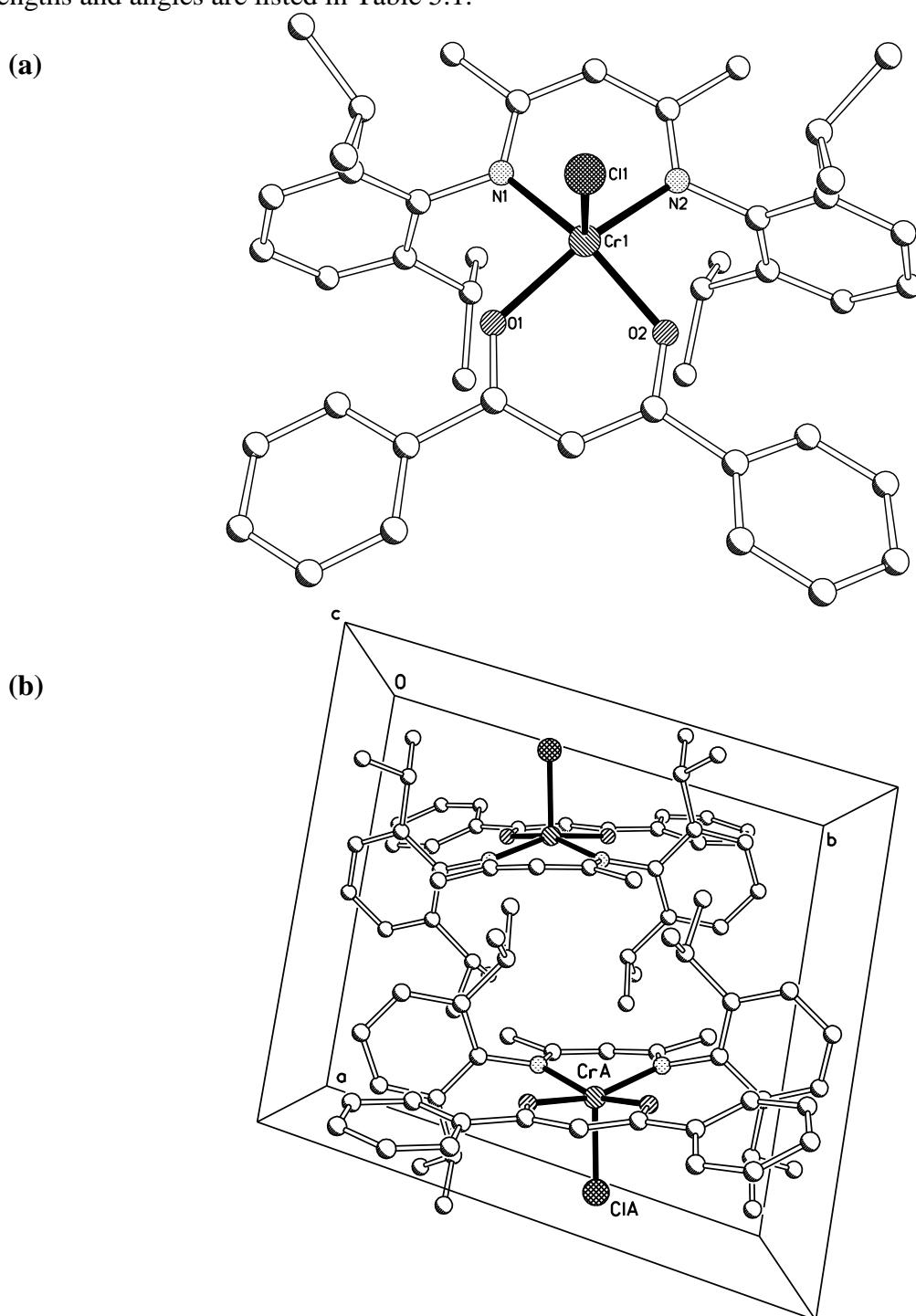

(a)

(b)

Figure 5.2 (a) Molecular structure of **21**[5] with partial atom labels; hydrogen atoms have been omitted for clarity. (b) Molecular packing diagram viewed down the crystallographic *c*-axis. Image generated from data obtained from the CSD.
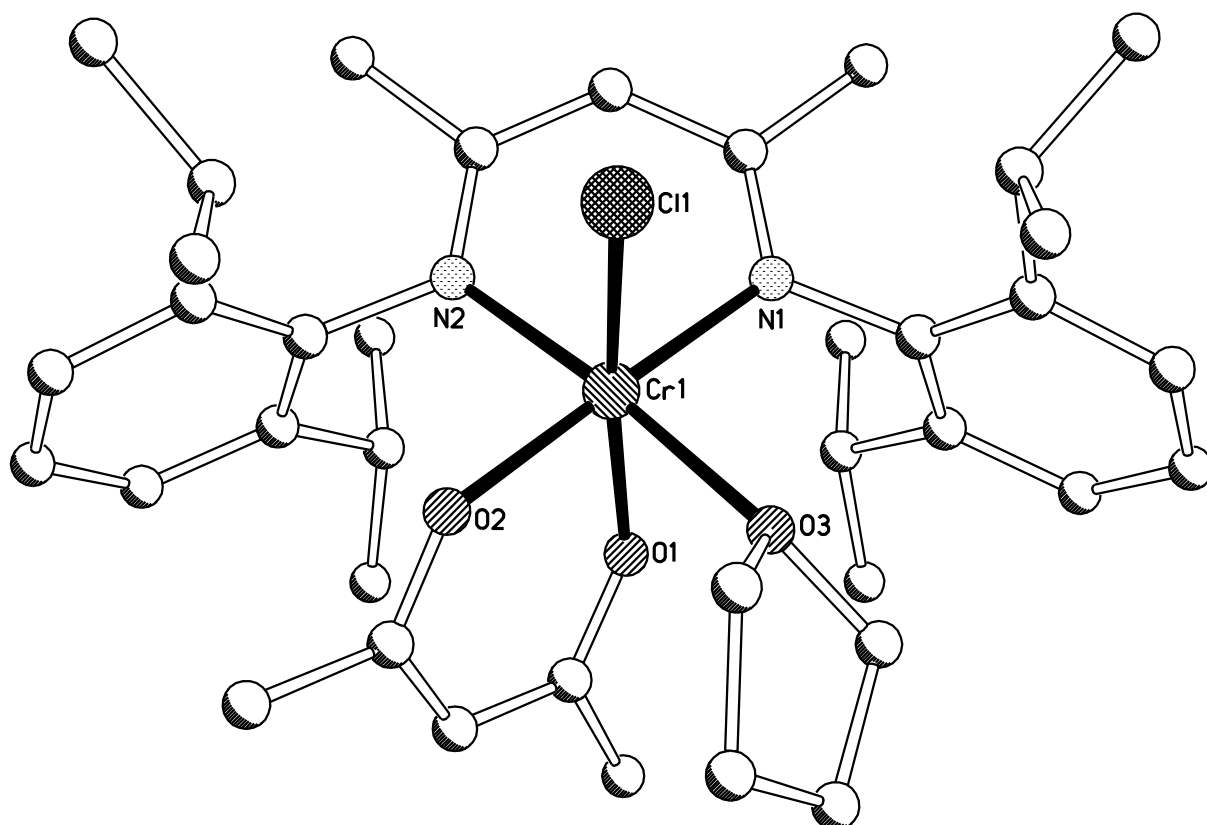
Figure 5.3 Molecular structure of **22** with partial atom labels; hydrogen atoms have been omitted for clarity.

Table 5.1. Selected bond lengths (Å) and angles (°) for **21**[5] and **22**.

	21[5]	**22**
Cr(1)–N(1)	2.020(3)	2.076(3)
Cr(1)–N(2)	2.032(3)	2.035(3)
Cr(1)–O(1)	1.958(3)	1.956(3)
Cr(1)–O(2)	1.961(3)	1.985(3)
Cr(1)–O(3)$_{THF}$	–	2.133(3)
Cr(1)–Cl(1)	2.2294(14)	2.3057(12)
N(1)–Cr(1)–N(2)	90.54(13)	90.62(11)
N(1)–Cr(1)–O(1)	87.83(12)	90.43(12)
N(1)–Cr(1)–O(2)	161.63(13)	178.04(12)
N(3)–Cr(1)–O(3)$_{THF}$	–	95.49(11)
N(1)–Cr(1)–Cl(1)	102.25(11)	91.42(9)
N(2)–Cr(1)–O(1)	161.27(13)	97.57(12)
N(2)–Cr(1)–O(2)	88.85(13)	89.44(11)
N(2)–Cr(1)–O(3)$_{THF}$	–	173.87(11)
N(2)–Cr(1)–Cl(1)	102.20(10)	91.58(9)
O(1)–Cr(1)–O(2)	86.89(11)	87.62(12)
O(1)–Cr(1)–O(3)$_{THF}$	–	82.90(11)
O(1)–Cr(1)–Cl(1)	96.02(10)	170.36(9)
O(2)–Cr(1)–O(3)$_{THF}$	–	84.47(11)
O(2)–Cr(1)–Cl(1)	96.18(10)	90.53(9)
O(3)–Cr(1)–Cl(1)	–	87.50(8)

The molecular structures of **21** and **22** both contain chelating nacnac and β-diketonate ligands along with a terminal chloride atom. However, **22** differs in that it displays an additional oxygen bound molecule of tetrahydrofuran which adopts the *envelope* configuration. The geometry of **21** can best be described as distorted SBP ($\tau = 0.01$), with the chloride atom filling the apical position. In contrast, the geometry of **22** can be described as distorted octahedral with a tetrahydrofuran ligand *trans* to N(2)$_{\text{nacnac}}$ and Cl(1) *trans* to O(1)$_{\text{acac}}$. Of the three Cr–O bond lengths in **22**, the Cr–O$_{\text{THF}}$ is the longest [2.113(3) Å] reflecting the dative interaction displayed by the neutral tetrahydrofuran molecule. The presence of co-ordinated tetrahydrofuran in **22** is likely attributable to the less sterically encumbered nature of the acetylacetonate ligand compared to dibenzoylmethanato in **21**.

The molecular packing diagram of **21** is highly aligned in the solid state with two symmetry related molecules present in the unit cell in which the neighbouring Cr–Cl bonds are oriented 180° to each other. On the other hand, **22** displays undesirable characteristics for a potential dichroic filter, firstly, the octahedral co-ordination geometry and secondly, the orientation between neighbouring Cr–Cl bonds of the four symmetry related molecules shows some degree of misalignment [tors: ClCr···CrCl = 35.01°].

Attempts to oxidise **21** and **22** using bench petroleum ether to form the chromium(IV) [(nacnac)CrO(β-diketonte)] were not successful (Scheme 5.1). Instead the chromium(V) dioxide species [(nacnac)CrO$_2$] was isolated in which a chelating β-diketonate has been effectively replaced by an oxygen atom.[15] A possible driving force for this oxidation is the stability associated with the high chromium(V) oxidation state.

5.2.2 Preparation of [(nacnac)MCl(β-diketonate)] (M = V, Ti) and conversion to the metal oxide
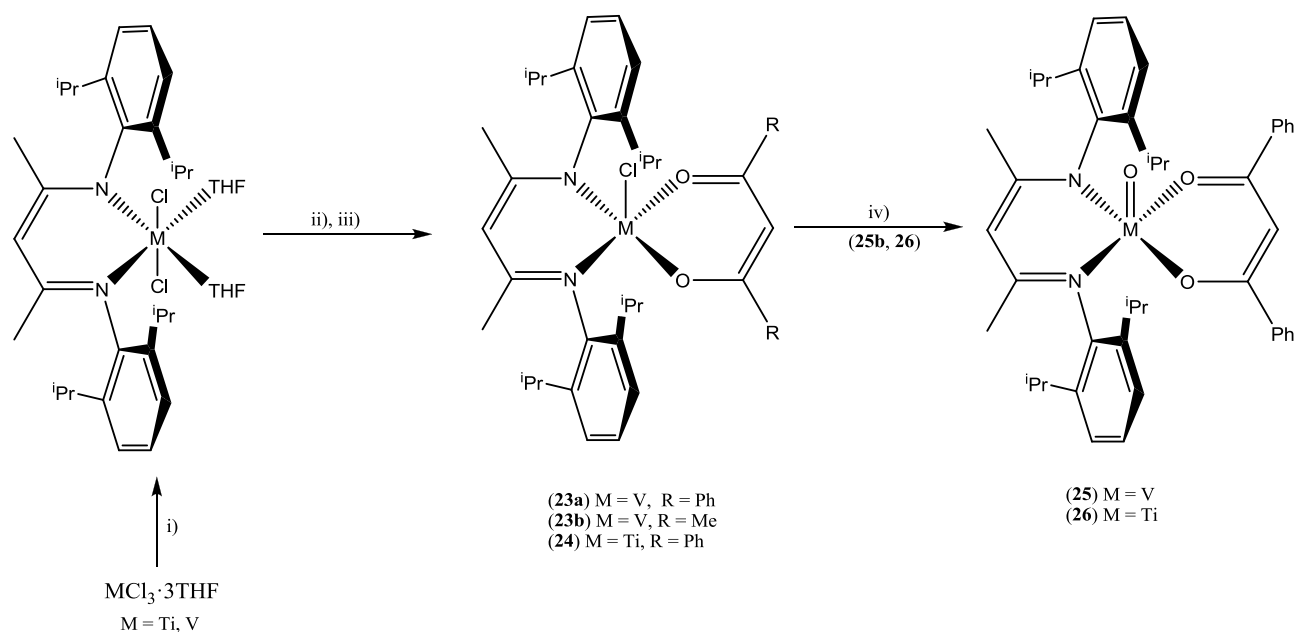
Scheme 5.2 *Reagents and conditions*; i) Li[nacnac], THF, -78 °C, 12 h; ii) Li[dbm], -78 °C, 12 h; iii) dry petroleum ether (b.p. 40–60 °C), -30 °C, N$_2$; iv) petroleum ether (b.p. 40–60 °C)/H$_2$O, -30 °C.

Treatment of MCl$_3$·3THF (M = V, Ti) with lithium nacnac in tetrahydrofuran at -78 °C followed by addition of the corresponding lithium β-diketonate (acac, dbm) at the same temperature gave, on recrystallisation from dry petroleum ether, [(nacnac)VCl(dbm)] (**23a**), [(nacnac)VCl(acac)] (**23b**) and [(nacnac)TiCl(dbm)] (**24**) in good yields, respectively (Scheme 5.2). The *mono*-nacnac intermediates [(nacnac)MCl$_2$(THF)$_2$] (M = V, Ti) were not isolated in any of these reactions. The complexes **23a**, **23b** and **24** have been characterised by a combination of FAB mass spectrometry, IR spectroscopy, magnetic measurements, elemental analysis and in addition for **23b**, by single crystal X-ray diffraction.

Crystals of **23b** suitable for the X-ray structure determination were obtained upon standing of a concentrated petroleum ether solution of the complex at -30 °C for 24 hours. The molecular structure of **23b** is depicted in Figure 5.4 along with its molecular packing picture; selected bond lengths and angles are listed in Table 5.2. The structure of complex **24b** is similar to **21** in that it consists of a V–Cl unit which is chelated to by the monoanionic, nacnac and acetylacetonate ligands to complete a distorted five co-ordinate, SBP geometry ($\tau = 0.40$) with the chloride atom

filling the apical position. However, the geometry is considerably more distorted towards TBP than in **21** ($\tau = 0.01$). It is notable that the metal centre is removed from the basal N,N,O,O plane by 0.722 Å which is greater than that observed for **21** (0.320 Å). The distortion in the molecular geometry can be envisaged to be the result of the difference in the chelating ligand bite angles, with the β-diketonate binding tighter than the β-diketiminate [O(1)V(1)O(2) = 84.68° *vs.* N(1)V(1)N(2) = 89.49°]; these values are less pronounced in **21** [O(1)Cr(1)O(2) = 86.77°, *vs.* N(1)Cr(1)N(2) = 90.46°].

The aryl rings of the nacnac ligand in **23b** are inclined at an angle of *ca.* 90° to the N,N,O,O plane and one pair of the aliphatic isopropyl groups are located directly underneath this basal plane offering some steric encumbrance to the sixth co-ordination site. Interestingly a *pseudo-agostic* interaction [C(15)H⋯V(1)] is present between the isopropyl CH protons of the 2,6-diisopropylphenyl-containing nacanc ligand and the vanadium metal centre with a close interaction of 3.102 Å. It is uncertain why a molecule of tetrahydrofuran is not co-ordinated in **23b** in a manner similar to **22**, however, it may be attributed to the distortions in the SBP geometry preventing the dative co-ordination. The molecular packing diagram (Figure 5.4b) of **23b** reveals two symmetry related molecules in the unit cell, in which the neighbouring V–Cl bonds are aligned 180° to each other. Molecules of disordered solvents were also present in the lattice.

Complexes **23a**, **23b** and **24** all reveal molecular ion peaks in their FAB mass spectra; fragmentation peaks corresponding to loss of the apical chloride are also evident in **25a** and **25b**. Magnetic moments for **23a**, **23b** and **24** were determined at 2.41, 2.56 and 1.87 BM respectively (Evans balance at room temperature) and were consistent with the presence of two unpaired electrons in **23a** and **23b** and one unpaired electron in **24**. Elemental analysis of **23b** was lower than that expected consistent with significant decomposition.

Recrystallisation of **23a** and **24** upon standing in bench petroleum ether at -30 °C gave the M(IV) oxide species, [(nacnac)MO(dbm)] [M = V (**25**), Ti (**26**)] as green and orange blocks in good yields, respectively (Scheme 5.2). The structure of **25** is depicted in Figure 5.5; selected bond lengths and angles for **25** and **26** are given Table 5.3.
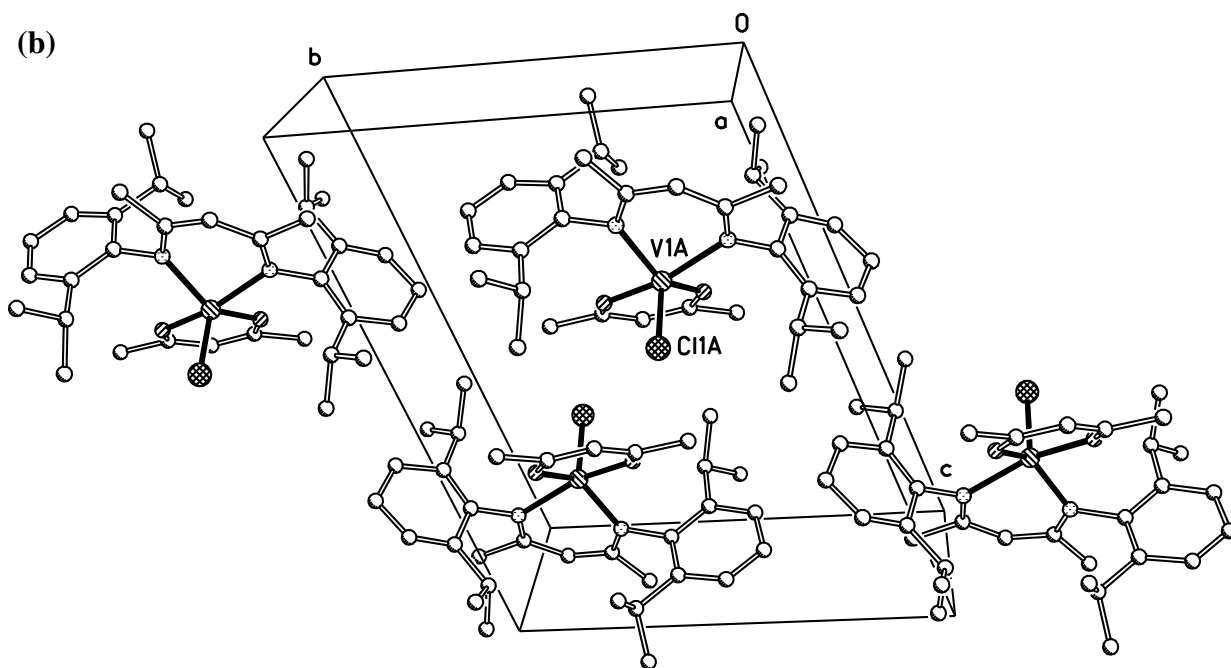
(a)
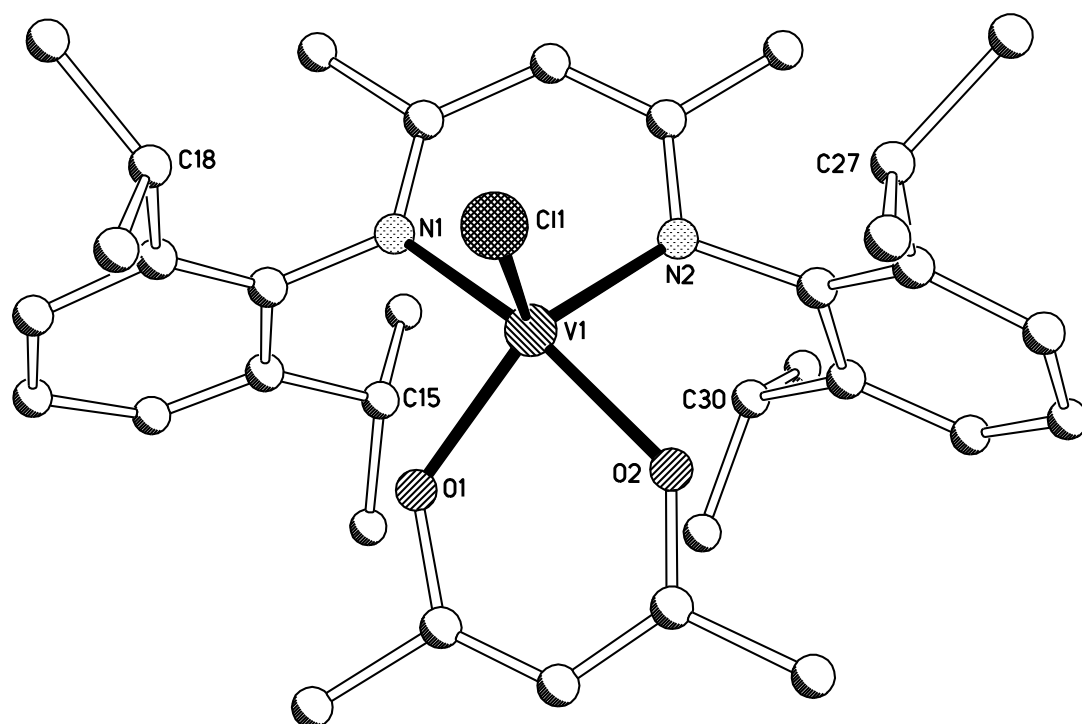
(b)

Figure 5.4 (a) Molecular structure of **23b** with partial atom labels; hydrogen atoms and selected carbon atom labels have been omitted for clarity. (b) The molecular packing diagram viewed off the *a*-axis.

Table 5.2 Selected bond lengths (Å) and angles (°) for **23b**.

	23b
M(1)–N(1)	2.099(10)
M(1)–N(2)	1.960(10)
M(1)–O(1)	1.945(9)
M(1)–O(2)	1.977(7)
M(1)–Cl(1)	2.122(6)
N(1)–V(1)–N(2)	89.5(4)
N(1)–V(1)–O(1)	84.2(4)
N(1)–V(1)–O(2)	160.8(4)
N(1)–V(1)–Cl(1)	102.9(3)
N(2)–V(1)–O(1)	136.6(4)
N(2)–V(1)–O(2)	88.0(3)
N(2)–V(1)–Cl(1)	109.1(3)
O(1)–V(1)–O(2)	84.7(3)
O(1)–V(1)–Cl(1)	114.2(4)
O(2)–V(1)–Cl(1)	95.9(3)

The structures of **25** and **26** are isostructural and consist of a metal-oxo unit supported by chelating nacnac and dibenzoylmethanato anionic ligands. The oxygen atom occupies the apical co-ordination site to complete SBP geometries with the complexes displaying τ-values of 0.03 and 0.10 for **25** and **26**, respectively. The M=O bond in **25** is also 0.036 Å shorter than that displayed in **26** due to periodicity effects, namely the increase in nuclear charge across the first row transition metal series. In both cases, a possible hydrogen bonding interaction can be observed between the C(27)H isopropyl proton and the apical oxygen atom [(O(3)···HC(27) = 2.776 Å (**25**), 2.607 Å (**26**)]. In addition, possible *pseudo*-agostic interactions between the C(15)H isopropyl proton with the metal centre are evident in **25** and **26** in a similar fashion to that described for **23b** with **25** displaying a much longer interaction [C(15)H···M(1) = 3.171 Å (**25**), 3.009 Å (**26**)]. The unit cells **25** and **26** contain four symmetry related molecules with **25** and **26** revealing similar intermolecular alignment with respect to the neighbouring M=O bonds [tors: OM···MO = 21.26° (**25**), 27.85° (**26**)]. Interestingly, during one attempt to prepare **25**, the vanadium(III) terminal hydroxide species [(nacnac)V(OH)(dbm)] was crystallised, a likely intermediate in the formation of **25**. Notably, the hydroxide species displays a V–O bond length of 1.731(4) Å, which is longer than that found in **25** and similar to a range of V–O bond lengths for vanadium-containing complexes containing bound terminal hydroxide ligands.[16–19]

The IR spectra for **25** and **26** gave peaks at *ca.* 800–900 cm^{-1} consistent with a bound v(M=O) stretch. The magnetic moment for **25** was determined at 1.78 BM (Evans balance at room temperature) and consistent with the presence of one unpaired electron associated with a V(IV) d^1 metal centre. Complex **26** was diamagnetic and revealed in its ^{1}H NMR spectrum, two 1H singlets at δ 4.59 and 4.79 corresponding to the CH protons of the dibenzoylmethanato and nacnac ligands. Unfortunately, the results of a NOE (Nuclear Overhauser Effect) two dimensional ^{1}H NMR experiment were inconclusive when attempting to determine the respective identities of these two protons.
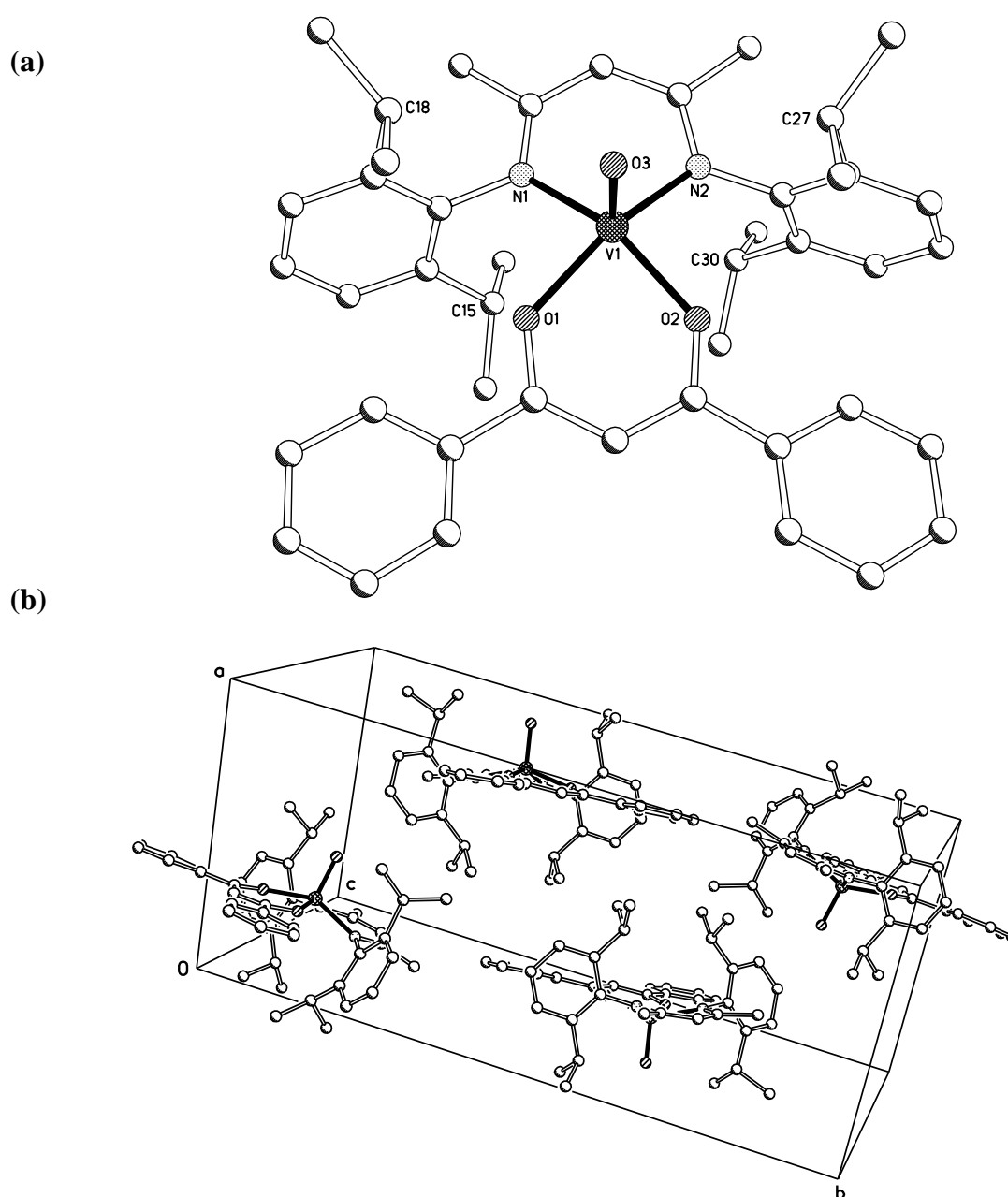

Figure 5.5 (a) Molecular structure of **25** with partial atom labels; hydrogen atoms and selected carbon labels have been omitted for clarity. (b) Off-axis molecular packing diagram for **25**.

Table 5.3 Selected bond lengths (Å) and angles (°) for **25** and **26**.

	25 (M = V)	**26** (M = Ti)
M(1)–N(1)	2.048(5)	2.101(3)
M(1)–N(2)	2.036(5)	2.107(3)
M(1)–O(1)	1.982(3)	2.002(3)
M(1)–O(2)	1.976(3)	1.996(3)
M(1)–O(3)	1.591(3)	1.627(3)
N(1)–M(1)–N(2)	88.92(17)	87.25(12)
N(1)–M(1)–O(1)	86.27(17)	85.15(10)
N(1)–M(1)–O(2)	151.22(17)	147.29(12)
N(1)–M(1)–O(3)	102.70(18)	103.25(13)
N(2)–M(1)–O(1)	149.34(17)	153.46(12)
N(2)–M(1)–O(2)	85.55(17)	88.63(10)
N(2)–M(1)–O(3)	103.97(18)	102.66(13)
O(1)–M(1)–O(2)	84.28(15)	82.24(9)
O(1)–M(1)–O(3)	106.63(17)	104.47(12)
O(2)–M(1)–O(3)	106.05(18)	109.35(13)

5.3. Attempted synthesis of [(nacnac)MnCl(β-diketonate)]

By analogy with the electronically driven SBP geometry employed in the copper(II) complexes described in Chapters 2 and 3, it was envisaged that a similar electronic bias would occur for high-spin d^4 configurations. In that vein, attempts to target manganese(III) complexes of the type, [(nacnac)MnCl(β-diketonate)] (β-diketonate = acac, dbm) were made. Unfortunately, the potential manganese(III) trichloride starting material has only been tentatively isolated and is not stable above -40 °C.[20] Additionally, the manganese(III) tribromide and triiodide derivatives have never been isolated,[21] with only manganese(III) trifluoride starting materials stable at room temperature.[21] As an alternative, a synthetic methodology could be envisaged which utilises the common manganese(II) chloride starting material leading to manganese(II) *bis*-chelates of the type [(β-diketiminate)Mn(β-diketonate] which could, in principle, be chemically oxidised at a later stage in the reaction; a methodology which has been shown to be successful in Chapter 4 with the oxidation of [(TPP)Mn(II)] to [(TPP)Mn(III)Br] using HBr as the chemical oxidant.
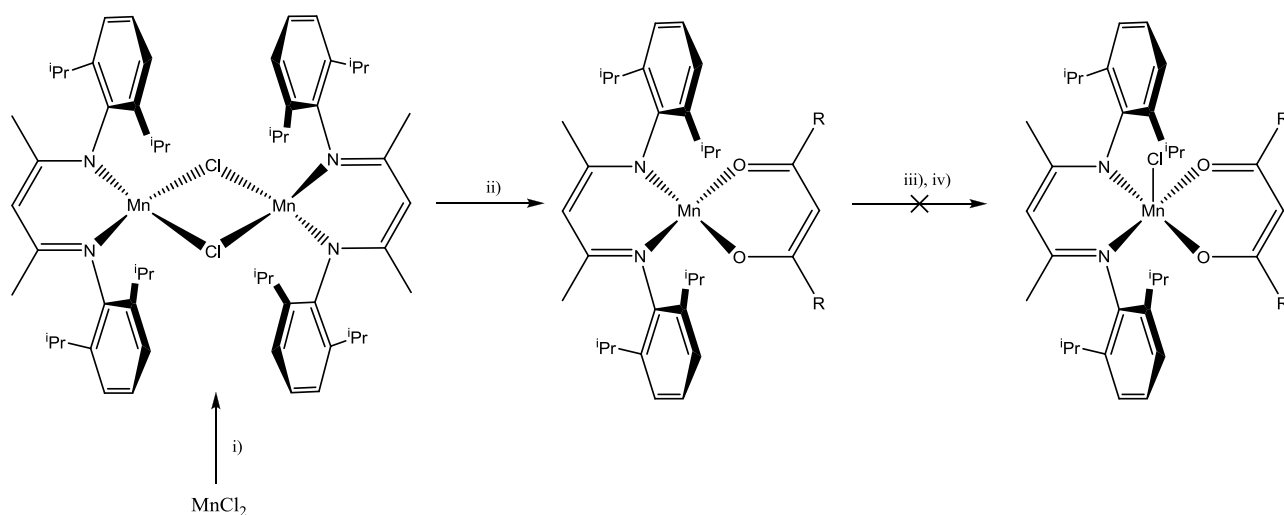
Scheme 5.3 *Reagents and conditions*: i) Li[nacnac], THF, 12 h, -78 °C; ii) Li[acac] or Li[dbm], -78 °C, 12 h; iii) [O], either HCl, SOCl$_2$, PCl$_5$, H$_2$O$_2$ or NaCl; iv) dry petroleum ether (b.p. 40–60 °C), -30 °C, N$_2$.

Hence, treatment of manganese(II) dichloride with the lithium salt of nacnac in tetrahydrofuran, followed by addition of the corresponding lithium β-diketonate (acac or dbm) gave, on the basis of FAB mass spectrometry, complexes of the type, [(nacnac)Mn(II)(β-diketonate)] (Scheme 5.3). Unfortunately, upon treating this intermediate with a range of oxidising agents, the desired target complexes could not be conclusively characterised, instead intractable products were isolated. Cobalt(III) derivatives were also targeted using this approach which lead to similar non-characterisable materials.

5.4 Prediction of the polarised XAS spectra of 21, 23b, 25 and 26 using an MS approach

On the basis of the successful FEFF calculations carried out in Chapters 2 and 4 to model experimental polarised XAS spectra, the MS technique will again be applied in this chapter in order to *predict* the spectral features of **21**, **23b**, **25** and **26** to establish their usefulness as potential dichroic materials. It is worth noting that these are preliminary screening calculations and therefore the results should be treated with caution.

5.4.1 FEFF calculations performed on 25 and 26

On inspection of the FEFF calculated polarised XAS spectra for the titanium and vanadium-containing oxide species **25** and **26** (Figure 5.6), it is apparent that they both show similar spectral features, namely the intense pre-edge peak, main-edge 1 (shoulder) peaks, broad main-edge 2 peaks and EXAFS regions. More notably however, the pre-edge peak occurs as a well-defined singlet-type structure occurring at 5470 and 4970 eV for **25** and **26**, respectively. It is also clear that, as with the titanium and vanadium oxide porphyrins discussed in Chapter 4, the pre-edge peaks in the FEFF calculated XAS spectra for **25** and **26** both show potential X-ray dichroism, with the most intense peak occurring in the χ_0 orientation. Dichroism is also apparent at the main-edge and EXAFS region with both spectra revealing main-edge 2 peaks in the χ_0 intensity [5505 eV (**25**), 5011 eV (**26**)] which differs in energy and intensity than the main-edge 2 in the χ_{90} orientation [5490 eV (**25**) and 4990 eV (**26**)]. In the χ_0 orientation, the peak intensity is greater for **25** than in **26** with the structure of the main-edge 2 in **25** appearing much less intense and significantly broader. Main-edge 1 shoulder peaks occur for both complexes in the χ_{90} orientation at 5483 and 4983 eV for **25** and **26**, respectively. In the EXAFS region, shallow differences in intensity occur over a broad energy range which are observable in both complexes [5522–5562 eV (**25**), 5032–5082 eV (**26**)] with the maximum difference in intensity occurring at 5548 and 5052 eV for **25** and **26**, respectively.

5.4.2 FEFF calculations performed on 21 and 23b

The FEFF calculated polarised XAS spectra of **21** and **23b** (Figure 5.7) are similar to those of **25** and **26** in that they both reveal pre-edge, main-edge and EXAFS regions. With specific regard to the dichroic pre-edge peak in **23b**, the peak is sharp and well defined (5470 eV), however, in **21** the feature is significantly reduced and appears almost as a shoulder within the main-edge 1 (5994 eV).
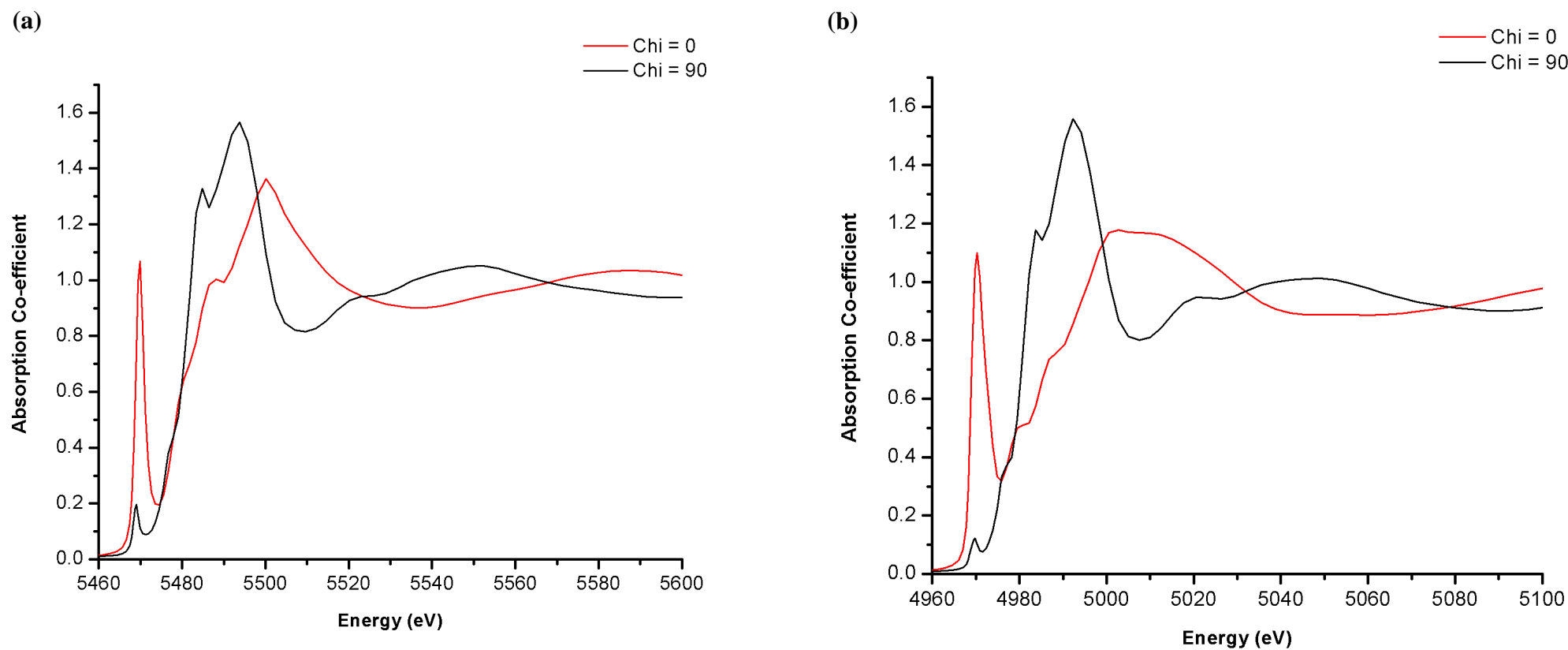
Figure 5.6 FEFF calculated XAS spectra for (a) **25** and (b) **26** at the V and Ti K-edges, respectively for orientations of χ_0 and $\chi_{90.}$

This observation is consistent with the FEFF calculated spectra of the higher energy cobalt containing **15a** in Chapter 4 (section 4.6) when compared to the vanadium-containing **18**$_{DCM}$. At the main-edge 2, the appearance of the edge shows some similarities in that the main-edge 1 shoulder is present in both spectra, prominent in the χ_{90} orientation [6008 eV (**21**), 5460 (**23b**)]. The main-edge 2 and EXAFS region in the χ_0 orientation in **21** appears flatter than that of **25**, **26** and **23b**. However, deep oscillations occur that continue into the EXAFS region with two prominent peaks evident around the main-edge 2 (6002 and 6023 eV). Complexes **23b**, **25** and **26** on the other hand display single main-edge 2 peaks occurring at 5505, 5507 and 5011 eV, respectively.

5.4.3 FEFF summary

As a preliminary attempt to use FEFF as a predictive tool, the theoretical data suggests that **21**, **23b**, **25** and **26** represent very promising materials that should be probed experimentally as dichroic filters. All complexes display the useful pre-edge peak which shows strong polarisation dependence in a fashion similar to the low K-edge energy systems discussed in Chapter 4 where experimental data has been obtained. Interestingly, the higher energy chromium-containing **21** reveals a diminished pre-edge peak, nevertheless it is still clearly observable. In addition dichroic features have been observed in the main-edge 1, main-edge 2 and EXAFS regions for all four complexes. From the quantification of X-ray dichroism in **15a**$_{DCM}$ and **18**$_{DCM}$ in Chapter 4, it was discussed that the dichroic response is weighted in terms of the specific dichroic regions, depending on the metal centre. Herein, this observation is also evident on inspection of the FEFF calculated polarised XAS spectra, where the lower energy vanadium- and titanium-containing complexes (**25**, **26**) reveal more significant dichroism in the pre-edge regions while in the higher energy chromium-containing **21** the dichroism in more weighted towards the main-edge.
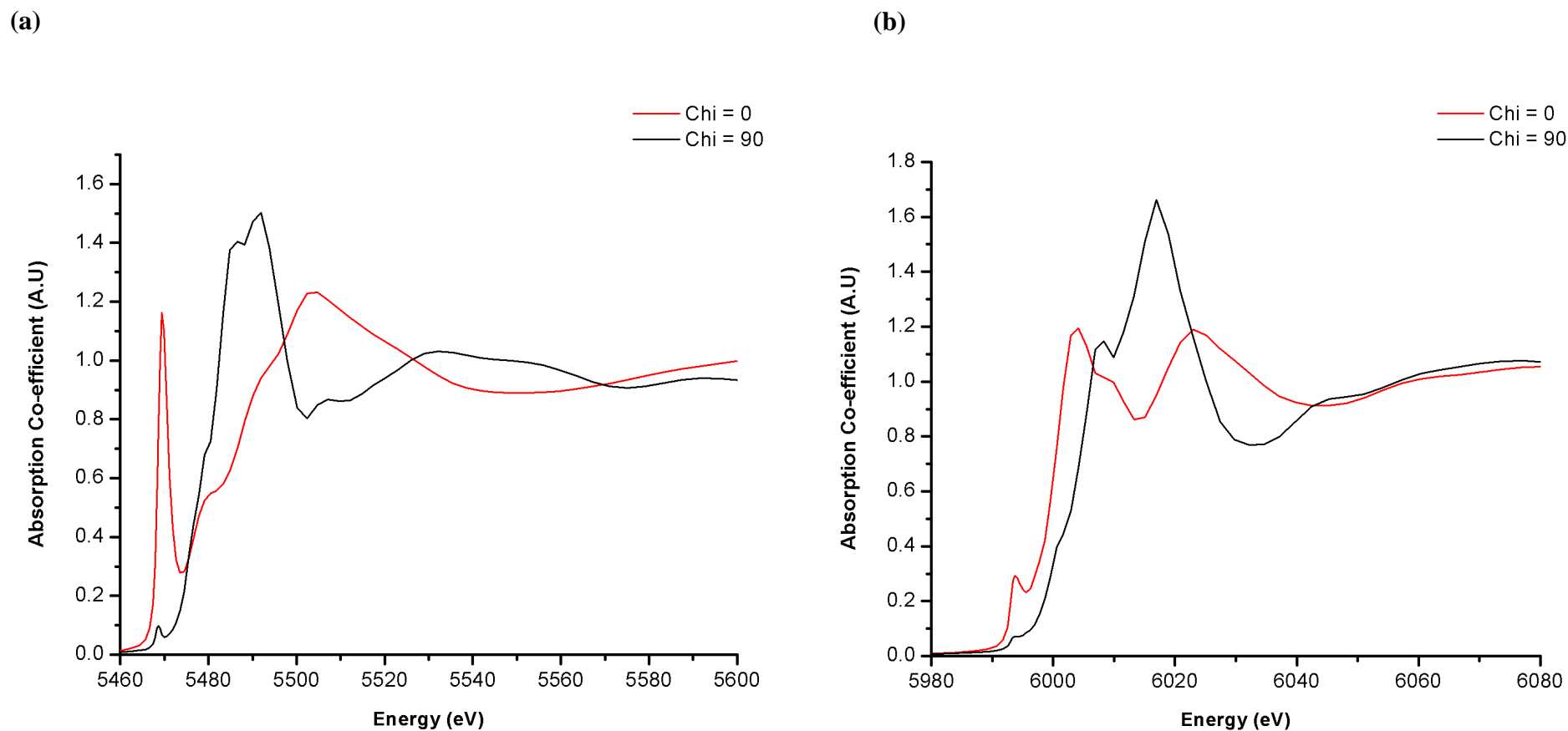
(a)

(b)

Figure 5.7 FEFF calculated XAS spectra for (a) **23b** and (b) **21** at the V and Cr K-edges, respectively for orientations of χ_0 and χ_{90}.

5.5 Conclusions

The highly ordered chromium-based [(nacnac)CrCl(dbm)] (**21**) has been re-examined in this work with a view to utilising its desirable structural properties as a potential single crystal dichroic filter material. In addition, its previously reported acetylacetonate derivative has herein been crystallographically characterised for the first time yielding [(nacnac)CrCl(acac)(THF)] (**22**) as a tetrahydrofuran adduct.

The extension of this synthetic methodology to other low K-edge energy materials has led to the isolation and characterisation of complexes of the type, [(nacnac)MCl(β-diketonate)] [M = V, β-diketonate = dbm (**23a**), acac (**23b**); M = Ti, β-diketonate = dbm (**24**)], where **23b** has been characterised using single crystal X-ray diffraction and is also highly ordered in the solid state. Attempts to prepare [(nacnac)MnCl(β-diketonte)] were unsuccessful. On the other hand, the hydrolysis/oxidation of **23a** and **24** provides a facile route to the crystallographically characterised metal oxides [(nacnac)MO(dbm)] [M = V (**25**), Ti (**26**)].

Four complexes, **21**, **23b**, **25** and **26** have been investigated by employing a multiple-scattering approach using FEFF in order to predict their potential dichroic behaviour. All four complexes display the expected spectral regions and all show a prominent pre-edge peak that reveals X-ray dichroism. It is clear that these dichroic responses are weighted between the pre-edge and main-edges depending on the metal centre employed. On this basis, it can be concluded that indeed, these materials are potential candidates for an experimental X-ray dichroic evaluation at the chromium (5989 eV), vanadium (5469 eV) and titanium (4966 eV) K-edges.

As a concluding remark, while these materials (**21** and **22**–**26**) can, in principle, be employed as potential dichroic filters (based on their desirable structural and morphological features along with basis of a preliminary theoretical dichroic evaluation), their sensitivity to aerobic conditions creates practical issues. The concept of passive encapsulation or lamination may present a potential remedy to preserving the integrity of the material.

5.6 General experimental

In addition to the experimental details described in Chapters 2, 3 and 4 (Chapter 2, section 2.9; Chapter 3, section 3.9; Chapter 4, section 4.13), all operations, unless otherwise stated, were carried out under an inert atmosphere of dry, oxygen-free nitrogen using standard Schlenk and cannular techniques or in a nitrogen purged glove box. Solvents were dried from appropriate drying agents.[22] The reagents $TiCl_3 \cdot 3THF$, $VCl_3 \cdot 3THF$, dibenzoylmethane (Hdbm) and *n*-butyl lithium (1.6M in hexanes) were purchased from Sigma Aldrich chemical company and used without further purification, whilst acetylacetone was distilled under reduced pressure prior to use. In addition, $CrCl_3 \cdot 3THF$[23,24] and the pro-ligand, nacnacH,[25] were synthesised in accordance with the previously reported methods.

5.6.1 Synthesis of 21 and 22

a) 21: A small Schlenk flask was evacuated, backfilled with nitrogen and charged with nacnacH (0.400 g, 0.956 mmol). Dry, degassed tetrahydrofuran (10 ml) was added and the solution cooled to -78 °C. A solution of *n*-butyl lithium (1.6 M in hexanes, 0.71 ml, 1.14 mmol, 1.2 eq.) was introduced at -78 °C and the solution stirred for 10 minutes before warming to room temperature and stirring for a further hour. After this time, the solution was re-cooled to -78 °C and $CrCl_3 \cdot 3THF$ (0.357 g, 0.956 mmol, 1 eq.) was added under nitrogen and the solution warmed to room temperature and the reaction mixture stirred overnight. Once again, the solution was cooled to -78 °C and a tetrahydrofuran solution of lithium dibenzoylmethanto (0.222 g, 0.956 mmol, 1 eq.; prepared in a similar fashion to lithium nacnac using 1.2 eq. of *n*-butyl lithum and 1 eq. of dibenzoylmethane), was added *via* cannula under nitrogen and the solution allowed to warm to room temperature with stirring for a further 12 hours. The solvent was removed under reduced pressure and the solid residue was dried for 1 h before extraction into dry petroleum ether (bp: 40–60 °C) (*ca.* 30 ml). Orange blocks of the title complex were obtained on standing at -30 °C overnight (0.150 g, 32%). Spectroscopic analysis was as previously reported.[5]

$a = 11.141(4)$ Å, $b = 12.740(3)$ Å, $c = 14.703(3)$ Å, $\alpha = 76.52(5)°$, $\beta = 84.97(5)°$, $\gamma = 80.52(4)°$, $V = 2005.4(6)$ Å^3; (*Literature*: $a = 11.1403$ Å, $b = 12.780$ Å, $c = 14.712$ Å, $\alpha = 76.519°$, $\beta = 84.967°$, $\gamma = 80.503°$, $V = 2006.2$ Å^3).[5]

b) 22: Using a similar approach and molar ratio of reactants to that described for **21**, **22** was obtained as brown plates (0.200 g, 40%). Spectroscopic analysis was as previously reported.[5] For X-ray data see Table 5.4.

5.6.2 Synthesis of 23a, 23b and 24

a) 23a: A small Schlenk flask was evacuated, backfilled with nitrogen and charged with nacnacH (0.400 g, 0.956 mmol). Dry, degassed tetrahydrofuran (10 ml) was added and the solution cooled to -78 °C. A solution of *n*-butyl lithium (1.6 M in hexanes, 0.71 ml, 1.14 mmol, 1.2 eq.) was added at -78 °C and the solution stirred for 10 minutes before warming to room temperature and stirring for a further hour. After this time, the solution was re-cooled to -78 °C and $VCl_3 \cdot 3THF$ (0.357 g, 0.956 mmol, 1 eq.) was added under nitrogen and the solution warmed to room temperature and stirred overnight. Once again, the solution was cooled to -78 °C and a tetrahydrofuran solution of lithium dibenzoylmethanato (0.222 g, 0.956 mmol, 1 eq.; prepared in a similar fashion to lithium nacnac using 1.2 eq. of *n*-butyl lithum and 1 eq. of dibenzoylmethane), was added *via* cannula under nitrogen and the solution allowed to warm to room temperature with stirring for a further 12 hours. The solvent was removed under reduced pressure using and the solid residue was dried for 1 h before extraction into dry petroleum ether (bp: 40–60 °C) (*ca.* 30 ml). The title complex was obtained as a green microcrystalline powder upon standing at -30 °C overnight (0.200 g, 28%). *m/z* (FAB), 693 (100%) [M - Cl]. μ_{eff} = 2.41BM

b) 23b: Using a similar approach and molar ratio of reactants to that described for **23a**, **23b** could be obtained as green blocks (0.230 g, 42%); ν_{max} (ATR)/cm^{-1} 1585, 1520, 1461, 1439, 1383, 1294, 1236, 1181, 1099, 1023, 898, 936, 858, 758, 678; *m/z* (FAB) 604 (10%) [M + H], 567 (100%) [M - Cl]; μ_{eff} = 2.56 BM; mp: >350 °C.

c) 24: Using a similar approach and molar ratio of reactants to that described for **23a**, **24** could be obtained as orange microcrystalline powder (0.100 g, 20%). ν_{max} (ATR)/cm^{-1} 1614, 1535, 1454, 1359, 1098, 935, 757; *m/z* (FAB), 689 (100%) [M - Cl]. μ_{eff} = 1.87 BM.

5.6.3 Synthesis of 25 and 26

a) 25: A small Schlenk flask was evacuated, backfilled with nitrogen and charged with nacnacH (0.400 g, 0.956 mmol) and dry, degassed tetrahydrofuran (10 ml). The solution was cooled to -78 °C and *n*-butyl lithium (1.6 M in hexanes, 0.71 ml, 1.14 mmol, 1.2 eq.) was added at -78 °C. The solution was stirred for 10 minutes before warming to room temperature and stirred for a further hour. After this time, the solution was re-cooled to -78 °C and VCl$_3$·3THF (0.357 g, 0.956 mmol, 1 eq.) was added under nitrogen and the solution warmed to room temperature and stirred overnight. Once again, the solution was cooled to -78 °C and a tetrahydrofuran solution of lithium dibenzoylmethanato (0.222 g, 0.956 mmol, 1 eq.; prepared in a similar fashion to lithium nacnac using 1.2 eq. of *n*-butyl lithium and 1 eq. of dibenzoylmethane) was added *via* cannula under nitrogen and the solution allowed to warm to room temperature with stirring for a further 12 hours. The solvent was removed under reduced pressure and the solid residue was dried for 1 h before extraction into bench petroleum ether (bp: 40–60 °C) (*ca.* 30 ml). The title complex was obtained as green blocks upon standing at -30 °C overnight (0.280 g, 44%). Found: C, 79.56; H, 4.93; N, 9.02; C$_{44}$H$_{55}$N$_2$O$_2$VO (710.86) requires: C, 79.44; H, 4.79; N, 8.74; ν_{max} (ATR)/cm^{-1} 1625, 1585, 1381, 1240, 1098, 981, 858, 761; *m/z* (FAB) 706 (20%) [M + H], 488 (100%) [M - Cl]; μ_{eff} = 1.78 BM; mp: >350 °C.

a) 26: Using a similar approach and molar ratio of reactants to that described for **23**, **24** was obtained as orange blocks upon standing in bench petroleum ether (bp: 40–60 °C) at -30 °C overnight (0.280 g, 44%). δ_H (400 MHz, CDCl$_3$, SiMe$_4$); 1.08 (d, *J* = 7.1, 6H, CH*Me$_2$*), 1.18 (d, *J* = 7.1, 6H, CH*Me$_2$*), 3.0 (sept, *J* = 4.5, 2H, C*H*Me$_2$), 4.59 (s, 1H, C*H*), 4.79 (s, 1H, C*H*), 6.50–7.50 (m, 16H, Ar*H*). Found: C, 69.78; H, 5.97; N, 3.13; C$_{44}$H$_{52}$N$_2$O$_3$Ti (704.75) requires: C, 69.92; H, 5.92; N, 3.66; ν_{max} (ATR)/cm^{-1} 1620, 1547, 1439, 1361, 1322, 1259, 1175, 1019, 789, 720, 699; *m/z* (FAB) 706 (20%) [M + H], 488 (10%) [M - nacnac]; mp: >350 °C.

5.7 X-ray crystallography

Crystallographic data analysis was carried out in collaboration with K. Singh (Department of Chemistry, University of Leicester). Data for **22**, **23b**, **25** and **26** were collected on a Bruker APEX 2000 CCD diffractometer, as was the unit cell determination performed on **21**. Details of data collection, refinement and crystal data are listed in Tables 5.4 to 5.5. All data were collected using a graphite monochromated Mo-K$_\alpha$ radiation (λ = 0.71073 Å) and the reflections were corrected for Lorentz, polarisation and absorption effects. The structures were solved by full-matrix least squares on F^2 using SHELXTL version 6.10.[26] Carbon bonded hydrogen atoms were included in calculated positions (C–H = 0.96 Å) with isotropic displacement parameters set to 1.2 Ueq(C). Non-hydrogen atoms were refined with anisotropic displacement parameters. Disordered butane molecules were removed from the unit cells of **23b** and **25** using the SQUEEZE option in PLATON.[27]

Table 5.4 Crystallographic parameters for **22** and **23b**.

Compounds	22	23b
Singh code	10122	10037
Formula	$C_{38}H_{56}CrClN_2O_3$	$C_{34}H_{48}ClN_2O_2V$
Mc	676.30	603.13
Crystal size (mm)	$0.31 \times 0.25 \times 0.17$	$0.20 \times 0.14 \times 0.09$
Temperature (K)	150(2)	150(2)
Crystal system	Monoclinic	Monoclinic
Space group	$P2(1)/c$	P-1
Lattice parameters		
a (Å)	9.199(3)	8.654(7)
b (Å)	17.102(5)	12.261(9)
c (Å)	23.308(7)	16.264(13)
α (°)	90	103.982(17)
β (°)	98.817(7)	101.956(17)
γ (°)	90	96.948(17
U (Å^3)	3623.6(17)	1611(1)
Z	4	2
D_c (Mg/m^3)	1.240	1.243
$F(000)$	1452	644
μ (Mo-K$_\alpha$)	0.427	0.422
Reflections collected	28095	10195
R(int)	0.1179	0.2349
Independent reflections	7111	5940
Parameters/restraints	0/418	0/371
R_1; $wR_2[I>2\sigma(I)]$	$R_1 = 0.0668$, $wR_2 = 0.1392$	$R_1 = 0.1415$, $wR_2 = 0.3009$
R_1; wR_2 (all data)	$R_1 = 0.1174$, $wR_2 = 0.1573$	$R_1 = 0.3243$, $wR_2 = 0.3886$
Goodness of fit on F^2 (all data)	0.972	0.900

Table 5.5 Selected bond lengths (Å) and angles (°) for **25** and **26**.

	25	**26**
Singh code	10025	10028
Formula	$C_{48}H_{62}N_2O_3V$	$C_{48}H_{62}N_2O_3Ti$
Mc	765.94	762.90
Crystal size (mm)	$0.24 \times 0.19 \times 0.14$	$0.39 \times 0.28 \times 0.11$
Temperature (K)	150(2)	150(2) K
Crystal system	Monoclinic	Monoclinic
Space group	$P2(1)/n$	$P2(1)/n$
Lattice parameters		
a (Å)	11.714(2)	11.708(11)
b (Å)	24.833(5)	24.79(2)
c (Å)	14.878(3)	14.907(14)
α (°)	90	90
β (°)	103.432(4)	103.936(17)
γ (°)	90	90
U (Å^3)	4209.7(15)	4199(7)
Z	4	4
D_c (Mg/m^3)	1.209	1.205
$F(000)$	1644	1640
μ (Mo-K$_\alpha$)	0.278	0.246
Reflections collected	32724	32532
R(int)	0.2277	0.1762
Independent reflections	8274	8243
Parameters/restraints	0/461	0/461
R_1; $wR_2[I>2\sigma(I)]$	$R_1 = 0.0811$, $wR_2 = 0.1524$	$R_1 = 0.0790$, $wR_2 = 0.1780$
R_1; wR_2 (all data)	$R_1 = 0.2617$, $wR_2 = 0.1930$	$R_1 = 0.1396$, $wR_2 = 0.1988$
Goodness of fit on F^2 (all data)	0.770	0.922

5.8. Theoretical calculations

As described in previous chapters, MS calculations were performed with guidance from Dr. M. Roy (Department of Physics and Astronomy, University of Leicester) using the FEFF 8.4 software package[28] on the ULARC and more recently, ALICE computer facilities at the University of Leicester.

5.9 References

1) L. Bourget-Merle, M. F. Lappert and J. R. Severn, *Chem. Rev.*, 2002, **102**, 3031.
2) F. Basuli, R. L. Clark, B. C. Bailey, D. Brown, J. C. Huffman and D. J. Mindiola, *Chem. Commun.*, 2005, 2250.
3) F. Basuli, B. C. Bailey, L. A. Watson, J. Tomaszewski, J. C. Huffman and D. J. Mindiola, *Organometallics*, 2005, **24**, 1886.
4) F. Basuli, B. C. Bailey, J. C. Huffman, M.-H. Baik and D. J. Mindiola, *J. Am. Chem. Soc.*, 2004, **126**, 1924.
5) V. C. Gibson, C. Newton, C. Redshaw, G. A. Solan, A. J. P. White and D. J. Williams, *Eur. J. Inorg. Chem.*, 2001, 1895.
6) L.-M. Tang, Y.-Q. Duan, X.-F Li and Y.-S. Li, *J. Organomet. Chem.*, 2006, **691**, 2023.
7) H. Fan, D. Adhikari, A. A. Saleh, R. L. Clark, F. J. Zuno-Cruz, G. S. Cabrera, J. C. Huffman, M. Pink D. J. Mindiola and M.-H. Baik, *J. Am. Chem. Soc.*, 2008, **130**, 17351.
8) F. Basuli, B. C. Bailey, J. Tomaszewski, J. C. Huffman and D. J. Mindiola, *J. Am. Chem. Soc.*, 2003, **125**, 6052.
9) W.-K. Kim, M. J. Fevola, L. M. Liable-Sands, A. L. Rheingold and K. H. Theopold, *Organometallics*, 1998, **17**, 4541.
10) P. H. M. Budzelaar, A. B. van Oort and A. G. Orpen, *Eur. J. Inorg. Chem.*, 1998, 1485.
11) G. B. Nikiforov, H. W. Roesky, P. G. Jones, R. B. Oswald and M. Noltemeyer, *Dalton Trans.*, 2007, 4149.
12) L. Kakaliou, W. J. Scanlon, B. Qian, S. W. Baek, M. R. Smith, III and D. H. Motry, *Inorg. Chem.*, 1999, **38**, 5964.
13) J. Chai, H. Zhu, H. W. Roesky, Z. Yang, V. Jancik, R. Herbst-Irmer, H.-G. Schmidt and M. Noltemeyer, *Organometallics*, 2004, **23**, 3284.
14) J. Chai, H. Zhu, H. W. Roesky, Z. Yang, Z. Jancik, R. Herbst-Irmer, H.-G. Schmidt and M. Noltemeyer, *Organometallics*, 2004, **23**, 5003.
15) Y.-C. Tsai, P.-Y. Yang, S.-A. Chen and J.-M. Chen, *J. Am. Chem. Soc.*, 2007, **129**, 8066.
16) W. H. Monillas, G. P. A. Yap, L. A. MacAdams and K. H. Theopold, *J. Am. Chem. Soc.*, 2007, **129**, 8090.
17) A. Pramanik and G. Das, *J. Chem. Crystallogr.*, 2009, **39**, 416.
18) Z. P. Li, Y. H. Xing, Y. H. Zhang, G. H. Zhou, C. G. Wang, J. Li, X. Q. Zeng, M. F. Ge and S. Y. Niu, *J. Coord. Chem.*, 2009, **62**, 564.
19) E. J. Tolis, M. J. Manos, A. J. Tasiopoulos, C. P. Raptopoulou, A. Terzis, M. P. Sigalas, Y. Deligiannakis and T. A. Kabanos, *Angew. Chem., Int. Ed.*, 2002, **41**, 2797.
20) R. B. King, *Encyclopedia of Inorganic Chemistry*, Wiley International, 1988, vol. 4.
21) B. Chiswell, L. F. Lindoy and E. D. McKenzie, *Comprehensive Co-ordination Chemistry*, Pergamon Press, Oxford, 1987, vol. 4.
22) W. L. F. Armarego and D. D. Perrin, *Purification of Laboratory Chemicals*, Elsevier, 4th edn, 1996.
23) J. Shamir, *Inorg. Chim. Acta*, 1989, **156**, 163.
24) P. J. Jones, A. L. Hale, W. Levason and F. P. McCullough, *Inorg. Chem.*, 1983, **22**, 2642.
25) M. Stender, R. J. Wright, B. E. Eichler, J. Prust, M. M. Olmstead, H. W. Roesky and P. P. Power, *J. Chem. Soc., Dalton Trans.*, 2001, 3465.
26) G. M. Sheldrick, SHELX-97, Programs for Crystal Structure Analysis, University of Göttingen, Göttingen, Germany, 1997.
27) A. L. Spek, *Acta Cryst.*, 1990, **A46**, 34.
28) FEFF 8.4, Aug. 2006, copyright by A. Ankudinov, B. Ravel and J. J. Rehr. Further information can be found online at: http://leonardo.phys.washington.edu/feff/.

CHAPTER 6

Conclusions

6.0 Conclusions

In an attempt to develop functional dichroic materials in the energy range 5–10 keV, for the purpose of X-ray astronomical polarimetry, the highly ordered square-based pyramidal bimetallic copper(II) bromide complex **1a** (Figure 6.1) has been synthesised and fully characterised by a suite of techniques including single crystal X-ray diffraction. In addition, **1a** has shown great promise as a dichroic material, displaying polarisation dependent features in several regions of its X-ray transmission and fluorescence spectra at the copper (8979 eV) and bromine (13474 eV) K-edges (Daresbury station 16.3 and Diamond Light Source station I16).
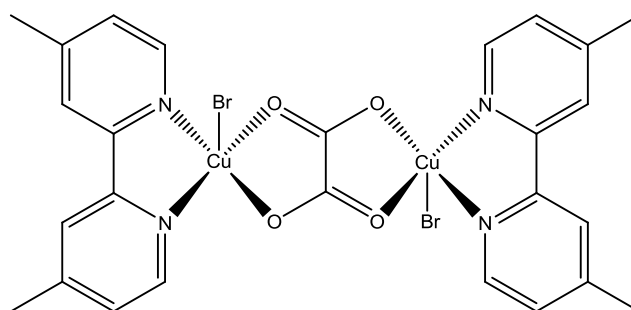

Figure 6.1 Bimetallic **1a**.

The dichroic behaviour of **1a** has been modelled using two theoretical approaches namely TD-DFT and FEFF; the former a molecular orbital approach, while the latter is a multiple scattering approach. Both these techniques have a track record in predicting X-ray absorption spectra. While overall, both approaches accurately model the polarisation dependent spectral features of **1a**, there are apparent differences in the nature of the excited states.

In an effort to simplify the design of the bimetallic copper motif, the bridging oxalate ligand in **1a** had been replaced by a structurally similar, terminally bound bidentate β-diketonate ligand. On the whole, the resultant mono-copper(II) bromide complexes were also highly ordered in the solid state and indeed acetylacetonato-containing **3a** gave a dichroic response at the copper K-edge (8979 eV) (Figure 6.2).
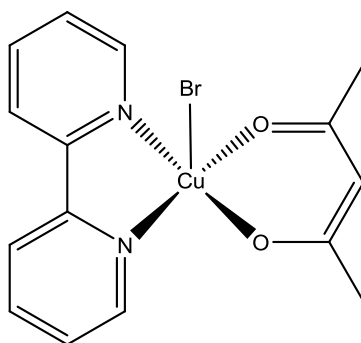
Figure 6.2 Monometallic **3a**.

Extension of this methodology to other 3*d* metal centres other than copper (*e.g.* Ni) in an attempt to expand the energy ranges was hampered by the preference for six co-ordinate geometries displayed in the resultant complexes. On that basis, alternative α-diimine ligands based on the *N*,*N*-pyridylarylimine motif bearing sterically bulky groups in the 6-pyridyl position were employed to enforce the more desired five co-ordinate geometry. Indeed, several five co-ordinate complexes of the type [(α-diimine)MBr(β-diketonate)] [M = Cu (**5**) (8979 eV), Ni (**6**) (8333 eV), Co (**7**) (7709 eV), Fe (**10**) (7112 eV), Mn (**11**) (6539 eV)] were successfully prepared and fully characterised by a range of techniques including single crystal X-ray diffraction (Figure 6.3). Unfortunately the geometrical flexibility of the *bis*-chelates, **6**–**11**, led to the less desirable TBP-like geometries in the solid state; copper-based **5** being the exception in which a square-based pyramidal geometry was exhibited.
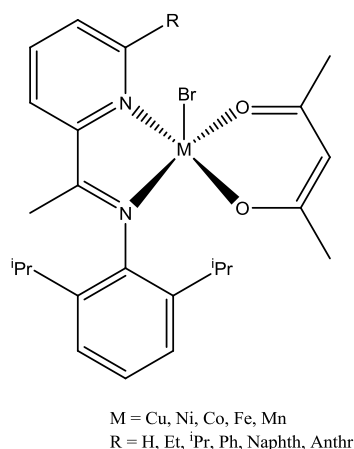

M = Cu, Ni, Co, Fe, Mn
R = H, Et, ^{i}Pr, Ph, Naphth, Anthr

Figure 6.3 Complexes of the type, [(α-diimine)MBr(β-diketonate)] (**5**–**11**; α-diimine = pyridylarylimine).

A synthetic methodology utilising the rigid *tetra*-dentate tetraphenylporphyrin ligand was employed in order to enforce more square-based pyramidal geometries. Hence, a number of TPP-supported metal halide and oxide complexes of titanium (**19**) (4966 eV), vanadium (**18**) (5465 eV), manganese (6539 eV) (**17**), iron (**16**) (7112 eV) and cobalt (**15**) (7911 **eV)** have been successfully prepared and fully characterised (Figure 6.4). Furthermore, these have been shown to exhibit substantial X-ray dichroism at their respective metal and in some cases, halide K-edges. In addition, the polarised X-ray absorption spectra based on tetraphenylporphyrin complexes of vanadium (**18**) and cobalt (**15**) have been modelled using a multiple scattering theoretical approach. In order to explore the possibility of more compact single crystal dichroic filters, iron(III) halide complexes bearing and additional K-edge within the porphyrin ligand framework (**20**) have also been reported and fully characterised herein.
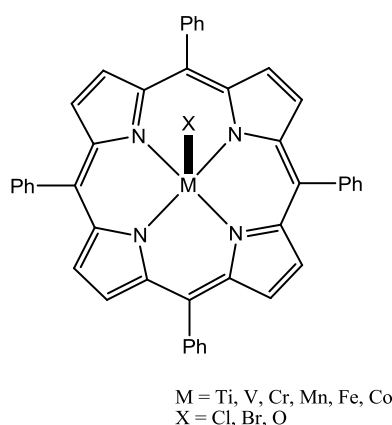

M = Ti, V, Cr, Mn, Fe, Co
X = Cl, Br, O

Figure 6.4 Metallo-tetraphenylporphyrin halide (**15–17**) and oxide (**18–19**) complexes.

Due to the enhanced dichroic response observed at the pre-edge for the titanium(IV) and vanadium(IV)-based oxo metallo-porphyrins (**18**, **19**), alternative molecular platforms designed to accommodate the high-valence nature of these metal centres were also targeted. Several *bis*-chelates based on the *N,N*-nacnac motif of titanium (**24**, **26**) (4966 eV), vanadium (**23**, **25**) (5465 eV) and chromium (**21**) (5986 eV) oxides and halides were successfully prepared and fully characterised. By using simulated polarised X-ray absorption spectra based on a multiple scattering approach, the potential of selected candidates to display X-ray dichroism for X-ray polarimetry has been successfuly demonstrated.
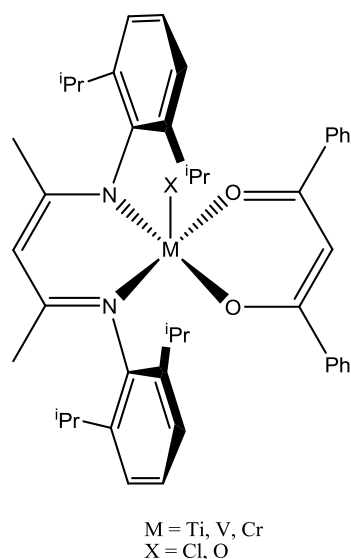
M = Ti, V, Cr
X = Cl, O

Figure 6.5 Monometallic [(nacnac)MX(β-diketonate)] complexes [X = Cl; M = V (**23**), Cr (**21**)] and [X = O; M = Ti (**26**), V (**25**)].

Overall, this thesis has shown by using suitable design and synthetic strategies that five co-ordinate square-based pyramidal dichroic materials can be accessed for the purpose of astronomical X-ray polarimetry. Furthermore, these materials have shown significant polarisation dependence in multiple regions of their X-ray absorption spectra at a range of K-edge energies within the remit of their intended application. With future emphasis placed on controlling crystal size and morphology, along with the application of some coating or passivation technology, these simple materials show great potential to be implemented into a functional X-ray astronomical polarimeter; an impact that may lead to answers of many fundamental questions about our early universe.

Additional Activities

Internal Examinations

Intermolecular Forces; Convenor: Dr. S. Yang.

X-ray Physics post-graduate module; Convenor: Dr. S. Gurman.

Presentations, conferences and symposia

- Presentation: Masters Prize Innovation Award, University of Leicester (UK), 16th May 2011.

    'Engineered materials for applications in X-ray astronomical polarimetry'

- Presentation: Inorganic group meeting, University of Leicester (UK), 14th November 2010.

    '*Synthesis of meso-tetraphenyl porphyrins via condensation of dipyrrolemethanes with N-tosyl imines'*

- Presentation: Annual departmental research day, University of Leicester (UK), 21st June 2010.

    'Engineering metallo-porphyrins for applications in astronomical X-ray polarimetry'

- Presentation: Space Research Centre seminar programme, University of Leicester (UK), 14th May 2010.

    'Engineered molecular inorganic materials as transmissive filters in X-ray polarimetry'

- Presentation: Inorganic group seminar, University of Leicester (UK), 10th September 2009.

    'EXAFS of copper(II) complexes at the air-water interface by a polarised total reflection X-ray absorption technique'

- Presentation: Astronomical X-ray polarimetry consortium meeting, University of Leicester (UK), 10th September 2009.

    'Transition metal co-ordination compounds as materials for X-ray colarimetry'

- Presentation: Astronomical X-ray polarimetry consortium meeting, University of Leicester (UK), 1st April 2008.

    '1st and 2nd generation dichroic filters (design optimisation)'

- Presentation: Inorganic group seminar, University of Leicester (UK), 8th November 2007.

    'Novel functional materials based on metal organic frameworks'

- Poster: Meeting of the RSC co-ordination chemistry discussion group, University of Leeds, 29–30th June 2010.

    'Metal organic frameworks (MOFs) as materials for X-ray polarisers (an experiemental and theoretical study)'

- Conference: RSC Dalton division award symposium, University of Warwick, 21st April 2009.

Internal Seminar Programme

- Diamond light source seminar, C. Norris, Diamond Light Source LTD, 20th October 2008.

- *Organic synthesis by gold catalysed alkyne actication*, P. Davies, University of Birmingham, 5th November 2008.

- *Generation of structural diversity by class 1 terpenoid synthases*, R. K. Allemann, University of Cardiff, 19th November 2008.

- *Asymmetric catalysis of C=O or C=N bond reduction*, M. Willis, University of Warwick, 25th Febuary 2009.

- *Green chemistry and the biorefinery*, J. Clark, University of York, 6th may 2009.

- *Using ruthenium to activate and break carbon-carbon triple bonds*, J. Lynam, University of York, 28th October 2009.

- J*uggling with electrons and anions: A Eulogy to metalcyclic compounds*, J.-P. Djukic, Institute de Chemie de Strasbourg 16th November 2009.

- G*old N-hetrocyclic carbene complexes in homogeneous catalysis*, S. P. Nolan, University of St. Andrews, 9th December 2009.

- *C–F bond construction and destruction*, V. Gouverneur, University of Oxford, 27th January 2010.

- *Adventures in conjugate addition chemistry from alkene hydroacylation to protein bioconjugation*, S. Caddich, University College London, 27th December 2010.

- *C–H and C–C bond making and bond breaking: Fundamentals though to catalysis*, A. Weller, University of Oxford, 9th March 2011.

Courses Attended

- Fire safety (October 2007).
- Team building and leadership (October 2007).
- Introduction to analytical techniques (October 2007).
- Demonstrating and teaching skills (October 2007).

Publications

Simple transmissive filters to measure astrophysical X-ray polarisation, A. Armitage, N. P. Bannister, S. P. Collins, D. V. Cotton, G. W. Fraser, K. D. M. Harris, B. Kariuki, A. Martindale, B. Palmer, M. Roy and G. A. Solan, *SPIE Newsroom*, 2009, DOI: 10.1117/2.1200904.1585.

Probing the effect of binding site and metal centre variation in pentadentate oligopyridylimine-bearing bimetallic (Fe$_2$, Co$_2$, Ni$_2$) ethylene oligomerisation catalysts, A. P. Armitage, H. Grigoli, J. D. A. Pelletier, K. Singh and G. A. Solan, *Eur. J. Inorg. Chem.*, 2008, 4597.

Metallo-porphyrin complexes as transmissive filters for X-ray polarimetry, A. P. Armitage, N. P. Bannister, S. P. Collins, D. V. Cotton, G. W. Fraser, K. D. M. Harris, M. Roy and G. A. Solan, 2011, *Inorg. Chem.*, In preparation.

The rationalisation of X-ray dichroism in copper(II) co-ordination compounds: a combined experimental and theoretical approach, A. P. Armitage, N. P. Bannister, S. P. Collins, D. V. Cotton, G. W. Fraser, K. M. Harris, M. Roy and G. A. Solan, 2011, *Phys. Rev. B*, In preperation

Phenolate substituent effects on the ring-opening polymerisation of ε-caprolactone by aluminum(III) complexes bearing 2-phenolate-6-(amidomethyl)pyridine chelates, W. Alkarekshi, A. P. Armitage, O. Boyron, C J. Davies, A. Gregory, K. Singh and G. A. Solan, 2011, *organometallics*, in preparation.